Absolute frequency measurement of an 171Yb lattice clock and optical clock comparisons

ScuDo

Scuola di Dottorato ~ Doctoral School

WHAT YOU ARE, TAKES YOU FAR

Doctoral Dissertation

Doctoral Program in Metrology (30^{th}cycle)

Absolute frequency measurement of an ^{171}Yb lattice clock and optical clock comparisons

By

Benjamin Rauf

******

Supervisor(s):

Dr. Davide Calonico, Supervisor

Doctoral Examination Committee:

Dr. Jérôme Lodewyck , Referee, SYRTE, Observatoire de Paris

Dr. Gabriele Ferrari , Referee, CNR–INO Trento

Prof. X.X, University of...

Prof. X.X, University of...

Prof. X.X, University of...

Politecnico di Torino

2018

Declaration

I hereby declare that, the contents and organization of this dissertation constitute my own original work and does not compromise in any way the rights of third parties, including those relating to the security of personal data.

Benjamin Rauf
2018

* This dissertation is presented in partial fulfillment of the requirements for **Ph.D. degree** in the Graduate School of Politecnico di Torino (ScuDo).

I would like to dedicate this thesis to my loving parents

Acknowledgements

I would like to acknowledge the various contributions from many helping hands without whom this work could not have been completed. First of all there is my supervisor, Davide Calonico, who is also leading the research group of the Yb optical frequency standard (and the optical metrological fibre network and femtosecond comb activities) at INRIM. Then there are my colleagues who have been working with me on the Yb lattice clock at INRIM: Marco Pizzocaro, Pierre Thoumany, Gianmaria Milani and Filippo Bregolin. The absolute and ratio frequency measurements with the Yb clock would not have been possible without the contributions of the cryogenic Cs-fountain and femtosecond frequency comb teams, namely: Filippo Levi, Giovanni A. Costanzo, Cecilia Clivati, Massimo Zucco, Anna Tampellini and Piero Barbieri. Further thanks go to Elio Bertone and Maria Carmen Vélez López. My work at NPL was conducted within and under supervision of the femtosecond frequency comb group lead by Helen Margolis. A great deal of the obtained results was due to the work of Antoine Rolland. I also extend my gratitude to my colleagues from the transportable Sr clock at PTB and the Yb ion, Sr ion and Sr lattice clocks at NPL.

Funding This work has been funded by the "European Metrology Program for Innovation and Research" (EMPIR) project 15SIB03 OC18. This project has received funding from the EMPIR programme co-financed by the participating states and from the European Union's Horizon 2020 research and innovation programme.

Abstract

The measurement of time and frequency is at the heart of many technological applications and scientific measurements alike. In fact, the SI-unit the second is by quite a margin the SI-unit with the best relative uncertainty (ca. 10^{-16}), given by the accuracies of Cs fountain clocks probing the $F = 3 \rightarrow F = 4$ ground-state transition in ^{133}Cs. Still, demands for even higher accuracy and especially stability (a Cs fountain needs up to two weeks for the statistics to reach its declared uncertainty) are uttered in support of technological advancements (e.g. geodesy and GNSS systems) as well as fundamental science (physics beyond the standard model, tests of relativity).

Nowadays optical lattice clocks confining a large number of neutral atoms in Stark shift free optical traps (the Stark shift free condition is characterised by a so-called "magic wavelength" of the trap) propose good candidates for a future redefinition of the SI-second in terms of an optical transition. Their accuracy and stability already surpass the Cs-fountains by two and three orders of magnitude, respectively. With further improvements to be expected in the near future, the application of optical lattice clocks to relativistic gravimetry, quantum computing, quantum simulation and fundamental physics keeps evolving.

This thesis describes the development and characterisation of an ^{171}Yb lattice clock at INRIM as well as its first frequency measurement campaigns and technologies towards improved optical frequency measurements. The lattice clock confines cold atoms in a 1D optical dipole trap at the magic wavelength, which also cancels any Doppler- and recoil-related effects on the ultra-narrow clock transition. The first chapter offers a general overview of the physics behind lattice clocks and optical frequency measurements.

In the second chapter the ^{171}Yb lattice clock developed during this work is expounded, including the trapping, state-preparation and state-probing of ultracold atoms inside the optical lattice. An exhaustive uncertainty budget for the clock

transition is given and discussed showing already a performance beyond state-of-the-art Cs fountain clocks. An absolute frequency measurement obtained during this work is laid out. The result represents the lowest uncertainty achieved in a measurement of this transition against a primary frequency standard so far and is in agreement with previous values obtained by other groups around the world.

A proof-of-principle experiment demonstrating for the first time the feasibility of transportable optical lattice clocks for geodesy and metrology applications outside of laboratory environments is described in chapter three. This experiment was conducted in collaboration with PTB and NPL and included a geodetic measurement with a transportable optical lattice clock that agreed with conventional methods as well as an optical $^{171}\mathrm{Yb}/^{87}\mathrm{Sr}$ frequency ratio measurement, enlarging the database on this particular ratio and thereby contributing to a possible redefinition of the SI-unit the second in terms of an optical transition or frequency-ratio matrix in the future.

The fourth chapter discusses improvements added to the Yb lattice clock after the aforementioned measurements, in particular the stabilisation of the cooling and trapping lasers on a single stable low-drift cavity using mirrors coated for three disparate wavelengths across the optical spectrum. The simultaneous offset sideband locking and a throughout characterisation of the cavity are discussed.

The last chapter is about the characterisation and optimisation of the NPL "universal oscillator", which was conducted during my secondment at the NPL research facilities in the UK. The universal oscillator consists out of a femtosecond frequency comb, an ultra stable master laser and six slave oscillators. The femtosecond comb is transferring the stability of the superior master oscillator cavity to all six slave oscillators, which includes five lasers ranging from the infrared to the visible region. The principle of operation is explained and the obtained high performance of the spectral purity transfer set forth and discussed. This experiment demonstrated an unprecedented spectral purity transfer performance in a multi-branch configuration, opening the way for the interrogation of whole clock ensembles by just one master oscillator.

Contents

List of Figures

List of Tables

Chapter 1

Optical Frequency Standards

1.1 Introduction

Throughout most of human history time had been related to astronomical events such as the orbit of the earth around the sun for a year or the lunar cycle for months and the rotation of the earth for days. At the advent of a basic unit, called the second, it was only natural to refer it to a fraction $(1/86400)$ of the mean solar day. This definition obviously goes well with human experience, but has the disadvantage of changing with time due to tidal/seasonal effects and long-time drifts of earth's orbit.

Since Niels Bohr described the electromagnetic oscillations of atomic systems with energy levels separated by a fixed energy difference, the discrete (or quantised) nature of atomic systems has been evident. The reason for that is the quantum-mechanical nature of the atom's core and electrons and their electro-magnetical (EM) interaction. Therefore, assuming these laws are universal, the difference energy between two atomic energy levels is the same for any unperturbed atom. When driven on resonance by an electro-magnetic wave this energy is absorbed or emitted as a photon of corresponding frequency, offering a universal frequency reference. Therefore the frequency of an atomic transition serves as a superior definition of the basic time unit, the second.

Since 1967 microwave clocks based on the $F = 3 \Rightarrow F = 4$ ground state Hyperfine-transition in ^{133}Cs constitute the standard for the SI-unit the second.

In recent years atomic clocks based on optical transitions in ions or neutral atoms have surpassed the current realisation of the SI-second with Caesium fountain clocks by more than one order of magnitude in accuracy as well as in stability [1] and have therefore been recognised by the "Bureau International Des Poids Et Mesures" (BIPM) [2] as secondary representations of the second. Among these atomic frequency standards is the spin and angular-momentum forbidden and therefore long-living ${}^1S_0 \rightarrow {}^3P_0$ transition in neutral ^{171}Yb.

The fermionic ^{171}Yb isotope has a nuclear spin of $I = 1/2$ leading to a two-level hyperfine structure, which makes it an interesting candidate not only as a frequency standard [3–7], but also for quantum computing [8] and quantum simulation [9, 10]. Its sensitivity to possible variations of the fine-structure constant makes it also an interesting proposal for fundamental science looking for physics beyond the current standard model [11].

Quantum Projection Noise And Allan Variance

Quantum mechanics imposes a limitation on the knowledge of the electronic state of a 2-level atom driven on resonance by an electromagnetic field called the "Quantum Projection Noise" (QPN). The EM field excites the atom into a superposition of excited- and ground-state. The relative amplitudes of these two states within the superposition depend upon the pulse area $A = \int_0^T \sqrt{\delta^2 + |\Omega|^2} dt$, where Ω denotes the Rabi frequency and δ the detuning of the photonic frequency from resonance. When measuring the electronic state of the atom its wavefunction collapses to either state with the corresponding probability. This uncertainty is present in any quantum-measurement and represents the uncertainty in a-priori knowledge of a quantum state before measurement. It limits the stability of any atomic clock. In the case of this work the interrogating laser exerts Rabi pulses with a π pulse area to the atoms in the ground state. The frequency difference between the atomic transition and the laser is calculated by taking the average value of two pulses applied on the fringes of the spectroscopic line and the result used to stabilise the laser to the transition. The maximum error signal sensitivity is obtained if the excitation probability is about 0.5 (corresponding to a detuning of half the transition linewidth). The projection operator $P_e = |e\rangle\langle e|$ has an expectation value of p, called the excitation probability. The variance of the excitation probability is:

$$\begin{aligned}(\Delta P_e)^2 &= \langle (P_e - \langle P_e \rangle)^2 \rangle \\ &= \langle P_e^2 - 2\langle P_e \rangle P_e + \langle P_e \rangle^2 \rangle \\ &= p(1-p)\end{aligned} \tag{1.1}$$

Taking N atoms the excitation probability turns into a binomial distribution with a variance of:

$$\sigma_p^2 = \frac{p(1-p)}{N} \tag{1.2}$$

This transfers to an uncertainty in frequency by multiplication of σ_p with the linewidth, γ. Here γ represents the full width at half maximum (FWHM) and consequently $p = \frac{1}{2}$ is assumed. A constant K is also introduced to account for different lineshapes ($K \approx 1$ for a lorentzian shape and $K = \pi$ for Ramsey and, in approximation, Rabi spectroscopy) [12]:

$$\delta\nu = \frac{\sigma_p \cdot \gamma}{K} \tag{1.3}$$

And introducing the quality factor $Q = \frac{\nu_0}{\gamma}$ it follows:

$$\frac{\delta\nu}{\nu_0} = \frac{\sigma_p}{K \cdot Q} \tag{1.4}$$

The stability of oscillators is commonly given in terms of the Allan-variance [13], a temporal uncertainty of the mean. The Allan-variance at a certain time τ is obtained by dividing the time of the measurement, T, into $M \in \mathbb{N}$ packages of duration τ and taking the average of the difference between adjacent packages. The Allan-variance is defined as:

$$\sigma_y^2(\tau) = \frac{1}{2M-1} \sum_{i=1}^{M-1} [\langle y \rangle_{i+1} - \langle y \rangle_i]^2 \tag{1.5}$$

where $\langle y \rangle_i$ is the i-th measurement of the average fractional frequency difference $y = \Delta\nu/\nu_0$ over duration $\tau = T/M$.

A cold atoms clock, such as the one described in this thesis, is usually operated in a pulsed operation mode. First the atomic sample is cooled and captured and then the clock transition frequency is interrogated. One single measurement point therefore corresponds to one cycle of atomic state preparation and subsequent interrogation of N atoms within a cycle time T_c. As a result during an integration time τ a total of τ/T_c atomic samples have been interrogated. Using π Rabi-pulses (probing the fringes of the Fourier-limited lineshape) the relative quantum projection noise of a spectroscopic line (for now ignoring the state-preparation time and assuming white noise) is then obtained by inserting equation 1.4 into equation 1.5 [14, 12]:

$$\sigma_y(\tau) = \frac{1}{2\pi Q\sqrt{N}}\sqrt{\frac{T_c}{\tau}} \tag{1.6}$$

It becomes clear that high Q and N (obtainable by high frequencies and large interrogated atomic samples) lead to low QPN. With cycle-times around 1 s the quantum projection noise of a nowadays achievable 1 Hz linewidth in the optical domain (10^{15} Hz) and 10^5 captured atoms results as $\sigma_y(\tau) = 10^{-18}\frac{1}{\sqrt{\tau}}$. This stability limit supersedes by about 4 orders of magnitude any modern microwave standard.

Dick Effect

In all optical atomic clocks the interrogation of the atomic sample with the clock oscillator cannot be continuous, as the preparation of the cold atomic sample and the state read-out demand a finite amount of time. In consequence, a dead time is introduced in the spectroscopy of the atomic line, during which the frequency of the oscillator is not compared to the atomic transition. This leads to a degradation in stability with respect to equation 1.6, as the frequency noise of the clock oscillator at Fourier frequencies near the harmonics of the inverse cycle time $1/T_c$ is down-converted into the spectroscopy [15, 16]. The exact degradation of the clock stability through this so-called Dick effect depends on the fraction that the dead time occupies within the cycle time, the interrogation method (Rabi or Ramsey spectroscopy) and the oscillator noise spectrum. It can be calculated via [15, 17]:

$$\sigma_y^2(\tau) = \frac{1}{\tau g_0^2}\sum_{m=1}^{\infty}(g_{c,m}^2 + g_{s,m}^2)S_y^f(m/T_c) \tag{1.7}$$

Here T_c is the clock cycle time and m an integer number. Consequently $S_y^f(m/T_c)$ is the one-sided power spectral density of the clock oscillator at the Fourier frequency m/T_c. The $g_{c,m}$ and $g_{s,m}$ factors are the Fourier sine and cosine series coefficients of the time-dependent sensitivity function $g(t)$. The coefficient g_0 normalises the Fourier series. It holds [17]:

$$g_{s,m} = \frac{1}{T_c}\int_0^{T_c} g(x)sin(\frac{2\pi mx}{T_c})dx \tag{1.8}$$

$$g_{c,m} = \frac{1}{T_c}\int_0^{T_c} g(x)cos(\frac{2\pi mx}{T_c})dx \tag{1.9}$$

$$g_0 = \frac{1}{T_c}\int_0^{T_c} g(x)dx \tag{1.10}$$

The sensitivity function g(t) gives the change of excitation probability $\delta P(t,\delta\phi)$ as a result of an infinitesimal phase-step of the clock oscillator, $\delta\phi$:

$$g(t) = 2\lim_{\delta\phi\to 0} \delta P(t,\delta\phi)/\delta\phi. \tag{1.11}$$

The function is calculated by looking at the excited state fraction with respect to probing time and detuning from resonance. In the case of Rabi spectroscopy with a π-pulse it is given by [18, 19]:

$$g(t) = \frac{\delta_{HM}}{(1+\delta_{HM}^2)^{3/2}}[sin(\Omega_1(t))(1-cos(\Omega_2(t))) + sin(\Omega_2(t))(1-cos(\Omega_1(t)))] \tag{1.12}$$

, where $\Omega_1(t) = \beta t/t_p$, $\Omega_2(t) = \beta - \Omega_1(t)$, $\beta = \pi\sqrt{1+\delta_{HM}^2}$ and the Rabi pulse time t_p and the half-maximum detuning $\delta_{HM} = 0.799$.

The Dick effect is a major limitation for the stability of contemporary optical atomic clocks based on neutral atoms. Therefore techniques to reduce this effect are being developed. Among these are improvements of the interrogating local oscillator [20–22]. Another approach is the reduction of the dead time using non-destructive measurements of the state occupation [23–25]. The comparison of more than one atomic clock system in a synchronous fashion [26–28] cancels the laser noise in

differential measurements, although the individual clocks are still limited by the Dick effect. A zero dead time clock with two cold atom ensembles and continuous interrogation of the atomic sample has recently been demonstrated, effectively suppressing the Dick effect [29].

1.1.1 Ion- and Neutral-Atoms Frequency Standards

After having established optical atomic transitions as preferred candidates, the question still remains how to suppress the perturbations acting on the atomic energy levels. Among these are most prominent the Doppler effect resulting from the movement of the atom (at room temperature often several hundred m/s) and the Stark shift (outer electric fields bending the level structure).

There are two quite diverse approaches to obtain Doppler-free spectroscopy of the so-called "clock-transition" in optical atomic clocks. The historically first method is to charge the atom and use static and RF electromagnetic fields which push and confine the atom to a tiny well-defined field-free region. The charged atoms are easy to control in Paul-traps or similar geometries and the electronic structure of the outer-shell electrons well predictable. Optical ion clocks have already demonstrated accuracies in the 10^{-18} region [30], trapping single atoms for as long as several weeks [31] and possibly even years.

But the charge the ion carries is also limiting this approach in one serious attribute: It prevents loading of multiple ions to be simultaneously interrogated inside the narrow (mm-scale) trapping region due to electric repulsion. Therefore ion clocks suffer from low stability due to the QPN of the single oscillator. Nowadays ion clocks reach stabilities on the order of 10^{-14} to 10^{-15} at 1 s [32].

Neutral atoms do not exert such long-range attractive or repulsive forces, making it possible to confine them with high density, but are harder to control. Therefore it is attainable to interrogate high numbers of oscillators (atoms) simultaneously, thereby reducing the QPN limit. In order to take advantage of the lower QPN limit in comparison to ions, highly stable lasers and Doppler-free trapping are necessary prerequisites. Cooling of atomic vapours to temperatures suitable for loading into Doppler-free traps has only been possible since the advent of laser-cooling technologies, which was first proposed in the 1970s [33, 34] and not too much later demonstrated[35, 36]. It is worth noting, however, that laser cooling was

first demonstrated in ion experiments and has since also become an important part of ion clocks for the same reason as in neutral atom experiments: Doppler-noise suppression. The Nobel prize in Physics 1997 was awarded to Steven Chu, Claude Cohen-Tannoudji and William D. Phillips for their ground-breaking research in the cooling of atomic vapours, including sub-Doppler cooling.

External electromagnetic fields induce dipoles in otherwise neutral atoms. These induced dipoles then interact themselves with the external fields, similar to the aforementioned ions, allowing the trapping of neutral atoms. In order to prevent interactions such as collisions between the atoms the confining electromagnetic field should also have a periodic structure constraining the atoms to separate pockets in space. An optimal trap would confine no more than one atom in each pocket, thereby eliminating shifts of the atomic level structure by the potential of the collision interactions.

High electromagnetic field strengths not only exist with DC and RF-fields, but also in focused laser beams. It is known that dipole oscillators driven with a frequency above resonance experience a force pushing them out of the field's region, whereas red-detuning acts like an attractive force to high field strengths. Self-reflection of such laser rays leads to interference patterns of $\lambda/2$ periodicity and even increased local field intensities as well as field-free regions, suitable for Doppler-motion suppression.

The established method of choice for trapping of neutral atoms are optical lattices. Optical lattices are formed by self-interfering optical fields, using high power lasers, to form a dipole trap with a standing-wave pattern. In any case, the lattice needs to be far-detuned from any atomic resonance as not to excite it. In the case of a red detuned optical lattice the atoms would then be captured at the anti-nodes of the standing wave and for blue detuning at the nodes. In such an optical lattice the atoms are confined to spaces of less than half a wavelength extension, allowing one to consider the atoms as being exposed to a constant AC electric field. The high intensity of the lattice laser results in a dipole potential forming a deep quantum well imposing a quantisation of the atomic motion inside, similar to the quantum-mechanical harmonic oscillator.

In order for the optical lattice to constitute an effective Doppler-free trap, the atomic movement needs to be constrained by suppressing the excitement of vibrational states. For the spectroscopy of the atomic transition not to excite such vibrational states, the sidebands to the clock transition lowering or raising the vibra-

tional quantum state by one quanta need to be separated from the carrier without any overlap. This condition is called the well-resolved sideband regime. A stronger requirement for the Doppler-suppression is the so-called Lamb-Dicke regime [37]. In this regime the recoil from a single (lattice) photon-atom collision is not sufficient to excite a vibrational state of the atom. Therefore an atom inside the lattice stays within its initial vibrational quantum state, removing the sensitivity of the transition to the Doppler- and recoil effects. A more detailed description of an optical lattice in the Lamb-Dicke regime is given in chapter 1.3. The temperature of an atomic ensemble in the lowest trap levels usually corresponds to a few μK [4, 38].

But with the optical lattice a new issue arises. The same potential trapping the atoms is also bending their energy levels. This effect is called the AC-stark shift (Stark shift induced by AC-fields). It results from the interaction between the external EM-field and the atomic electron shell. In contrast to the low-frequency fields of ion traps the action of the optical EM-wave on the level structure is not only dependent upon its intensity at the position of the atom, but also its frequency and polarisation. With the polarisability of ground-and excited state of the clock transition usually not being exactly equal this means an intensity-, polarisation- and wavelength-dependent shift of the clock-transition, far from an unperturbed state.

But luckily for the alkaline-earth elements and electronically similar atoms (e.g. Sr, Yb, Hg, Mg etc.) there do exist several lattice-wavelengths for which the dynamic polarisability $\alpha(\omega)$ of ground- and excited-state are equal (independent of laser intensity to first order) and polarisation-insensitive, leading to an operating condition where not the individual electronic levels, but the clock transition between them is unperturbed by the lattice-field. This specific lattice-laser wavelength is called the "magic wavelength" [39] and a theoretical evaluation of the magic wavelength of ^{171}Yb is shown in figure 1.1.

The principle of operation in an optical lattice clock comprised of capturing, cooling and probing an atomic transition is unchanged, regardless of the atomic species under investigation. Nowadays various groups worldwide are using optical lattices at the magic wavelength to trap a whole bunch of different alkaline-earth like atomic species with ultra-narrow clock-transitions. Among these are Sr [39], Hg [40, 41], Yb [4, 42, 43], Mg [44], Cd [45] and Ca [46] in various bosonic and fermionic isotopes, some of which (^{87}Sr, ^{88}Sr, ^{199}Hg, ^{171}Yb, ^{40}Ca) have been recognised by the Bureau international des poids et mesures (BIPM) as secondary

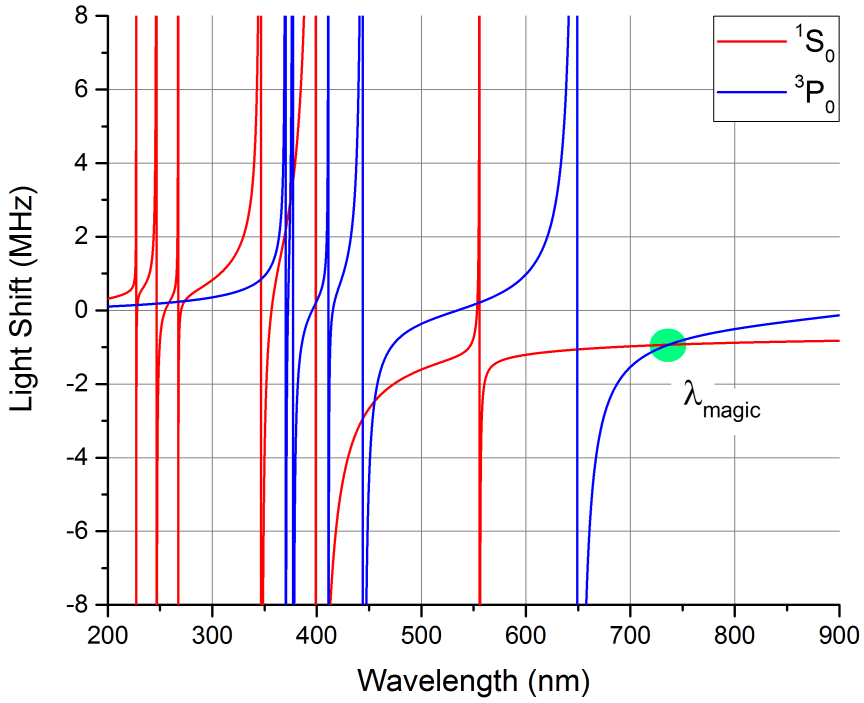

Fig. 1.1 Calculated AC Stark shift of the ground-state ($^1S_0$) and excited-state ($^3P_0$) of the clock transition in ^{171}Yb for a lattice intensity of 25 kW cm^{-2}. The polarisability (and thereby the AC Stark shift) is independent of the lattice polarisation and changes sign around resonances. There are several crossings where $\alpha(^1S_0) = \alpha(^3P_0)$ holds true, but the minimum slope of the difference between those two curves at a position of equal shift is around 760 nm.

representations of the SI-unit the second [47]. All these elements have different advantages and disadvantages over the others. At INRIM the choice for an optical lattice clock fell on the fermionic ^{171}Yb isotope. This element features optical transitions suitable to fast and efficient laser cooling and its spin- and angular-momentum forbidden inter-combination clock-transition features an ultra-narrow linewidth with a near-infrared magic wavelength and low susceptibility to external fields (see chapter 2).

Optical lattice clocks have already demonstrated accuracies similar to the best ion clocks in the low 10^{-18} region and stabilities below 1×10^{-16} at 1 s [48, 49]. Due to the high number of simultaneously interrogated oscillators (10^3 to 10^5) the QPN limit is not yet the limiting factor to the stability, but the interrogation-laser stability [50]. The QPN limit is however a growing matter of concern [49] and proposals to overcome it by squeezing of the atomic states [51] have become a subject of increasing attention [25, 52].

1.2 Laser Cooling

1.2.1 The Light Force

In this chapter a quantitative understanding of the force an electromagnetic wave exerts on a 2-level atom at rest shall be deduced. The mathematical calculations will be abbreviated to shine more light on the physical interpretation, since these calculations are easily found elsewhere [33, 34, 53].

Starting point is a 2-level atom at rest in the centre of the laboratory coordinate-system and a classical electromagnetic wave detuned from resonance. Spontaneous Emission is a result of the non-classical treatment of the electromagnetic fields (precisely the interaction of the vacuum modes with the atom), but the electromagnetic fields in laser cooling can mostly be described as classical fields. Therefore in the following and as to simplify the equations it is viewed as a given attribute of the atom, allowing a semi-classical treatment. The Hamiltonian of such system is:

$$\hat{H} = \frac{\hat{\vec{P}}^2}{2M} + \hbar\omega_A |e\rangle\langle e| - \hat{\vec{D}} \cdot \vec{E}(\hat{\vec{R}}, t) \tag{1.13}$$

The first two terms denote the kinetic and internal energy of the atom, whereas the Dipole operator $\hat{\vec{D}}$ couples the atom and the electromagnetic wave. Calculation of the corresponding force can be found in most basic literature on atom-matter interaction. In short, perturbation theory is applied to the above Hamiltonian and the rotating wave-approximation implemented, taking only frequency terms close to resonance and thereby cancelling off-resonant mixing terms in the potential. For detailed calculations see [54].

The resulting force is the sum of two terms: one contribution proportional to the gradient of the electromagnetic phase (dissipative force), and the other one proportional to the amplitude-gradient of the laser field (conservative force).

The dissipative force is:

$$\vec{F}_{dissip} = \hbar \vec{k} \Gamma \frac{\Omega^2/4}{\delta^2 + (\Gamma^2/4) + (\Omega^2/2)} \tag{1.14}$$

Here $\delta = (\omega - \omega_0)$ is the detuning of the laser from resonance, Ω the Rabi-Frequency and Γ the inverse lifetime (spontaneous emission rate of the excited state). $\vec{k}$ is the usual wave vector with length $k = 2\pi/\lambda$.

The conservative force can be written as the result of a potential (dipole-potential) U_{dip}:

$$\vec{F}_{dip} = -\vec{\nabla} U_{dip} \text{ ,with } U_{dip} = \frac{\hbar\delta}{2} ln\left[1 + \frac{\Omega^2/2}{\delta^2 + (\Gamma^2/4)}\right] \tag{1.15}$$

1.2.2 Doppler Cooling

Having established the radiation pressure force in the previous paragraph its usage for the cooling of an atomic ensemble undergoing thermal motion shall now be considered. An atomic ensemble's velocity distribution is characterised by two parameters: the mean velocity $\langle v \rangle$ and the velocity spread δv around the mean. The attribute "temperature" is defined only in case of a Maxwell-Boltzmann distribution of velocities, but in case of a non-zero mean value an "effective temperature" can be defined over the velocity spread. The usage of a slower beam had already proven to be an effective method in reducing the mean velocity [55] and consequently cooling by radiation pressure force was a natural next step [56]. A cooling mechanism

necessarily has to exert a velocity-dependent force in all directions, leading to what is called an "optical molasses", which does not trap, but can slow down atoms to the so-called Doppler limit by exposing them to 6 red-detuned uniform laser beams in 3 orthogonal space directions with pairwise counter-propagating beams. A quantitative understanding of the laser cooling in optical molasses shall now be established, starting first with one red-detuned laser beam applying the following (purely dissipative, homogeneous field) force on the atoms in the rest frame of the atoms:

$$\overrightarrow{F}(v) = \hbar \overrightarrow{k} \Gamma \frac{\Omega^2/4}{(\omega - \overrightarrow{k}\overrightarrow{v} - \omega_0)^2 + (\Gamma^2/4) + (\Omega^2/2)} \tag{1.16}$$

Here ω and k_L denote the laser frequency and wavevector, respectively, and ω_0 the resonance frequency of the atomic transition. With the laser counter-propagating the atoms a first order power series expansion of the force near $v = 0$ gives:

$$\begin{aligned} F(v) &= F(0) + F'(0) \cdot (v - 0) \\ &= -\hbar k \Gamma \frac{\Omega^2/4}{(\omega - \omega_0)^2 + (\Gamma^2/4) + (\Omega^2/2)} \\ &\quad - v \cdot \hbar k^2 \frac{s}{(1+s)^2} \frac{(\omega_0 - \omega)\Gamma}{(\omega - \omega_0)^2 + (\Gamma^2/4)} \end{aligned} \tag{1.17}$$

where $s = (\Omega^2/2)/[(\omega - \omega_0)^2 + \Gamma^2/4]$ is called the saturation parameter.

Two components of the dissipative force are therefore left: First there is a constant term in the direction of the laser beam and second comes a velocity-dependent force slowing down the atoms. In the limit of low intensities ($s \ll 1$) the force can be simplified to:

$$F(v) = F(0) - v \cdot \hbar k^2 s \frac{(-\delta)\Gamma}{\delta^2 + (\Gamma^2/4)} \tag{1.18}$$

A single beam does not make a molasses, but is sufficient to work as slower beam in one direction. In fact many high-performing atomic clocks use such a slower beam to initially decelerate the atoms entering the science chamber from e.g. a hot atomic oven. The gain of such a system can further be improved by chirping the

laser frequency or implementing a Zeeman-slower [57]. These technologies serve to readjust the detuning from resonance of the Doppler-shifted electromagnetic wave as the atoms slow down along their path to keep an optimised impinging light force. The most common technology, the Zeeman-slower, adjusts, rather than the laser frequency, the atomic resonance by a position-dependent magnetic field resulting in the well-known Zeeman-splitting of the transition, thereby compensating the change in Doppler-shift [58].

Now back to laser cooling: the counter-propagating molasses beam is added to the picture with equal intensity and frequency. One sees directly from equation 1.17 that the constant forces cancel out, leaving only the viscous parts acting on the atom. The laser light facing the atomic movement is Doppler-shifted towards resonance, therefore its action on the atoms is increased, whereas the co-propagating beam is further red-shifted, therefore its force on the atoms is reduced significantly. Adding both forces independently (and thereby neglecting interference effects) is justified for low intensities and spatial averaging , as shown e.g. in[59].The resulting force to first order around $v = 0$ is given by:

$$F(v) = -\alpha v \; with \; \alpha = 2\hbar k^2 s \frac{(-\delta)\Gamma}{\delta^2 + (\Gamma^2/4)} \tag{1.19}$$

where the constant α acts as the friction coefficient of the viscous force F. α is maximum if $\delta = -\Gamma/2$ ($\alpha_{max} = 2\hbar k^2 s$)

An optical molasses is formed by Doppler-cooling in all three space-dimensions.

The Doppler Limit

As each emission process comprises a momentum kick of the atom in a random direction, the atom experiences a random walk, setting a lower limit for atomic motion, and thereby temperature, inside the molasses. To understand the minimum temperature achievable with Doppler cooling a closer look at the momentum dispersion of the atom in a time interval t inside a molasses proves helpful:

$$\delta p^2 = \hbar^2 k^2 \left(\frac{dN}{dt}\right) t \tag{1.20}$$

where $dN/dt = 2s\Gamma$ signifies the absorption rate (kicks per unit time) for low intensities.

This represents a Brownian motion in 3 dimensions ($\delta p^2 = 6D \cdot t$) with a Diffusion coefficient $D = 1/3\hbar^2 k^2 s\Gamma$. This Brownian motion competes with the cooling force. At steady state the heating rate of the Brownian motion, $\delta p^2 (2m \cdot t)^{-1}$, equals the cooling rate, $F(v) \cdot (v)$. Combining equations 1.19 and 1.20 and using the relation between velocity and temperature: $k_B T = m\langle v^2 \rangle$, this leads to an equilibrium temperature T [59]:

$$T = \frac{\hbar\Gamma}{4k_B}\left(\frac{2|\delta|}{\Gamma} + \frac{\Gamma}{2|\delta|}\right) \tag{1.21}$$

The Doppler limit (minimum temperature) results as:

$$T_{Doppler} = \frac{\hbar\Gamma}{2k_B} \tag{1.22}$$

There are various methods for sub-Doppler cooling, some reaching even below the recoil-temperature (the temperature associated with the energy transfer of a single photon recoil event). One very common technology uses polarisation gradients in red-detuned optical molasses creating potential walls to be climbed by the atoms before being pumped to a dark state, thus reducing the kinetic energy of the atom [60, 61]. Other methods exploit the quantum nature of the electromagnetic wave or cool by evaporation, to name just two methods among many others [62–64]. These techniques are especially important for Bose-Einstein-Condensates (BEC) [57].

1.2.3 The Magneto-Optical Trap

The Magneto-Optical Trap (MOT) is the workhorse of cooling in contemporary optical lattice clocks [12]. It is a combination of Doppler-cooling with a magneto-optic trapping mechanism allowing to cool efficiently large numbers of atoms and store them inside a small volume in order for a subsequent transfer into a dipole-trap to take place.

A sketch of the working principle is depicted in figure 1.2. Six laser beams form a red-detuned optical molasses at the position of the atomic cloud. Each pair of counter-propagating laser beams has one beam polarised as $\sigma+$, the other one $\sigma-$.

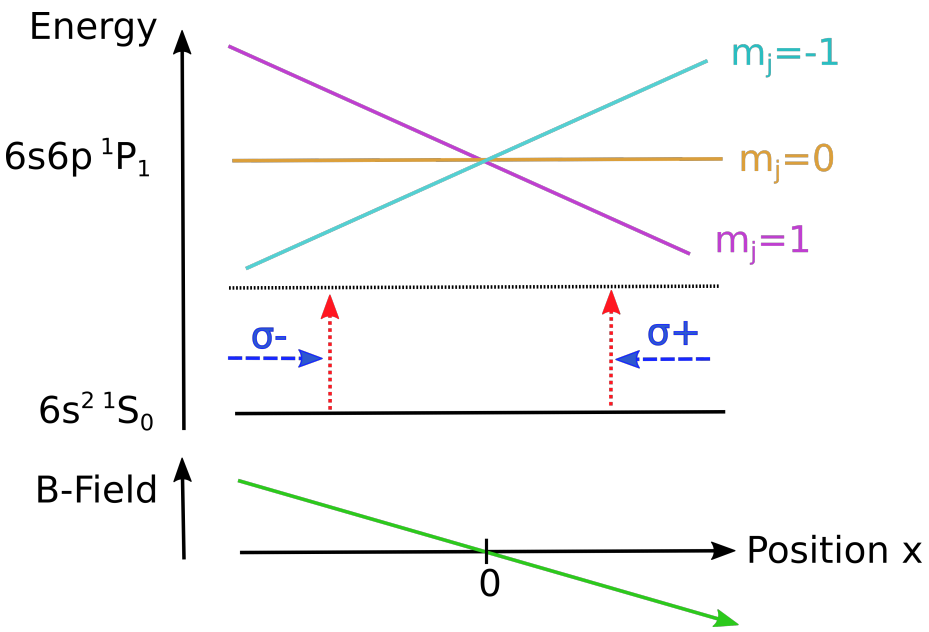

Fig. 1.2 Scheme of a MOT. The magnetic field gradient leads to a position-dependent detuning of the counter-acting circular-polarised lasers, giving an imbalance of net-force. This force is zero only at the centre of the trap where the magnetic field vanishes. The energy-bending of the atomic states is shown in the case of a 399 nm ^{171}Yb MOT (not to scale).

Two coils in anti-Helmholtz configuration lead to a magnetic field with a zero value in the centre of the trap and increasing field strength towards the trap-ends with opposing directionality. In consequence The energies of the excited Zeeman-split m_J states are bend in opposite direction as the atom moves from the centre of the trap. This state-bending then detunes the beam pushing the atom towards the centre closer to resonance and the other beam further away, leading to an effective force restoring the atom to the field-free trap centre. In addition with the velocity-dependent force of the molasses the MOT thus captures and stores atoms in the field-free region around the centre of the trap.

The MOT nowadays is a common method of choice in cold atomic physics with fast (fractions of a second) loading times for large (millions) and dense ($10^{10} {atoms}/{\mathrm{cm}^3}$ atomic samples. The exact number of atoms of a certain element as well as their density and temperature depend strongly on the electromagnetic wave's detunig and intensity and the magnetic field gradient applied. The temperatures achievable in a MOT are on the same order as for Doppler-cooling, with momentum-kicks due to photon-absorption and collisions heating the trapped sample.

1.3 Trapping With Optical Lattices

Trapping of neutral atoms is far more difficult than in the case of ions. Therefore historically optical atomic clocks were at first ion- or beam-clocks [65]. An ion is well controlled by static- or RF electric fields. In the case of neutral atoms a different approach is necessary. Fountain clocks have proven a great success in the context of microwave transitions in neutral atoms (e.g. ^{133}Cs and ^{87}Rb), but optical transitions are more sensitive to the Doppler effect, requiring a trapping mechanism that practically cancels any atomic movement [12].

In order to find a suitable trap for neutral atoms the first question is obviously regarding the suppression of the Doppler-shift and the second concerning the interaction between the clock transition, or more general the outer and inner degrees of freedom of the atom, and the trapping mechanism. In fact, a good trap should not perturb the electronic structure of the atom in order to preserve the clock-transition, but strongly act on the outer degrees of freedom of the atoms. To enable the advantage of neutral atoms, higher densities, to be fully exploited, the trap should also

allow for simultaneous confinement of a high number of atoms in a small space, nonetheless with very few collisions between the atoms happening.

It has already been seen in section 1.2.1 that the interaction of any electromagnetic wave with a 2-level atom leads not only to the dissipative, but also to a conservative force, which is proportional to the field-amplitude gradient. Recalling equation 1.15 it becomes clear that the conservative force is running against the amplitude gradient in case of a red-detuned wave and with it for blue detuning. This means that in the case of e.g. a 2-level atom inside a focused laser beam the conservative force will push the atom towards the focal point, where the amplitude (intensity) of the beam is the highest, for red detuning and into the field-free region outside the beam in case of blue-detuning. This allows the construction of various one to three dimensional trapping geometries in the case of red detuned beams, whereas the blue-detuning calls necessarily for a 3D configuration to actually confine the atoms [66].

The focused beam trap, first demonstrated in [67], has one obvious major disadvantage: The focal area needs to be larger than the atomic cloud in order for the atoms to experience a uniform field, meaning that the atomic movement (sparked e.g. by collisions photon-atom or atom-atom) during the clock-transition interrogation is still a major factor. This problem can be overcome by interfering two laser beams of the same frequency and shape (in practice that means usually one retro-reflected beam), leading to a standing wave with a periodicity of $\lambda/2$, called an optical lattice [68].

Given sufficient intensity each trapped atom is then confined to one "pancake" (see figure 1.3) in the case of a 1D lattice, whereas the 2D and 3D lattices result in much smaller trapping regions (e.g. cigar-shaped traps for 2D lattices, "crystal structures" in the 3D case). A blue-detuned lattice always constitutes a 3D round-shaped field free region. Otherwise the atoms escape along a non-confining axis. The exact geometry of these trapping regions is determined by the relative phase and intensity of the involved beams. By introducing a variable phase-mismatch between laser beams the interference pattern and with it the atoms trapped inside can be moved. Red-detuned lattices are very widespread traps for optical lattice clocks, since they can be used with all geometries. On the other hand the 3D beam configuration in a blue detuned lattice always leads to some ellipticity of the resulting lattice polarisation. Contemporary optical lattice clocks feature mostly 1D lattices [7]. These offer the advantage of uniform polarisation over higher dimensional

lattices, allowing a complete cancellation of the vector light shift. On the other hand they are susceptible to cold collision shifts, especially in the case of bosonic isotopes, as multiple atoms might get trapped in each "pancake". But this effect is rather small for spin-polarised fermionic samples [69]. Another apparent issue is the change of the trapping potential along the weak confinement directions, leading to excitation inhomogeneities [70]. A 3D lattice configuration on the other hand promises very low cold collision rates when less than one atom is trapped in one lattice site and also a uniform potential in all directions. But these advantages come at the cost of unavoidable polarisation inhomogeneities with non-zero vector light shifts for isotopes carrying some angular momentum $F \neq 0$. These lattice configurations are also technically more complex to realise [71]. An optical clock with a 3D lattice configuration has been demonstrated using a bosonic isotope [72] and a 2D geometry with Fermions [73] . In the following treatment only a 1D Gaussian beam lattice is regarded, as this is also the only geometry used in this thesis' experiment, although most of the results can be easily transferred to higher dimensions.

The 1D lattice is best analysed using cylindrical coordinates. Along the beam direction the atoms are captured in deep potential wells of periodicity $\lambda/2$. The red-detuned laser light leads to an attractive interaction with the atoms, limiting the atomic movement to the centre of the trap. In contrast the radial direction is much more spread out, since the individual trapping regions (pancakes) have basically the same size as the retro-reflected beam, typically 10^3 times the extension along the beam axis. Therefore the atoms are much less constrained to move along the radial lattice direction. Inserting a retro-reflected Gaussian beam (standing wave) into the dipole-potential, equation 1.15, leads to a trapping potential of the following form (cylindrical coordinates):

$$U_{dip} = U_0 \cdot cos^2(kz) \left[1 - 2 \left(\frac{r}{w_0} \right)^2 - \left(\frac{z}{z_R} \right)^2 \right] \tag{1.23}$$

, with U_0 the peak-potential and wave vector k.

This potential can fairly well be approximated as harmonic in the z- as well as the r-direction:

$$U_{dip}(r,z) = U_0 \cdot (1 - k^2 z^2) \left[1 - 2 \left(\frac{r}{w_0} \right)^2 \right] \tag{1.24}$$

The focusing of the beam along the z-axis has been omitted, since it is usually a very small effect. The radial and axial directions of the problem are completely decoupled and consequently treated independently. The atomic motion along the strong-confinement direction(s) is governed by the laws of quantum-mechanics, since the atomic deBroglie wavelength at a few μK is on the same order of magnitude as the size of the trapping region ($\lambda/2$) [57]. The external degrees of freedom of an atom inside such a potential are therefore described by eigenstates and -energies similar to the quantum-mechanical harmonic oscillator:

$$E_{vib} = U_0 + \hbar\omega_{vib}\left(n + \frac{1}{2}\right) \tag{1.25}$$

with $\omega_{vib} = k\sqrt{\frac{2U_0}{m}}$ along the strong confinement axis (z-axis) and $\omega_{vib} = \omega_r = \frac{2}{w_0}\sqrt{\frac{U_0}{m}}$ in the radial direction. In the following the discussion revolves about the strong confinement axis, unless otherwise noted.

1.3.1 Lamb-Dicke and Resolved-Sideband Regime

A sufficiently deep trapping potential along the lattice direction(s) allows for the atoms to reach the "Lamb-Dicke regime" [37, 74]. In the Lamb-Dicke regime the atomic movement is confined to within one eigenstate of the potential, because the momentum kick from a single photon-atom collision is not sufficient to excite a transition of the atom's vibrational level. Therefore the spectroscopy of the clock transition is (fairly) free of any motional effects, especially the first order Doppler shift. The Energy E_r transferred during one recoil event can simply be expressed in terms of a corresponding frequency ω_{rec}, with $\omega_{rec} = E_r/\hbar$. The Lamb-Dicke regime is consequently characterised by the Lamb-Dicke parameter $\eta = \sqrt{\omega_{rec}/\omega_{vib}}$, and if $\eta \ll 1$ is true, then an atom inside the lattice remains within its initial vibrational state.

Another desired attribute of an optical lattice is the resolved-sideband regime. This simply means that excitations of the clock transition that lower or increase the vibrational state of the atom (red/blue detuned by $\hbar\omega_{vib}$) are well resolved in the spectroscopy signal from the main "carrier" π-transition(s), so that the probe light driving the clock transition does not change the vibrational state of the atoms. This is also called recoil free spectroscopy. These vibrational sidebands are sometimes

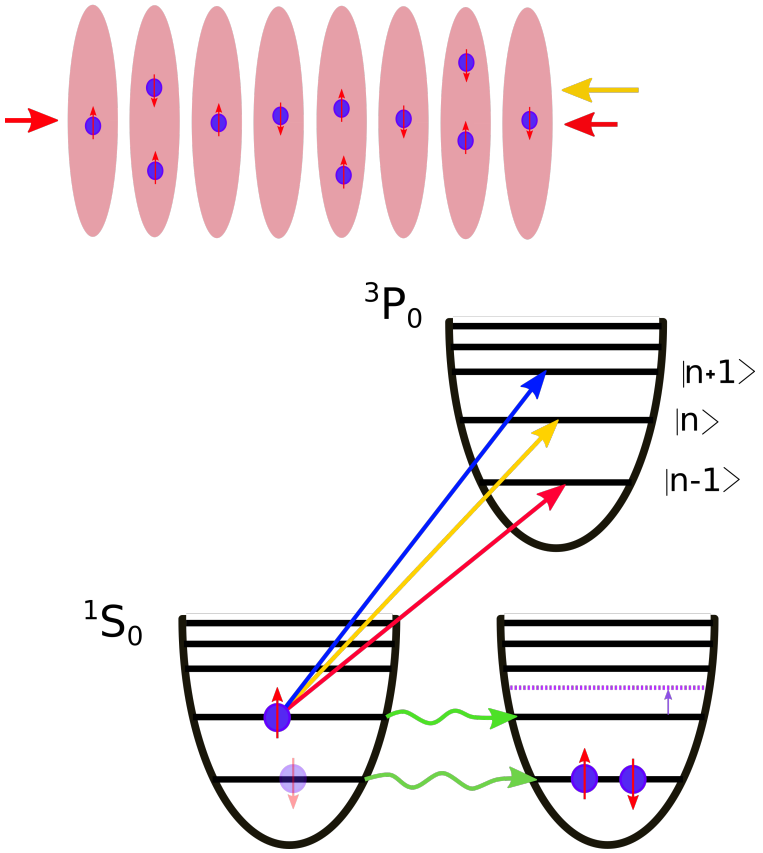

Fig. 1.3 Top: A 1D optical lattice is formed by the standing wave of a self-reflected Gaussian beam (red), the probe beam (yellow) is co-axial oriented.
Bottom: Harmonic potential vibrational states, partially filled with Spin-1/2 atoms. Main transition (yellow) and sidebands (red/blue), which change the vibrational level by one quanta. Tunnelling between neighbouring sites symbolised in green and the Lamb-Dicke regime in purple (the recoil energy from a lattice photon is not sufficient for vibrational level excitation)

used to control the temperature of the atoms inside the lattice. In the case of optical clocks this means that the red-detuned sideband is used to transfer all atoms to the vibrational ground-state of the trap, reducing the spatial and velocity-spread of the atomic sample [75].

1.3.2 Lattice AC Stark Shift

Unfortunately the interaction of the lattice light is not confined to the external states of the atoms. Indeed, as can be seen in the light-force equations (1.14, 1.15), it is solely based upon the connection between the electromagnetic wave and the atomic electronic states. The resulting potential-change is in general not equal for ground- and excited states. The transition suffers an AC-Stark shift, dependent upon the frequency, intensity and possibly also polarisation of the lattice beam. The solution to this problem is to design the perturbation to act equally on ground- and excited state, thus realising the unperturbed transition.

For maximum precision the atom-lattice interaction-operator $\hat{V}$ includes not only the usual dipole-, but also quadrupole- and magnetic-field-interaction [76]:

$$\hat{V} = \hat{V}_{E1} cos(kx) + \left(\hat{V}_{E2} + \hat{V}_{M1}\right) sin(kx) \tag{1.26}$$

The magic wavelength results from a linearisation and is therefore also called the "$E1$ magic wavelength". In contrast to the higher-order contributions, which depend also upon the lattice geometry and polarisation, the magic wavelength is a property of the atomic electronic states and should not depend on the experimental realisation. Therefore the clock transition of a lattice clock is carefully chosen to involve minimum polarisation- and high-order dependencies in order for the magic wavelength to resemble a constant. With lattices far detuned from resonance the polarisabilities of the ground- and excited states need to be calculated including several transitions, weighting by the oscillator strength of each of them [42]. The polarisability α of an atom in state a perturbed by an optical lattice of frequency ν and polarisation vector $\overrightarrow{\varepsilon}$ can be expressed explicitly using the electric dipole matrix elements $\overrightarrow{D}$ and transition frequencies ν_{ab} between states a and b as:

$$\alpha_a(\omega) = \sum_b \frac{2|\langle a|\,\vec{D}\,\vec{\varepsilon}\,|b\rangle|^2}{h} \frac{\nu_{ab}}{\nu_{ab}^2 - \nu^2} \tag{1.27}$$

This equation can be expanded into complicated scalar, vector and tensor terms, as given in [77]. The vector term depends strongly upon the polarisation of the laser. For elliptical and circular polarisation this term gives rise to an interaction that behaves exactly as an artificial magnetic field, whereas in the case of linear polarisation the effect vanishes. The tensor correction depends upon the lattice polarisation, but most of all upon the hyperfine structure / the total angular momentum of the trapped atom. Important in the perspective of this thesis is that for a linear polarised lattice the vector contribution vanishes and the tensor shift disappears for spin-1/2 systems (such as ^{199}Hg or ^{171}Yb).

As optical lattice clocks have progressed, attention has also been given to subtle effects such as hyperpolarisability caused by two-photon resonances near the lattice wavelength [78]. These transitions introduce not only a shift, but also a polarisation-dependence into the lattice interaction with the internal atomic states, even in the case of spin-1/2 systems. Taking into consideration all these effects leads to an energy of a ground-state (g) or excited-state(e) atom in the n-th vibrational eigenstate of the lattice of [76]:

$$\begin{aligned} E_{g(e)}(I,n,\alpha_{g(e)},\beta_{g(e)}) = U_{0g(e)} + \hbar\Omega(I,\alpha_{g(e)},\beta_{g(e)}) \cdot (n+\frac{1}{2}) \\ -E_{anh}(\alpha_{g(e)},\beta_{g(e)},I) \cdot (n^2+n+\frac{1}{2}) \end{aligned} \tag{1.28}$$

with I the single travelling wave intensity, α the polarisability , β the hyperpolarisability , Ω the vibrational frequency and E_{anh} the anharmonic corrections in a spatial Taylor-expansion of the lattice potential around one intensity maximum. For real lattices this is a small correction to the harmonic potential. In practice the trap-depth is directly accessible via spectroscopy of the sideband frequencies applying eq. 1.25. Trap depths are usually given in units of recoil energies U_e/E_r, with U_e being the effective trap depth (the atoms see due to their radial motion moving them away from the centre of the beam a lower trapping potential). After a lengthy calculation the AC Stark-shift of the clock-transition can be given as follows [79, 76, 28]:

$$\begin{aligned}\Delta f = &\left[a\Delta\nu + \frac{3}{4}d(2n^2+2n+1)\right]\frac{U_e}{E_r} - d\left(\frac{U_e}{E_r}\right)^2 \\ &+(a\Delta\nu - b)\left(n+\frac{1}{2}\right)\left(\frac{U_e}{E_r}\right)^{1/2} + d(2n+1)\left(\frac{U_e}{E_r}\right)^{3/2}\end{aligned} \tag{1.29}$$

where a is coming from the ground and excited-state E1 dipole-interaction (eq. 1.26), while b represents the multipolar (E2, M1) corrections and d the hyperpolarisability. Furthermore, $\Delta\nu$ is the detuning from the frequency where the dipole-interaction for ground- and excited-state is equal (this is called the "magic wavelength"). It can be extracted by setting $b = d = 0$. The E1-dipole interaction is the dominant interaction and it is linear in wavelength and trap depths (intensity), whereas the multipolar-corrections as well as the hyperpolarisability introduce non-linear terms and polarisation-dependence to the transition's Stark-shift.

As atomic clocks are pushing the accuracy limitations further down in the 10^{-18} region, realising the unperturbed transition becomes more complex as the contributions of the non-linear term demand careful attention. But there is also one advantage coming with these interactions: The linear- multipolar- and hyperpolarisability-shifts can be used to work against each other by a careful choice of lattice frequency and polarisation, in order to design the Stark-shift of the spectroscopic line to be less sensitive to intensity fluctuations [79], giving a better knowledge of the offset introduced in the experiment to the unperturbed transition than by trying to realise exactly the shift-free spectroscopic line. In this case one speaks of an "operational magic wavelength".

1.3.3 Tunnelling

The periodic lattice potential 1.23 has yet another attribute to be considered: Since the potential walls and their separation is finite tunnelling between adjacent lattice-sites can occur. The tunnelling strength depends on the geometry and depth of the lattice and one might expect it to be very small. But for atomic clocks even these small effects play a role, because tunnelling does lead to the formation of band-structures of the vibrational levels, broadening the clock-transition (see figure 1.3) [80].

Starting again from the dipole-potential 1.23 the interaction-Hamiltonian trapping the atom is:

$$H_{ext} = \frac{\hbar^2 k^2}{2M} + \frac{U_0}{2}\left[1 - cos(2k\hat{z})\right] \tag{1.30}$$

The eigenstates $|n,q>$ are Bloch-states and therefore periodic in q with period $2k$. They are characterised by quantum numbers n and q for band-number and quasimomentum. Calculation of the Bloch-states according to [80] is performed numerically, using the periodicity of the Bloch states. One obtains the eigenenergies and -states. The eigenenergy of any single state varies with quasimomentum q. The variation of the states energy within the first Brillouin-zone $q \in]-k,k]$ gives the bandwidth of the atom's vibrational levels.

The tunnelling effect can be effectively suppressed by introducing a site-dependent potential over the optical lattice lifting the degeneracy of neighbouring sites, leading to so-called Wannier-Stark states [81]. A convenient way (not excluding alternatives) is to align the lattice with an angle between 0 and 90° against the gravitational field of the earth. Even a small angle can be sufficient to make the band structure a negligible contribution to the performance of contemporary optical lattice clocks [82].

1.3.4 Parametric Heating

Fluctuations in the lattice intensity or phase, produced by laser noise, but also mechanical noise on optical components along the optical path, cause parametric excitations of vibrational levels. These lead to a heating of the atomic sample and, together with atom-atom collisions, limit the lifetime of the trap [83]. The exact photon-atom scattering rate caused by these effects depends on the power spectral density (PSD) of the intensity- or phase-noise. A detailed treatment of parametric heating can be found in [84, 85].

Applying an amplitude-modulation of the lattice laser power at the transition frequency of the vibrational lattice modes causes the atoms to transfer to higher lattice states until they are leaving the lattice. The prime resonance occurs at a frequency of $2\omega_{vib}$, just like in classic parametric harmonic oscillator theory [86]. Additional resonances are also found at values of $2\omega_{vib}/n$ with $n \in \mathbb{N}$, as mechanical theory predicts. Another resonance appealing at $4\omega_{vib}$ is not predicted from harmonic

theory, but is a result of the sinusoidal potential shape. The harmonic approximation of the lattice potential in equation 1.24 becomes less accurate for high mode numbers and in fact the sinusoidal lattice potential (equation 1.23) leads to slightly smaller energy spacing than the harmonic oscillator for atoms further away from the trap centre. As a consequence the maximum loss of atoms inside the lattice occurs at slightly lower modulation frequencies than $2\omega_{vib}$. This effect is taken into account by using the effective trap depth U_e.

Following the calculations in [84], the heating of an atomic sample due to laser intensity noise out of a $200\mathrm{E_r}$ deep lattice at 759 nm is calculated in the following: The energy (temperature) of the atoms increases exponentially with the rate constant Γ_ε:

$$\Gamma_\varepsilon = \pi^2 \omega_{vib}^2 S_\varepsilon(2\omega_{vib)} \tag{1.31}$$

After a time t_{ph} of about $t_{ph} = \frac{2}{\Gamma_\varepsilon}$ an atomic sample with an initial temperature of 5 µK is heated out of a 38 µK lattice.

Taking a realistic fractional intensity noise power spectrum of $S_e(\omega) = 10^{-12} 1/\mathrm{Hz}$ at twice the trap-frequency ($2\omega_{vib} = 2 \times 57\,\mathrm{kHz}$) and inserting into equation 1.31, the atomic lifetime results as $t_{ph} = 62\,\mathrm{s}$. In many cases this effect is rather small compared to losses by background-gas collisions (see section 1.4.2).

Effective suppression of parametric heating is achieved through power-stabilisation and phase-locking of the lattice beam. Alternatively it may also be used to investigate the characteristics and dynamics of the optical lattice [85] or to selectively heat atoms of certain vibrational frequencies out of the lattice [87].

1.4 Further Perturbations Of The Clock Transition

As optical lattice clocks are advancing towards new frontiers in accuracy and stability of atomic frequency standards, more and more details of perturbations resulting from environmental or technical sources around the atoms need to be considered. Here the perturbations evaluated with the INRIM Yb lattice clock in chapter 2 are discussed.

1.4.1 Cold Atoms Collisions

As previously shown the atomic motion inside the lattice is described by quantum-mechanics/electrodynamics. The ^{171}Yb isotope is a fermion, therefore the Pauli-exclusion principle holds true and one does expect less cold-atom collisions to happen than in the case of bosonic isotopes. Nevertheless significant shifts from cold atomic collisions were reported in lattice clocks probing the fermionic ^{87}Sr and ^{171}Yb isotopes [88, 4].

Aside from being an obstacle in lattice clocks, the control and measurement of cold-atom collisions in optical lattices has been proposed as an integral part of quantum logic [89, 90] and quantum simulation [91–93] experiments. In these cases the collisional dynamics represent an adjustable interaction between the atoms in the same or neighbouring (mediated by tunnelling) lattice sites.

In lattice clocks the atomic ensemble is spin-polarised to one m_F state before probing. Thus the electronic states of the fermions are degenerate and therefore susceptible to the Pauli-principle, forbidding s-wave collisions. P-wave scattering on the other hand needs higher energies and consequently is largely suppressed at low temperatures. Nevertheless a non negligible s-wave scattering was observed in a 1D lattice capturing ^{87}Sr [70]. This was explained by the radial spread of the atoms, leading to an excitation inhomogeneity lifting the degeneracy of the trapped fermions [94]. Using lattice clocks based on ^{171}Yb the collision processes have been found to be dominated by p-wave scattering [69].

The p-wave interaction is bound to collisions between ground- and excited states, needing an angular momentum between the involved atoms. The collisional shift depends upon the density of the atomic ensemble, namely the number of atoms per lattice site, and the Rabi-pulse area. In the case of spin-polarised ^{171}Yb the resulting shift changes direction when the state-occupation is changed from the ground- to the excited state and has a zero-passing around 0.5 excited-state occupation. The exact position of the zero-passing is shifted from this value by the residual s-wave scattering introduced by the excitation inhomogeneity mentioned before. Furthermore, the slope around the zero-passing is well approximated by a linear slope [95, 96]. With ^{171}Yb a spin-polarisation of 99% is accessible [4], but reducing this ratio leads to significant s-wave scattering appearing due to hyperfine-substates of the clock ground- and excited state colliding. In practice this means a shift of the

excitation-fraction corresponding to a vanishing density shift [95]. The magnitude and uncertainty of the cold collision shift in a contemporary fermionic lattice clock based on Yb or Sr can be as small as a few parts in 10^{18} [96, 48].

1.4.2 Background Gas Collisions

Only a small fraction of hot Yb atoms exiting the oven are cooled and captured during a clock cycle. Therefore collisions between captured cold and free hot atoms can occur. These collisions usually kick the cold atom out of the trap and thereby limit the lifetime of the atomic ensemble inside the lattice. The lifetime of atoms inside the lattice is often on the order of a few seconds [50, 38]. In addition, by calculating the interference between the unperturbed and the perturbed atomic matter-wave stemming from those collision events, one finds that the atomic resonance is shifted approximately by [97]:

$$-\frac{\Delta\nu}{\nu} = \frac{\Delta A}{13.8\pi\nu T_R}\frac{\Delta C_6}{C_6} \tag{1.32}$$

with the amplitude-loss ΔA during the interrogation time T_R and C_6 the Van-der-Waals coefficient of Yb. The magnitude of this shift can be as low as a few parts in 10^{18} [98] in optical lattice clocks.

1.4.3 Black-Body-Radiation

The Black-Body radiation (BBR) induces a systematic Stark-shift on the atomic energy levels, which can be calculated using the spectral density distribution of the BBR. The spectrum of the BBR at room-temperature is largely concentrated in the far-infrared and above wavelengths. Therefore in ^{171}Yb the Stark Shift induced is largely given by the static polarisabilities of the clock states, with the $6s6p^3P_0 \rightarrow 5d6s^3D_1$ resonance giving rise to a dynamic correction factor, η. Other resonances are in practice irrelevant, because their frequency is too far away from the BBR spectrum.

The polarisability of the ground- and excited-state against frequency is given in figure 1.4. The static polarisability can be measured directly by applying strong DC electric fields to the vacuum system as in [99] and the dynamic polarisability from the lifetime of the resonances affected by the BBR [100].

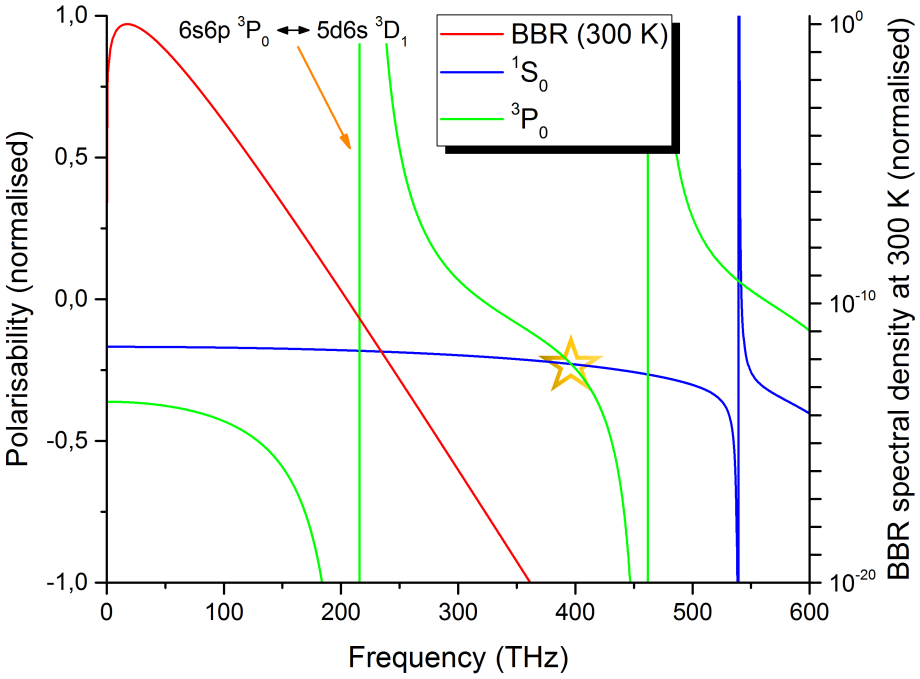

Fig. 1.4 Calculated static and dynamic polarisability of the ground (blue) and excited (green) clock state in ^{171}Yb. The red curve is the BBR spectral density at room temperature. The only relevant transition leading to hyperpolarisability shifts in the range of the BBR emission is marked with an arrow and a yellow star points out the magic lattice frequency.

The BBR shift is finally given by [101, 99]:

$$-\frac{1}{2}\left(\alpha^{DC}_{excited}-\alpha^{DC}_{ground}\right)<E^2>_T\,(1+\eta_{clock}(T)) \tag{1.33}$$

With the averaged field intensity $<E^2>_T$ evaluated at the point of the atoms, usually through modelling of the atom's BBR environment assisted by measurements of the room- and vacuum chamber temperatures.

The uncertainty on the knowledge of the BBR shift as in eq. 1.33 is governed by two contributions: The uncertainty on the value of the polarisability (both static and dynamic) and the environmental field. The first problem is addressed by improved measurements of α [102], while the later needs a combined approach of providing an environment featuring uniform temperature distributions in materials resembling more closely a black-body radiator [103] and/or lower (cryogenic) temperatures [104, 5]. Both of these approaches have successfully reduced the BBR shift uncertainty in an optical lattice clock to no more than 1 part in 10^{18} [103, 5].

1.4.4 Zeeman Contributions

In atomic clocks the hyperfine structure sublevels are often split up by magnetic fields according to the Zeeman-effect. The unperturbed line is then taken as the average value between two $+m_F$ and $-m_F$ states [4]. Magnetic field inhomogeneities or fast temporal variations thereof lead to an uncertainty in knowledge of the mean value, resulting in an effective shift of the measured value from the unperturbed line. Another effect is the second order Zeeman shift. The applied magnetic field mixes the transition's atomic states with nearby ones, introducing a quadratic shift in magnetic field [105, 106]. Assume a three-state system $|1\rangle$, $|2\rangle$ and $|3\rangle$. With the clock-transition being $|1\rangle \rightarrow |2\rangle$ and $E_2-E_3 \ll E_2-E_1$ an external magnetic fields introduces a coupling $\hbar\Omega_B = \langle 2|\,\hat{\mu}\,\overrightarrow{B}\,|3\rangle$, leading to a shift of level $|2\rangle$ of:

$$\Delta_B = -\frac{\Omega_B^2}{\Delta_{32}} = \beta\,\overrightarrow{B}^2 \tag{1.34}$$

Using small magnetic fields this uncertainty contribution can effectively be suppressed. An evaluation of the Zeeman effect in a lattice clock reaching uncertainties well within the 10^{-19} region has been conducted [48].

1.4.5 Probe Light Stark Shift

The (ultra-stable) radiation probing the clock-transition, for this work the ${}^1S_0 \rightarrow {}^3P_0$ line of ^{171}Yb, is usually low in saturation intensity to realise a narrow linewidth, but the polarisability of those states is not equal (see figure 1.1). Therefore the AC Stark shift due to the probe light is a concern. Given the small interrogation intensity stabilising the probe beam power with an active control is usually sufficient to keep the shift-uncertainty low. The shift and uncertainty of this effect can even surpass the 10^{-19} region in highly stable lattice clocks [48].

1.4.6 Line Pulling

Nearby transitions such as hyperfine transitions or lattice sidebands shift the resonance frequency by a quantum interference between the near- and far-detuned transitions. The resulting shift of resonance $|a\rangle \rightarrow |b\rangle$ through the line pulling of nearby transition $|a\rangle \rightarrow |c\rangle$ for interaction times small compared to the state lifetime (as it is in general the case in contemporary optical lattice clocks) is given by:

$$S_0 = \frac{\Gamma_b \Gamma_c + |\Omega_c|^2}{4\omega_{bc}} \tag{1.35}$$

with $\hbar\omega_{bc}$ the energy difference between the states $|b\rangle$ and$|c\rangle$; $\Gamma_{b,c}$ the respective natural lifetime and Ω_c the Rabi-Frequency given by $\sqrt{\Omega_b^2 + \omega_{bc}^2}$. The absolute magnitude of this effect is negligible in many optical lattice clocks and its uncertainty well within the 10^{-18} region [38] or below [48].

1.4.7 Residual Doppler Effect

The linear Doppler effect is cancelled almost completely inside an optical lattice due to the probing direction being the same as the one featuring the strong confinement of the atoms. However, some contribution to the linear Doppler effect can result if the phase between the lattice- and probe-lasers is not fixed. By transferring into the rest frame of the probe laser this becomes equivalent to the atoms experiencing acceleration and deceleration, leading to a linear Doppler shift contribution. This effect is eliminated by establishing a common phase-reference for both lasers. The

lattice is often very sensitive to the mirror reflecting the laser after it has passed through the trapping region, thereby forming the standing wave. Using this mirror as the reference of the Doppler-noise cancellation of the probe laser can reduce the residual Doppler contribution significantly [27].

The confinement in the radial direction is much smaller than in the longitudinal one. Therefore the second-order Doppler effect needs to be considered for atomic motion orthogonal to the strong confinement axis. The transverse relativistic Doppler effect, with the receiver-frame having primed observables, is given by:

$$f' = f\sqrt{1-\frac{v^2}{c^2}} \tag{1.36}$$

The second order Doppler effect is usually negligible, while the first order contribution can reach a few parts in 10^{17} [38].

1.4.8 Fibre Links

For practically all lasers of an optical atomic clock fibre links are the tool of choice to transport light over long distances, preserving good mode-quality and polarisation. But this convenience of optical fibres over free-space paths has one important drawback: The fibres transfer mechanical noise (seismic/acoustic noise etc.) from the environment into optical frequency noise [107]. Changes of environmental conditions, especially the temperature, also alter the optical pathlength of a fibre, leading to slow phase drifts. The same effects appear also for free-space optical paths, but are often less pronounced in laboratory environments. This noise can be relevant to the stability of the laser probing the ${}^1S_0 \rightarrow {}^3P_0$ transition and therefore the fibres connecting this laser to the ultrastable cavity, the science chamber or any other stability-demanding part are commonly actively phase-stabilised. A widespread stabilisation-technique also used in this work is described in [108]. The fibre-path to be stabilised is used as an interferometer by reflecting a part of the light at its end back through the same path to the input, where it is overlapped with a sample of the input light, generating a phase-error-signal. This is then used to correct (feedback or feed-forward) the laser light arriving at the output of the fibre by steering the laser-frequency, often by acting on the frequency of an acousto-optic modulator (AOM). Such optical fibre links are able to maintain the spectral purity of an optical

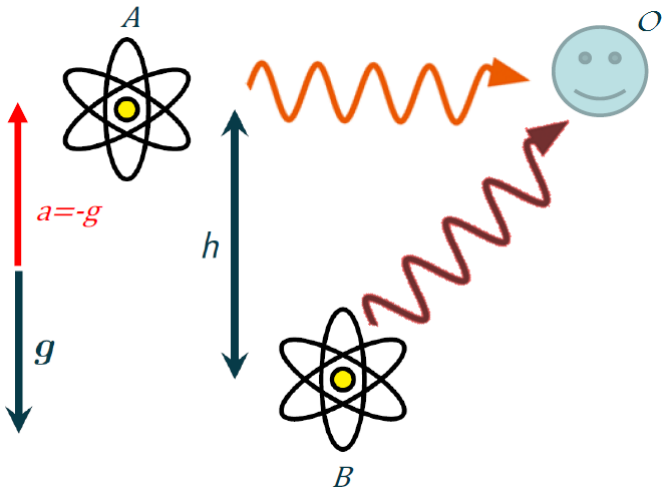

Fig. 1.5 An observer O at rest (right) with atom A inside the accelerated frame of earth's gravitational pull sees light coming from atom B red-shifted with regard to radiation reaching him from atom A

frequency even across continental distances [109–112] and are often contributing with uncertainties below 1×10^{-18} to the measurement.

1.4.9 Gravitational Redshift

Consider two atoms, A and B, located somewhere on the earth's surface suffering the gravitational pull of the planet, just as in figure 1.5. An observer O is at rest with atom A. Atom B on the other hand is located directly below the observer and atom A at a vertical distance h. The Einstein equivalence principle [113] declares that the gravitational pull is locally equivalent to an acceleration in the opposite direction with equal magnitude. Therefore one can think of the atoms and the observer also as travelling inside a spaceship far from earth in outer space, accelerating with $\overrightarrow{a} = -\overrightarrow{g}$ in the opposite direction to the earth's gravitational field.

A photon emitted by atom A with frequency ν_A retains its original frequency and reaches the nearby observer almost instantly. A photon originating at atom B and of frequency ν_B, reaching for the observer, however, needs at least a flight time $t = h/c$. During this time the flight velocity of the accelerated frame, v_t, changes as $\Delta v_t = at = ah/c$. The linear Doppler effect of at the position of the observer follows as $\nu_B = \nu_A(1 - ah/c^2)$.

The gravitational redshift of a frequency emitted with frequency ν_0 in the inertial system of the emitting atom directed against the gravitational pull and detected at height h above, results as:

$$\nu = \nu_0 \left(1 - \frac{gh}{c^2}\right) \tag{1.37}$$

This means that the frequency is red-shifted as the electromagnetic wave moves away from the earth's centre of mass. The unperturbed frequency of the transition is the one emitted in the resting frame of the atomic clock itself. Therefore, when comparing optical clock frequencies, this effect needs to be subtracted from the results. On earth the shift is about $1 \times 10^{-16} m^{-1}$. It is therefore necessary to know the gravitational potential potential difference when comparing remote optical atomic clocks. The common way is to perform geodetic measurements at the sites of the clocks.

Another approach is to turn this situation around and use optical atomic clocks with their outstanding stability and accuracy to determine differences in gravitational potentials [110]. Such experiments have already been performed connecting mostly stationary clocks [114, 110], but a recent measurement involving a transportable optical lattice clock has been demonstrated within this thesis' work and is described in chapter 3 [115].

1.5 Ultra-Stable Lasers and Cavities

1.5.1 Stabilising Lasers

When interrogating a narrow line such as the ${}^1S_0 \rightarrow {}^3P_0$ transition in ^{171}Yb with a natural linewidth well below 1 Hz, the limiting factor for the spectroscopic linewidth and stability is currently the interrogating laser and not the QPN limit of the atomic ensemble, but there are great efforts underway towards reaching that boundary [32, 49].

Current commercial stable laser sources feature linewidths of a few tens of kHz. In order to reduce this to a Hz- or even sub-Hz-level, the laser needs to be stabilised to a reference with outstanding stability especially on short time scales

such as the interrogation time with the atoms. On longer timescales the laser drift in clock-operation is then compensated by a reference to the atomic transition itself.

There are various approaches to provide such a reference for the laser, for example spectral hole-burning [116, 117], ultra-stable cavities [118, 21] and transition lines of hot atomic beams [38]. For the most demanding applications optical cavities are still the common choice due to their overwhelming performance. The short-term reference needs - aside from high stability - to give out a steep-slope and good signal-to-noise ratio error-signal. The generation of a proper error signal is usually achieved by the Pound-Drever-Hall (PDH) method [119], while the stabilisation is often taken care of by a two-stage PID-control acting with one high-bandwidth stage upon the laser's current (e.g. Diode laser) or an AOM/EOM (fibre, solid-state lasers) and the second stage with lower bandwidth acting upon a laser piezo voltage or temperature. The following is a brief summary of the PDH method. The PDH error signal is generated by modulating the phase of the incident beam with a RF frequency, typical in the MHz-region, giving rise to corresponding sidebands of the carrier in the Fourier-analysis. The reflected beam from the cavity changes its phase by π across one cavity resonance. Looking at the reflected beam with a photodiode the interference between carrier and sidebands gives rise to a signal at the phase modulation frequency, which does resemble a linear error-signal around the resonance. This signal is then extracted by demodulation/mixing and filtering from the photodiode-signal.

1.5.2 Cavities - General Approach

Ultra-stable cavities are an important tool within contemporary metrology and science. From gravimetry and gravitational wave detection [120, 121] to laser stabilisation [122] ultra-stable cavities are a mean to the provision and measurement of ultra-precise frequencies. A cavity in its simplest manner consists out of two plan-parallel and opposing mirrors. A coherent light beam entering the gap between them parallel to their surface normals would bounce back and forth between them, giving rise to a standing wave, which stores up energy. The wave intensity depends upon the mirrors reflectances, while the cavity-geometry restrains the possible light-frequencies.

There are also other cavity-configurations possible and part of current scientific development. Most notably are whispering gallery microresonators that utilise a running wave moving in a circle through a tiny (μ-scale) disk-shaped medium [123, 124]. But for high performance laser stabilisation two-mirror cavities are the asset of choice, therefore all other cavity-geometries are disregarded in this thesis.

In the following a cavity is examined consisting out of a horizontally (z-direction) aligned circular spacer of length d and two opposing mirrors with radii R1 and R2. The origin of the coordinate system shall be in the centre of mirror 1. This shall also be the mirror through which the light enters the system.

An arbitrary monochromatic standing wave inside this cavity has the form $U(z) = A \cdot sin(k \cdot z)$ (disregard time evolution due to fast timescales averaging) with wave-vector **k**.

In the following the electric field inside the cavity is taken into account, while the magnetic part is neglected. This is justified by the fact that electric- and magnetic field are behaving exactly similar as waves out of phase by $\pi/2$ and with the same amount of energy stored within them. The wave-vector needs to fulfil the equation $k = q\pi/d$, with $q \in \mathbb{N}$, thus restricting the possible light frequencies to multiples of:

$$\nu_F = \frac{c}{2d} \tag{1.38}$$

, where ν_F is also called the free spectral range. The light impinging on the cavity is reflected, unless it obeys the above condition of the cavity modes. In a real resonator the overlapping beams do not match as perfect as presumed here. Instead the amplitude decreases on each round-trip by a factor r. In the presence of no other loss-channel but the mirrors themselves, it remains: $r = \sqrt{r_1 \cdot r_2}$, with mirror-reflectivities $r_1$and r_2 (reflectivity is defined via intensities). The phase after one round-trip is: $\varphi = 2kd + 2\pi + \delta$

With δ resulting from mirror-imperfections, the intersection medium or occurring from the light frequency having a slight deviation from eq.(1.38). So with each round trip the wavefunction of the beam changes with respect to the incident beam by a factor $a = r \cdot e^{-i\varphi}$. The standing wave is the result of the superposition of all part-waves. Its amplitude A_i is therefore given by ($|a| < 1$ gives geometric series and A_0 signifies the amplitude of the incident beam):

$$A_i = \sum_n A_n = \sum_n A_0 \cdot a^n = \frac{A_0}{1-a} \tag{1.39}$$

Here the dimension-less Finesse F is introduced that is defined as the quotient of FSR over the linewidth of a single cavity resonance. It is also an indicator of how many times an incident light beam bounces back-and-forth between the cavity mirrors. It depends only on the mirrors reflectivities and cavity losses, which can also be viewed as a reduced mirror reflectance.

$$F = \frac{\nu_F}{\Delta\nu} = \frac{\pi r}{1-r^2} \tag{1.40}$$

1.5.3 Finesse And Ring-Down-Time

A high Finesse accounts for high cavity-mirror reflectances and low losses, resulting in a narrow mode-bandwidth. The electric field inside the cavity interferes on every round trip with itself and also with the incoming laser light. Only if the cavity-length is a multiple integer of the half wavelength of the incident beam do all beams interfere constructively with each other after one round trip and so the light power inside the cavity rises. If this condition does not hold true, destructive interference hinders light from entering the cavity. Therefore the cavity acts as a frequency-filter.

An excellent laser stabilisation restrains the laser to a small fraction of the cavity-linewidth. In our case the goal for laser-linewidth is 5 Hz. This kind of laser-locking, usually achieved with the PDH method, requires a stable and narrow linewidth reference, which also delivers a strong error signal. The sources of (in)-stability will be addressed later. A narrow linewidth in a cavity of fixed length is equivalent to a high Finesse and also results in a steep slope error signal. Therefore a high Finesse is an important attribute of ultra-stable cavities. Typical values for 10 cm ultra-stable cavities with a target laser linewidth in the Hz-range are between $F = 100\ 000$ and $F = 300\ 000$. This corresponds to cavity mode linewidths of a few kHz. A stabilisation to one per mille of such a resonance is often achievable with low optical powers circulating inside the cavity.

The Finesse of a cavity is normally assessed using the cavity-ring-down method. The Finesse is determined by a measurement of the decay time of the transmitted light power out of the cavity after the initial beam has been shut down.

First, consider the time-evolution an initial electric field intensity I_0 inside a cavity with the incident beam shut off at time $t = 0$.

Since the laser-light fulfils the resonance condition, the intensity after n round trips is:

$$I(t = n \cdot \frac{2d}{c}) = I_0 \cdot (r^2)^n = I_0 \cdot exp\left[\frac{t \cdot c}{2d} \cdot log\left(r^2\right)\right] \overset{cont.n}{=} I_0 \cdot exp\left[-\frac{t}{\tau_p}\right] \quad (1.41)$$

, where $\tau_p = -\frac{2d}{c}\frac{1}{log(r^2)} = \frac{2d}{c \cdot log(1/r^2)}$ with $1/r^2 \geq 1$ is called the photon lifetime (decay time).

The special case after one round-trip gives:

$$I(t = \frac{2d}{c}) = I_0 \cdot r^2 = I_0 \cdot exp\left[-\frac{2d}{c \cdot \tau_p}\right] \Longleftrightarrow r^2 = exp\left[-\frac{2d}{c \cdot \tau_p}\right] \quad (1.42)$$

Combining (1.40) together with (1.42) results in:

$$F = \frac{\pi\sqrt{exp\left(-\frac{d}{c \cdot \tau_p}\right)}}{1 - exp\left(-\frac{d}{c \cdot \tau_p}\right)} \approx \frac{\pi c \tau_p}{d} \quad (1.43)$$

The Finesse therefore only depends upon the photon lifetime τ_p.

1.5.4 Spherical Cavities

The defining feature of spherical cavities are spherical mirrors. In order for the light inside the cavity to bounce back-and forth between the mirrors and not to escape the cavity, the beam needs to reproduce itself after a finite times of round-trips. This is the case, if the transfermatrix of mirror-spacer-mirror-spacer is the identity after a certain number of roundtrips. After some algebra, calculated in [125], one finds the stability condition as:

$$0 \leq \left(1 - \frac{d}{R_1}\right)\left(1 - \frac{d}{R_2}\right) \leq 1 \quad (1.44)$$

Modes of the Cavity

The laser light inside the cavity is restricted not only by eq.(1.38) in the z-direction, but also in the transverse directions by the shape and size of the mirrors. The incident laser light can be written as:

$$\psi(x,y,z) = \psi'(x,y) \cdot exp(-ikz) \tag{1.45}$$

Insertion of eq. (1.45) into the scalar wave equation $\nabla^2\psi + k^2\psi = 0$ yields:

$$\frac{\partial^2\psi}{\partial x^2} + \frac{\partial^2\psi}{\partial y^2} - 2ik\frac{\partial\psi}{\partial z} = 0 \tag{1.46}$$

The solutions to this equation form a complete and orthogonal set of modes. These solutions are the Hermite-Gaussian- and Laguerre-Gaussian-modes, the first having rectangular and the later cylindrical symmetry. The fundamental mode in both cases is the Gaussian beam. Optical cavities have usually (and also in this work) cylindrical symmetry, featuring circular mirrors.

Yet in real systems only Hermite-Gaussian modes do play a role. This is due to the fact, that the Laguerre-modes are very restricted concerning the radial component of the field (transversal direction), while for Hermite-Gaussian modes the two transversal axes (x, y in eq. (1.45)) are almost independent [125]. Therefore the Laguerre-Gauss modes are disregarded in the following.

A Gaussian beam is at every point along the propagation axis totally determined by its $1/e$ field amplitude radius w(z), distance from the beam-waist z, radius of curvature of the phase-front R(z) and the phase ϕ(z) itself. The parameter beam size, as used all throughout this thesis, means the $1/e$ drop of the field amplitude. The variable w_0 is defined as the radius at the beam-waist and z_0 the distance z along the beam-axis, at which $\frac{w(z_0)}{w_0} = \sqrt{2}$ holds true.

The high-order modes are also characterised by R(z) and w(z) with the difference of a larger total spread of the wavefunction and the appearance of transversal nodes. A significant difference appears in the phase velocity that varies for the high-order modes.

$$\phi(z) = kz - (m+n+1)arctan\left(\frac{z}{z_0}\right) \tag{1.47}$$

With m and n being whole numbers determined by the order of the Hermite-Gaussian mode.

Remark: m and n give the number of the mode's nodes in x- and y-direction with the special case of $m = 0, n = 0$ being the Gaussian beam.

The mode shape of the Gaussian beam inside the resonator follows out of the self-consistency of the resonator's transfer matrix after several round-trips and the fact that the phase-fronts R(z) at the positions of the mirrors need to match the curvature of the mirrors.

Finally resonance occurs when the phase shift in equation (1.47) of the light from one mirror to the other is a multiple integer of π.

$$\triangle\phi = \phi(z_2) - \phi(z_1) = kd - (m+n+1)\left[arctan\left(\frac{z_2}{z_0}\right) - arctan\left(\frac{z_1}{z_0}\right)\right] = \pi(q+1) \tag{1.48}$$

Converting from phase to frequency finally gives [125]:

$$\nu = (q+1)\,\upsilon_F + \frac{\upsilon_F}{\pi}(m+n+1)\,arccos\sqrt{(1-{}^{\mathrm{d}}/_{\mathrm{R}_1})(1-{}^{\mathrm{d}}/_{\mathrm{R}_2})} \tag{1.49}$$

So far the cavity had an infinitely large aperture, meaning the mirrors were infinitely large, therefore no loss of the electromagnetic field at the mirror edges appeared. This assumption is obviously not accurate. In real systems there is always a small fraction of the light field passing over the mirror edges and exiting the cavity. This loss is characterised by the Fresnel-number $N = a^2/(\lambda d)$;with a the characteristic size of the aperture (here the mirror's radius). Calculations of these losses for certain cavity-geometries can be found in [125].

1.5.5 Thermal Noise Limit

The stability of an ultra-stable cavity is the stability of the optical pathlength between its mirrors. This distance is perturbed by vibrations and temperature changes of the mirrors and the connecting spacer as well as changes of the optical density of the medium inside, impinging laser power fluctuations and ageing of the material. Fortunately nowadays all of the above effects can be controlled very well with multi-stage temperature- and power-controls, active vibration cancellation and ultra-high vacuum systems. Therefore the performance of contemporary ultra-high cavities is basically given by brownian motion within the spacer and the mirror-substrates and coatings [126, 127]. Especially the later is exceptionally challenging, since the substrates need to combine superb mechanical and optical performance at the same time.

Using the fluctuation-dissipation theorem a direct approach to calculate the effect of Brownian thermal noise [128] was developed and then first used by Numata et al. [129] to estimate its effect on the length stability of an optical cavity. This was later refined in [130]. In the following only the basic idea and results are given.

The dissipated power by thermal fluctuations is represented by an external force, F_0, working on the cavity comprised out of the spacer (sp), the mirror-substrates (sb) and -coatings (ct). These have maximum elastic strain energies $U_{sp,sb,ct}$ and loss angles $\Phi_{sp,sb,ct}$, which are calculated from material and geometrical constants. For precise estimates and optimised geometry, a finite element analysis is used. The spectral density of length-fluctuations of a cavity with length L at a given temperature T is given by [130]:

$$S_l(f) = \frac{4k_B T}{\pi F_0^2} \frac{(U_{sp}\Phi_{sp} + 2U_{sb}\Phi_{sb} + 2U_{ct}\Phi_{ct})}{f} \tag{1.50}$$

,where the maximum elastic strain energies are:

$$U_{sp} = \frac{LF_0^2}{2\pi E A_{sp}}, \;\; U_{sb} = \frac{(1-\sigma^2)F_0^2}{2\sqrt{\pi}Ew}, \;\; U_{ct} = \frac{2}{\sqrt{\pi}} \frac{1-2\sigma}{1-\sigma} \frac{d_{ct}}{w} U_{sb} \tag{1.51}$$

,with A_{sp} being the spacer cross-area, σ Poisson's ratio of the substrate material, E Young's modulus, d_{ct} the thickness of the coating and w the $1/e^2$ beam radius of the cavity mode.

The length-fluctuations convert directly into frequency-fluctuations via equation 1.38. The power spectral density of fractional frequency fluctuations follows directly as: $S_y(f) = S_l(f)/L^2$. This is a $1/f$ flicker frequency noise process and leads to a constant Allan deviation of the frequency noise:

$$\sigma_y = \sqrt{2ln(2)S_y(f)f} \tag{1.52}$$

Contemporary optical cavities reach theoretical thermal noise limits in the 10^{-17} region [20, 21]. Looking at equation 1.50 and 1.52 there are three strategies to reaching lower Brownian noise limits in cavities: Using materials with lower $U\Phi$ (less Brownian motion), longer spacers (less sensitivity to thermal motion) or cryogenic temperatures [131].

The spacer and mirror substrates are chosen out of materials such as ultra-low expansion glass (ULE), Zerodur and silica due to their low thermal sensitivity. Optical coatings in modern cavities are made from dielectric coatings, which do not offer the best thermal attributes, but have been without alternative until the recent appearance of optical crystalline mirrors. Most common nowadays are ULE spacers due to the fact that this material's thermal expansion coefficient (CTE) vanishes around room-temperature. The mirror substrates are either also ULE or fused silica, because of the lower thermal noise in fused silica at room temperature. This lower Brownian noise comes at the expense of a different and higher linear thermal expansion coefficient than ULE. Therefore these mirrors are completed with ULE compensation rings on the outside to counter-act the expansion of the silica material [131]. The best stability results achieved so far with a room-temperature cavity consisting out of a ULE spacer with silica mirror-substrates and ULE compensation rings were just stepping into the 10^{-17} region [20].

Another approach successfully applied is taking single-crystal silica spacer and mirror substrates, proposed already more than 20 years ago [132], but first realised more recently [122]. This has the advantage of much lower Brownian noise in the spacer. On the other hand silica's freezing zero CTE point of 124 K means that these cavities are necessarily cryogenic. Performance of this kind of ultra-stable cavity

has reached similar values to the best aforementioned ULE/silica room-temperature cavities [21].

In current state-of-the-art cavities the main contribution to the total Brownian noise comes from the dielectric coatings. To overcome this limitation coatings out of single crystals have been developed and are now coming close to a stage of providing the first ultra-stable cavities with projected thermal noise limits well within the 10^{-17} [133, 22].

1.5.6 Seismic Noise

In order to reach the thermal noise limit the residual vibrational noise acting on the cavity needs to have a negligible effect. Therefore Ultra-stable cavities feature vibration-optimised designs [122, 134] to detach the cavity mechanically from its environment. Careful finite-elements analysis is conducted to find optimum support-geometries. The support is often located around the Airy-points of the cavity, since this configuration by definition is the one in which the cavity ends, where also the mirrors are located, is not bent by outside forces. Contemporary acceleration-sensitivities reach the $10^{-12}\frac{\mathrm{m}}{\mathrm{s}^2}$ region [21].

1.6 Frequency Combs

One of the main challenges of optical clocks in their early days was finding a way to reference the optical frequencies of these clocks to the current microwave SI-standard and standard time-keeping electronics as well as other optical frequencies. What was needed was a frequency "ruler" capable of connecting radio frequencies and the whole optical spectrum, whose noise characteristics would cancel out in the bridging process, allowing for the superb optical clock's performance to be used.

The first access to frequency measurements in the optical region were cascade laser-systems. These used chains of multiple-frequency generation and injection locked lasers, starting from microwaves up to optical wavelengths. These chains were very complicated to operate, filled whole buildings and needed to be physically adjusted, depending on the target frequency [135–137].

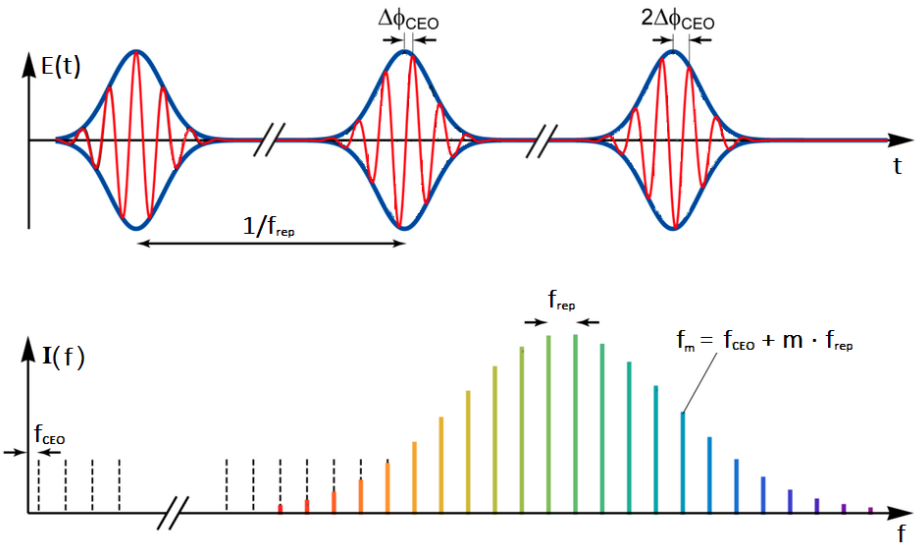

Fig. 1.6 Schematic output of a femtosecond frequency comb, showing the connection between the time- (top) and frequency-picture (bottom).

The use of mode-locked femtosecond lasers finally brought a breakthrough in optical frequency measurements and the Nobel-prize in 2005 was awarded for the development of the optical frequency comb to J. Hall and T.W. Hänsch. [138–141].

The pulsed operation of a mode-locked laser is achieved by introducing some Kerr-lens [142] or nonlinear polarisation-rotating medium [143] into the laser cavity and combining it with an aperture or polariser, leading to pulsed operation suffering less attenuation than cw-light and consequently "winning" the mode-competition. A Fourier transformation reveals the spectrum of such pulsed laser, as it is depicted in figure 1.6. The width of the comb-emission is given by the Fourier-limit of the width of each single pulse. The delay between two subsequent pulses divides the spectrum into evenly spaced peaks. Cross-phase modulation in microstructured fibres is a very common tool to broaden the emission of a frequency comb from a few nm in the near-infrared to the as much as one octave, potentially covering the whole visible spectrum [144].

The frequency of each of these spectral modes can be written in terms of two radio-frequencies and one mode-number [145, 146]:

$$f = f_{CEO} + m \cdot f_{rep} \tag{1.53}$$

The carrier envelope offset (CEO) frequency is, as in figure 1.6, given by the offset between the carrier-and envelope-phase introduced between two consecutive pulses and the repetition rate frequency by the laser pulse rate. Here it is sufficient to see that through self-referencing of the mode-locked laser one can control f_{CEO} and f_{rep} [147], enabling absolute frequency measurements and also frequency ratios in the optical domain with high accuracy. The frequency comb itself is working as a flywheel, meaning that in the final results, whether it be microwave/optical or optical/optical frequency ratios, the mode-locked laser noise is rejected - well below the accuracy limits of modern atomic clocks [148]. A further treatment of the frequency comb and how to exactly cancel out the mode-locked laser in measurements will continue in chapter 5 together with an introduction of a relatively novel application of the femtosecond comb laser.

Chapter 2

^{171}Yb Lattice Clock At INRIM Absolute Frequency Measurement

2.1 Introduction

In this work an optical lattice clock based on ^{171}Yb in operation at the "Istituto Nazionale di Ricerca Metrologica" (INRIM) in Turin is presented. The principle of operation of this frequency standard is explained in this chapter, followed by a presentation of its physical realisation and, finally, the uncertainty evaluation of the clock-transition undertaken during this work. Much of the key results of this chapter have been published in [38].

$^{171}_{70}$Yb is a fermionic isotope of the lanthanide element ytterbium. The interest of time metrologists in Yb is caused by its earth-alkali like electronic structure, high atomic mass and transitions in the optical region which are suitable for fast, yet effective, laser cooling. It as well features a spin- and orbital-momentum forbidden $^1S_0 \rightarrow {}^3P_0$ transition, guaranteeing a narrow linewidth with an AC-Stark shift cancelling magic wavelength in the near-infrared at 759 nm, which is fairly well independent of lattice polarisation. Yb has seven stable isotopes, out of which only the ^{171}Yb, ^{173}Yb and ^{174}Yb have been used for metrological applications. The bosonic ^{174}Yb is the most abundant (32%) one, whereas the other two are less common (^{171}Yb abundance 14%, ^{173}Yb abundance 16%).

In the fermionic isotopes ^{171}Yb ($I = 1/2$) and ^{173}Yb ($I = 5/2$) the non-zero nuclear spin I leads to a small hyperfine-mixing amplitude of the $^3P_1$ and $^1P_1$ states with

electronic angular momentum $J = 1$ into the $^3P_0$ state. As a result the $^1S_0 \rightarrow {}^3P_0$ transition becomes weakly allowed, with a natural linewidth estimated around 10 mHz [42]. In the bosonic isotope ^{174}Yb a finite transition probability can be enforced by the same mechanism if an external magnetic field is applied [43].

Of all these isotopes the choice at INRIM fell on ^{171}Yb. Among the fermionic isotopes it has a simpler electronic structure than ^{173}Yb. Using the bosonic isotope on the other hand introduces further complexity to the experimental control, since the transition strength depends upon the magnetic field and the nature of bosons leads to higher atomic collision rates than in the case of fermions, where s-wave scattering is forbidden by the Pauli-exclusion principle.

All relevant atomic levels and transitions for clock operation are shown in figure 2.1.

An optical lattice clock is always run in a pulsed operation, consisting out of cooling and capture of an atomic ensemble, a subsequent transfer into an optical lattice and finally the clock-transition state preparation and read-out.

During one cycle the atomic sample is prepared and interrogated in an ultra-high vacuum science chamber. With a melting point of 824°C for Yb sufficient vapour pressure is generated by evaporation in a diffusion-oven. The travelling hot atomic sample is decelerated by a slower beam using the light-pressure-force. Some designs use a Zeeman-slower to augment the process efficiency [149]. At INRIM this feature was omitted in favour of a short path from the oven to the science chamber, leading to a less divergent atomic beam. The slower beam enables a two-stage Magneto-Optical-Trap (MOT) to capture and cool an atomic ensemble. The first-stage (in the following called the blue stage) uses the strong $^1S_0 \rightarrow {}^1P_1$ (linewidth 29 MHz) transition at 399 nm to cool down the atoms to about 1 mK. A second (green) MOT stage acts upon the weaker $^1S_0 \rightarrow {}^3P_1$ transition (linewidth 182 kHz). The Doppler-limit of this transition is 4.4 µK.

The atomic ensemble is subsequently transferred into the standing-wave of an optical lattice, operated at the magic wavelength 759 nm. The trap-depth is often given in units of the recoil-energy (of a single lattice photon) E_r or the maximum temperature of trapped atoms. Typical lattice depths amount to a few hundred E_r or micro-kelvin in temperature units.

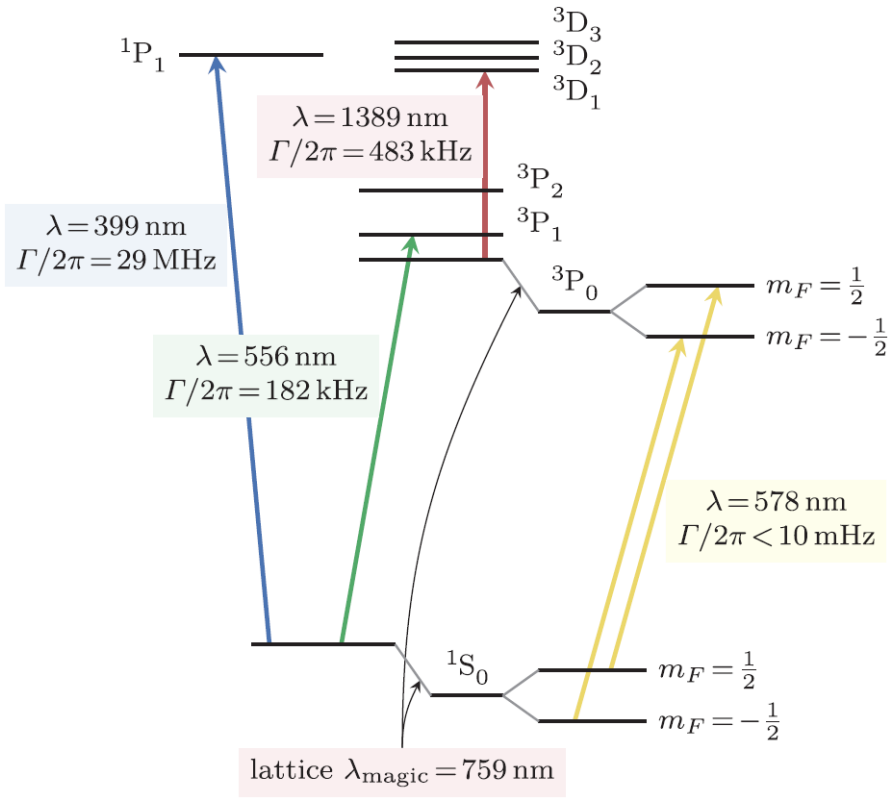

Fig. 2.1 The relevant atomic transitions in ^{171}Yb. Blue and green arrows show the two stages of Magneto-Optical Traps, reaching a Doppler-limited temperature around 15 µK in the 2nd green stage. The brown repumper-transition decays via the $^3P_1$ state to the ground-state, but has a loss channel towards the long-lived $^3P_2$, which is included in state-occupation calculations.

Inside the lattice a few thousand to a hundred thousand atoms are captured. The temperature of the atoms can be further decreased, if necessary, by sub-Doppler cooling mechanisms. There are many different ways towards this goal, such as evaporative cooling (decreasing lattice depth to evaporate hot atoms) [150] or Sisyphus cooling [62, 63]. But for atomic clocks sideband-cooling of the captured atoms inside the lattice is a reasonable choice, since it it easy to implement and leads only to low losses. Sideband cooling is executed by a laser resonant to the red-detuned sideband of the clock transition, followed by repumping. As the atoms fall back to the ground state, their vibrational level is decreased. Eventually nearly all atoms are found in the vibrational ground state of the lattice [151, 70].

The ground-state as well as the excited-state of the clock-transition have two hyperfine Zeeman-substates. Increasing spectroscopic contrast and decreasing collisions as well as line-pulling, the ground-state is spin-polarised by a short pulse driving the $^1S_0, m_F = \mp 1/2 \rightarrow {}^3P_1, m_F = \pm 1/2$ transition.

The $^1S_0 \rightarrow {}^3P_0$ clock-transition spectroscopy is performed by a laser stabilised to an ultra-stable cavity. Due to the long excited-state lifetime a repumper laser at 1389 nm is used to transfer the atoms back into the ground-state. The atoms in the $^3P_0$ state are excited into the $6s6d\ ^3D_1$ or $6s7s\ ^3S_1$ state, from which they relax to the ground state via the $6s6p\ ^3P_1$ state, with a small loss channel leading to the $^3P_2$ state. The magnitude of losses to $^3P_2$ can either be estimated from the oscillator strengths (dipole-matrix elements $\langle 1|D|2\rangle$), resulting in calculated 3% losses [152], or a 2nd repumper be installed [153]. The read-out of the ground-and excited state population can simply be performed on the strong 399 nm transition.

2.2 Physics Package

In figure 2.2 and 2.3 the physical apparatus of the Yb lattice clock at INRIM is displayed. The atoms are emitted in a collimated beam by an effusion oven at a temperature of around 400°C. The distance between the atomic oven and the trapping region, called the science chamber, where the atoms are captured and interrogated, is kept minimal (21 cm) in order to increase the flux of atoms, allowing to dispense of a Zeeman-slower for the slower-beam described below. All lasers are delivered to the vicinity of the science chamber by polarisation-maintaining fibres. Mechanical shutters and RF switches acting on the AOM-controls are controlled via software

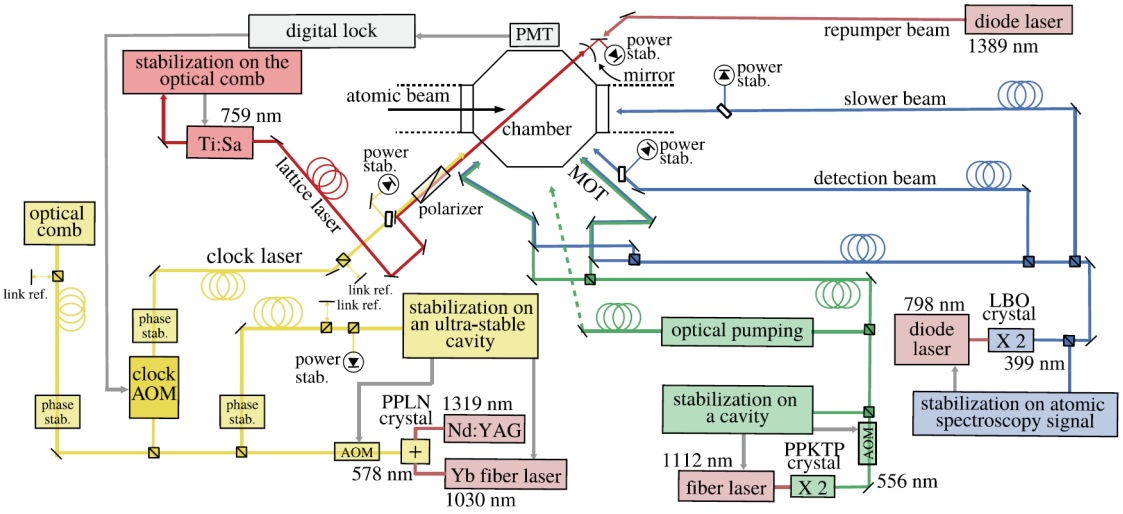

Fig. 2.2 Physical Setup scheme with the science chamber on one breadboard and all lasers, except for the repumper, guided by optical fibres to the experiment. Beam samplers and splitters provide reference points for fibre phase-noise cancellations (link ref.) and power stabilisations. The MOT uses a 3D beam arrangement (here vertical direction omitted for clarity).

and shut the slower, MOT and probe beams on and off. A normalised atomic state readout is performed by fluorescence-detection on the ${}^1S_0 \rightarrow {}^1P_1$ transition via a photo-multiplier tube.

Figure 2.3 shows the science chamber and its surrounding. An ultra-high vacuum of less than 10^{-9}mbar is maintained by two ion pumps situated below the science chamber and one non-evaporable getter pump. Stainless steel fittings connect the oven through a vacuum differential tube with the science chamber and the slower-beam entrance as well as all ion-pumps. The science chamber itself consists out of an aluminium frame with large, dielectrically coated silica windows (eight in total) for optimised access and indium-sealing. Ten platinum resistance thermometers are distributed over the outer surface of the chamber to enable a precise evaluation of the black-body-radiation. A pair of magnetic coils is arrayed vertically (z-direction) on the chamber and is working in an anti-Helmholtz configuration, providing the magnetic gradients for the MOT. Water cooling serves to keep the temperature of the coils as well as the chamber constant during operation. Three pairs of Helmholtz coils compensate the stray magnetic field at the position of the captured atomic cloud in all three dimensions.

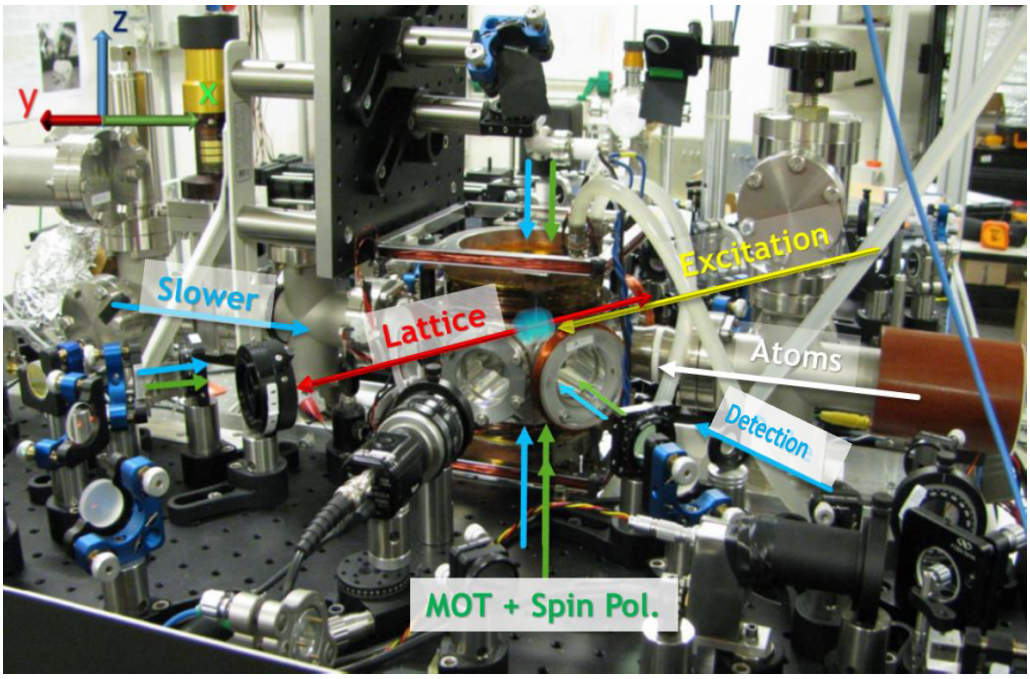

Fig. 2.3 View of the physical apparatus. In the centre there is the science chamber; the water-cooled anti-Helmholtz MOT coils are arrayed vertically on the chamber. One pair of Helmholtz-coils is placed in each room-direction, around the windows of the chamber (x, y-direction) and above/below the MOT coils (z-direction). In the forefront are optics to probe and detect the atomic state. The direction the atoms are exiting the effusion oven is indicated by a white arrow. The directions of the laser beams for cooling, trapping, spin-polarisation, probing and detection of the atoms are indicated.

2.3 The Blue MOT

Before capture and cooling in the blue MOT the atoms are faced with a high-power red-detuned (at 399 nm) beam, which enters the vacuum-apparatus by a side-window. For the very first measurements obtained during this work the slower-beam was not redirected over an intra-vacuum mirror, but entered by a heated window facing the oven. The black-body radiation emitted by this window bathed the captured atoms inside the lattice through a direct line of sight connection, leading to some excess BBR shift uncertainty, and was therefore replaced with the aforementioned mirror.

The blue MOT traps the atoms from the slower-beam. The 399 nm radiation is obtained through second-harmonic generation (SHG) of a 798 nm amplified external-cavity diode laser with an output power of up to 3 W. The SHG utilises a lithium-triborate (LBO) crystal as nonlinear-medium inside an enhancement cavity [154]. This cavity is locked to the laser by regulation of the cavity length via a piezo behind one of four cavity-mirrors. The error signal for stabilisation is generated applying the Hänsch-Couillaud technique, where a polarising element inside the cavity enables the measurement of the polarisation-change of the reflected light over a resonance [155]. In this way a total power of 400 mW at 399 nm is gained from an input power of 1.2 W of infrared light and subsequently distributed among the slower beam, the MOT beams and the state detection.

In order to achieve a stable operation the laser linewidth should be significantly below the (power-broadened) linewidth of the engaged transition. In this case the diode laser itself has a sufficient linewidth of about 300 kHz. Therefore only a drift-compensation needs to be implemented. The laser is stabilised at the correct wavelength through side-of-fringe locking to the transverse spectroscopy signal of an auxiliary hot atomic beam of ^{171}Yb.

The slower beam punches the atoms with about 35 mW of light power at a detuning of -360 MHz from resonance. A fraction of the magnetic field generated by the MOT coils leaks outside of the science chamber and is supporting the deceleration similar to a Zeeman-slower.

The power in all six MOT beams adds up to about 30 mW, with an $1/e^2$ radius of 1 cm and a detuning from resonance of -20 MHz.The magnetic field gradient along the z-axis (as in figure 2.3) is $0.35\,\mathrm{T/m}$

The slower prepares an ensemble of up to 4×10^7 cold atoms, depending on the cycle time. Out of this an estimated maximum of 2×10^5 atoms are cooled and then trapped by the blue MOT at a temperature of 1 mK. In a typical clock cycle the slower beam and the blue MOT are operated simultaneously for 50 ms and then shut down mechanically.

2.4 The Green MOT

The second stage MOT at 556 nm uses laser light generated from SHG of an amplified Yb-doped fibre laser creating 1 W at 1112 nm. After single-pass through a periodically-poled potassium titanyl phosphate (PPKTP) crystal about 10 mW of usable radiation is obtained. A stable operation throughout one day of measurement requires a drift below 100 kHz and places a similar constraint on the linewidth. The actual linewidth of the unstabilised laser is around 20 kHz and the drift as fast as few MHz in a minute.

The frequency-stabilisation of this radiation is obtained by a Pound-Drever-Hall (PDH) lock to an ultra-stable 10 cm cavity made (both, spacer and mirrors) out of Corning ultra-low expansion glass (ULE). The stabilisation acts upon the RF frequency supply of an AOM and the fibre-laser's piezo voltage for fast and slow locking, respectively. The cavity is operated a few degrees away from the point of vanishing CTE due to technical limitations. However, the resulting drift of the stabilised laser is at least a factor 10 below the above mentioned requirements. The short-term stability limit of this cavity has been evaluated before in [156], being a few parts in 10^{-15} at 1 s, well below the requirements set here.

The green MOT beams carry a total power of 2 mW with a $1/e^2$ radius of 0.5 cm. These beams are simultaneously turned on with the blue MOT and kept on until the atomic transfer to the lattice is completed. The green stage of the MOT lasts for 60 ms and is divided into three sub-stages with varying laser frequency and intensity, as well as different magnetic field gradients in order to maximise the fraction of atoms transferred to the optical lattice.

The first substage (30 ms) of the 556 nm MOT is loaded from the blue MOT with an efficiency of 70% once the blue beams are shut off. This substage is designed to transfer the maximum amount of atoms from the blue MOT and uses a field

gradient of $0.13\,\mathrm{T/m}$ combined with full beam intensity. The 2nd substage lasts 20 ms and reduces the temperature of the captured atomic ensemble to $10\,\mu\mathrm{K}$ moving the frequency closer to resonance, while decreasing the intensity by tenfold and raising the magnetic field gradient to $0.2\,\mathrm{T/m}$. The temperature measurement is performed by a measurement of the size of the atomic cloud after a short free-fall time once the magnetic fields are shut off. The size measurement uses another focused 399 nm beam horizontally displaced from the MOT position, allowing the determination of the cloud extension as it passes through. The 3rd substage features a higher magnetic field gradient of $0.23\,\mathrm{T/m}$ and a slight deviation in intensity and frequency from the 2nd one in order to enhance the transfer-efficiency of the atoms into the optical lattice. The efficiency of the transfer from the 2nd green MOT stage to the lattice, mediated by the 3rd stage, is typically around 7%.

2.5 The Lattice

The lattice is formed by a retro-reflected, horizontal beam at the magic wavelength (759 nm). The radiation is generated by a commercial diode-pumped Ti:Sa Laser. The maximum optical output power at 759 nm is around 2 W. To assert the uncertainty on the absolute frequency of the clock transition related to the lattice Stark shift at a level below 1×10^{-18}, the laser frequency needs to be stable during the time of one measurement (typically 10 h) to 120 kHz (for our typical trap depth of 200 E_r and the optical power to within a few percent.

The laser has a spectral width of 20 kHz at 1 s, but drifts over several MHz in few minutes. The frequency of the lattice is constantly recorded with a Er-fibre frequency comb, whose repetition-rate and carrier-envelope-offset are stabilised to a 10 MHz H-maser signal. Therefore a slow digital lock uses the beatnote-signal between the comb and the lattice laser to compensate the lattice laser drift, acting on the length of the internal laser-reference cavity. An AOM between the laser output and the fibre to the science chamber is used for an active power-control. The laser itself is situated on the same optical table as the science chamber, at a distance of around 2 m. The radiation is directed to the experimental apparatus by high-power polarisation-maintaining fibre.

At the output of the PM-fibre, as in figure 2.2, typically 1 W of light power is available. The radiation is subsequently overlapped with the clock laser and then

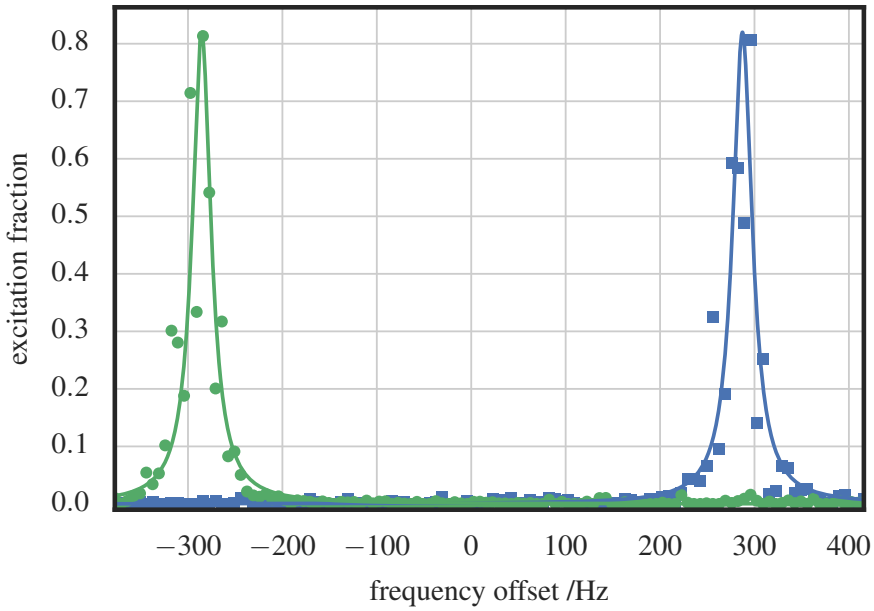

Fig. 2.4 Spin-polarisation with efficiency 98%. The plot is composed out of two scans over the Zeeman-split resonance with spin-polarisation to either m_F state.

the polarisation of both lasers cleaned and parallel aligned along the z-axis by a Glan-Thompson polariser. The lattice is focused at the position of the green MOT with an $1/e^2$ waist radius of 45 µm and retro-reflected by a curved mirror. The beam is tilted from the horizontal axis by 60 mrad.

The operating lattice-depth is around 200 E_r, where E_r signifies the energy associated with a single photon-atom collision inside the lattice (recoil-energy): $E_r = \frac{\hbar^2 k^2}{2m}$. The exact number of atoms trapped is regulated in clock operation (e.g. to measure the cold atomic collisions shift) by adjustment of the slower beam duration between 40 ms and 150 ms. In this way up to 10^4 atoms are stored inside the lattice at a temperature of $7(3)$ µK. The lifetime of an atom inside the lattice is 2.7 s. The main limitation to the trapping lifetime is related to background-gas collisions [157], kicking atoms out of the lattice.

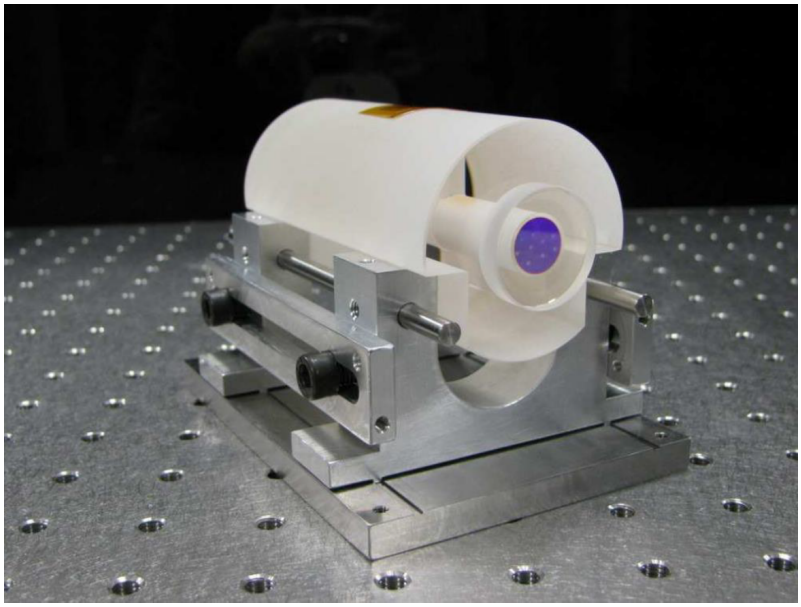

Fig. 2.5 Picture of the ultra-stable 10 cm cavity on its supports.

2.6 Spin-Polarisation

The spin-polarisation is performed by optical pumping on the Zeeman-sublevels of the same transition as the one used for the green MOT. A linearly polarised 1 ms pulse and a magnetic field of 0.4 mT are applied along the vertical (z-) axis as in figure 2.3. The efficiency of the spin-polarisation has been confirmed by spectroscopy on the Zeeman-split clock transition to reach 98% with either m_F-substate, as shown in figure 2.4. Prior to the polarisation-pulse the magnetic field is building up during a 15 ms waiting time.

2.7 Ultra-Stable Clock Laser

The radiation probing the ${}^1S_0 \rightarrow {}^3P_0$ clock-transition is generated via sum-frequency generation (SFG) of a 1319 nm neodymium-doped yttrium aluminium garnet (Nd:YAG) laser with an erbium fibre laser at 1030 nm in a waveguide periodically-poled lithium niobate (PPLN) crystal [156]. Up to 7 mW of light power are available after the crystal. The laser is actively stabilised to an ultra-stable cavity using the PDH method.

The cavity consists out of a 10 cm ULE spacer with fused silica mirrors (One flat, one concave, with radius -0.5 m), featuring ULE compensation rings and dielectric coatings at 578 nm.

The resonator is suspended horizontally on 4 receptors in a vibration-insensitive configuration. Based on a finite-element analysis the vibrational sensitivity should be expected in the 10^{-11}s^{2}m^{-1} to 10^{-10}s^{2}m^{-1} region. The vacuum chamber is placed inside an anti-acoustic chamber and on top of a passive vibration-isolation system.

The cavity is situated inside an aluminium chamber under an ultra-fine vacuum maintained by an ion pump. The chamber features two shells around the cavity, one inner- and one outer-shell, both temperature-stabilised to enhance the uniformity of the temperature distribution around the cavity. The temperature control uses 4-wire resistance measurements of platinum Pt1000 sensors to measure the temperature of each shell individually. The temperature-control is a low bandwidth (< 1 Hz) digital realisation of the Active Disturbance Rejection Control (ADRC), using Peltier-elements to regulate the temperature of the shells. The ADRC, described in [158], uses an estimate of the temperature fluctuations sensitivity to actively counteract the thermal fluctuations. The temperature control keeps the inner-shell of the cavity around the zero-CTE point of 301.15 K with an in-loop temperature error of 0.1 mK. Taking the linear thermal expansion coefficient of ULE around room temperature as 10^{-8}K^{-1} and the FSR of 1.5 GHz, a frequency uncertainty of the TEM00 modes of 1.5 mHz follows. At 578 nm this is equivalent to few parts in 10^{-17}. This estimate is, of course, based on an in-loop signal and does not take into account the actual low-pass filtered transfer of the inner-shell temperature to the cavity. But it shows that the temperature control does not pose a limitation to the envisioned stability of the cavity (10^{-15} at 1 s).

The expected ultimate limitation of any ultra-stable cavity is Brownian motion of the mirror coatings and, to a lesser degree, of the spacer and the mirror substrates. Using equation 1.50 we calculated a thermal noise limit of around $1 \times 10^{-15}\tau^{-1/2}$. From measurements with similar cavities [156] we expected the resulting flicker-floor limitation of the laser to be somewhat below 3×10^{-15} at 1 s.

Since there is no other laser at the INRIM laboratories with a stability at or below this value, the ultimate measure of stability is the atomic spectroscopy.

The laser power impinging on the cavity is stabilised at an optimised level, where the sum of shot-noise in the error signal detection and thermal noise due to heating

of the cavity mirrors is minimised. Shot noise is associated to the photon-number fluctuation of an electromagnetic field in the presence of the vacuum states. Taking an upper limit for the cavity sensitivity of $70\,\mathrm{Hz}/\mu\mathrm{W}$, the input power fluctuations were found to be compatible with a stability better than 3×10^{-17} at 1 s.

Clock Laser Finesse Measurement

One important aspect of ultra-stable cavities is highly-reflective mirrors, leading to high quality factors of the cavity modes. This is necessary in order to obtain a high spectral resolution that allows to transfer the stability of the cavity to the clock spectroscopy laser. The Finesse as measure of the quality-factor was determined via the cavity ring-down method. In order to measure the cavity ring-down-time the laser was first stabilised via PDH-locking unto one cavity-resonance. The AOM stabilising the light (fast lock) on the resonance had a TTL (Time to live) trigger in the signal loop of the driving RF-input, which was switched electronically to extinct the RF power to the AOM and thereby stopping any laser light from entering the cavity. A photo-diode behind the cavity sensed the transmitted power, which was recorded on an oscilloscope triggered by the same TTL mentioned before. A series of 9 lifetime-measurements was taken, and the resulting ring-down-time is $15.816\,\mu\mathrm{s}$ with an associated uncertainty of (take student-t-distribution):

$$\mu(\tau_\mathrm{p}) = \left(\frac{\mathrm{n}-1}{\mathrm{n}-3}\right)^{\frac{1}{2}} \frac{\mathrm{s}}{\sqrt{\mathrm{n}}} = 0.067\,\mu\mathrm{s} \tag{2.1}$$

Since the decay-time is the only input-quantity for the Finesse, one needs to look at possible uncertainties contributing to this time. These uncertainties cannot be measured directly with this experimental setup, but need to be taken into account from a theoretical perspective.

The resonance condition is altered by temperature and impinging light power as well as mechanical vibrations, but these do not influence the mirror-reflectance or losses. On the other hand care has to be given to include the photodiode, trigger and oscilloscope bandwidths as well as the RF extinction out of the AOM. Most of the data can be taken from specification sheets. The TTL is home-built and therefore its shut-down time, which artificially expands the measured photon-lifetime, was measured: Shutdown-time was assessed at $0.4\pm0.25\,\mu$s (rectangular uncertainty).

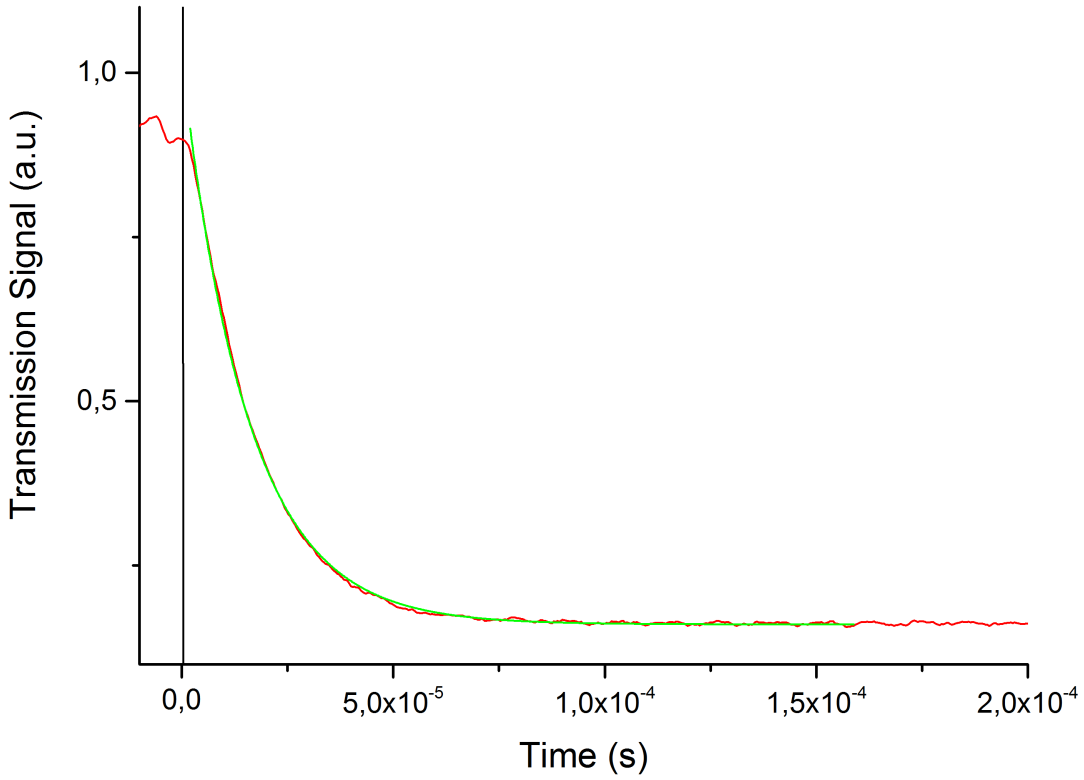

Fig. 2.6 Exemplary photon lifetime measurement as normalised transmitted power against time (red). The black vertical line marks the triggering event (applied voltage to trigger) and the green curve is an exponential fit with a lifetime of 15.59 µs.

Taking the other mentioned shifts and their uncertainties the Finesse finally follows as:

$$\mathrm{F} = 144 \times 10^3 \pm 2 \times 10^3 \tag{2.2}$$

This value corresponds to a mode linewidth of about 10 kHz and is well within the range of contemporary ultra-stable cavities. According to experience this result is compatible with the targeted Hz-level laser linewidth.

Zero Coefficient Of Thermal Expansion Point

ULE glass has a zero CTE temperature around 300 K, which can be designed to be within a convenient target range of a few K. But silica has an even higher mechanical quality factor than ULE, meaning a low loss angle, reducing the thermal noise limit in equation 1.52. The problem with silica is that its most prominent zero CTE crossing is found at 124 K, demanding cryogenic temperatures. Therefore the mirrors of the clock laser cavity are made out of silica, while the spacer is fabricated from ULE glass. Small rings of ULE glass are attached to the silica mirror-substrates and at the same time optically contacted to the spacer in order to compensate for the thermal expansion of the silica material, as shown in figure 2.5. This solution combines the low thermal noise of the silica with the zero CTE of the ULE glass at a more convenient temperature.

The zero CTE point measurement was conducted as follows: The laser was stabilised to the ultra-stable cavity and the laser's frequency measured by an Er-fibre frequency comb, while the temperature of the inner-shell of the vacuum chamber (and thereby also the cavity temperature itself) was linearly increased with time across the presumed zero CTE temperature and then again decreased. The frequency vs. inner-shell temperature plot is shown in figure 2.7. These data show a hysteresis curve due to the slow temperature transfer to the cavity. The intermediate value of the two zero CTE crossings recorded is taken as the actual, static zero CTE temperature. The zero CTE temperature results as $301.15(5)\,\mathrm{K}$.

Despite of the vanishing CTE at the operational temperature, a constant drift below $0.1\,\mathrm{Hz/s}$ of the cavity frequency is observed. A residual drift of this order of magnitude is common for ULE glass cavities and is attributed to ageing processes

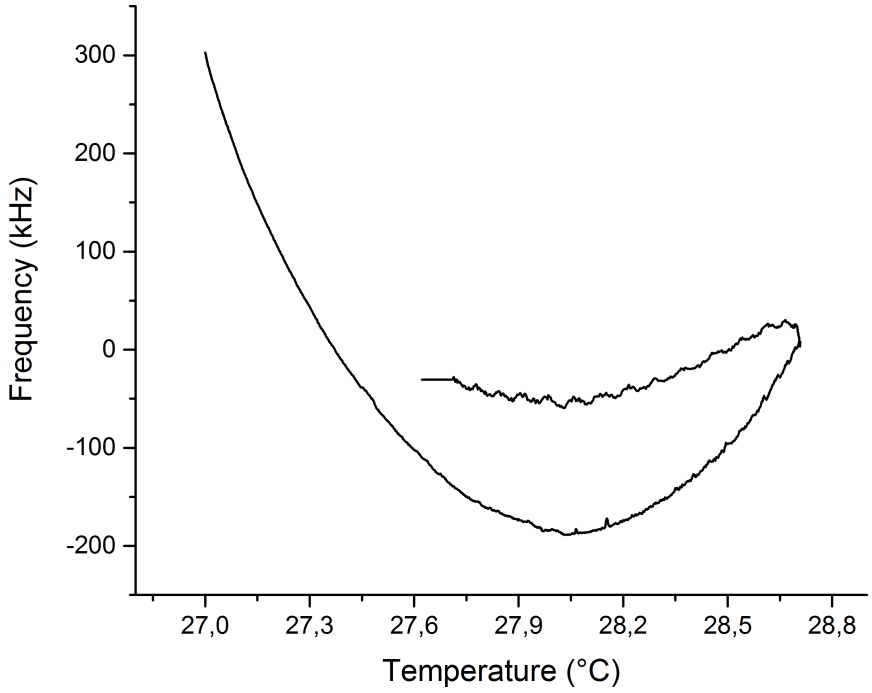

Fig. 2.7 The cavity stabilised laser frequency measured by the frequency comb as a function of the inner vacuum shell temperature

[159]. This constant drift is automatically corrected in a feed-forward scheme by a synthesizer steering an AOM.

Fibre Network

The 578 nm radiation is sent to the ultra-stable cavity for stabilisation, but simultaneously also to the science chamber for spectroscopy and to a frequency comb to compare it to INRIM's primary frequency standard, the ITCsF2 cryogenic fountain clock. The distribution of the radiation is done by polarisation-maintaining fibres of 20 m length each. This kind of fibre is engineered in the panda style, meaning that the fibre birefringence preventing crosstalk between the polarisation axis is obtained through stress rods pulling on the core. In this configuration the polarisation fluctuations induced by mechanical noise acting on the fibre are greatly reduced in comparison to single-mode fibres. But this also means that the polarisation of the output radiation is sensitive to thermal fluctuations of the fibre environment [160]. About 2 m of uncompensated free-space optical path lays between the 3 fibres inside an acrylic enclosure. The optical pathlength inside this enclosure is quite stable, whereas the optical fibres suffer mechanical acoustic and seismic noise as well as small cyclic temperature variations induced by the AC conditioning of the laboratories. In order to assure the phase and frequency stability of the laser everywhere, the phase noise along the fibre paths needs to be actively cancelled. The optical setup and the electronic feedback-loop as well as a throughout characterisation of the phase noise cancellation are discussed in chapter 4.4. Here it shall only be mentioned that the stability of the fibre links was better than either the 578 nm laser or the Yb lattice clock for all timescales and the accuracy of the link was limited solely by statistics to 1×10^{-18} after 1000 s of integration time.

2.8 Frequency Comb

The frequency comb used to link the optical frequency of the Yb clock to the microwave generated SI-second and to stabilise the lattice laser on an H-maser, is a commercial Er-doped fibre laser, featuring separate amplifiers and non-linear broadening for the f-2f CEO offset frequency detection interferometer and the Yb

frequency detection. The CEO-frequency f_{CEO} and the repetition-rate f_{rep} are locked to the universal 10 MHz frequency reference in the laboratory taken from a H-maser.

In order to assess the comb's contribution to the absolute frequency measurement, the same laser frequency was measured simultaneously by this comb and a second one with a similar set-up. The difference was taken as the uncertainty on the laser frequency. The comb contributes with 1×10^{-16} to the measurement uncertainty. This result is limited by the comb's electronic noise level after an averaging time of 10 000 s.

2.9 Repumper Laser

The repumper laser is a commercial pigtail distributed feedback laser with a centre wavelength of 1389 nm, acting on the $^3P_0 \rightarrow {}^3D_1$ transition. 10 mW of radiation broaden the transition to about 300 MHz. Consequently, active frequency stabilisation is not required. The 6 ms repumper pulse has a transfer efficiency of 90%. The loss channel to the long-lived $^3P_2$ is included in the calculation of the excitation fraction by considering the relative transition strengths from the $^3D_1$ level [152] with 3% as well as heating losses (see section 2.5) with another 2.2%.

2.10 Spectroscopy Of The $^1S_0 \longrightarrow {}^3P_0$ Transition

A single spectroscopic sequence consists out of state preparation, interrogation and read-out. The state preparation starts with the 50 ms blue MOT, followed by the green MOT in three sub-stages and a total duration of 60 ms, transferring about 10^4 atoms into the lattice. A bias magnetic field lifts the degeneracy of the m_F spin-states and the spin-polarisation beam transfers 98% of all atoms into one of them within a total duration of 16 ms. After spin-polarisation we wait 30 ms for the magnetic field transients to decay and the field to stabilise at the value used for spectroscopy, typically 0.14 mT, leading to a Zeeman shift of the two π-transitions of 290 Hz. Spectroscopy across the Zeeman-split transition is depicted in figure 2.8.

The interrogation of the $^1S_0 \longrightarrow {}^3P_0$ transition is executed by the 578 nm clock laser. The clock laser is collinear to the lattice laser with an $1/e^2$ waist radius of 200 µm, assuring flat phase-curvature at the position of the lattice, and an incident

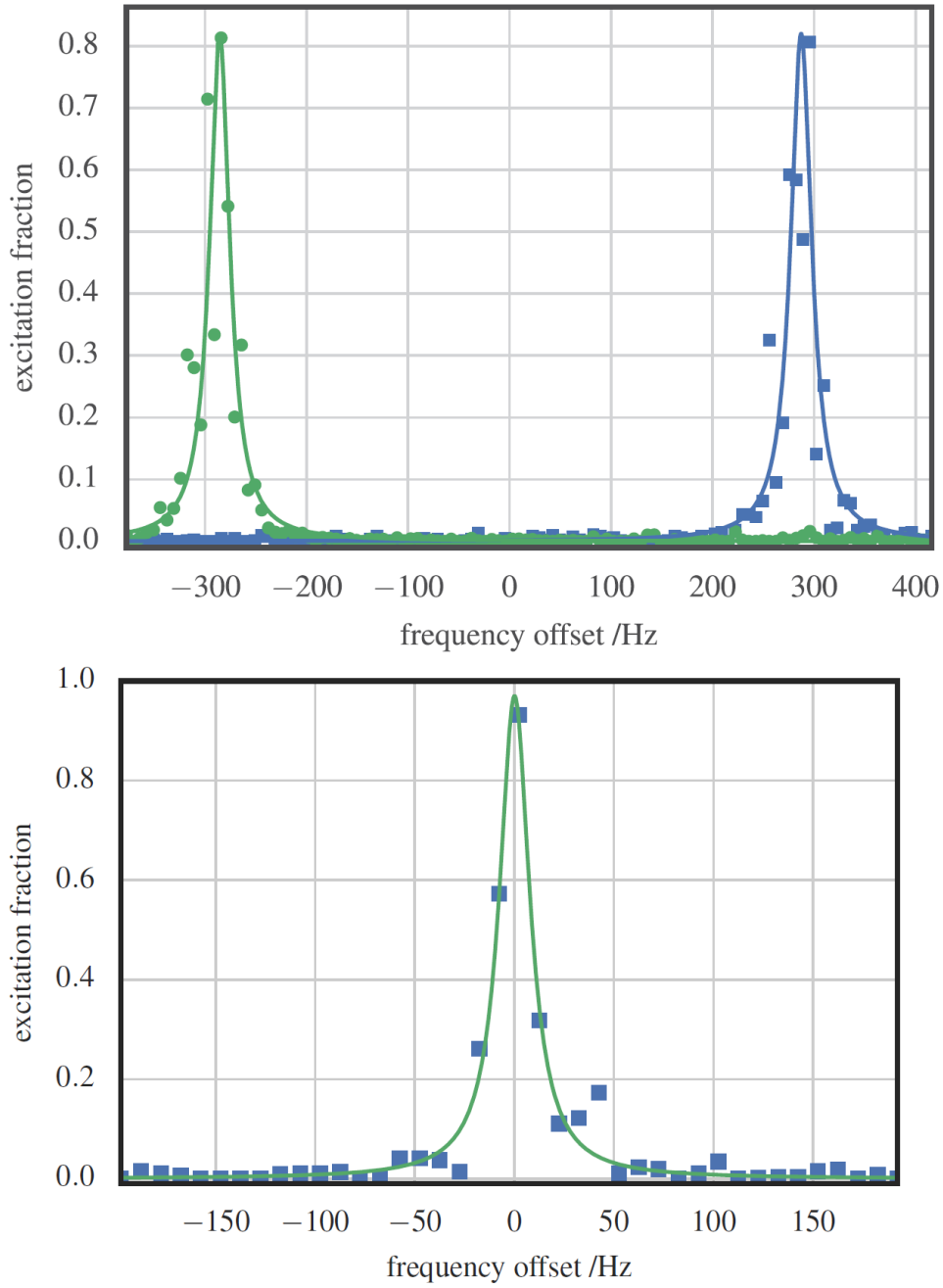

Fig. 2.8 Top: Spectroscopy across the Zeeman-split (shift of 290 Hz) clock transition. The full picture consists of two scans, each spin-polarising the transition to one $m_F = \pm 1/2$ state. Blue and green dots are measurement points, the lines Lorentzian fits.
Bottom: Zoom-in on one Zeeman-split transition with an FWHM of the central line (green) of 18 Hz

power of 70 nW. The power impinging on the atoms is actively stabilised. The polarisation is linear and cleaned by the same Glan-Thompson polariser (extinction ratio 100000 : 1) as the lattice radiation, thereby aligning lattice and clock-laser polarisation among themselves. The applied vertical magnetic field is lifting the m_F-states degeneracy in order to to suppress the linear Zeeman-effect and residual vector-shifts [4, 42]. For our usual trap depth of 200 E_r the residual vector light shift can be as low as 3 mHz when assuming perfect alignment. During our measurements of the AC Stark shift we detected a residual vector light shift of $0.16(0.29)$ Hz. The degree of circular polarisation - as defined in [42] - follows as $A = 3.5 \times 10^{-4}$ for the mean value. Such a circular component could be introduced either by a misalignment of the lattice polarisation vector or some birefringence in the windows of the science chamber. But it has to be emphasized that the measurement is also consistent with a zero shift. The lattice back-reflector is anti-reflection coated at 578 nm, revealing a residual reflectivity $< 1\%$ at this wavelength.

The clock-laser pulsed operation is achieved by switching the frequency of the light impinging on the atoms with an AOM. The laser is detuned about 1 MHz from resonance during its dead-time, assuring that it does not interact with the atoms, and turned to resonance after the spin-polarisation for the duration of a π-pulse. Mechanical shutters block all radiation except from the lattice- and clock-laser during the 60 ms of interrogation.

The excitation fraction is destructively detected and normalised by three 2.5 mW 399 nm pulses with a waist of 0.5 mm resonant to the $^1S_0 \rightarrow {}^1P_1$ transition. The atomic fluorescence of the strongly saturated transition is caught by a photo-multiplier tube (PMT), whereupon the incoming signal is integrated for 2 ms.

A total of 26 ms is needed in order to read-out the normalised excitation fraction and the total number of atoms. The first pulse measures the excitation in the ground state, the second pulse the fluorescence coming from the hot background gas and the third pulse the excited state population, after a short pulse from the repumper laser has transferred the atoms back into the ground-state. The number of atoms and the excitation fraction are recorded and given out in a live-display by a home-written programme. The total time of one spectroscopic sequence is 242 ms with 60 ms (about $1/4$) of it being spectroscopy.

The clock-transition is typically observed with a linewidth of about 20 Hz. This is larger than the expected 5 Hz and attributed to excess seismic noise acting on the

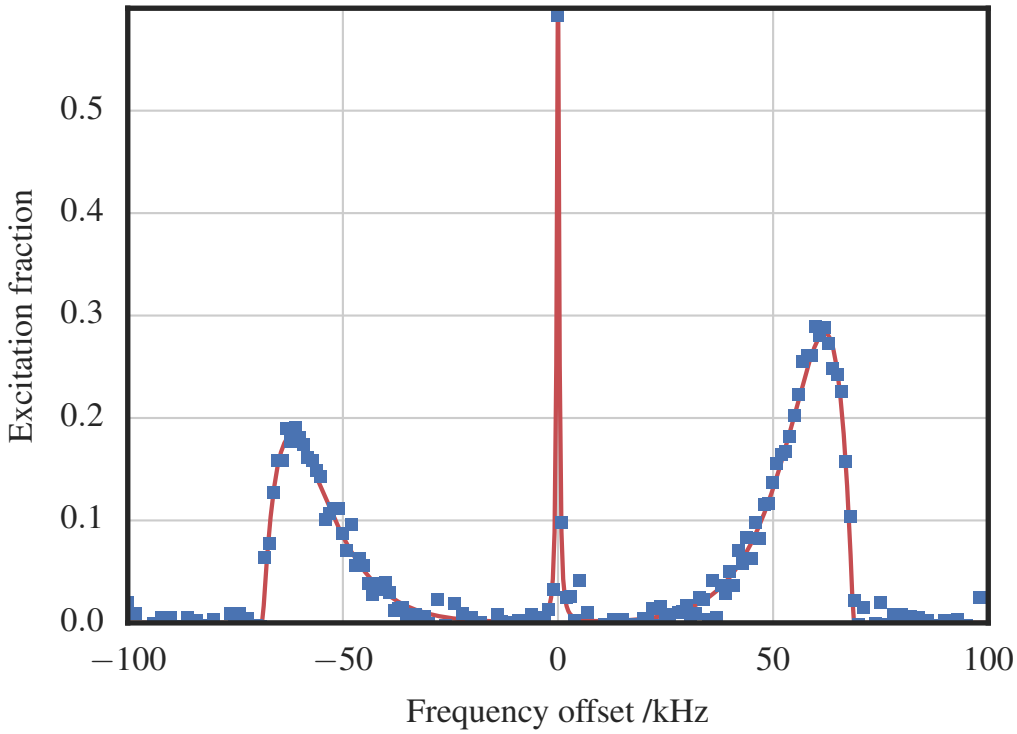

Fig. 2.9 High-power spectroscopy across the vibrational sidebands of the unperturbed transition (centre). Blue dots = measured values, red line = fit

ultra-stable cavity, which is not cancelled by the passive vibration isolation platform and the intra-vacuum cavity supports.

To investigate the state of the trapped atoms, high power (broadening the clock transition to more than 1 kHz) spectroscopy was conducted, observing the sideband-spectrum (figure 2.9) consisting out of the $^1S_0 \rightarrow {}^3P_0$ clock transition and one blue- and red-detuned sideband, raising or lowering the vibrational level of the interrogated atom, respectively.

These data allow one to determine the longitudinal trap-depth from the frequency of the sidebands relative to the carrier clock-transition through equation 1.25 and the atomic temperature by the ratio of their integrated sideband absorption cross sections, b_{br}. We shall approximate the vibrational level occupation by a Maxwell distribution (quantum effects are not yet relevant at the temperatures here), using the following equation from [70, 161]:

$$k_B T = h\nu_z / \ln(b_{br}) \tag{2.3}$$

The usual operating trap depth was $U_0 = 200\,\mathrm{E_r}$ ($\nu_z = 57.6\,\mathrm{kHz}$) with an atomic temperature inside the lattice of $7(3)\,\mu\mathrm{K}$. The shape of the sidebands is smeared out towards the carrier due to the reduced lattice intensity seen by atoms at a radial displacement from the axis. The radial trap-frequency was calculated as $218(10)\,\mathrm{Hz}$, little more than 10% of the 2 kHz recoil-frequency.

From the trap-depth and temperature the mean-vibrational state is easily accessible by fitting a Gaussian distribution. We calculated that 70% of all atoms occupy the lowest three vibrational levels. From the spread of the longitudinal trap-frequency in figure 2.9 we assessed that the atoms see an effective trap depth (meaning an average value) of $U_e = \xi \cdot U_0$ with $\xi = 0.8(1)$. Tunnelling broadens the discrete levels of the harmonic oscillator forming band-structures with increasing width by raising quantum number. We estimated the width of the third band, solving equation 1.30 numerically, as 2 mHz for usual lattice conditions.

2.11 Clock Operation

The frequency standard is running in a pulsed operation. One full clock cycle consists out of four single spectroscopic sequences. We alternatively interrogate the two sides of each Zeeman-transition ($m_F = \pm 1/2$) to derive an error-signal for each transition separately. The clock-laser frequency is controlled by a software implementing a digital lock steering the clock AOM (figure 2.2). The excitation fraction of all four measurements is recorded to deduct the frequency of both transitions during one clock cycle, allowing the tracking of the Zeeman-splitting. Averaging between the two π-transitions in post-processing then gives the frequency of the unshifted (no magnetic field) transition, suppressing the first-order Zeeman-effect and the residual vector light shift stemming from an imperfect lattice polarisation.

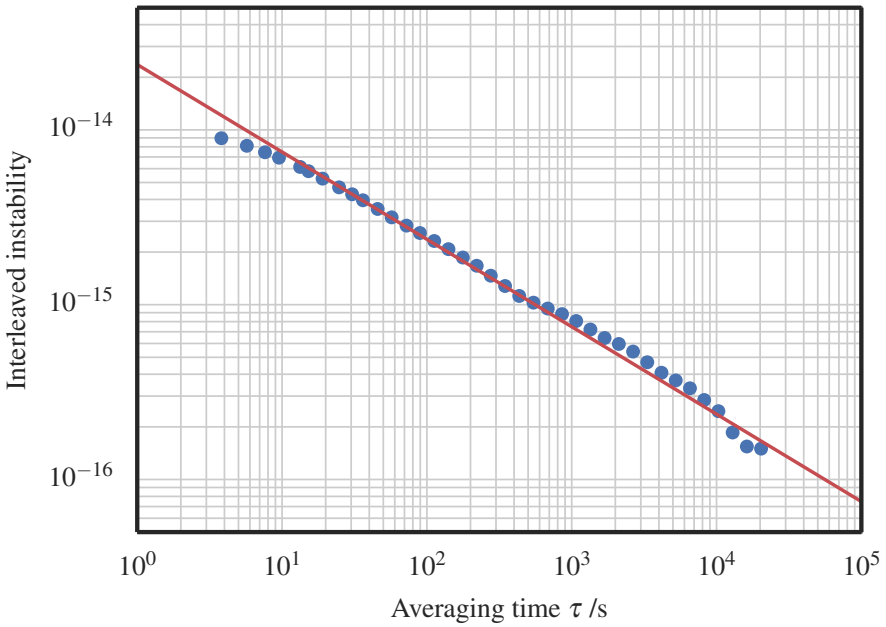

Fig. 2.10 This measurement served to estimate the lattice light shift. The blue dots are the stability of the frequency difference between two virtual clocks with low and high lattice intensity.

2.12 Uncertainty Evaluation

In order to evaluate systematic shifts we interleave two independent clock sequences, giving not two, but four independent locks. The data is then post-processed to extract the difference between the two "virtual clocks", interpolating at common time tags. The exemplary stability of the difference-signal between these two clocks during one measurement is shown in figure 2.10. The Allan deviation here runs as $2.3 \times 10^{-14}\tau^{-1/2}$ for a total measurement time of 22.5 h. This white frequency noise level is compatible with the 20 Hz linewidth observed. This stability is a full order of magnitude worse than expected and we were not able to improve it during our absolute frequency measurement campaign, resulting in averaging times more than three times the expected value, ultimately limiting the uncertainty evaluation of the AC Stark- and density-shift. The difference between the expected and observed stability is most likely explained by an insufficient vibrational noise elimination by the passive vibration isolation platform and the cavity's posts.

The uncertainty budget of INRIM's ^{171}Yb optical lattice clock is shown in table 2.1. The frequency of the $^1S_0 \rightarrow {}^3P_0$ transition is associated with a fractional

uncertainty of 1.6×10^{-16}. In the following the individual contributions are discussed in detail.

2.12.1 AC Stark Shift

Let us recall the lattice light shift from equation 1.29:

$$\begin{aligned}\Delta f = &\left[a\Delta\nu + \frac{3}{4}d(2n^2+2n+1)\right]\frac{U_e}{E_r} - d\left(\frac{U_e}{E_r}\right)^2 \\ &+(a\Delta\nu - b)\left(n+\frac{1}{2}\right)\left(\frac{U_e}{E_r}\right)^{1/2} + d(2n+1)\left(\frac{U_e}{E_r}\right)^{\frac{3}{2}}\end{aligned} \tag{2.4}$$

, with $\Delta\nu$ the detuning from the E1 magic wavelength, U_e the effective trap depth, a the linear E1 slope of the polarisability, while b and d give multipolar and hyper-polar corrections, respectively. The quantum number n is the average vibrational lattice state occupied by the atoms.

We first measured the linear part of the AC Stark shift and the corresponding magic wavelength by measuring the frequency difference of the clock transition between interleaved clock cycles with high $(U_0 = U_H)$ and low $(U_0 = U_L)$ lattice intensity. From the difference we extracted the total shift in the case of low intensity, assuming only a linear shift in intensity. The total shift was then corrected by accounting for the multipolar effects and hyperpolarisability, inserting the known values of $b = -0.68(71)\,\mathrm{mHz}$ and $d = -1.9(8)\,\mu\mathrm{Hz}$ for Yb in a linear polarised lattice [28, 78] in equation 2.4.

The lattice intensity is steered by changing the RF power driving the AOM at the output of the Ti:Sa laser, altering its diffraction efficiency. Thereby the spectral characteristics of the lattice laser remain independent of the intensity. No spectral filtering of the laser-output was conducted during our absolute frequency measurement campaign. An optical grating was introduced at a later point in time (see chapter 5). The power of the lattice is actively controlled and stabilised by a PID steering the AOM diffraction efficiency and the error signal generated from a photodiode observing the lattice light leaking through the back-reflection mirror, as shown in figure 2.2. In order to exclude additional shifts (e.g collisions) to

Table 2.1 Table of the ^{171}Yb clock-transition uncertainty estimation stemming from the individual effects discussed in this chapter.

Effect	Shift / Hz	Unc. / Hz	Rel. Shift / 10^{-17}	Rel. Unc. / 10^{-17}
Linear AC Stark	-0.02	0.04	-4	8
Nonlinear AC Stark	-0.07	0.05	-12	10
Zeeman	-0.14	0.02	-27	4
BBR room	-1.219	0.013	-235.3	2.5
BBR oven	-0.011	0.004	-2.1	0.8
Density	-0.01	0.03	-2	6
Background gas	$--$	0.008	$--$	1.5
Probe light	0.005	0.018	1	3.5
DC Stark	$--$	0.005	$--$	1
Line pulling	$--$	0.002	$--$	0.4
Doppler	$--$	0.03	$--$	5
Tunnelling	$--$	0.002	$--$	0.4
Servo	$--$	0.005	$--$	1
AOM switching	$--$	0.002	$--$	0.4
Fibre links	$--$	0.0005	$--$	0.1
Total	$\mathbf{-1.465}$	**0.08**	$\mathbf{-281.4}$	**16**

compromise the measurement of the lattice light shift, the atoms are always loaded at low lattice power U_L. In order to measure the shift with high trap depth, the lattice power is abruptly raised to high intensity U_H (using the RF input power of the AOM) within 0.1 ms just before the spectroscopy laser turns into resonance with the clock transition.

For our absolute frequency measurement we ran the lattice not exactly at the magic wavelength, but at our working point of $\nu = 394\,798.238\,\mathrm{GHz}$. Therefore we measured the shift between U_L and U_H with this specific lattice frequency and subsequently assessed a linear shift at U_L of $-0.02(4)\,\mathrm{Hz}$.

From sideband spectroscopy we obtained the values of U_H, U_L, ξ and n. They resulted as $U_H = 348(5)\,\mathrm{E_r}$, $U_L = 196(4)\,\mathrm{E_r}$, $\xi = 0.8(1)$, and $n = 2.1(10)$ at U_L and $n = 1.5(8)$ at U_H.

With these results we corrected the shift at the working point with the hyperpolar and multipolar corrections in equation 2.4. The hyperpolar and multipolar shifts resulted as $-0.13(6)\,\mathrm{Hz}$ and $64(32)\,\mathrm{mHz}$, respectively. The nonlinear lattice shifts then sum up to a total of $-0.07(5)\,\mathrm{Hz}$, the single largest contribution in the uncertainty evaluation (see table 2.1). This uncertainty mainly stems from the uncertainties of the coefficients b and d, which are contributing stronger to the result as the lattice depth increases.

The calculated AC Stark shift at a lattice depth of $200\,\mathrm{E_r}$, assessed by interleaving tow virtual clock cycles between high and low lattice depth and changing the lattice frequency, is shown in figure 2.11. For this measurement we used lattice depths of $U_L = 208(2)\,\mathrm{E_r}$ and $U_H = 333(4)\,\mathrm{E_r}$. The shift was corrected for higher-order contributions and subsequently we fitted the curve with a second-order Taylor expansion around the magic wavelength:

$$\Delta f = a\Delta\nu(\frac{U_e}{E_r}) + c\Delta\nu^2(\frac{U_e}{E_r}) \tag{2.5}$$

The fit gave $a = -27(3)\,\mathrm{mHz\,GHz^{-1}}$ and the quadratic coefficient $c = -0.16(3)\,\mathrm{mHz\,GHz^{-2}}$. The uncertainty stated is limited by the knowledge of ξ, not the statistics.

Combining the measured shift at the working point with the linear coefficient and subtracting the nonlinear corrections, we determine the E1 magic frequency as $394\,798.205(17)\,\mathrm{GHz}$. This value, as well as previously reported ones [4, 162–

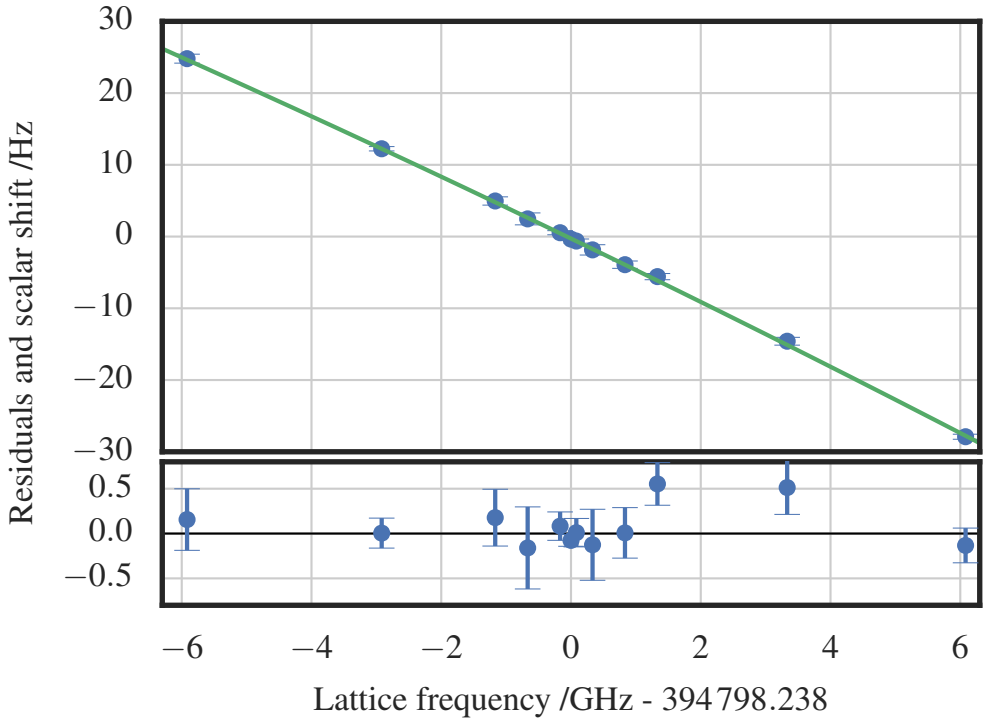

Fig. 2.11 Total AC Stark shift against lattice frequency at $U_0 = 200\,\mathrm{E_r}$, extracted from interleaved measurements between lattice depths of $U_L = 208(2)\,\mathrm{E_r}$ and $U_H = 333(4)\,\mathrm{E_r}$ and with the application of multipolar and hyperpolarisability corrections. Blue points are measured data points and the green line a quadratic fit. Bottom panel shows fit residuals.

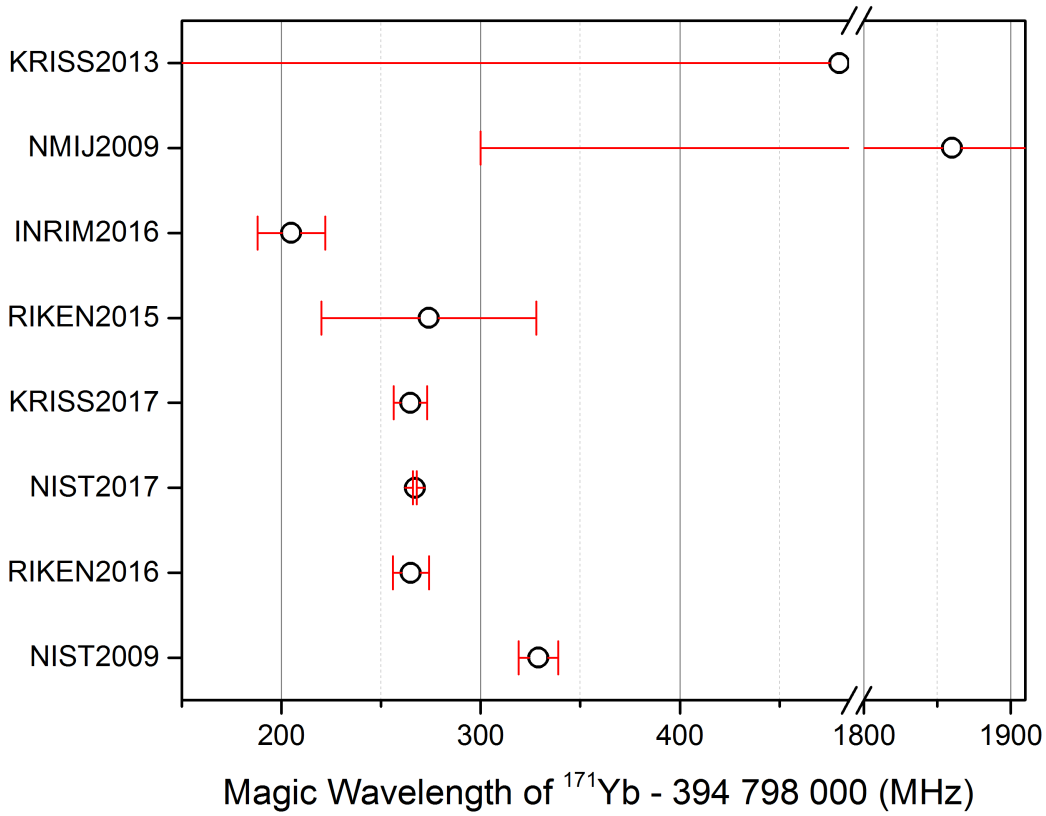

Fig. 2.12 The magic wavelength of ^{171}Yb (circles) with respective uncertainties (red bars) as measured in this work (INRIM2016) [38] compared to other recent and previous values by NIST [4, 165], NMIJ [162], RIKEN [5, 28] and KRISS [163, 166]. It is noteworthy that the most precise values (RIKEN2016, KRISS2017, NIST2017) are in agreement with each other and that for these measurements the ASE spectrum of the lattice laser was suppressed through optical filtering with Bragg-gratings or enhancement cavities.

164, 5, 28, 165, 166], are not consistent with each other, see figure 2.12 (The value of [164] has no stated uncertainty and is therefore neglected here). This is probably due to the unique details of the laser emission spectrum - precisely the amplified spontaneous emission (ASE) - of each laser system used introducing an additional AC Stark shift of the clock transition. The magic wavelength is thereby offset with respect to a pure monochromatic wave if this spectrum is not filtered out (e.g. by a grating or a cavity) [167].

2.12.2 Zeeman Shift

During each spectroscopic cycle we apply an external, vertical magnetic field (directions as in figure 2.3) and spin-polarise the atoms to one of the $m_F = \pm 1/2$ states. The frequency difference between the two split states, evaluated in two spectroscopic cycles, gives directly the Zeeman-shift and thereby the applied magnetic field. During clock operation the Zeeman shift was chosen to be $290.1(3)$ Hz (relative to the center), corresponding to a magnetic field of $B = 138(1)\,\mu$T, taking first- and second-order Zeeman-coefficients from [4]. The drift of the magnetic field was evaluated to be lower than $0.1\,\mu\mathrm{T/h}$. Averaging over the two hyperfine-states removes the first-order Zeeman contribution. The 2nd order Zeeman shift was evaluated using the quadratic Zeeman coefficient for Yb in [4], $7(1)\,\mathrm{Hz/mT}$. The resulting shift is $-0.14(2)$ Hz.

2.12.3 BBR Shift

Recalling the black-body radiation shift in equation 1.33:

$$-\frac{1}{2}\left(\alpha^{DC}_{excited} - \alpha^{DC}_{ground}\right) < E^2 >_T (1 + \eta_{clock}(T)). \tag{2.6}$$

For ^{171}Yb we have $\Delta\alpha^{DC} = \alpha^{DC}_{excited} - \alpha^{DC}_{ground} = 36.2612(7)\mathrm{kHz(KVcm)}^{-2}$ and $\eta_{clock}(T = 300\,\mathrm{K}) = 0.0179(5)$ [99, 103]. The BBR impinging on the atoms can be separated according to origin: The vacuum system, consisting out of the science chamber and connection tubes, and the Yb oven.

The science chamber itself, shown in figure 2.3, consists out of an Al body with large silica viewports, AR-coated at the wavelengths used for the Yb frequency standard operation. In the wavelength-region of the BBR these windows are opaque. Therefore the shift calculation needs to take into account only the BBR from sources inside the vacuum system. The vacuum system temperature is constantly monitored at ten different positions by Pt1000 platinum resistance thermometers. Eight of those thermometers are spread across the Al science chamber, another one close to the Yb oven and the last piece at a maximum distance far away from it. Gradients in temperature stem from the Yb oven, dissipated power within the MOT coils and their water-cooling system. The Pt1000 have a calibration uncertainty of 0.2 K and

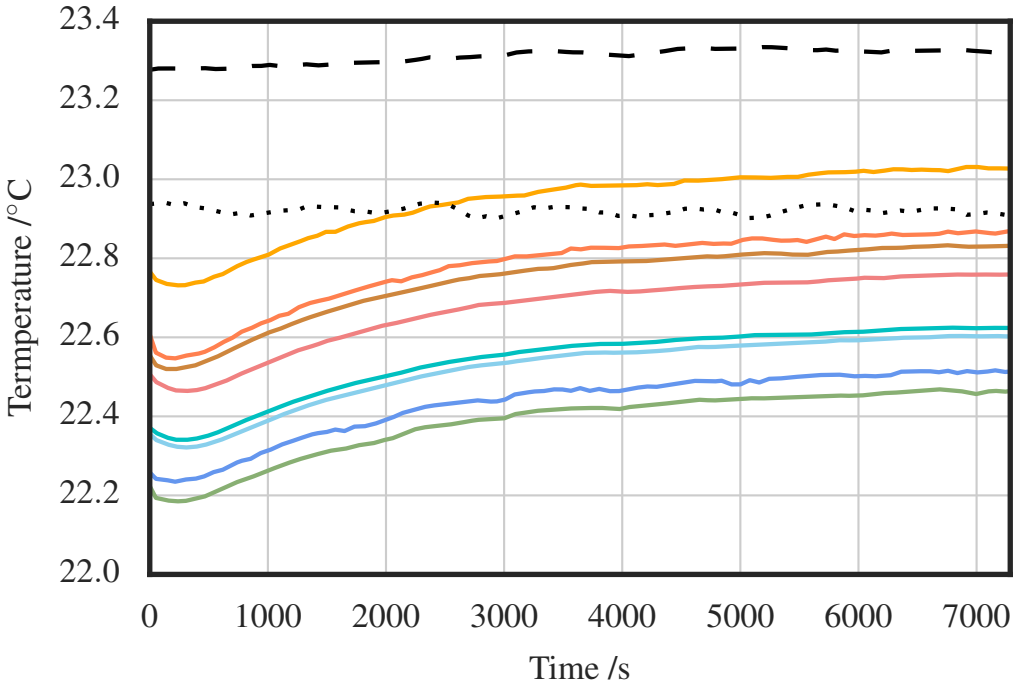

Fig. 2.13 Temperature readings of the ten Pt1000 thermometers across the vacuum chamber during a single measurement. Solid coloured lines are the temperature readings around the science chamber, while the black dashed and dotted lines are the values recorded close to the atomic oven and far away, respectively.

are read-out by 4-wire resistance measurements with an additional uncertainty of 0.06 K.

With the temperature inside the lab controlled at the 0.5 K level by an AC system typically a spread between the thermometer readings of up to 2 K across the vacuum chamber was observed. This gradient would usually be increased when starting the experiment due to rising temperatures inside the oven or the MOT coils. During our measurements we would often wait for the temperature to reach its equilibrium before taking data. A typical data set of thermometer readings is shown in figure 2.13. For each individual measurement the read-out temperature distribution across the vacuum system was approximated as a rectangular probability distribution with an average value of $T = (T_{max} + T_{min})/2$ and associated uncertainty $\mu_T = (T_{max} - T_{min})\sqrt{12}$, where T_{max} and T_{min} signify the maximum and minimum temperature recorded during one single measurement. The temperature uncertainty of the data shown in

figure 2.13 is $\mu_T = 0.8\,\mathrm{K}$. After many measurements the BBR shift associated to the vacuum system resulted as $-1.219(13)\,\mathrm{Hz}$.

The Yb evaporation oven temperature is monitored by a thermocouple. During clock operation the oven reaches a temperature of 400(10) °C . The rather large uncertainty results as the accuracy of the thermocouple and the temperature spread between the oven tip and the sensor position are taken into account. The BBR emitted by the oven reaches the position of the atomic cloud through a copper vacuum differential tube with a length of 15 cm (total distance oven-atoms: 20 cm) and an inner diameter of 0.5 cm. Therefore a BBR estimation needs to take into account, that also radiation undergoing reflections inside the tube can reach the atoms. With the emissivity of copper as :$\varepsilon_{Cu} = 0.4(2)$ a ray tracing analysis can be performed to calculate the effective solid angle under which direct and reflected radiation impinges on the atoms. It turns out that up to two reflections are relevant to the calculation. The BBR shift contribution due to the Yb oven has been thus evaluated as $-0.011(4)\,\mathrm{Hz}$.

During the very first absolute frequency measurements the slower beam was not sent unto an intra-vacuum mirror, but faced the hot atomic beam directly through a heated window (to reduce Yb condensation and coating). This window's temperature was at 230(5) °C. The effective solid angle for its BBR was modelled with 5 reflections from the stainless steel surface of the tube connecting it to the science chamber and one from inside the Al chamber itself. The emissivities here are $\varepsilon_{steel} = 0.5(3)$ and $\varepsilon_{Al} = 0.13(10)$. The calculated BBR shift was $-0.12(15)\,\mathrm{Hz}$. After a few measurements the hot window was replaced with the aforementioned cold intra-vacuum mirror, removing this shift-contribution entirely. While the highest contribution to the clock's uncertainty evaluation therefore stems from the environmental temperature distribution as 2.5×10^{-17}, for our absolute frequency measurement campaign we were averaging data with and without the hot window, resulting in a final contribution of the BBR shift as 5×10^{-17}.

2.12.4 Collisions

The shift arising from atomic collisions is separated into two distinct regimes of cold and hot atoms with associated density and background-gas shifts, respectively.

Background Gas Shift

The hot background gas consists out of the hot atomic beam of Yb atoms, passing right through the lattice position, and residual atmospheric gases (especially hydrogen). The collisions appearing here kick the cold atoms out of the lattice and are therefore related to the lattice lifetime by equation 1.32. We observed a lifetime (of the cold atoms inside the trap) of 2.7 s. Taking the C_6 Van-der-Waals coefficients for Yb dimers [168] we calculate a shift of 8 mHz. We inflate the error bars to the same value to account for the uncertainty of the background gas composition.

Density Shift

The captured ^{171}Yb atoms are fermions, therefore the density shift is dominated by p-wave cold collisions, while small s-wave contributions arise from inhomogeneities during the Rabi excitation. Therefore the shift depends on the exact details of the Rabi interrogation pulse and the efficiency of spin-polarisation. The density shift is evaluated similarly to the AC Stark shift, exchanging the lattice depth modulation with a variable atomic density inside the lattice.

We measure the density related shift between interleaved clock cycles with two distinct numbers of atoms loaded into the trap. The lattice frequency and intensity is maintained constant throughout all measurements. The atomic density can be varied over a wide range by alternation of the duration of the slower beam during the first stage MOT. This way the trapping conditions remain unchanged for high- and low-densities alike, justifying also the assumption that the number of atoms is proportional to the density.

The trap region's dimensions are set by a projection of the cold atomic cloud of the second/third stage MOT unto the lattice. The trap radius is given by the lattice radius as 45 µm and its length by the cloud-extension of 0.5 mm.

We assessed an atomic density of $\rho_0 = 4 \times 10^{14}$ m^{-3}, corresponding to ca. 1 atom per lattice site (per "pancake", figure 1.3). The estimated number of atoms is always associated with a fractional uncertainty of 20%, but the relative density uncertainty during each measurement was only 1%.

Assuming only a linear shift, we measured the density shift against the relative density difference between the high-density and low-density clock cycles, using

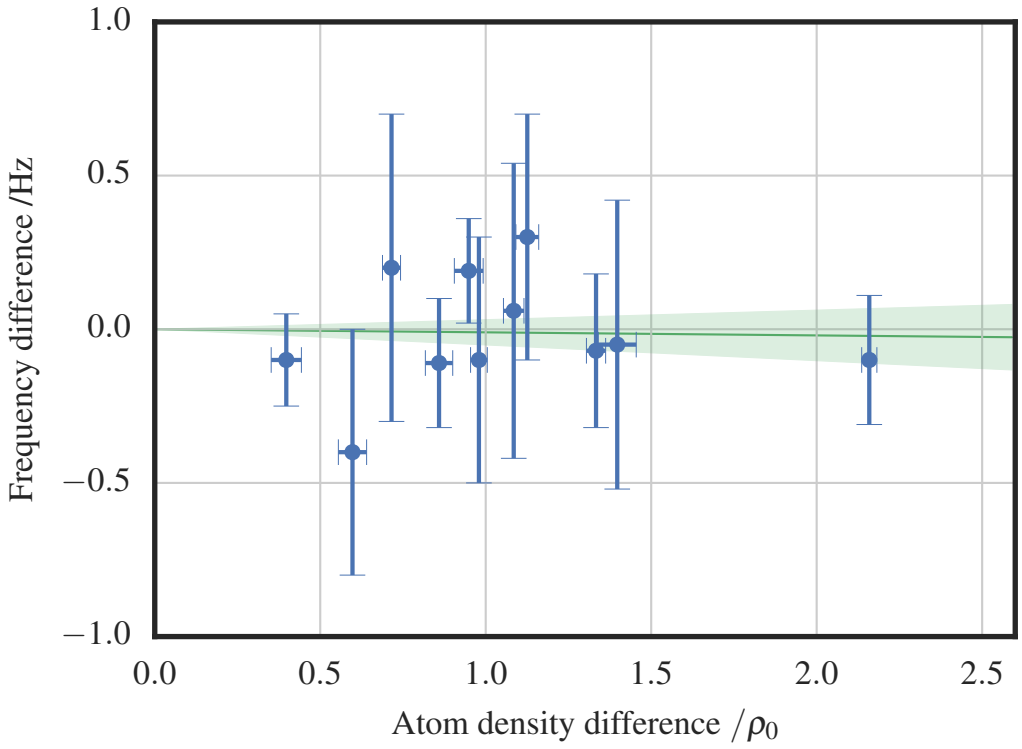

Fig. 2.14 Frequency shift between interleaved clock cycles with high and low number of atoms in the lattice and an average excitation fraction of 0.39(2) at the side-of-fringe locking positions against the difference in atomic density at high and low atom number. Blue dots are experimental data with their uncertainty. Green line is linear fit and shaded region its uncertainty.

density pairs in the range between $\rho \simeq 0.1\rho_0$ and $\rho \simeq 3\rho_0$. The resulting density shift measured as a function of the atomic density difference is shown in figure 2.14. Here the sample is always spin-polarised and the excitation fraction of each clock sequence, measured after the Rabi pulse, is 0.39(2). This fraction is fixed by our choice of the locking point on the side of the resonances, but a minimal density shift can be expected around 0.5 [95]. Applying a linear fit with no offset at zero density gives a density shift related slope of $-0.01(4)\text{Hz}/\rho_0$. We measured the density shift also at a slightly different excitation fraction (achieved by changing the locking point) of 0.34(2) in the same way, measuring a slope of $-0.4(2)\text{Hz}/\rho_0$. This dependence of the density shift on excitation fraction agrees with the theoretical predictions of p-wave scattering [95].

Our normal working conditions for the lattice clock lead to an atomic density $\rho \simeq 0.7\rho_0$ and an excitation fraction of 0.39(2) with an associated density shift of $-0.01(3)$ Hz. The uncertainty is larger than the shift itself due to statistics.

2.12.5 Probe Light Shift

The probe laser interrogating the $^1S_0 \rightarrow {}^3P_0$ transition at 578 nm causes an AC Stark shift, despite its low power of ca. 70 nW, as it is far from the magic wavelength (759 nm). We calculated the corresponding shift from the value published in [4]. This is possible, since in both cases the atoms were interrogated with with a π Rabi-pulse. The Rabi area is proportional to the Rabi time and the square root oft the laser intensity. Therefore in comparing our situation with the aforementioned publication we apply that for a π-pulse the laser intensity is proportional to the inverse square of the pulse time. From this reflection we deduce a probe laser Stark shift of $0.005(18)$ Hz.

2.12.6 DC Stark Shift

An external static electric field (field-strength $E = V/d$, Voltage V on electrodes of separation d) induces a dipole in the cold atoms, leading to a shift of the atomic levels. This shift is given by:

$$\Delta\nu = -\frac{1}{2}\Delta\alpha E^2 \tag{2.7}$$

, with $\Delta\alpha$ the difference in static polarisability between ground- and excited state, taken from [99].

The science chamber consists out of an aluminium body with silica windows. Therefore the body acts as a Faraday cage shielding external fields, but significant charges can build up on the window surfaces inside the vacuum environment [169].

There are two windows relatively close to the atomic cloud (25 mm). They have radii of 38 mm and are 12 mm thick. Assuming these to be the plates of a simple capacitor a capacitance of 0.6 pF is assigned to the windows. Taking the resistivity of fused silica of $10^{18}\Omega$m a time constant for charges on the inner surface of a window to travel to the surface outside the vacuum system is estimated as ca. 50 d [169]. We assume that outside the vacuum system the time for surface-charges to decay is negligible compared to this timescale.

Having operated the vacuum system of our frequency standard for several years, charges initially present should have decayed by now, giving a Stark shift $< 1 \times 10^{-17}$. Consequently we estimate the associated uncertainty as 1×10^{-17}.

2.12.7 Line Pulling

The light driving the clock transition is linearly polarised (Glan-Thompson polariser, extinction ratio 100k : 1), effectively cancelling the σ transitions. The m_F state spin polarisation then effectively cancels out the line pulling from any nearby hyperfine Zeeman-split resonance (98% state polarisation). The only relevant line pulling is imposed by the vibrational lattice sidebands (peak value about 50 kHz away from the carrier). The resulting line pulling is estimated at 2 mHz that we take also as the uncertainty.

2.12.8 Doppler Shifts

The uncertainty attributed to the actively noise cancelled fibre links of the 578 nm is taken as the measured 1×10^{-18} from section 2.7. But looking back at figure 2.2 it becomes clear that the reference mirror for the fibre noise cancellation is not identical with the lattice back-reflector. Instead they are about 30 cm apart, giving rise to (linear) Doppler noise between the optical lattice and the clock laser. We discovered some phase-noise through an optical beatnote of the 578 nm radiation from these

two references. This noise was partially synchronous with the clock cycle, most probably due to MOT coils switching. We measured a Doppler noise contributing some 5×10^{-17} to the frequency-standard's uncertainty. The second-order Doppler contribution at 7 µK is below the 10^{-20} level and was therefore neglected.

2.12.9 Tunnelling

With 70% of all atoms in the lowest three vibrational levels we assess the uncertainty of the transition frequency by taking the width of the third band, 2 mHz (see paragraph 2.10) as uncertainty.

2.12.10 Servo and AOM switching

The stabilisation of the 578 nm laser to the frequency standard of the atomic transition is a digital side-of-fringe lock. Taking the average of the error signal recorded over several weeks of our absolute frequency measurement campaign we investigated a possible systematic locking offset against the actual transition frequency caused by the digital electronics. We observed a zero shift with an uncertainty of 1×10^{-17}.

The clock laser light is switched during one spectroscopic cycle to resonance for the interrogation, while being detuned 1 MHz otherwise. This switching might introduce a phase-shift, but is still preferable over a change of the AOM RF-power, since the latter introduces thermal effects, changing the Gaussian beam characteristics. No shift introduced by the AOM was observed with an uncertainty of 2 mHz in the measurement, evaluated through heterodyne interferometry.

We further investigated the reaction of the phase-noise cancellation to the sudden switch of the AOM frequency. Following the argument of [170] we estimate a phase-jump to appear with an amplitude of 0.5 mHz that we take as uncertainty.

2.12.11 Gravitational Redshift

The gravitational redshift is not driving the frequency of the atomic transition away from the unperturbed state, but is rather a result of the relativistic time dilation between two accelerated reference frames. The knowledge of the difference in

gravitational pull between the location of two frequency standards is necessarily impinging the accuracy of any frequency ratio measurement between them.

The gravitational potential at INRIM's labs was measured in 2013 relative to the geoid as part of a joint effort towards timescales with optical clocks within the European project "International Timescales with Optical Clocks" (ITOC) [171, 172]. The measurement was conducted in tow ways: By geodetic levelling and GNSS (Global Navigation Satellite System) measurements [173].

The gravitational potential at the position of the Yb atoms resulted as $C(Yb)_{lev} = 2336.25(35)\ \mathrm{m^2 s^{-2}}$ from the levelling approach and was assessed as $C(Yb)_{GNSS/geoid} = 2336.48(27)\ \mathrm{m^2 s^{-2}}$ by the GNSS system [174]. Geometric levelling offers a higher accuracy over short distances, but accumulates greater systematic shifts over distances above 1000 km [175]. This means that for comparisons of optical clocks in separate laboratories across Europe by means of satellite- or fibre-links, the GNSS measurements provide a lower uncertainty. Using equation 1.37 the GNSS potential at the position of the Yb atoms results in a gravitational redshift relative to the geoid of 13.474(3) Hz and a fractional uncertainty of 6×10^{-18}, limited by the uncertainty of the model geoid potential W_0. The reference potential for both measurements was the International earth Rotation and Reference System Service (IERS) 2010 conventional reference potential $W_0 = 62636856.0(5)\ \mathrm{m^2 s^{-2}}$ [176, 177].

2.13 Absolute Frequency Measurement

The absolute frequency of the ${}^1S_0 \rightarrow {}^3P_0$ transition in ^{171}Yb was measured relative to the primary frequency standard at INRIM, the cryogenic caesium fountain ITCsF2. The measurement campaign lasted from January until May of 2016. A scheme of the setup is shown in figure 2.15. The gap between the 518 296 GHz of the Yb optical frequency standard and the 9.2 GHz transition frequency of the primary frequency standard was bridged by an Er-fibre comb from Menlo Systems with a repetition rate of 250 MHz and the CEO-frequency at 20 MHz, both stabilised to a hydrogen maser. A detailed treatment of how to bridge optical to microwave frequencies with a frequency comb acting as flywheel oscillator is found in chapter 5. The SI-standard fountain clock continuously tracks the maser frequency relating it to the atomic transition between the ground-state hyperfine-split $6^2S_{1/2}$ $F = 3$ and $F = 4$ levels.

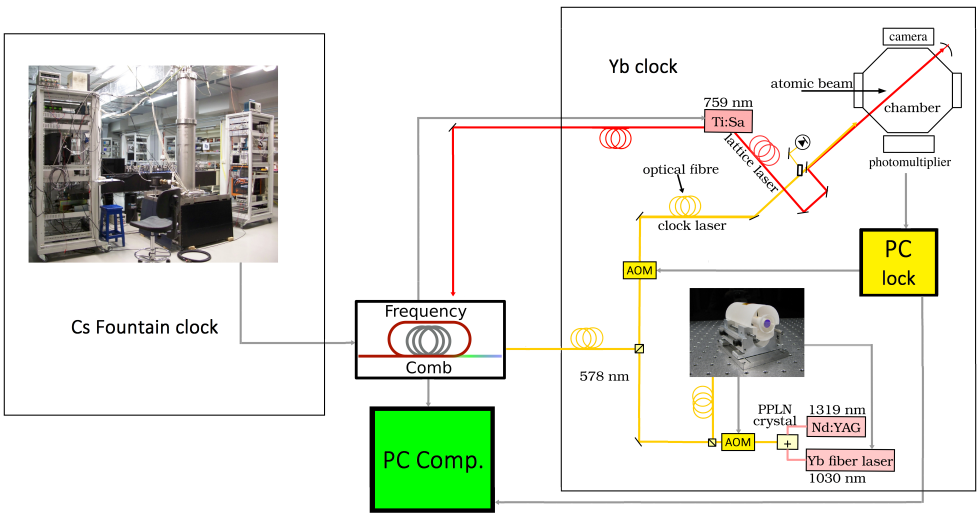

Fig. 2.15 Schematic of the absolute frequency measurement. The grey connections are RF signals or data channels. The lock of the ultra-stable laser on the ^{171}Yb clock transition and the frequency measurement against the ITFCsF2 primary frequency standard are done with the support of software signal processing.

A part of the 578 nm radiation stabilised to the ultra-stable cavity is sent to the frequency comb by fibre and another one to the atoms for interrogation with an AOM bridging the frequency difference between the cavity mode and the atoms. All these fibre links are phase-noise cancelled with the same relative uncertainty evaluated after 1000 s of integration time: 1×10^{-18}.

Consequently the comb did not measure the frequency of the atoms, but of the cavity. Two different computers synchronised to INRIM's Network Time Protocol (NTP) server recorded the frequency of the beatnote with the frequency comb and the Yb atoms of the optical frequency standard. The comb and the Yb clock recorded the data at different rates . Therefore the data points were averaged and interpolated to common timestamps. The server synchronisation had an uncertainty of 3 ms. Together with the maximum observed frequency drift of the cavity of 0.1 Hzs^{-1} we calculated an uncertainty contribution related to synchronisation of 6×10^{-19}.

The comb measuring the frequency ratio between the microwave reference from the maser and the optical radiation has a related uncertainty that is assessed by a synchronous measurement of this ratio (equivalent to the input optical laser's frequency) with two identical combs. The uncertainty results as 1×10^{-16} and is limited by the comb's electronic noise after an averaging time of 10 000 s. The beatnote between the cavity-stabilised laser and the frequency comb was measured redundantly in

order to detect cycle slips in the counter. Data points with a disagreement of the two counter-readings worse than 0.2 Hz were discarded in the absolute frequency evaluation.

2.13.1 ITCsF2

The cryogenic caesium fountain ITCsF2 had been characterised previously [178]. During our measurement campaign the clock ran in two different atomic density regimes. The low density regime comes with an uncertainty of 3.0×10^{-16} and a stability of $3.6 \times 10^{-13}\tau^{-1/2}$ (τ as always in seconds). The high density regime on the other hand offers an improved stability of $2.5 \times 10^{-13}\tau^{-1/2}$ at the price of an increased uncertainty of 4.8×10^{-16}. We considered the tracking of the hydrogen maser by the fountain only during the time of the operation of the Yb secondary frequency standard.

The gravitational potential of the atoms inside the fountain was determined in the same ITOC campaign as mentioned before. The results of the levelling and GNSS asppproach were: $C(Cs)_{lev} = 2334.8(10)\mathrm{m}^2\mathrm{s}^{-2}$ and $C(Cs)_{GNSS/geoid} = 2335.0(10)\mathrm{m}^2\mathrm{s}^{-2}$. Using the GNSS value for the gravitational redshift gives a relative shift of $2.599(1) \times 10^{-14}$.

The height difference between the Yb atomic cloud and the average integrated height of the Cs atoms along their ballistic flight trajectory is $h(Yb-Cs) = 0.15(2)\,\mathrm{m}$ with an associated relative gravitational redshift of $1.6(2) \times 10^{-17}$.

2.13.2 Measurement

During our measurement campaign we took a total of 31 measurements during which both frequency standards (Cs and Yb) were running continuously, resulting in a total 227 h of measurement time.

Table 2.2 shows the individual contributions to the uncertainty of the absolute frequency measurement. The absolute frequency results as $f_{^{171}Yb} = 518\,295\,836\,590\,863.59(31)\,\mathrm{Hz}$.

The different measurements and their respective uncertainties are shown in figure 2.16 as a function of the modified Julian date (MJD). During each individual measurement the uncertainty is limited by the fountain instability. The various

Table 2.2 Table of the individual uncertainty contributions to the absolute frequency measurement

Contribution	Uncertainty / Hz	Rel. Uncertainty / 10^{-17}
ITCsF2	0.21	40
Statistics	0.20	39
Yb	0.08	16
Comb	0.05	10
Gravitational redshift	0.001	0.2
Fibre link	0.0005	0.1
Synchronisation	0.0003	0.06
Total	**0.31**	**59**

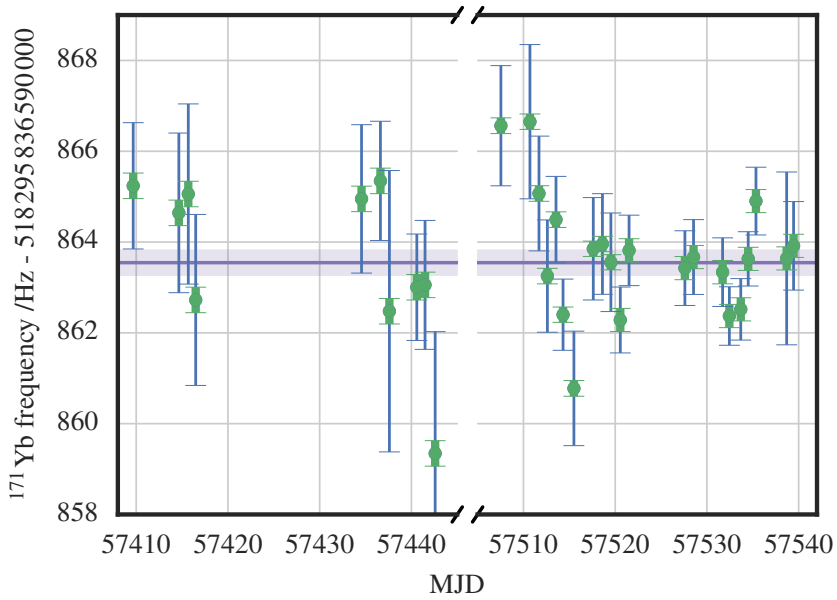

Fig. 2.16 The individual measurements between January 2016 and May 2016 on the absolute frequency of the ^{171}Yb clock transition against ITCsF2. Blue thin bars mark combined statistical and systematic uncertainty of the respective measurement and green thick bars the combined systematic uncertainty of the two atomic clocks. Violet bar and shaded region denote the resulting mean and its uncertainty σ.

systematic uncertainties associated to individual measurements are related to the density regimes of the fountain and the Yb clock as well as the reduced BBR shift uncertainty on the Yb system after the removal of the hot window after the first 10 measurements.

The individual measurements with their varying uncertainties were evaluated in a statistical analysis based on the Gauss-Markov theorem [179, 180] that considers correlations between data-sets (measurements) with different systematic shifts [181]. The reduced χ^2 with 30 degrees of freedom for the average, calculated from the complete correlation matrix of the measurements [181], is $\chi^2_{red} = 1.36$ with a p-value of 10%. The statistical uncertainty resulted as 3.4×10^{-16}, but accounting for the $\chi^2_{red} > 1$ gave a total contribution of 3.9×10^{-16}.

The fountain gave an uncertainty contribution of 4.0×10^{-16}, taking into account the two different density regimes, while the Yb clock uncertainty remained as low as 1.6×10^{-16}.

The relative uncertainty associated with the absolute frequency measurement finally resulted as 5.9×10^{-16}.

A comparison of our measurement with the CIPM recommended frequency of the $^1S_0 \rightarrow {}^3P_0$ transition in ^{171}Yb is shown in figure 2.17. The recommended value by the CIPM for the acknowledged secondary frequency standard ^{171}Yb is $f_{^{171}Yb} = 518\,295\,836\,590\,864.0(10)$ Hz [47].

The other, previous measurements shown are referring the Yb frequency to absolute frequency standards (Cs fountain clocks) [4, 163, 162, 182] and to values deduced from frequency ratio measurements against ^{87}Sr secondary frequency standards [28, 164, 5]. In the later case we scaled the frequency ratios with the recommended frequency for the $^1S_0 \rightarrow {}^3P_0$ transition of $f_{^{87}Sr} = 429\,228\,004\,229\,873.2(2)$ Hz with its uncertainty of 5×10^{-16} [47].

2.14 Conclusion

We measured the absolute frequency of the unperturbed $6s^2\ {}^1S_0 \rightarrow 6s6p\ {}^3P_0$ transition in ^{171}Yb with a fractional uncertainty of 5.9×10^{-16}. The measurement uncertainty was mainly limited by the systematic shifts of the primary frequency standard and not the optical lattice atomic frequency standard or statistics. The transition

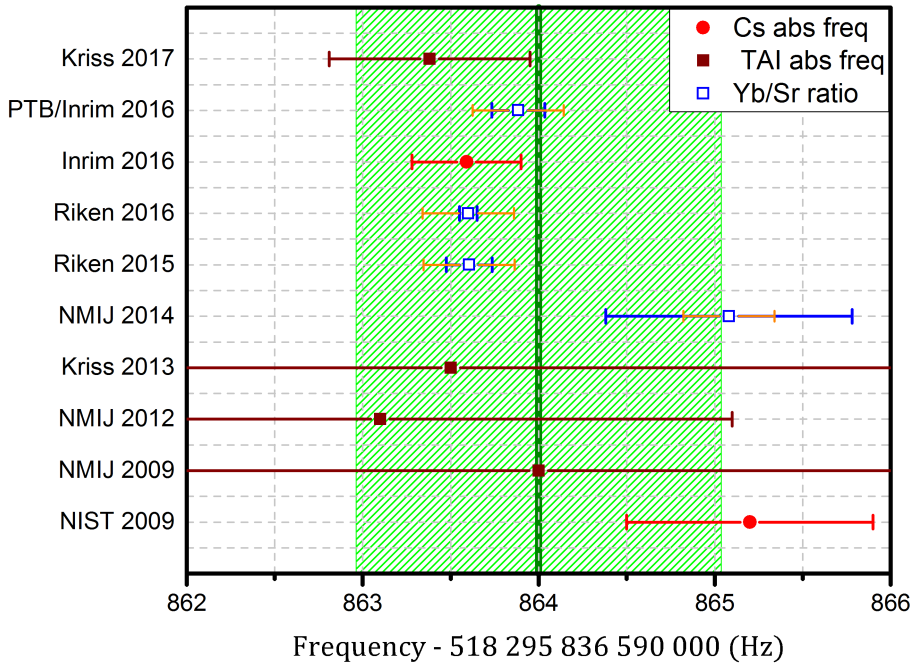

Fig. 2.17 Comparison of our result to previous absolute frequency measurements of the clock transition in ^{171}Yb against Cs-fountain clocks (circles) and such measurements that were mediated by microwave clocks referenced to the international atomic time (TAI) (full squares) as well as to deduced values from ^{171}Yb/^{87}Sr ratio measurements (open squares) with their respective uncertainties of measurement (blue) and of the ^{87}Sr recommended frequency (orange). Green line and shaded area mark the recommended frequency of ^{171}Yb as a secondary representation of the second by the CIPM (2015). The measurements are taken from: NIST [4], NMIJ [164, 162, 182], KRISS [163, 166] and RIKEN [28, 5]

frequency results as $f_{^{171}Yb} = 518\,295\,836\,590\,863.59(31)\,\mathrm{Hz}$, in agreement with the recommended value of the secondary frequency standard published by the "International Committee for Weights and Measures" (CIPM). The uncertainty of this absolute frequency measurement is the lowest achieved so far for this particular transition. Our measurement is independent from previous approaches and the first one of this transition in Europe after all precessing ones were conducted in east Asia and North America. Obtaining agreements between several measurements from different groups is important, especially under the light of a possible redefinition of the SI-unit the second.

The uncertainty of the Yb optical frequency standard was evaluated as 1.6×10^{-16}. The stated limitation is mostly due to the poor short-term stability of the clock transition laser referenced to an ultra-stable cavity hindering a better assessment of the individual shifts, especially density- and Stark-shift, through interleaved measurements. We expect that this uncertainty can be reduced to the low 10^{-17} level once the stability of the laser is improved. The improvement of the ultra-stable laser was conducted as soon as the measurement campaign ended. The means of improvement was, most of all, a replacement of the ultra-stable cavity. Further details on this improvement as well as a partial implementation of those mentioned below are reported and discussed in chapter 4.

The nonlinear components of the AC Stark shift can be reduced if smaller lattice depths are used and by improved measurements of multipolar and hyperpolarisability contributions. The multipolar effects are estimated from the non-linearity of the AC Stark shift against the lattice intensity [28] and the hyperpolarisability from the lattice shift at wavelengths around two-photon transitions [78]. Another approach would be to reduce these contributions using a "magical ellipticity" [79] to cancel out the hyperpolarisability and to introduce sideband-cooling on the red lattice sideband of the clock-transition to reduce the multipolar effects.

The residual (2nd order) Zeeman effect is diminished when applying smaller magnetic fields. The Doppler uncertainty is effectively dealt with by using the lattice back-reflector mirror as reference for the fibre noise cancellation of the interrogating laser, keeping lattice and laser in phase. Much of the BBR shift stemming from the Yb oven as well as a great deal of the background gas collisions vanish when implementing an automated mechanical shutter in the path of the atomic beam and steering it in phase with the clock spectroscopy.

The DC Stark shift can be evaluated more precisely applying a high voltage to electrodes placed on the vacuum chamber windows, following the approach of [99].

The environmental BBR shift is very likely to be the ultimate limitation to the uncertainty budget of this frequency standard. The current contribution is estimated at 2.5×10^{-17}. Improving the thermal isolation of the vacuum system from its surrounding heat-sources, especially the MOT coils and the atomic oven and waiting for thermal transients to decay before recording a measurement might help to reduce this contribution towards 1×10^{-17}.

A further reduction of the uncertainty estimation (a clock with an accuracy in the 10^{-18}s) will necessarily need an improved BBR intra-vacuum environment. So far two different approaches have been exploited to reach such levels of BBR shift uncertainty: Reducing the environmental temperature to cryogenic levels [104, 1] or designing intra-vacuum chambers with special coatings to improve the knowledge of the BBR environment of the atoms at room temperature [103, 48].

Chapter 3

First Measurement Campaign With A Transportable ^{87}Sr Clock

3.1 Geodesy, Metrology And The Need For Optical Clock Comparisons

The work presented in this chapter has been published in [115]. With optical lattice clocks reaching accuracies in the low 10^{-18} region after few hours of measurement [48, 49], the way to novel approaches for tests of physical theories [183, 184] and a revision of the international system of units (SI) [7, 185] has been opened. Absolute frequency measurements of optical clocks are nowadays limited by the current realisation of the SI-standard the second with Cs-fountain clocks [28].

Direct optical comparisons[5, 28] offer a way out of this dilemma. The frequency ratio gained by such measurements is independent of the SI-standard, allowing to investigate systematic uncertainties and clock stabilities when comparing two clocks utilising the same atomic transition [1, 50, 186]. Ratio measurements of optical atomic clocks based on different elements are performed bridging the frequency difference with optical frequency combs [187–189]. Such frequency ratio measurements offer a way to create a "frequency matrix" of optical transitions as secondary frequency standards with higher precision than absolute frequency measurements based on the SI-second [181, 190]. Reaching consistency of these matrix values

across laboratories around the world would be an important milestone towards a redefinition of the SI-unit the second in terms of an optical transition.

Another important application for optical clock comparisons is found in the search for physics beyond the standard model. Some unifying theories predict that the fine-structure constant, $\alpha = e^2/\hbar c$, and the proton-electron mass-ratio, $\mu = m_p/m_e$, may be subject to temporal change [191]. Looking at the frequency ratio between several clock transitions over time, the differential sensitivity of the atomic levels to changes in α or μ , already places a constraint on the possible variation of the fine-structure constant and proton/electron mass-ratio [184, 183].

When comparing two optical atomic clocks in two distant locations connected through fibre links, general relativity predicts a frequency shift related to their relative heights in the geoid potential, allowing to probe the gravitational potential by means of optical clock comparisons (chronomatic relativistic geodesy) [192]. Classical (mechanical) and satellite-based geodetic height systems show discrepancies at the decimetre level [175]. In terms of the gravitational redshift of an optical transition 10 cm correspond to an accuracy level of 1×10^{-17}. Optical atomic clocks, when connected with high performance frequency dissemination [109, 111, 193], promise to surpass these values uniting high spectral resolution with a small error accumulation over large distances [110].

3.2 Relativistic Gravimetry Campaign at INRIM

The "Physikalisch-Technische Bundesanstalt" (PTB), the "National Physical Laboratory" (NPL) and the "Istituto Nazionale di Ricerca Metrologica" (INRIM) joined together for a proof-of-principle geodetic measurement utilising a transportable ^{87}Sr optical lattice clock from PTB [194] and the atomic clock ensemble at INRIM, comprised out of Italy's primary frequency standard, the cryogenic Cs-fountain ITCsF2 [178], and an ^{171}Yb optical lattice clock [38], which has already been discussed in chapter 2. Furthermore, a local optical frequency ratio measurement between the two optical lattice clocks provided an important check on the consistency of independently developed optical clocks. The gravitational redshift in equation 1.37 can be used to determine the gravitational potential difference experienced by the same atomic transition of frequency ν_0 in two locations:

$$\Delta\nu = \nu_0\left(1-\frac{gh_1}{c^2}\right) - \nu_0\left(1-\frac{gh_2}{c^2}\right) = \frac{\Delta U}{c^2}\nu_0 \tag{3.1}$$

, with $\Delta U = g(h_2 - h_1)$ the gravitational potential difference for locations close to the geoid surface.

It is important to note, that, in order to resolve the gravitational frequency shift, a side-by-side measurement of the frequency ratio needs to be conducted. Taking the published uncertainty budgets of optical atomic clocks for certain might result in fatal errors, since only few of them have been verified in optical-optical comparisons to the low 10^{-17} region or better [1, 186, 109, 195]. Using a transportable clock is therefore not only increasing the flexibility of the setup, but also reducing the risk of systematic errors to go undetected by enabling a local calibration with the INRIM clock ensemble.

The first chronometric levelling measurements were already taken decades ago. A proof-of-principle measurement conducted by the "Istituto Elettrotecnico Nazionale Galileo Ferraris" in 1977 used two microwave Cs beam clocks. They were synchronised in Turin and then one of them was transported to an elevated location (height 3.5 km above sea level) in the Alps. A radio link between the two clocks was established to measure the frequency difference between both clocks. The resulting accumulated time-delay between both locations over 66 days of actual measurement time agreed with the prediction to within the measurement uncertainty [196].

A few measurements resolving the gravitational potential difference between the locations of a pair of optical atomic clocks have been conducted prior to the measurement campaign demonstrated here within the recent years. A local measurement [114] used two Al^+ ion clocks in the same building, connected by a short fibre link. One of the two clocks was mounted on an elevation platform. An optical frequency ratio measurement between the two clocks was conducted. The clock situated on the elevation platform was then lifted by 30 cm and the measurement repeated. The relativistic frequency shift was resolved at a low 10^{-17} level. More recently a chronometric geodesy measurement involving optical lattice clocks has been demonstrated. Some 15 m of height difference between the cryogenic ^{87}Sr lattice clocks at RIKEN and the University of Tokyo were resolved with an accuracy of 5 cm or, in terms of the relative frequency shift, several parts in 10^{-18} [110]. Another remote comparison between Sr optical lattice clocks located at PTB and

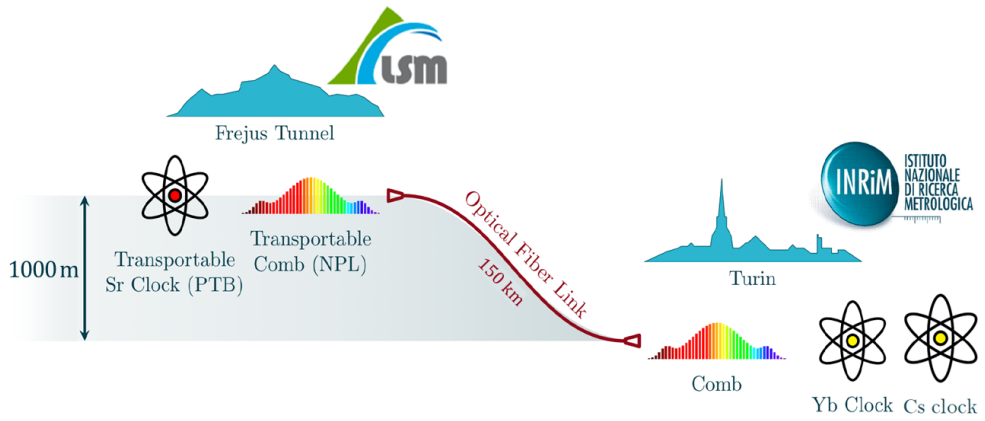

Fig. 3.1 Scheme of the geodetic measurement campaign. A transportable Sr lattice clock is operated inside the facilities of the LSM laboratories, deep inside the mountains. The Sr clock is connected to the INRIM atomic clock ensemble (one cryogenic Cs fountain and a Yb lattice clock) by a Doppler-noise cancelled fibre link operating in the infra-red region. Femtosecond frequency combs from NPL and INRIM employ the transfer oscillator technique [146] to bridge the frequency gaps between the atomic clock oscillators and the fibre link laser, facilitating a virtual beat between the atomic clocks. The Sr clock is then transported to INRIM and the measurements repeated, revealing the gravitational redshift by the difference between those two measurements and furthermore expanding the database on the Yb/Sr frequency ratio and Sr absolute frequency.

Syrte laboratories in Paris and Braunschweig connected via a 1415 km fibre link resolved the gravitational redshift with a precision of 3 parts in 10^{-17} [109].

While these experiments demonstrated the potential of optical (lattice) clocks for geodetic measurements, they were not yet resembling the conditions geodetic measurements face when operated outside of designated laboratories, as is the common modus operandi in geodesy. The novelty in the experiment presented here with respect to the previous ones is that for the first time chronomatic relativistic geodesy has been conducted under realistic experimental conditions.

The location to demonstrate chronometric levelling with the transportable lattice clock was chosen to be the facilities of the “Laboratoire Souterrain de Modane” (LSM) in France, with INRIM in Italy serving as the reference site. The LSM was selected due to its particular position: The site is located in the middle of the 13 km long Fréjus tunnel, deep inside a mountain (rock coverage 1700 m) in an area exhibiting long-term land uplift (Alpine orogeny) together with a secular gravitational potential variation of high potential geodetic interest. The transportable clock was operated in a storage area without air-conditioning (except for the one

provided by the transportable setup itself) that offered none of the amenities (stable temperature, low seismic noise, full equipment) of a typical atomic clock laboratory. Daily traffic and mining works in the vicinity meant an unprecedented stress test for the reliability of the transportable optical lattice clock.

The clock ensemble at INRIM is connected to LSM by a 150 km noise-compensated optical fibre link. On both ends the oscillators driving the clock transitions (lasers at 698 nm and 578 nm for Sr and Yb lattice clocks, respectively, and a 9.2 GHz microwave oscillator for the Cs fountain) were connected to a femtosecond fibre comb measuring the frequency ratio with regard to the 1.5 µm ultra-stable link laser transmitted from INRIM. At LSM a transportable frequency comb provided by the "National Physical Laboratory" enabled the transfer between the atomic clocks and the link laser and at INRIM a similar commercial system was used. In this way the atomic clocks were first related to the link laser individually and the frequency-ratios calculated a posteriori, eliminating the link as common-mode. The technique applied is called the "transfer oscillator", introduced first in [146] and described in detail for the transportable frequency comb from NPL in chapter 5 of this work. The reference comb NPL-FC3 (section 5.2.8) there is the transportable comb used during the geodesy campaign described here. The fibre link was also used to disseminate a 100 MHz reference frequency from INRIM to synchronise the frequency combs, frequency counters and AOMs used at LSM and INRIM.

In case of the transportable Sr clock all laser systems involved in the cooling, trapping and state preparation of the atoms were operated in a dedicated air-conditioned car trailer from PTB, which also housed the vacuum system and control electronics. The NPL frequency comb was operated next to the trailer at LSM. The ultrastable clock laser interrogating the narrow $^1S_0 \rightarrow {}^3P_0$ transition in ^{87}Sr was placed outside the trailer in the underground laboratory, since the vibrations induced by the trailer's air-conditioning might otherwise compromise its performance.

For the subsequent local comparison of the clock conducted in Turin, the Sr clock was compared to INRIM's clock ensemble by ratio measurements mitigated by an INRIM frequency comb without the need for a dedicated link laser. The PTB trailer was placed in a parking spot close to the atomic clock laboratories and the ultra-stable laser placed inside the ITCsF2 laboratory, connected to the Sr vacuum system and the frequency comb by Doppler-cancelled fibre links.

The height difference of approximately 1000 m between LSM and INRIM corresponds to a fractional relativistic redshift of 1×10^{-13}. The transportable clock was operated in both locations, LSM and INRIM, and each time an absolute frequency measurement with the cryogenic Cs fountain ITCsF2 conducted. The frequency difference between those two measurements yielded the gravitational redshift.

3.2.1 Sr lattice clock

The transportable ^{87}Sr ($I = 9/2$) lattice clock represents in principal a very similar setup as the ^{171}Yb ($I = 1/2$) frequency standard and it is presented in detail in [194]. The electronic structure of Sr is very similar to Yb with 2 valence electrons in the outer shell. This means that the concepts used for cooling, trapping and interrogation of Yb atoms can be applied just the same in a Sr lattice clock. A beam of hot Sr atoms is generated in an evaporation oven (natural abundance of the fermionic ^{87}Sr is 7%) inside a vacuum chamber. During one clock cycle the atoms are cooled and captured in a MOT and then loaded into an optical lattice operated at the magic wavelength, where the clock transition is interrogated and subsequently the state occupation measured. A Zeeman slower supports the MOT in capturing atoms. The MOT is sub-divided into two stages with the first one acting on the strong $^1S_0 \rightarrow {}^1P_1$ transition at 461 nm (linewdith 32 MHz) and the second stage exploiting the much weaker $^1S_0 \rightarrow {}^3P_1$ transition at 689 nm (linewdith 7.5 kHz). The optical lattice, generated by a Ti:Sa laser and operated around the magic wavelength of 813 nm, is tilted with respect to the gravitational field by circa 50°. The typical lattice depth during this measurement campaign was 100 E_r and the atomic temperature reached about 3.5 µK, as it was measured by clock-transition sideband spectroscopy. The lattice and MOT lasers are frequency stabilised to dedicated Fabry-Perot cavities.

The atoms inside the lattice are spin-polarised in alternating cycles to either one of the two $|m_F| = 9/2$ states and the residual population of the Zeeman-split sublevels expelled form the lattice with a powerful 461 nm pulse. The actual $^1S_0 \rightarrow {}^3P_0$ clock transition at 698 nm (natural linewdith 1 mHz) is driven by a laser referenced to an ultra-stable vibration-insensitive cavity. The fraction of the atoms excited to the $^3P_0$ state after the application of a π-pulse is read out in the same way as in the case of the INRIM Yb lattice clock by destructive fluorescence spectroscopy on the $(5s^2)^1S_0 \rightarrow (5s5p)^1P_1$ transition. The only difference is that the repumping of the excited atoms to the $^3P_1$ state traverses the $(5s6s)^3S_1$ state and includes the loss

Table 3.1 Table of the individual uncertainty contributions to the absolute frequency measurement of the ^{87}Sr clock transition

	^{87}Sr at LSM		^{87}Sr at INRIM	
Systematic Effect	Correction / 10^{-17}	Rel. Unc. / 10^{-17}	Correction / 10^{-17}	Rel. Unc. / 10^{-17}]
AC Stark shift	0	24	0	17
Nonlinear lattice shifts	−1.0	0.7	−0.5	0.7
Density shift	−1.2	3.0	−2.2	5.3
2nd order Zeeman shift	34.2	0.5	11.7	0.2
BBR	500.3	3.4	515.3	1.8
Probe light shift	0.2	0.2	0.3	0.3
DC Stark shift	0	0.1	0	0.1
Servo error	0	9.4	0	3.7
Line pulling	0	4.1	0	1.1
Optical path length	0	0.8	0	1.3
Total	**532**	**27**	**524**	**18**

channel to the $^3P_2$ state by using two repumper lasers, one acting on the $^3P_0 \rightarrow {}^3S_1$ transition at 679 nm and the other one on the $^3P_2 \rightarrow {}^3S_1$ line at 707 nm.

Evaluation of the uncertainty budget for this clock was performed, just as in the case of the INRIM Yb lattice clock, with a mixture of self-referenced measurements (e.g. lattice AC Stark shift, density shift), theoretical calculations (e.g. higher order lattice shifts) and combinations of theoretical modelling and measurements (e.g. black-body radiation).

The uncertainty budget of the transportable ^{87}Sr clock from PTB is given in table 3.1. After the clock was moved from LSM to INRIM in April 2016, small changes to the cooling lasers and the air conditioning of the car trailer were adapted,

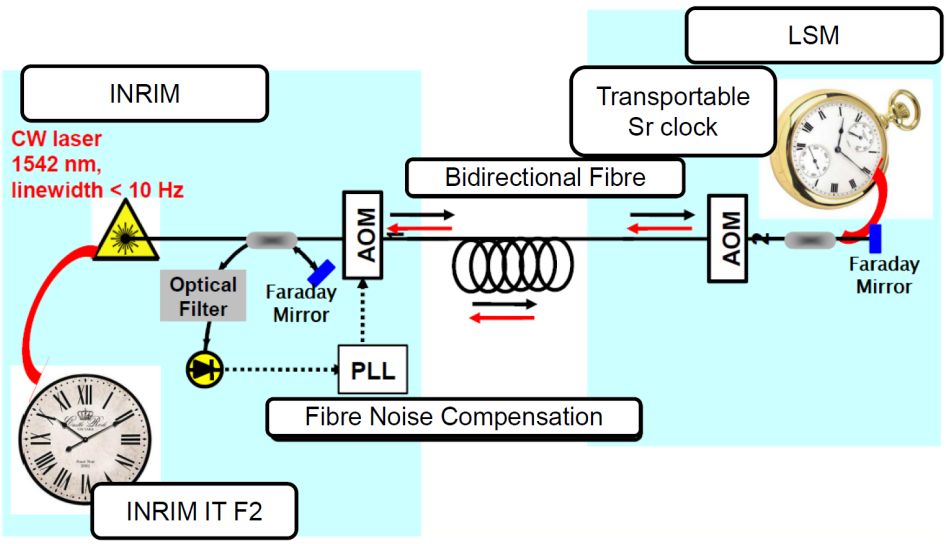

Fig. 3.2 Scheme of the fibre link between LSM and INRIM. The Yb lattice clock is not depicted, but is implemented analogue to the Cs-fountain. The 1.5 µm fibre laser is connected to both clocks simultaneously through a virtual beat with a femtosecond laser. A part of the laser light originating at INRIM is extracted before entering the link fibre to form a phase reference. The light entering the fibre is then offset by an AOM and partially reflected at the other end of the fibre at LSM. This reflected light is then overlapped with the reference radiation on a photodiode (PD). The PD signal is used to perform a phase-lock of the reflected light on the reference radiation by fine-adjusting the AOM frequency.

improving the reliability of the clock. With these changes a renewed evaluation of some systematic effects was conducted and served resulting in a reduction of the uncertainty on some systematic effects.

3.2.2 Fibre link

The remote clock comparison between the INRIM atomic clock ensemble to the transportable ^{87}Sr lattice clock at LSM was conducted utilising a 150 km Doppler-cancelled fibre link set up by INRIM between the two locations [197]. The link itself features a 1542.14 nm ultra-stable laser with frequency combs on both ends relating the link laser to the probe lasers of the optical atomic clocks at 578 nm and 698 nm and the Cs microwave oscillator at 9.2 GHz. The loss along one round-trip is 120 dB and is compensated, although not fully, by 5 bi-directional erbium-doped fibre amplifiers. Both combs emit primarily in the infrared region (Er-fibre combs) and bridge the spectral gap between the link and the optical clock lasers in a multi-

branch configuration (see also chapter 5). The femtosecond comb laser noise was inherently extracted from the comparison by implementation of the transfer oscillator technique [146], described in more detail in chapter 5.

The link laser is stabilised to an ultra-stable cavity resulting in a short-term stability of 2×10^{-14} at 10 s (Allan deviation). The long-term drift is removed by a low-bandwidth phase-lock to a H-maser with a frequency comb, reducing the drift of the beatnotes with the clock lasers and augmenting reliability of the frequency counters during measurements.

The setup of the fibre link is depicted in figure 3.2. After passing through the bidirectional fibre, a part of the light is reflected back and compared to the radiation in front of the fibre. An AOM is steered by a phase-locked loop to counteract the noise imprinted on the laser in the fibre. A second identical fibre running parallel to the link one has been used to characterise the performance of the Doppler noise cancellation and the results are shown in figure 3.3. The stability of the link was found to be below the expected stability of the optical lattice clocks for all timescales. The total contribution of the fibre link to the fractional uncertainty of any frequency measurement was identified to be 3×10^{-19}. At LSM a laser phase-locked to the link was used to ensure a high sinal-to-noise ratio (> 30 dB with 100 kHz bandwidth) avoiding cycle-slips.

The location at LSM did not feature a common stable reference for electronics and the frequency comb. Since GNSS-disseminated signals were also no option due to the fact that there would be no way of receiving them in an underground laboratory, a 100 MHz signal referenced to a H-maser was delivered by amplitude modulation of a second infrared laser running through a parallel optical fibre. The phase noise introduced by this unstabilised fibre was low enough to deliver the RF signal with an uncertainty and instability below the 10^{-13} level, even for long timescales. The resulting uncertainty imprinted on the link laser to Sr clock laser frequency ratio was below 1×10^{-19}.

3.2.3 H-maser as flywheel oscillator

A H-maser represents a very reliable and stable oscillator and thus can be used to bridge down-times in the comparison between a less reliable, but very stable system, such as the transportable PTB Sr clock at LSM, and a Cs primary frequency

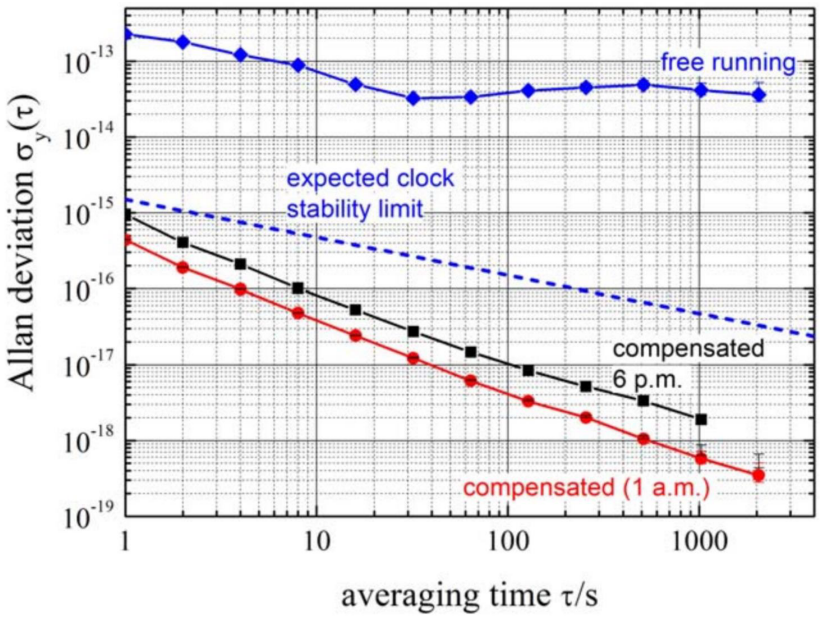

Fig. 3.3 Performance of the 150km fibre link between INRIM and LSM. The Doppler-compensated fibre link superseded the requirements set by the estimated thermal noise floor of the optical lattice clock laser cavities for all timescales, whether at night (red) or during the evening rush hour (black) when the nearby highway was most active.

standard with lower stability [198]. The Sr clock acted as a frequency reference to the free-running H-maser, enabling us to calculate the frequency ratio ν_{Sr}/ν_{Cs} from the ν_{Sr}/ν_H and ν_H/ν_{Cs} using datasets of quite different lengths. The H-maser does exhibit its own noise and a slow drift. Therefore the datasets between the Cs fountain and the H-maser had different average frequencies than the shorter H-Sr ones. Luckily, this additional uncertainty can be calculated [198] for well characterised oscillators, such as H-masers. The H-maser noise was modelled by a superposition of flicker phase noise $6\times10^{-14}\tau^{-1}$ ($1\times10^{-13}\tau^{-1}$), white frequency noise $5\times10^{-14}\tau^{-1/2}$ ($4.5\times10^{-14}\tau^{-1/2}$) and flicker noise at 1.7×10^{-15} (1×10^{-15}) in during our measurement campaigns with the transportable Sr clock at LSM (INRIM), respectively.

3.2.4 Gravitational potential detection

Prior to this experiment a geodetic campaign determining the gravitational potential at INRIM and LSM was conducted by the university of Hannover. This campaign aimed at a refinement of the model of the gravitational potential around the clock

sites, improving the reliability of the derived geoid model [175]. Two absolute (one at LSM and one at INRIM) and a host of relative gravity measurements were conducted, leading to a total of 36 new gravity reference points established at INRIM and 123 at LSM. The methods used included state-of-the-art gravimeters determining the gravitational acceleration g in free-fall Michelson-Moorely interferometers, spirit levelling and ellipsoidal height determinations with global navigation satellite systems (GNSS).

As a result the gravitational potential difference between the positions of the Sr clock at LSM and at INRIM was assessed as $\Delta U = 10\,032.1(16)\ \mathrm{m}^2/\mathrm{s}^2$. The value for the nearby markers from the geodetic campaign at both locations is $\Delta U = 10\,029.7(6)\ \mathrm{m}^2/\mathrm{s}^2$. These uncertainties are given by the geoid model in the Alpine region, the GNSS system results and the levelling measurements. The increase of uncertainty for the clock positions with regard to the markers is due to the method used to determine the local height of the clock position with regard to the markers.

3.2.5 Measurement Results

Due to the harsh environmental conditions inside the Frejus tunnel (temperature fluctuations and mining works in the vicinity), the laser system providing the 461 nm radiation worked less reliable than previously encountered. Therefore the uncertainty evaluation of the clock consumed more time than planned and with the transportable clock operating only for a total of 2.8 h over two days at the end of the LSM campaign in March 2016, simultaneous operation was only achieved with the ITCsF2 fountain clock, but not the Yb lattice clock.

The uncertainty budget of the INRIM clock ensemble has already been given in table 2.1 and 2.2. During the measurement campaign presented here the cryogenic Cs-fountain was running in a low density regime (reduced density-shift) with an associated uncertainty budget of 3×10^{-16}. The Yb clock total uncertainty remained at 1.6×10^{-16}. The uncertainty contribution stemming from the fibre link and the NPL femtosecond frequency comb [148] were both below 1 part in 10^{-19}. The INRIM frequency comb accuracy was characterised by measuring the same frequency ratio with a second comb and looking for discrepancies. Due to a short measurement time the associated uncertainty was limited by statistics to 2 parts in 10^{-17} for this measurement campaign.

The low stability of the Cs-fountain ($3 \times 10^{-13}\tau^{-1/2}$) in regard to both, the Sr and the Yb optical lattice clocks meant that the gravitational redshift uncertainty was dominated by statistics. Bridging down-times with a H-maser as flywheel oscillator, as decribed in paragraph 3.2.3, allowed to extend the measurement time to 48 h, leading to a statistical uncertainty of the ^{87}Sr frequency measurement of 17×10^{-16} and an estimated uncertainty of the absolute frequency evaluated by the Cs-fountain of 18×10^{-16}.

After the end of the LSM campaign the Sr clock was transported to INRIM and the trailer set up outside the same building that the INRIM clock ensemble and the frequency comb was situated. The Sr clock laser was placed inside the same laboratory as the Cs fountain. Small upgrades to the cooling laser distribution and the thermal management in the car trailer resulted in a significant improvement of the clock reliability.

In order to resolve the gravitational redshift the frequency measurement against the fountain clock was repeated. The systematic uncertainties of the Sr lattice clock (1.8×10^{-16}) were slightly improved in comparison to the LSM measurements. The absolute frequency measurement uncertainty improved by a factor of two to 9×10^{-16}. In consequence the relativistic redshift was resolved at a level of 19×10^{-16} or 47.92(83)Hz.

Taking equation 3.1, a potential difference of $10034(174)\mathrm{m}^2/\mathrm{s}^2$ was calculated, in excellent agreement with the value of $10032.1(16)\mathrm{m}^2/\mathrm{s}^2$ determined from the geodetic measurement campaign by the university of Hannover, described in paragraph 3.2.4.

The chronometric levelling at LSM and INRIM compared an ^{87}Sr lattice clock to a primary frequency standard, the ITCsF2 cryogenic Cs fountain. Therefore the results can also be used to increase the dataset on absolute frequency measurements of the ^{87}Sr $^1S_0 \rightarrow {}^3P_0$ clock transition. Taking the results of the conventional geodetic measurement campaign at LSM and INRIM, a correction to the Sr frequencies at both locations - recorded by the Cs fountain - is applied in order to account for the different gravitational redshifts. The average frequency of the Sr lattice clock results as 429 228 004 229 873.13(40) Hz. The obtained value at LSM and INRIM is shown in comparison to several recent measurements of the same clock transition in figure 3.4. The accuracy and mean value obtained during the PTB-NPL-INRIM campaign with a transportable clock are in agreement with other measurements.

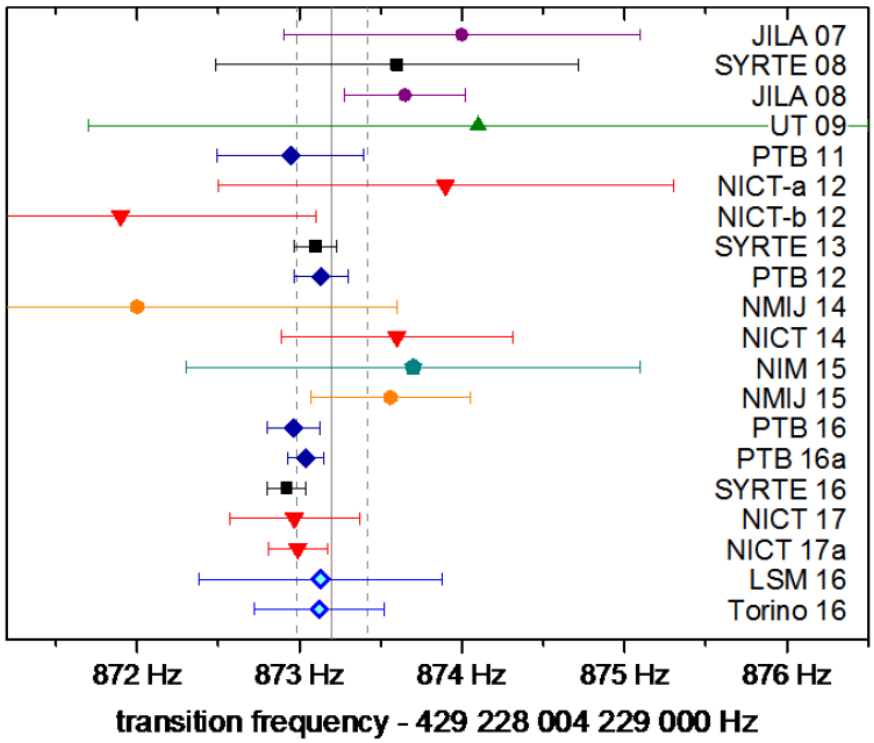

Fig. 3.4 Absolute frequency measurements of the ^{87}Sr clock transition. The data obtained during the chronometric geodesy campaign are corrected for the gravitational redshift derived from geodetic measurements. The vertical line indicates the recommended value of the CIPM and its uncertainty (dashed line) [47]. Other values are taken from [199–205, 82, 206–210, 198, 211–213].

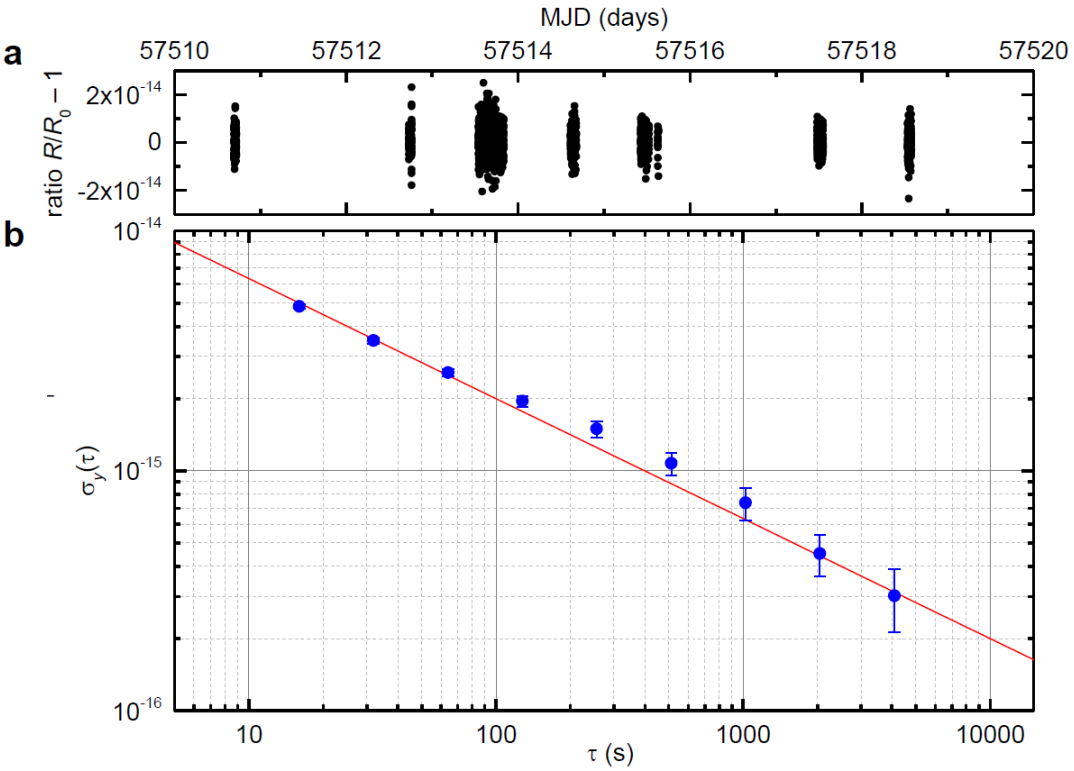

Fig. 3.5 (a) Data of the fractional optical frequency ratio R/R$_0$ as a function of the modified Julian date (MJD) with R$_0$ chosen as $R_0 = 1.207507039343338122$ (b) Fractional Allan deviation of R/R$_0$ from the combined datasets in (a). The red line is a fit of a $2 \cdot 10^{-14}\tau^{-1/2}$ stability.

3.3 ^{171}Yb / ^{87}Sr Frequency Ratio Measurement

With the transportable Sr lattice clock working reliably at INRIM, a total of 31 000 s of common operation with the stationary Yb lattice clock were reached over a period of 7 days. With both atomic clocks linked together by a frequency comb, an optical frequency ratio measurement was conducted between the $^1S_0 \rightarrow {}^3P_0$ transitions in ^{171}Yb and ^{87}Sr, which are found at 578 nm and 698 nm, respectively. Due to the higher stabilities of these optical clocks with respect to the microwave Cs fountain, the result was limited by the systematic uncertainties of the clocks and not statistics. The fractional optical frequency ratio recorded over these 7 days is shown in figure 3.5. The stability of the ratio measurement shown there agrees with the individual stabilities of the two clocks when running interleaved measurements to determine the uncertainty contribution of some of the systematic effects.

A total of eight different frequency ratio measurements were conducted. The data recorded on different days had varying statistical and systematic uncertainties due to the length and experimental conditions of each measurement. A statistical analysis was used to merge these datasets together, considering the correlations stemming from the individual measurements with different systematic shifts and uncertainties. Calculating the covariance matrix of all 8 datasets, a generalised least square fit was used to determine the average [180, 181]. The systematic uncertainties of the clocks were regarded as fully correlated and the statistics (depending mainly upon the measurement time) as uncorrelated.

The ^{171}Yb / ^{87}Sr frequency ratios measured on the individual days of the PTB-NPL-INRIM campaign as well as a comparison to previous results are depicted in figure 3.6. The averaged frequency ratio from our campaign was assessed as $R = \nu_{Yb}/\nu_{Sr} = 1.207\,507\,039\,343\,338\,41(34)$. This value is within two standard deviations of the most accurate previous measurement (RIKEN 2016, figure 3.6) [28]. The "Yb & Sr abs. Freq." value was calculated from the average of the ^{87}Sr frequencies in figure 3.4 (429 228 004 229 873.05(05) Hz) and the ^{171}Yb clock transition frequency taken from [4, 182, 38, 162, 163, 166] as 518 295 836 590 863.75(25) Hz.

3.4 Discussion

This measurement campaign was an important proof-of-principle of geodesy and metrology with transportable optical lattice clocks. For the first time has an optical lattice clock been used outside of a laboratory environment and obtained results for the gravitational redshift as well as a local frequency ratio with another lattice clock in agreement with the recommended values for secondary frequency standards by the "Committee of weights and measures" (CIPM) [47]. Thus mapping of the gravitational potential by means of transportable optical lattice clocks has proven applicable. The use of a transportable lattice clock for high-precision metrology was likewise demonstrated for the first time. The results of the chronometric levelling did not yet compete with the conventional approach regarding uncertainty, but prove the excellent agreement obtainable with these two approaches, raising confidence in the usefulness of this method. With the reliability of the Sr lattice clock improved during the local comparison at INRIM, chronometric levelling using the optical frequency ratio ν_{Yb}/ν_{Sr} would have the potential for a much improved stability, leading to a

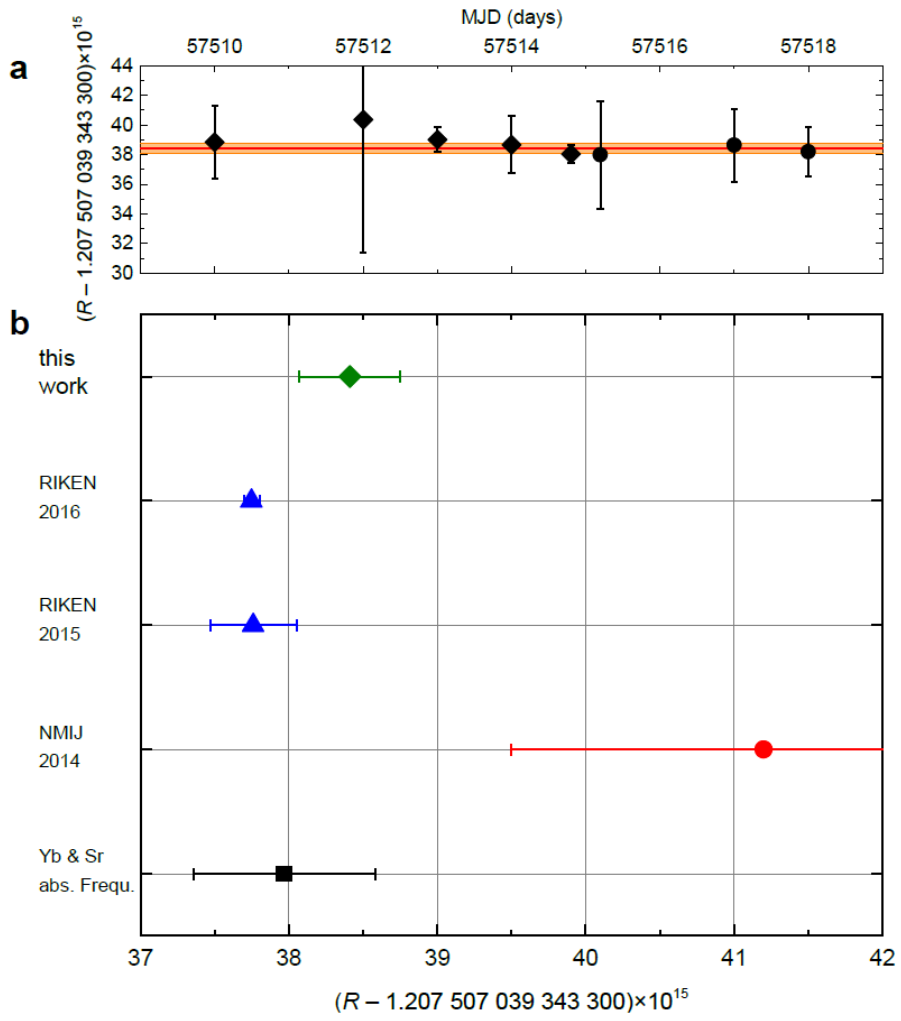

Fig. 3.6 (a) The Frequency ratio ^{171}Yb/^{87}Sr as measured on different days and their average (line) with its uncertainty (coloured bar). Diamonds (circles) signify operation of the Sr lattice clock with a shallow (deep) lattice. (b) Optical frequency ratio ^{171}Yb/^{87}Sr as measured by this work and [28, 5, 164]. The lowest point was calculated from published absolute frequency values for ^{171}Yb and ^{87}Sr.

better resolution in just few hours. The current limitations of the clock uncertainty budgets have been identified and careful improvements to the experimental setups are being undertaken. Both optical clocks are expected to ultimately reach an uncertainty in the low 10^{-17} region with the implementation of some known setup improvements. This would allow to resolve altitudes with 10 cm uncertainty, a region hard to reach with conventional gravimeters. The absolute frequency of the ^{87}Sr clock transition assessed here agreed with previous results. Including this campaign, the Yb-Sr frequency ratio has been measured by three independent groups worldwide. Establishing a larger database, such measurements raise confidence in the consistency of optical clocks and open the way for a redefinition of the SI-unit the second.

Chapter 4

Improvements of the INRIM Yb lattice clock

4.1 Multi-wavelengths Cavity

4.1.1 Introduction

The Yb clock at INRIM uses a wide range of wavelengths across the whole visible spectrum for laser cooling and trapping of the atoms. These lasers demand a stabilisation in the kHz to MHz range. Precisely a laser linewidth of less than 100 kHz (1 MHz) at 556 nm (399 nm) has been found to be optimal for an efficient excitation of the respective $^1S_0 \rightarrow {}^3P_1$ and $^1S_0 \rightarrow {}^1P_1$ MOT transitions. The maximum allowed drift for the MOT lasers follows at about the width of the 556 nm transition as 180 kHz during a typical day-long measurement ($\approx$ 10 h). The stabilisation of the 759 nm lattice laser on the other hand is challenged by the requirement that the AC Stark shift must add less than 1×10^{-18} in relative uncertainty due to laser frequency drift within the same measurement time. Applying the previously measured first-order clock transition sensitivity of 21.6 mHz/(GHz E_r) [38] an upper limit of 12 kHz/h for the drift of the reference emerges. Combining these demands, the requirements for the linewidth and drift of the laser and thereby also for the short-term stability and drift of the laser's reference result as 100 kHz at 556 nm (1.9×10^{-10}) and 3.3 Hz/s at 759 nm (8.4×10^{-15} s^{-1}), respectively.

During the absolute frequency measurement campaign (chapter 2) and the Yb/Sr frequency ratio measurement (chapter 3) these laser-stabilisations used various techniques, as shown in figure 2.2. They included stabilisation to an ultra-stable cavity in case of the 556 nm radiation and side-of-fringe locking to a transversal hot Yb beam for 399 nm light, as well as a stabilisation to a maser referenced frequency comb of the 759 nm lattice laser.

In order to simplify the setup and increase robustness, a common reference for all three radiations was introduced. The short-term stability of the three lasers used is already sufficient for their task. Therefore this new reference has the primary requirement to exert a low and constant drift. The choice fell on a stable ULE glass cavity, operated at the temperature of zero CTE. The work presented here was published in [214].

The mismatch between the cavity modes and the frequency actually needed for the experiment is often compensated by one or more AOMs or EOMs. In the latter case frequency modulation (FM) [215] or serrodyne phase manipulation [216] bridges the frequency gap. For the simultaneous locking of three wavelengths to the same cavity we implemented the offset sideband locking technique [217]. This technique involves the use of only one (broadband) EOM driven by an RF frequency (Ω_{gap}) to bridge the frequency gap. The RF signal is phase-modulated (PM) by a (typically smaller) modulation frequency (Ω_{PDH}), leading to the rise of first order sidebands at Ω_{gap} with additional phase-modulated sidebands around them spaced by Ω_{PDH}. This signal (carrier angular frequency ω_c and modulation depths $\beta_{1,2}$) has the following form:

$$E = E_0 exp(i\omega_c t) \cdot exp[i\beta_1 sin(\Omega_{\text{gap}} t + \beta_2 sin\Omega_{\text{PDH}} t)] \tag{4.1}$$

Such a modulation allows the generation of an error signal for the Pound-Drever-Hall (PDH) [218] locking method in the usual manner with the exception that not the carrier, but one sideband is stabilised to the cavity. The PDH error signal is generated using a demodulation frequency at Ω_{PDH}, resulting in a dispersive signal at the position of the Ω_{gap} sidebands. This also clarifies the principal advantage the offset sideband locking technique has over single- or double-sideband locking approaches: It is the lack of a spurious error signal (and affiliated PM sidebands) generated at the

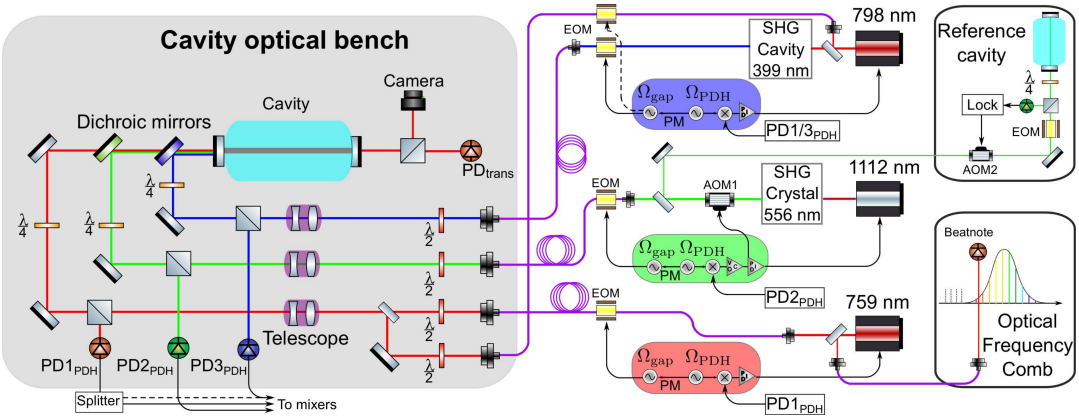

Fig. 4.1 Sketch of the multi-wavelengths cavity: black lines are electrical signals , dashed lines the electrical signal path for the 798 nm laser stabilisation and coloured paths mark free-space laser light. Purple connections are polarisation maintaining fibres. The reference cavity and the frequency comb (right) are used to characterise the setup.

carrier frequency. The use of the PDH method makes the stabilisation less sensitive to power fluctuations, increasing further the robustness of the system.

The sideband locking technology allows greater flexibility in a smaller package in comparison to combined AOM and EOM setups which lock the carrier to a cavity mode, since the FM modulation of EOMs is often adjustable over a large range without any influence on the optical path. The light power inside the cavity is not altered in a sideband locking approach as compared to conventional ones as long as $\Omega_{\text{gap}} \gg \delta\nu$ holds true. Here $\delta\nu$ is the FWHM of one cavity mode. No deterioration in performance of such single EOM sideband-locking setups in comparison to combined EOM/AOM setups was observed, as a similar previous approach reported [219], where different lasers were stabilised to three optical cavities in a single ULE block using the sideband locking technique.

4.1.2 Setup

A sketch of the overall system is given in figure 4.1 and a picture of the physical system in figure 4.2. The whole setup is located on a single Aluminium breadboard (60 cm × 90 cm × 10 cm) to ensure transportability, including the cavity, the EOMs and fibre output couplers, as well as the optical mode-matching and coupling components and three PDH photodiodes. No custom manufactured elements were used. The multi-wavelength cavity is a commercial 10 cm (FSR = 1.5 GHz) hemispherical

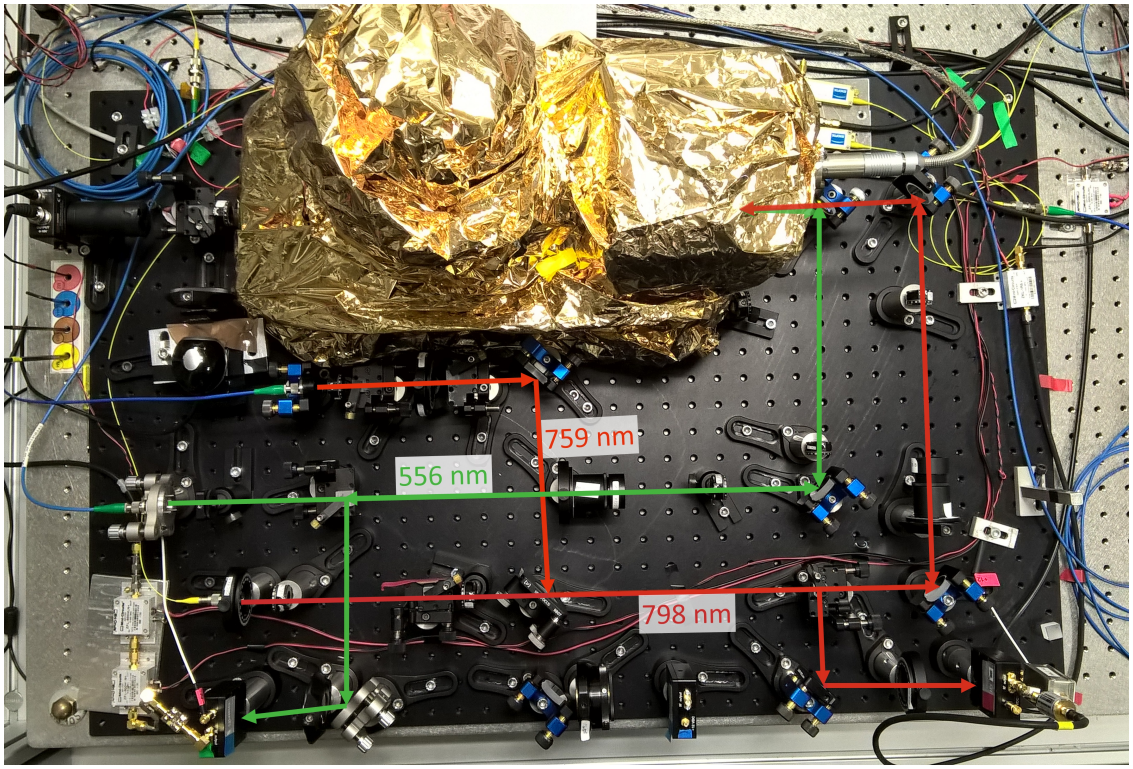

Fig. 4.2 The multi-wavelengths stabilisation breadboard with the cavity on top covered by Mylar foil and all optics below. On this picture the system is used to stabilise the 798 nm, the 759 nm and the 556 nm light simultaneously. Beam paths are indicated.

optical resonator by Advanced Thin Films with a cylindrical ULE spacer and silica mirrors with ULE compensation rings. The cavity is suspended horizontally inside a vacuum housing temperature stabilised at the point of vanishing thermal expansion coefficient (zero CTE).

The entry mirror is flat and the opposing one has a radius of curvature of -0.5 m. Both of them feature triple-v coating designed for 399 nm, 556 nm and 759 nm. The manufacturer declared a Finesse of more than 15000 at 556 nm and between 1000 and 3000 at 399 nm and 759 nm evaluated on coating design.

The cavity is suspended on four points in a vibration insensitive configuration inside the stainless steel vacuum chamber. The chamber is sustained at an ultra high vacuum by one ion pump. An outside thermistor reads out the temperature, which is actively stabilised using the "Active Disturbance Rejection Control" (ADRC) method [158] by acting on a heater placed on its outside bottom.

The vacuum chamber is thermally isolated by a thick layer of insulating foam and Mylar foil. Inside the chamber ten layers of crumpled Mylar foils support the thermalisation of the cavity.

The 556 nm radiation is produced by single pass SHG in a non linear crystal of an amplified 1112 nm fibre laser. The 759 nm lattice light on the other hand is directly provided by a commercial Ti:Sa laser. SHG is again used to provide radiation at 399 nm from a tapered amplified diode laser at 798 nm [154]. Initially the 399 nm radiation was stabilised to the cavity, but later an additional path stabilising the direct output of the laser at 798 nm to the cavity was added, allowing to stabilise the laser either way.

All wavelengths reach the breadboard of the cavity through polarisation maintaining fibres of a few metres length. At 556 nm, 759 nm and 798 nm, fibre based broadband EOMs (bandwidth ≈ 1 GHz) are used, driven by commercial synthesizers allowing phase modulations with an RF power of up to 50 mW. The 399 nm channel features a free-space QBIG EOM with two resonance frequencies tunable in the range of $0.6 - 1$ GHz and $1 - 1.6$ GHz (11 MHz PM bandwidth). This modulator is driven by a synthesizer from QUBIG GmbH delivering up to 4 W of RF power. Three optical paths for the 759 nm, 556 nm and 399 nm radiations are laid out across the breadboard, featuring individual mode-matching telescopes, polarisation control and photodiodes. The 798 nm radiation is overlapped with the 759 nm one on a 50/50 beamsplitter.

Table 4.1 Initial parameters used in laser stabilisation. The bridge frequency for the 759 nm laser is adjusted according to experimental needs around the magic wavelength.

λ/nm	P_{in} /μW	Ω_{gap}/MHz	Ω_{PDH}/MHz
399	60.5	850.4	8.1
556	6.3	327.0	10.7
759	13.0	/	11.5
798	6.5	174.1	5.9

All beams are overlapped on two dichroic mirrors before entering the cavity through the flat mirror side. A camera and photodiode observe the transmission through the cavity. All beams are coupled into the cavity with high efficiency and the light power at each wavelength impinging on the cavity is reported in table 4.1. Three PDH photodiodes (PD_{PDH}) detect the light reflected by the cavity. The phase modulation frequencies needed to generate the PDH error signal are set far away from each other for the individual wavelengths and the electrical signals of the photodiodes filtered with narrow bandwidths to avoid crosstalk between wavelengths. The 759 nm and 798 nm beams impinge on the same PDH photodiode ($PD1_{PDH}$). Therefore the electrical signal output is subsequently splitted and separately filtered. All photodiode outputs are amplified and down converted, generating independent error signals. The 399 nm, 798 nm and 556 nm FM frequencies (Ω_{gap}) are set using the MOT signal as reference. The initial parameters used in the stabilisation of each wavelengths are given in table 4.1.

The 556 nm radiation is stabilised to the cavity by a fast lock (bandwidth 90 kHz) acting on an AOM and a slow lock steering the fibre laser's (sub-harmonic 1112 nm) piezo (bandwidth (3 kHz) using a PID combined with a voltage controlled oscillator (VCO) driving the AOM. All the other wavelengths use low-bandwidth (3 kHz) PIDs acting on the respective laser's piezo. The lasers are locked on a first order FM sideband generated by the EOM. Figure 4.4 shows exemplary the signals of $PD1_{PDH}$ and PD_{trans} using the 798 nm laser, where the carrier is depleted in favour of the sidebands. The RF power sent to the EOM (table 4.1) is adjusted maximising the error signal.

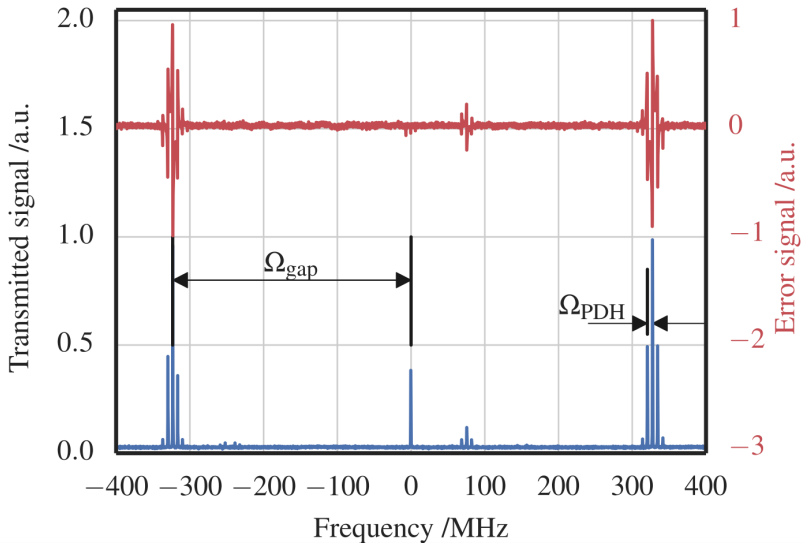

Fig. 4.3 PDH error signal (red) and transmission spectrum (blue) at 556 nm. The depleted carrier is separated from the first order sidebands by Ω_{gap} and the second order PM sidebands are spaced by Ω_{PDH}. The carrier is not PM modulated. Smaller peaks arise from high order cavity modes.

4.1.3 Measurements

We measured the cavity's finesse with the cavity ring-down method described in chapter 1. The ring-down was initiated by shutting the EOM power while the laser was locked on a cavity resonance. The high bandwidth PD_{trans} recorded the the extinction of the transmitted light through the cavity. The shut-down time of the EOM RF power supplies and rise time of the photodiode were taken into account to obtain a conservative estimate of the photon lifetime and thereby the Finesse, using equation 1.43.

The results obtained for all four wavelengths used are shown in table 4.2, together with the ratio of the output to the input light power at each wavelength. We always coupled solely into the TEM_{00} mode for all measurements at all wavelengths. The Finesse at 798 nm resulted as 1200 ± 150 with a measured throughput of 69%. The cavity was not requested to be coated at this wavelength. Therefore these results are quite satisfactory. At 759 nm the Finesse is 1670 ± 150 and thereby inside the range declared by the manufacturer, while the throughput is 65%. The measured Finesse of 13900 ± 600 at 556 nm is slightly below the specifications (15k) and the throughput was assessed as 20%. At 399 nm the Finesse measurement was performed comparing

Table 4.2 Table of the Finesse and throughput (relation of outgoing to incoming optical power) measured for the TEM00 modes of the respective wavelengths. Note that the mirror coatings were designed only for 399 nm, 556 nm and 759 nm.

λ / nm	Finesse declared	Finesse measured	Throughput / %
399	$1000-3000$	550 ± 60	3
556	15000	13900 ± 600	20
759	$1000-3000$	1660 ± 150	65
798	/	1200 ± 150	69

the linewidth of a TEM_{00} cavity resonance to the FSR due to the low ring-down time of the cavity. We assessed a Finesse of only 550 ± 60 and a throughput of 3%, indicating an unexpected high optical absorption at this wavelength.

The 399 nm laser radiation is usually available for continuous periods of six hours, limited by the doubling cavity lock. Therefore also the stabilisation at this wavelength is limited to this timescale. The 556 nm, 759 nm and 798 nm radiation on the other hand can be stabilised to the multi colours cavity for days without unlocks. This lock also remains stable when the carrier frequency is changed. We altered the sideband gap frequencies as fast as $1\,\mathrm{MHz/s}$ for a total span of 500 MHz without the lasers unlocking.

The temperature where the ULE cavity's thermal expansion coefficient vanishes (zero CTE) was assessed using an ultra-stable cavity, characterised in [156], as reference. An independent PDH (bandwidth 100 kHz) stabilisation of the 556 nm laser to the reference cavity was set up, acting upon a separate AOM (see figure 4.1) in a dedicated branch of the 556 nm radiation previously already stabilised to the multi colours cavity. The frequency difference between the reference and the multi colours cavity can therefore be assumed as being equal to the frequency correction sent to AOM2. The signal sent to AOM2 was therefore taken as a virtual beatnote between two lasers stabilised to the two cavities. The zero CTE measurement data is shown in figure 4.4. Over the course of one week the temperature of the multi colours cavity was changed in steps and the virtual beatnote with the reference cavity recorded. The drift of the reference cavity during this time was a negligible

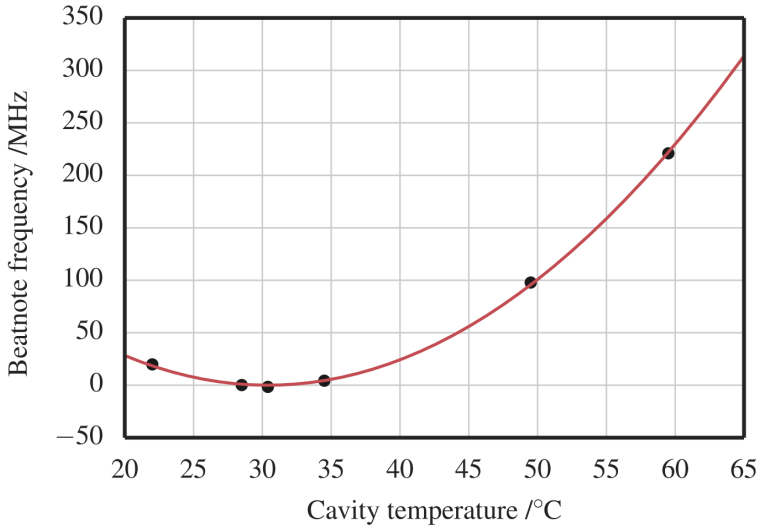

Fig. 4.4 Frequency difference between the two cavities (black dots) and quadratic fit to determine the zero CTE point.

contribution to the measurement uncertainty. The temperature of vanishing CTE was taken as the minimum of the parabolic fit to the beatnote versus temperature plot and the result is 30.4 ± 0.3 °C.

The virtual beatnote between the two cavities was monitored by a spectrum analyser and a phasemeter, demonstrating a linewidth of less than 300 Hz (sweep time 80 ms and 100 Hz resolution), as seen in figure 4.5. The noise of this beatnote (and therefore also the linewidth) was attributed solely to the multi wavelengths cavity, since the reference cavity had been characterised at a much superior level.

The phasemeter recorded the power spectral density (PSD) of the same signal (figure 4.6), revealing a white noise floor of $25\text{Hz}^2/\text{Hz}$ and a flicker noise of $225\text{Hz}^2/\text{f}$, with f being the frequency. Noise peaks between 10 Hz and 130 Hz are accounted to acoustic perturbations. The fractional frequency stability at 1 s was evaluated as 3×10^{-14} (normal Allan deviation).

In order to measure the drift of the multi colours cavity, an optical fibre link was set up from the 759 nm laser to a hydrogen maser referenced frequency comb in our laboratories. In this link the laser light resonant with the cavity is sent to the comb and the beatnote with one comb tooth recorded by a fast photodiode. The signal is then filtered, amplified and counted with an electronic frequency counter (K+K). We measured the drift of the 759 nm radiation, sequentially stabilising the other two

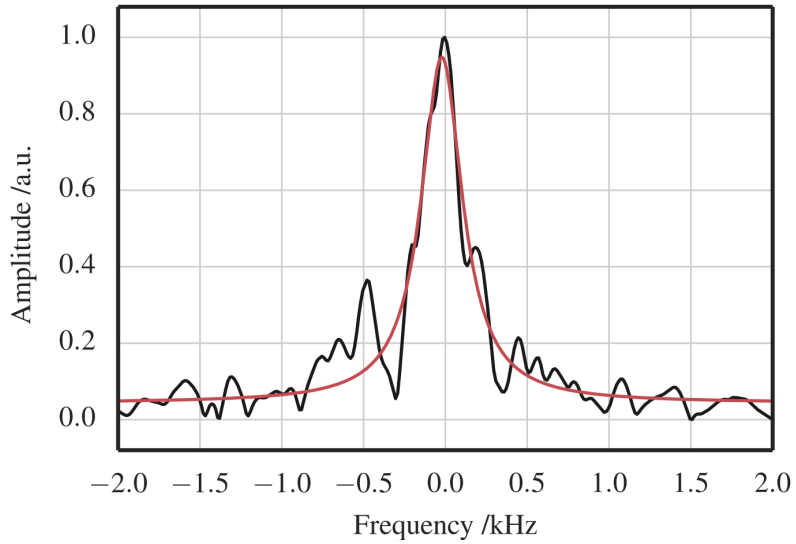

Fig. 4.5 Beatnote at 556 nm between the two cavities taken at 80 ms sweeping time and 100 Hz resolution (black) with 300 Hz FWHM Lorentzian fit (red).

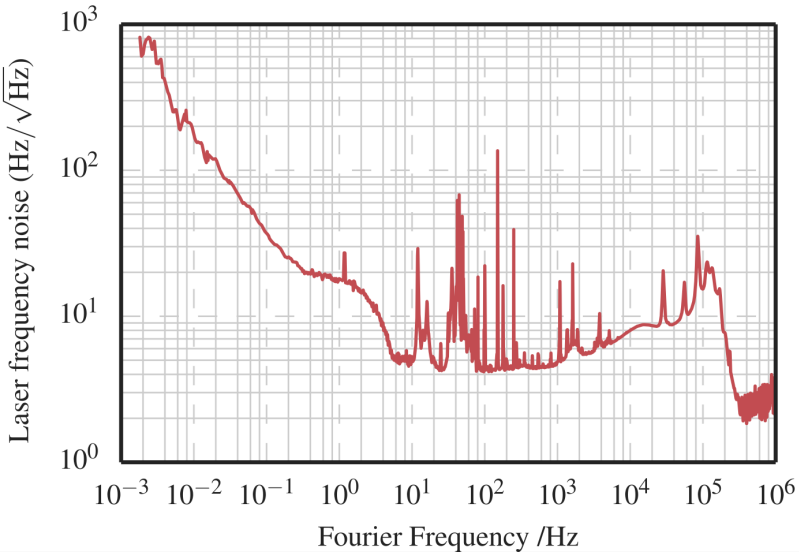

Fig. 4.6 Frequency noise spectral density of the beatnote at 556 nm between the branch locked to the multi colours cavity and the reference cavity.

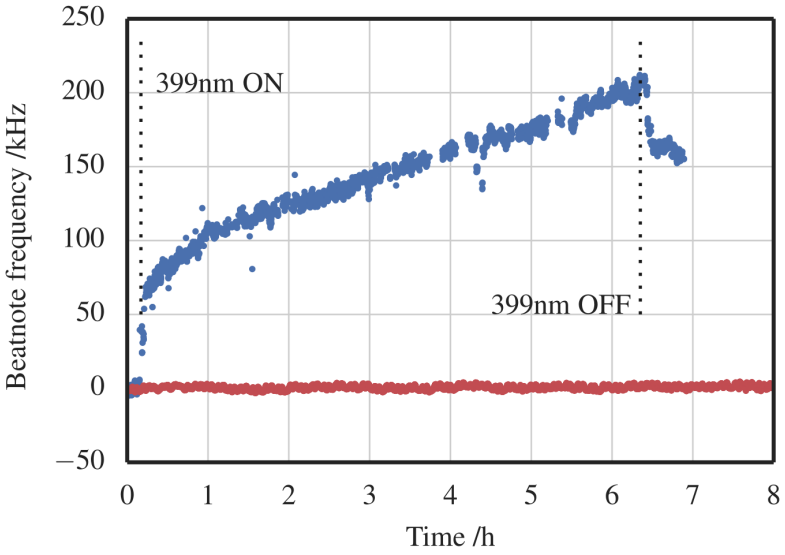

Fig. 4.7 Beatnote frequency between the 759 nm laser and the frequency comb stabilised to a H-maser. Red: 798 nm, 759 nm and 556 nm lasers simultaneously locked to the multi colours cavity. Blue: 759 nm and 399 nm lasers sequentially stabilised.

lasers (556 nm and 399 nm or 798 nm) to the cavity to observe any optical effects stemming from the simultaneous presence of all the lasers inside the cavity.

The results are shown in figure 4.7. When the 759 nm, 556 nm and 798 nm lasers are simultaneously locked to the multi colours cavity, the observed drift is less than 2 kHz/h. But when the stabilisation of the 798 nm light was swapped for the 399 nm radiation (759 nm and 556 nm locked all the time), a fast drift of about 50 kHz in 4 minutes was measured (seen at the beginning of the trace), followed by a linear drift of 22 kHz/h. This significant alteration of the behaviour at this wavelength compared to all the other ones can be explained by the higher absorption of the mirror coatings at 399 nm (see table 4.2) heating the mirrors up, leading to a rapid shift at first, followed by an augmented drift rate. In the long term this thermal effect could damage the cavity optics. The drift rate in this case is higher than the requirements (12 kHz/h set by the lattice light shift uncertainty). Therefore the 399 nm light is always stabilised via its sub-harmonic at 798 nm.

4.1.4 Conclusion

The objective of the multi colours cavity was to substitute individual laser stabilisations for the MOT and lattice lasers with a compact, transportable and robust

solution. Our setup supersedes all requirements set by the operation of the Yb lattice clock. Three different lasers (399 nm and 798 nm as two harmonics of the same laser) are locked to one stable ULE cavity operated at the temperature of vanishing CTE through the offset sideband locking technique. This method allows to bridge the frequency gap between the cavity and the demanded frequency of the Yb lattice clock for all wavelengths simultaneously. The laser with the highest stability requirement in this setup, the 2nd stage MOT laser at 556 nm, was characterised with a linewidth of 300 Hz and a stability (Allan deviation) as good as 3 parts in 10^{14} at 1 s. This result is quite encouraging, especially since no efforts were undertaken to reduce acoustic and seismic noise impinging on the cavity.

The 399 nm radiation proved problematic, causing unacceptable high drifts of the cavity, attributed to excess absorption of the mirror coatings at this wavelength. Therefore a stabilisation of the sub-harmonic at 798 nm was implemented and demonstrated a good performance, compatible with a lattice light shift uncertainty below 1×10^{-18}.

We tested the multi colours cavity setup locking simultaneously the 556 nm, 759 nm and 798 nm/399 nm lasers and operating the MOT for about 10 h without observing a change in the number of atoms trapped in the lattice.

We demonstrated a compact and robust solution for the simultaneous stabilisation of the MOT and lattice lasers in an Yb lattice clock, which in principle could also be used for spectroscopic applications. This system is planned to be further improved by implementing an automatic drift compensation.

4.2 Optical Lattice Improvements

The magic wavelength of the ${}^1S_0 \rightarrow {}^3P_0$ transition determined during our absolute frequency measurement campaign (chapter 2) does not agree with the results obtained by other groups [5, 28, 165, 166]. The spontaneous emission background of the lattice laser spectrum has been identified as a possible source of this discrepancy [167]. This background radiation in the laser light has the consequence that the measured magic wavelength is shifted to an effective value where the spontaneous emission effect is cancelled, too.

We use a diode-pumped Ti:Sa laser to generate the lattice, because this laser type is known for its robustness and high achievable output power. This kind of laser also features a wide spontaneous emission spectrum, typically supporting radiation across tens of nm. It is therefore also used to generate frequency combs. The amplified spontaneous emission background of each laser is unique in terms of its amplitude below the carrier, asymmetry and temporal stability.

In order to extinguish the spontaneous background radiation, the laser output radiation needs to be filtered. Common techniques are the use of Fabry-Perot cavities and optical gratings.

We included an optical grating (Optigrate "BragGrate" bandpass filter, 759 nm) in the path of the lattice laser, precisely in front of the coupling to the high power PM fibre, as sketched in figure 2.2. The grating filtering bandwidth is 20 GHz. This allows adjusting the lattice frequency by ± 10 GHz around the magic wavelength while running the experiment. We expect this element to suppress most of the spontaneous emission background of the Ti:Sa laser. In order to support a more precise assessment of the AC Stark shift, the implementation of an enhancement cavity using mirrors outside of the vacuum chamber is underway. This cavity will allow the use of deeper lattices, reaching conditions where the influence of the an-harmonic terms of the lattice light shift (equation 1.29) is clearly visible. Through an extensive mapping of the lattice shift across frequency and intensity these terms can be measured with higher precision than the literature values we used before and thus the accuracy of the lattice light shift estimation will increase.

A renewed measurement of the magic wavelength and improved statistics on the AC Stark shift should enable us to operate the Yb clock with a lattice light shift uncertainty in the low 10^{-18} region.

4.3 Spectroscopy Laser and Other Upgrades

The uncertainty budget (table 2.1) is currently dominated by the AC Stark shift contributions and to a lesser degree, by cold atom collisions and the Zeeman effect. The uncertainties given for these systematic effects are mainly limited by statistics. An improved stability of the clock transition probe laser will enable a more precise evaluation in a shorter time. Since the probe laser stability did not display the

expected performance, a number of changes to its setup were applied. In a first step the acoustic isolation chamber of the cavity was placed in a different lab and on the floor at a position where a measurement showed less seismic noise than in the initial position close to the Yb clock. Subsequently the vibration isolation platform was exchanged for an active vibration isolation (Optosigma OSDVIT-45A). The ultra-stable cavity was exchanged for a different model that had been characterised previously in [156] with a short-term stability in the low 10^{-15} region and a linewdith below 3 Hz. This cavity consists out of an ULE spacer supported in a vibration-insensitive configuration and combined with ULE mirrors coated at 578 nm. Meanwhile the original cavity was sent back to the manufacturer to exchange the mirrors, as they had featured a disturbing high order mode always present in the background. Generation of the 578 nm laser radiation was also changed, replacing the fibre and solid-state lasers with a single diode laser at 1156 nm, followed by second harmonic generation in a PPLN crystal. The stabilisation of the laser to one cavity mode was also changed. The fast lock is now acting on the current control of the laser diode. This allowed us to remove the AOM used for this task so far and furthermore to engage a higher bandwidth in the PDH control (300 kHz). The drift compensation (bandwidth 3 kHz) is now acting upon the internal cavity length of the diode laser by steering a piezo voltage.

First spectroscopic results in May 2017 resolved a linewidth of 7 Hz for the $^1S_0 \rightarrow {}^3P_0$ transition, shown in figure 4.8, and a stability of 4 parts in 10^{-15} at 1 s , shown in figure4.9. This result agrees with the performance of this cavity (see also chapter 2). With these changes an evaluation of the AC Stark shift (stemming from the lattice and the probe laser) and the density shift at an equally low 10^{-18} level will be undertaken in the near future.

4.4 Optical fibre network

The fibre noise cancellation systems reported in section 2.7 used orthogonal polarisations in the reference and back-reflected beams. This gave the advantage of an easy adjustment of optical power levels with half-wave plates and polarising beam splitters. On the other hand we recognised a noise floor in the Allan deviation at 6×10^{-19} after about 2000 s of measurement time and we suspected this being the result of polarisation to amplitude noise conversion. Therefore the setup was

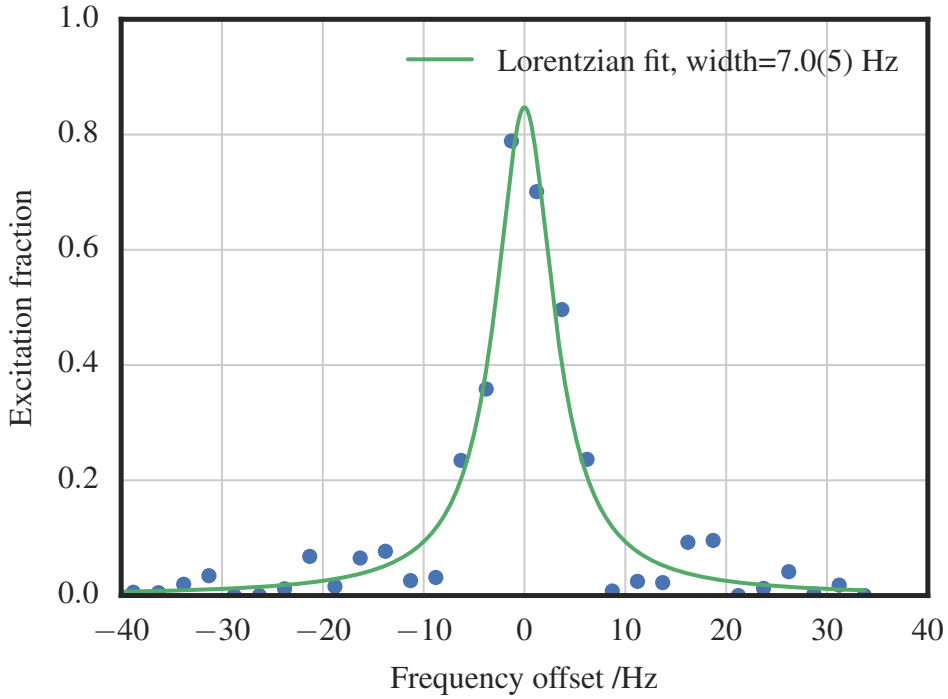

Fig. 4.8 Spectroscopy of the $^1S_0 \rightarrow {}^3P_0$ transition with a FWHM of 7 Hz in 2017 after improvements to the ultra-stable laser system

changed to incorporate the same polarisation throughout the phase noise detection interferometer, thereby reducing the sensitivity to polarisation noise. In the following the optical and electronic setup is described and characterised.

4.4.1 Setup

The dissemination of the 578 nm laser to the ultra-stable cavity, the frequency comb and the atomic spectroscopy using PM fibres is depicted in figure 4.10. The diode laser is situated in a neighbouring laboratory of the Yb lattice clock and connected to the dissemination breadboard via optical fibre. After passing through the SHG crystal some 7 mW of optical power at 578 nm are distributed among the three branches. About 80% of this power are sent to the frequency comb in order to achieve high SNR in the beatnote with the comb light. The atomic spectroscopy and the ultra-stable cavity on the other hand use only some nW to µW of light power. Therefore the fibre noise cancellation systems, which are identical in all three branches, are set up to function even with optical powers of about 100 µW circulating inside the

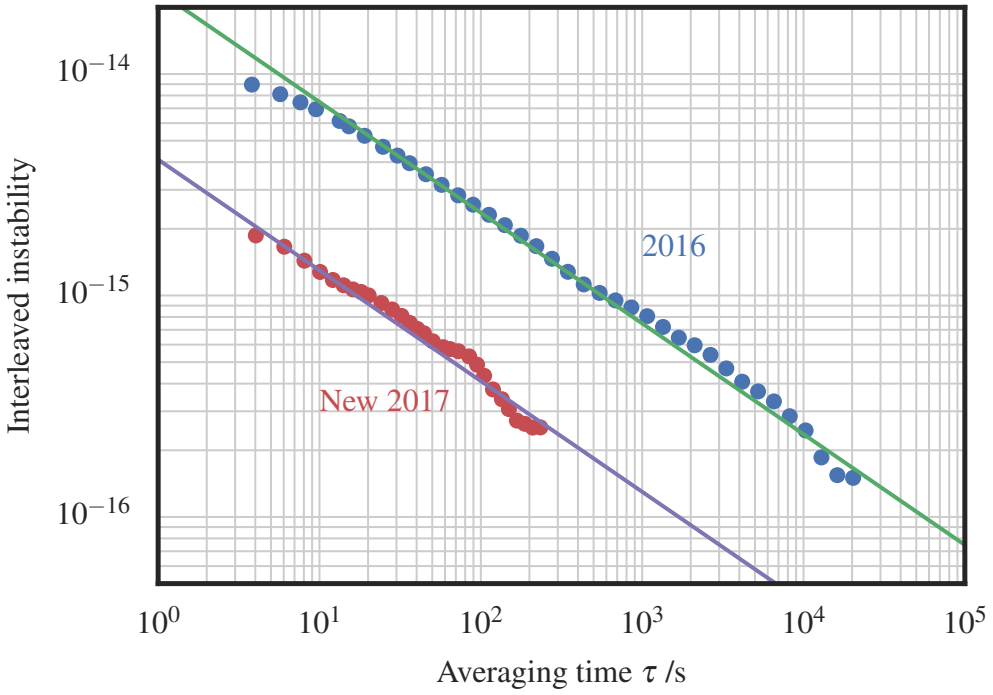

Fig. 4.9 Stability of interleaved clock cycles in comparison before (blue) and after (2017) the recent upgrades to the ^{171}Yb lattice clock. This improvement in stability allows a faster and more precise measurement of systematic effects on the clock transition as well as faster optical frequency comparisons.

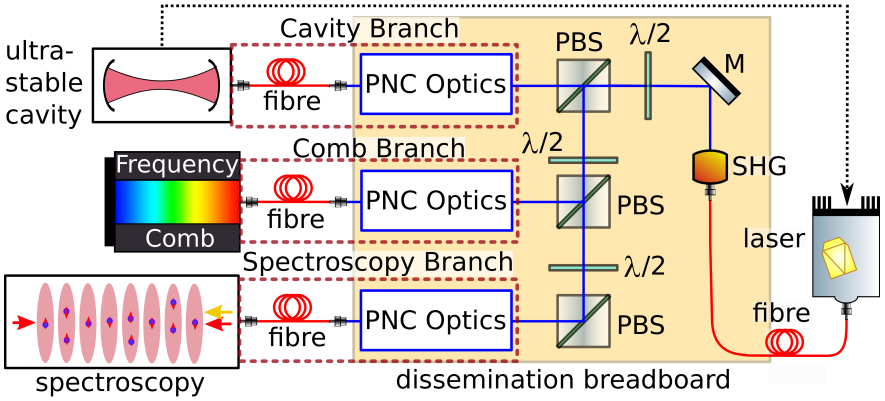

Fig. 4.10 Dissemination of the 578 nm clock laser. The laser light is distributed to the ultra-stable cavity, the frequency comb and the atomic spectroscopy by phase-noise cancelled (PNC) fibre links (called branches, inside red dotted boxes). SHG = second harmonic generation, M = mirror, PBS = polarising beam splitter, $\lambda/2$ = half-wavelength retardation plate, blue lines follow the free-space optical path. The black dotted line denotes DC signals of the laser stabilisation to the ultra-stable cavity.

two interferometer arms. Only a small fraction thereof is actually available for the generation of the phase noise error signal. In order to obtain sideband spectra of the clock transition (see figure 2.9), the power of the 578 nm radiation impinging on the atoms is raised by a factor of about 100 (re-routing some light from the frequency comb branch), in order to improve the contrast of the blue/red sidebands. This power broadens the $^1S_0 \rightarrow {}^3P_0$ line beyond an FWHM of 100 Hz and into a regime where a fibre noise cancellation is no longer necessary. Therefore sideband spectra are obtained without the engagement of active fibre noise cancellation. The distribution of the laser light between the branches and the optics of the pathlength noise cancellation systems are placed on the same stainless steel breadboard and enclosed by an acrylic cover shielding the free-space paths from any airflow.

The laboratories containing the whole Yb lattice clock experiment are temperature stabilised by an air conditioning system. Nevertheless, a residual quasi-sinusoidal oscillation with an amplitude of 0.2 K and a period of 15 min remains. The airflow changes accordingly in intensity. As a result the temperature inside the laboratories experiences temperature excursions with an amplitude of up to $0.5\,\mathrm{mK\,s^{-1}}$ (maximum at half-period time). As for the unstabilised PM fibres these oscillations of temperature introduce phase noise through changes of the fibre length and index of refraction (applying the corresponding sensitivities of pure silica [220]) with relative magnitudes of about 1×10^{-17} and 1×10^{-16} at 450 s, respectively.

Within the free-space path of the laser light on the dissemination breadboard there remain up to 2 m thereof that are not shared between two adjacent branches and are also located outside of the phase-noise cancellation interferometer. The acrylic glass enclosure shields efficiently airflow and acoustic noise. But the breadboard itself experiences temperature fluctuations (albeit damped by its mass) caused by the air conditioning oscillations. The periodicity of these fluctuations is the same as of the surrounding air, but the amplitude is much smaller, namely 4 mK. This transforms into a Doppler shift of the free-space optical path of estimated 1×10^{-18} at 450 s. This shift is also present when the phase noise cancellation is engaged.

A sketch of one fibre noise stabilisation branch is depicted in figure 4.11. Upon entry the laser frequency is first shifted by a double-pass AOM (AOM_{gap}) in cat-eye configuration [221], bridging the gap between the nearest fundamental mode of the ultra-stable cavity and the atomic resonance. Then a power beamsplitter extracts a small reference beam (30% of the incoming beam reflected) as the short arm of an

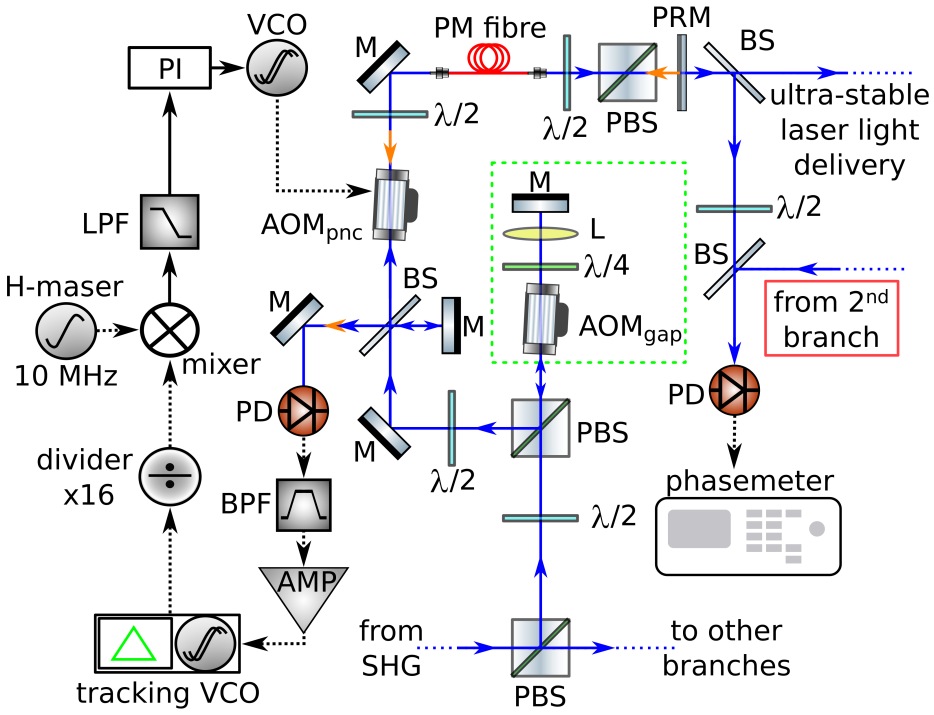

Fig. 4.11 Sketch of the fibre noise cancellation setup and its assessment. The laser light enters the branch coming from the SHG crystal. The double-pass AOM in cat-eye configuration is marked with green dots. The laser light is signalled with blue arrows, but the retro-reflected beam path with orange arrows. PD = photodiode, VCO = voltage controlled oscillator, LPF = low-pass filter, AMP = amplifier, BPF = band-pass filter, L = lens, PRM = partial reflecting mirror, PI = proportional-integral controller, BS = power beam splitter

imbalanced optical interferometer. The remaining part, the long interferometer arm, is subsequently shifted by 80 MHz in an AOM (AOM_{pnc}) and then enters the 20 m PM fibre. A half-wave plate aligns the polarisation of the incoming light to the slow axis of the PM fibre, thereby minimising polarisation noise.

After passing the fibre the laser polarisation is cleaned using a $\lambda/2$ plate and a PBS (polarisation extinction ratio at least 1000 : 1) and then about 40% of the light power are retro-reflected with a partial reflecting mirror. On the comb branch the reflected ratio is actually smaller ($\approx 15\%$) due to the higher optical power in the beam exiting the fibre. The polarisation cleaning ensures that the retro-reflected beam is also aligned on the slow axis of the fibre. This suppresses amplitude noise in the optical interferometer due to the fibre birefringence, which is sensitive to temperature changes in panda-style PM fibres [160] and therefore of concern.

Approximately 20 µW in optical power are delivered after the partial reflecting mirror in case of the ultra-stable cavity and a few hundred nW with the atomic spectroscopy branches, whereas in the comb-branch these are some 1.5 mW.

The retro-reflected light passes once again the $\mathrm{AOM_{pnc}}$, experiencing a total shift of 160 MHz and then interferes with the reference beam. The beatnote of these two beams, which is carrying the information on the phase noise error accumulated along the optical path, is recorded on a photodiode (bandwidth 400 MHz) and subsequently the interference part at 160 MHz filtered out (bandwidth 14 MHz) and amplified.

All our fibres use angle flat connectors (a variation of angle polished connectors manufactured by OZ optics) to reduce back-reflection from the fibre tip. We found that this back-reflection gives rise to a signal 30dB smaller than the one from the retro-reflector. The beatnote signal is tracked by a voltage-controlled oscillator (VCO), which has a bandwidth of 3 MHz. Using a tracking VCO has the advantage of providing the fibre noise cancellation electronics with a high SNR input signal of constant amplitude, even when the SNR and amplitude of the actual signal is small or fluctuating. This improves the robustness of the system, especially when working with low optical powers. The output signal of the VCO is divided by 16 and this signal directly mixed with a 10 MHz H-maser reference signal. A subsequent low-pass filter (bandwidth 500 kHz) selects the DC part of this signal.

The result is a DC error signal, directly proportional to the accumulated phase noise in the long interferometer arm. A proportional-integral (PI) control, set to an optimised bandwidth of around 20 kHz for each branch separately, finishes the

feedback-loop by controlling the voltage-controlled oscillator driving the AOM_{pnc}, adding the opposite phase to the laser light of the instantaneous interferometer phase error, thus realising an unperturbed laser signal at the output of each branch.

4.4.2 Results

The performance of the fibre noise cancellation on all three branches has been evaluated forming pairwise beatnotes between the outputs of the phase noise cancelled branches, as shown in figure 4.11. The laser light after the partial reflecting mirror is beat against the output of a 2^{nd} identical setup in a short free-space optical path covered by a separate acrylic enclosure. The beatnote is recorded with a phasemeter or frequency counter to assess the residual phase noise.

If the input signal of the tracking VCO becomes very small, the electronics fail to properly follow the phase evolution of the signal and cycle slips (phase jumps by an integer number of 2π) occur.

We determined the minimum input light power within the interferometer of one branch (in figure 4.10 after the PBS whereupon the light enters directly from the SHG) after which cycle slips compromise the performance of the phase noise cancellation as 90 µW.

The possibility of cycle slips appearing on long term measurements using normal input powers was investigated recording the beatnote between the two branches with low input light power for a total of 20 hours. A histogram of this measurement is shown in figure 4.12. All data points were within 0.05 Hz (1 part in 10^{16} or $\frac{1}{10}\pi$), proving the absence of cycle slips.

We investigated the influence of turbulent air inside the free-space parts of the laser branches on the phase noise cancellation. For this measurement we compared the phase noise between two stabilised branches with and without the lid of the acrylic enclosure attached to the system. As shown in figure 4.13, the turbulent air increases the phase noise between 0.1 Hz and 10 Hz. This means that relevant noise levels act at the same timescale as a single clock cycle (0.1 s to 0.5 s). Such noise could lead to systematic errors. The acrylic enclosure suppresses this effect efficiently.

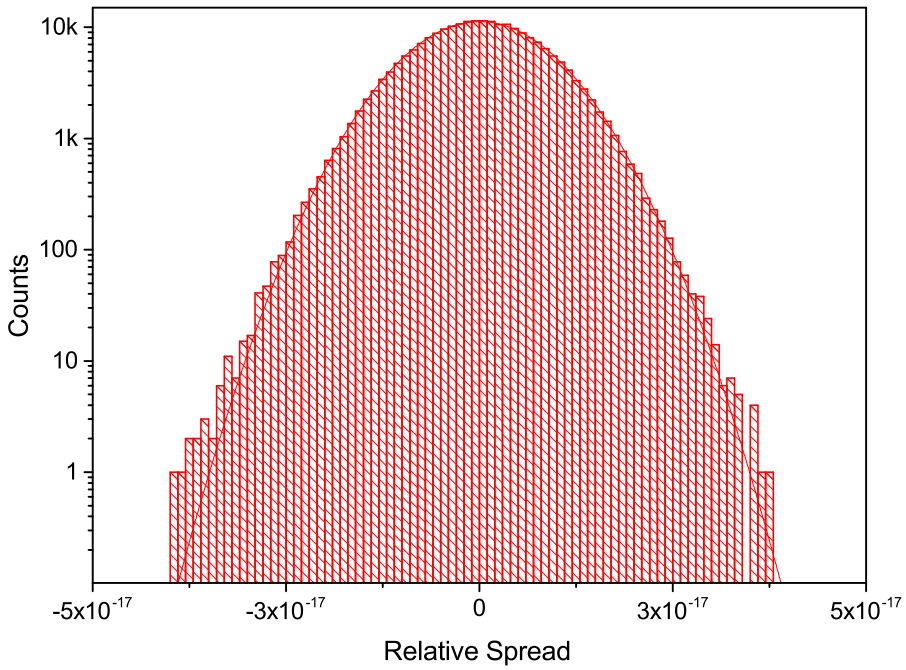

Fig. 4.12 Histogram of a 20 hours measurement looking for cycle slips in the beatnote. No points were recorded outside of the scale used for the abscissa.

The power spectral density of a typical phase noise measurement between two laser branches is shown in figure 4.14. At low frequencies (0.1 mHz to 0.1 Hz white frequency noise dominates (f^{-2} behaviour). A variety of noise peaks around 10 Hz and between 300 Hz and 500 Hz follow, stemming mostly from acoustic noise. Electronic noise is obviously present with the power line at 50 Hz and its harmonics represented. Subsequently a white phased noise pedestal is visible between 4 kHz and 20 kHz. The later value is also equal to the control bandwidth of the phase noise cancellation. The phase noise level ($\approx$ 90dBc/Hz) agrees with the detection noise of the beatnote on the photodiode (SNR 42 dB in 100 kHz). At higher frequencies than 20 kHz only electronic noise of low amplitude is detected.

The corresponding Allan-deviation of this measurement is shown in figure 4.15 (blue line), together with a measurement of the unstabilised phase noise (green), a long term measurement (red) and reference stabilities of ultra-stable cavities (orange) and an ensemble of optical atomic clocks (light green). We measured the phase noise with a bandwidth of 500 Hz and a gate time of 1 ms, with the notable exception of the 4 days measurement that was obtained using a high resolution K+K FXE counter (Λ-variance) and a gate time of 1 s (bandwidth 0.5 Hz).

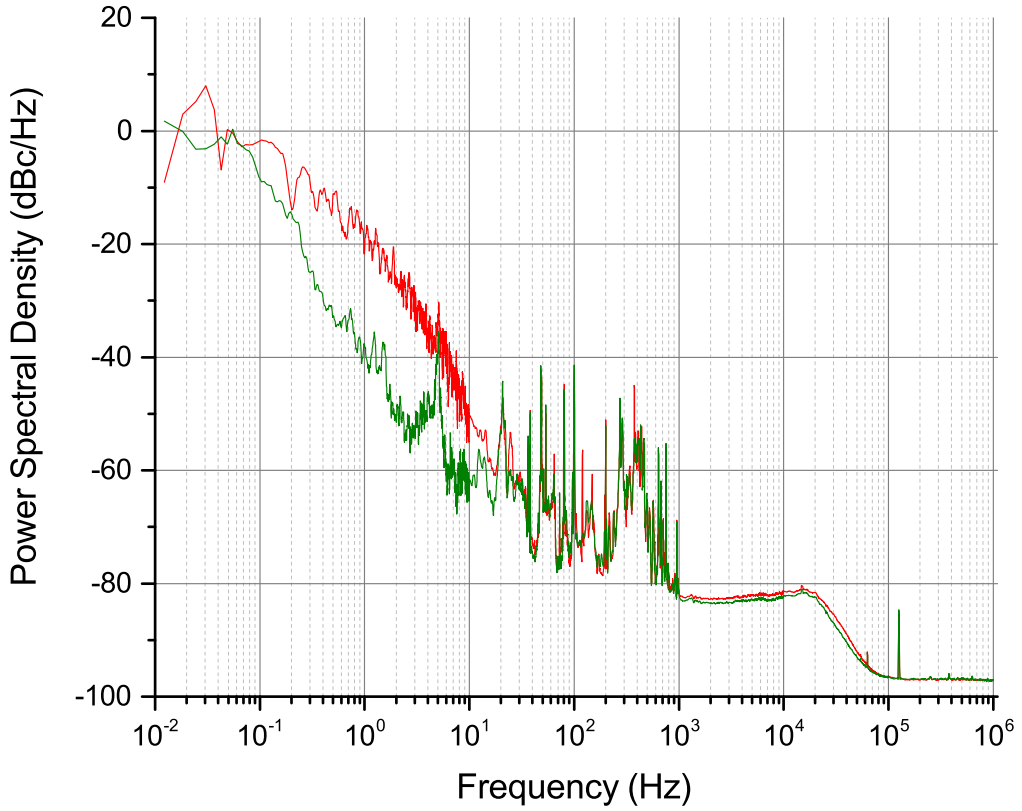

Fig. 4.13 Power spectral density (PSD) of the beatnote between two branches with (green) and without (red) the lid of the acrylic enclosure attached. The slightly higher phase noise level compared to fig. 4.14 is due to different optical and electronic power levels during this measurement. The results are nonetheless transferable to the current setup.

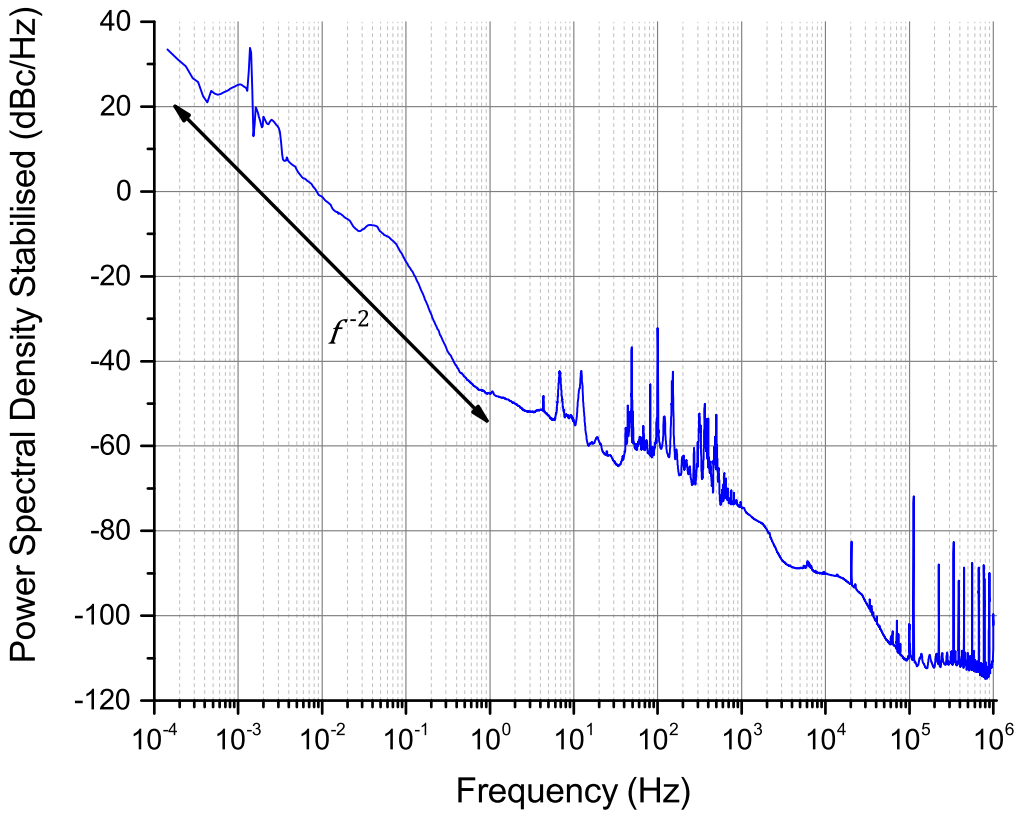

Fig. 4.14 Power spectral density of the beatnote between the output laser radiation of two phase-noise cancelled fibre links, measured with a Microsemi 5125A phasemeter

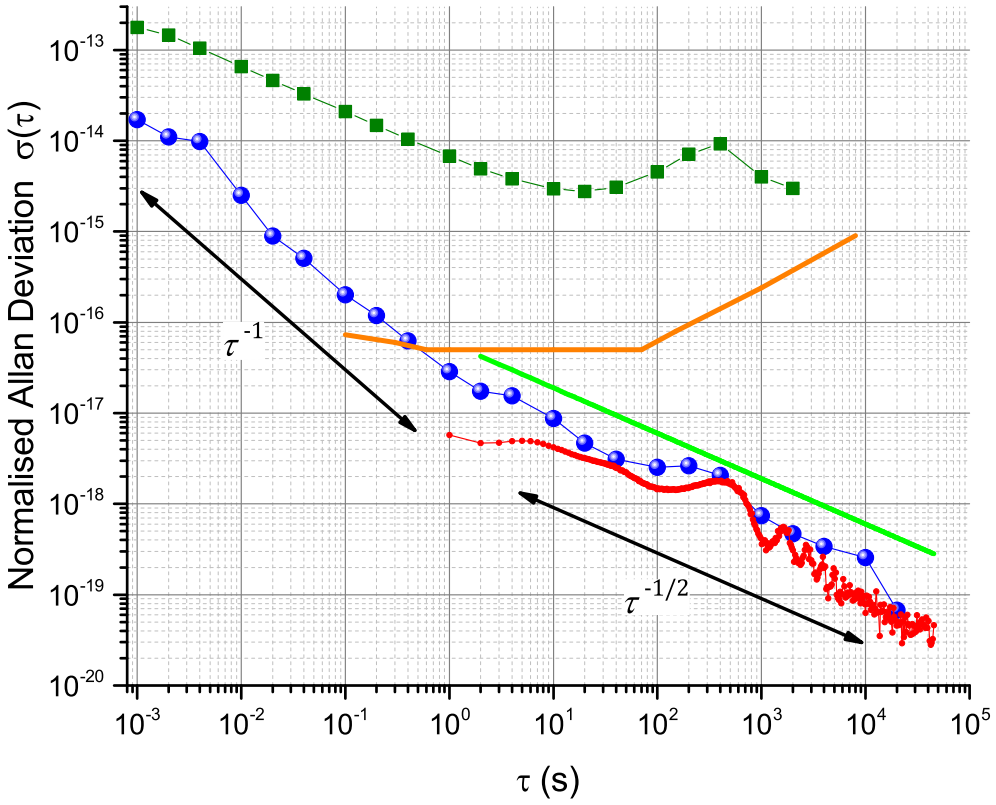

Fig. 4.15 Allan-deviation of the same measurement as in fig. 4.14 (blue), compared with measurements of the unstabilised link performance (dark green) and a 4 days long assessment of the fibre link performance (red). The best reported stabilities of an optical cavity [21] (orange) and of an ensemble of optical lattice clocks [49] (light green) are shown as benchmarks.

It is clearly visible that the unstabilised optical fibre link is not compatible with the performance requirements set by state-of-the-art ultra-stable lasers and optical lattice clocks.

The phase noise cancelled link averages down as white phase noise ($1/\tau$) at short integration times ($\tau < 1\,\mathrm{s}$). For $\tau > 4\,\mathrm{s}$ the slope changes towards a $\tau^{-1/2}$ slope, matching white frequency noise. The long-term measurement (red curve) gives some deeper insight into the cause of this white frequency noise. The noise level at timescales $\tau \geq 450\,\mathrm{s}$ is in agreement with the calculated periodic noise induced by the periodic temperature changes inside the laboratory.

The Allan deviation measured with the frequency counter is a bit lower than the corresponding values obtained with the phasemeter, because the Λ-variance of the high resolution counter used has a reduced sensitivity to white phase noise (here the dominating noise at short timescales) in comparison to a phasemeter [222, 223]. For integration times τ larger than 10 s the noise behaviour resembles white frequency noise and at long timescales the blue and red line agree well.

We assessed the stability of two phase noise cancelled laser branches as 2×10^{-17} at 1 s, following a $7 \times 10^{-18}\tau^{-1/2}$ slope for long timescales ($\tau \geq 1000\,\mathrm{s}$), as shown in figure 4.15. The measured uncertainty of 5 parts in 10^{20} was only limited by statistics. No offset in the frequency of the beatnote between a pair of phase noise cancelled fibre links was detected. This performance supersedes the best so far published stabilities and accuracies of ultra-stable lasers [21] and an optical clock ensemble [49].

4.4.3 Discussion

We have developed and characterised an optical fibre noise cancellation working on all three branches of the ultra-stable 578 nm laser of the Yb lattice clock at INRIM. The phase noise cancellation systems are working even with very low optical powers available (90 µW per laser branch). The pairwise evaluation of the phase noise cancellation demonstrated a (statistical) uncertainty of 5×10^{-20} and a long-term stability following a $7 \times 10^{-18}\tau^{-1/2}$ evolution, surpassing the best published results for lasers stabilised to an ultra-stable cavity [21], as well as the stability and accuracy limits of all contemporary optical clocks [224, 49].

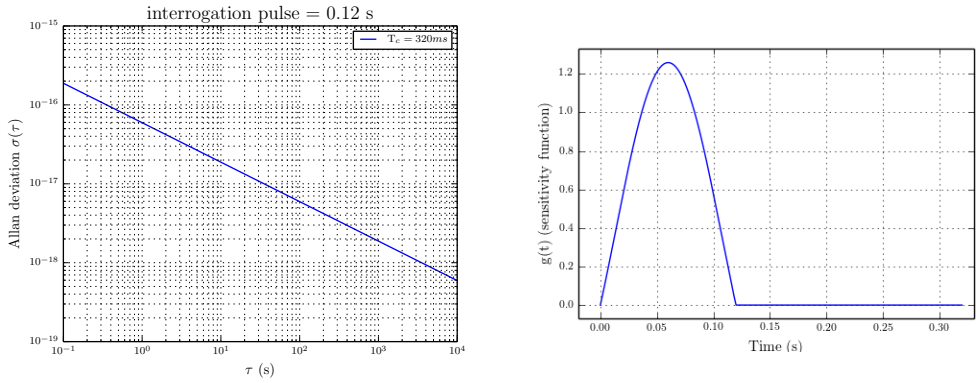

Fig. 4.16 Left: Contribution of the Dick effect due to fibre noise to the clock stability. Right: The sensitivity function g(t)

With the power spectral density in figure 4.14, the Dick-effect contribution of the fibre noise to the clock stability can be calculated. Inserting an interrogation time t_p of 120 ms, a total clock cycle time of $T_c = 320$ ms and the power spectral density shown in figure 4.14 in equations 1.7, 1.8, 1.9, 1.10, 1.12, the Dick-limit follows as: $\sigma_{Dick}(\tau) = 5.9 \times 10^{-17}\tau^{-1/2}$, almost 2 orders of magnitude smaller than the stability of the INRIM Yb lattice clock. The sensitivity function g(t) and the Dick-effect limited stability are displayed in figure 4.16

The main limitation to our system are periodic temperature changes inside the laboratory acting on the length of the optical path inside each branch that is situated outside of the feedback loop. The amplitude of these oscillations (occurring at a period of 450 s) agree with our predictions. These temperature oscillations show an almost sinusoidal behaviour and therefore average down in the Allan deviation as white frequency noise ($\tau^{-1/2}$) for $\tau \gg 450$ s. The assessed stability and accuracy of our system is consistent with the delivery of spectrally pure laser radiation in state-of-the-art optical clocks. An even higher performance could be achieved by either eliminating the optical path between the dissemination branches (figure 4.10) using the same reference mirror for all fibre links (this would need an advanced electronic setup), or by a thermal insulation of the steel breadboard supporting all the free-space optics of the laser branches and fibre noise cancellation systems.

4.5 Perspectives

With these improvements implemented and the other augmentations and measurements discussed at the end of chapter 2 in preparation, the uncertainty budget of the ^{171} Yb lattice clock is likely to be re-evaluated at a low 10^{-17} level in the near future.

Chapter 5

Multi-Branch Universal Synthesizer At NPL

5.1 Introduction

Recent progress made in the field of optical atomic clocks is closely connected to the invention of the frequency comb linking the microwave- and optical-domain, thus providing a connection between the primary standard of the SI unit the second with the $F = 3 \rightarrow F = 4$ hyperfine ground-state transition in ^{133}Cs and realisations of secondary optical frequency standards in optical transitions [225].

At the very heart of any such atomic clock is an ultra-stable oscillator interrogating the narrow clock-transition. The stability of optical lattice clocks, as for example the one demonstrated in this work, is usually limited by the reference stabilising the ultra-stable oscillator, as already discussed in chapter 1. The most stable laser sources nowadays depend upon thermal-noise limited optical cavities and projected performance improvements rely upon complex (such as cryogenic temperatures [226]) and often wavelength-dependent (like crystalline mirror coatings [22, 133]) solutions.

In order to fully exploit the benefits of these novel technologies and to profit from the superb performance of single ultra-stable cavities, transfer of the spectral purity from the wavelength of one ultra-stable oscillator to multiple others becomes necessary.

More recently optical frequency combs have begun emerging from their initial role as extended frequency rulers into even being a part of the atomic spectroscopy itself by transferring spectral purity between optical/optical or optical/microwave oscillators [227, 228].

The transfer oscillator technique allows to cancel out the noise of the femtosecond laser itself in any optical/microwave or optical/optical measurement making it a valuable toolbox for spectral purity transfer from one ultra-stable cavity to any other wavelength in the emission-range of the comb (typ. VIS or NIR) or the microwave domain [229].

A good spectral purity transfer requires that the noise introduced by the stability transfer is negligible compared to the noise of the ultra-stable cavity. The transfer oscillator technique starts with the general description of an arbitrary comb tooth m ($m \in \mathbb{N}$), whose frequency can be written in the following form [146]:

$$f_m = f_0 + m \cdot f_{rep} \tag{5.1}$$

The repetition rate f_{rep} originates from the delay between subsequent femtosecond laser pulses, whereas f_0 results from a delay between the carrier- and envelope-phase (laser cavity dispersion) of subsequent pulses with the total output bandwidth determined by the pulse duration.

But actual femtosecond combs often feature fibre-amplifiers, 4 wave-mixing in non-linear fibres and frequency doubling in order to reach sufficient comb light power at the desired wavelength. These elements and additional fibre/free-space paths add further noise to the frequency ratio measurement. Therefore a careful evaluation of the limits of the stability transfer is necessary.

One way to reduce the noise from these sources is to use the same amplifier and mixing fibre for all wavelengths, cancelling their noise as common-mode (Single branch comb [230]). But this approach has the disadvantage that sufficient (typ. 30 dB in 100 kHz bandwidth) signal-to-noise ratio (SNR) across several wavelengths is difficult to reach. This again can be aided by tight locking of the comb's repetition rate to an ultra-stable reference (e.g. cavity) combined with low-bandwidth tracking oscillators and counters [228].

But since even this approach faces limitations with an increasing number of wavelengths involved in this work a multi-branch comb was set up and characterised. A multi-branch optical femtosecond comb means that every frequency measured features its own fibre amplifier and non-linear fibre, resulting in strong beatnotes and avoiding the need for tight locking of the femtosecond laser. The most advanced atomic clocks today reach their estimated accuracy of few parts in 10^{18} after about 10 000 s of integration time τ (averaging down with a stability of about $1 \times 10^{-16} \tau^{-1/2}$) [49, 1, 48, 6, 50], while the most advanced cavities reach a stability of 5×10^{-17} on a timescale between 1 and 10 seconds [21, 20].

Therefore the frequency comb needs to surpass these values with a margin in order to be ready for further improvements to be expected in the near future.

State-of-the-art transfer evaluations showed frequency stability limits of about 3×10^{-16} at $\tau = 10\,\mathrm{s}$ for multi-branch [231, 227, 232] and 4×10^{-18} at $\tau = 10\,\mathrm{s}$ for single-branch [228] frequency combs.

In this work a multi-branch femtosecond frequency comb with an ultimate spectral-purity transfer limitation of inter-branch noise as low as 1.5×10^{-17} at $\tau = 1\,\mathrm{s}$ in stability, averaging down slightly faster than $\tau^{-1/2}$ and 2×10^{-19} of residual uncertainty is presented. The comb is operated at the "National Physical Laboratory" in Teddington, UK. I was seconded to this institution in late 2016 and early 2017 in order to assess and improve the frequency transfer of the universal synthesizer, which had already successfully been employed in the operation of the optical clocks ensemble at NPL. In this chapter the results obtained during my secondment are presented.

This chapter is organised as follows: A complete description of the universal synthesizer consisting of an ultra-stable-cavity and a frequency comb is given in section 2. The laser spectral purity transfer scheme and the reference comb as well as the counter synchronisation and beatnote detection are also described. The 3rd section unfolds the results of the frequency ratio measurement performance of the individual combs, the counter measurement limitations and finally the full spectral purity transfer stability and accuracy of our system. The last section classifies these results in the light of other contemporary results and gives an outlook to future developments.

5.2 Universal Synthesizer

The universal synthesizer, comprised of a commercially available Menlo Systems Er-doped-fibre comb (NPL-FC4) with six individual amplification and broadening branches for different wavelengths and an ultra-stable cavity, is located in a temperature-controlled ($\pm 0.5\,\mathrm{K}$) laboratory. In order to measure the performance of the system we use a single-branch reference comb (NPL-FC3), that had been evaluated before [148].

This reference comb, another Menlo Systems product, is located in another laboratory featuring a refined temperature control ($\pm 100\,\mathrm{mK}$) with noise-cancelled fibre-links and RF cables connecting the labs. All relevant RF signals from both systems are referenced to the same H-maser. Both combs are equipped with high-resolution overlapped-Λ counters from K + K (named C3 for NPL-FC3 and C4 for NPL-FC4). For synchronous measurements all signals from both combs relevant for optical-to-optical frequency ratios are counted on the individual counters, with software synchronisation of gate times to the UTC (NPL) time signal keeping the difference between the 1 s gate times of the combs below a few milliseconds.

Both comb-systems are enclosed within acrylic glass and metal boxes to reduce air currents and acoustic noise on free-space and uncompensated fibre-paths. The universal synthesizer setup is sketched in figure 5.1 and the reference comb measuring its performance in figure 5.6. In the following primed and un-primed variables refer to attributes of NPL-FC3 and NPL-FC4, respectively.

5.2.1 Universal Synthesizer NPL-FC4

NPL-FC4 is a commercially available (Menlo Systems FC1500) optical frequency comb based on a mode-locked Er-doped fibre laser (pumped by a 980 nm diode laser) exploiting the nonlinear-polarisation-rotation mechanism [233, 234].

The principle of operation of these lasers is similar to the Kerr-lens and self-phase-modulation of Ti:Sa-Combs, where the gain-medium's non-linearity in connection with some aperture inside the laser cavity leads to a favoured operation in the pulsed laser regime. Here the fibre birefringence and cross-phase modulation induced by the Kerr nonlinearity cause an intensity dependent rotation of elliptically polarised light. As a consequence placing a polarising element inside the laser cavity can lead

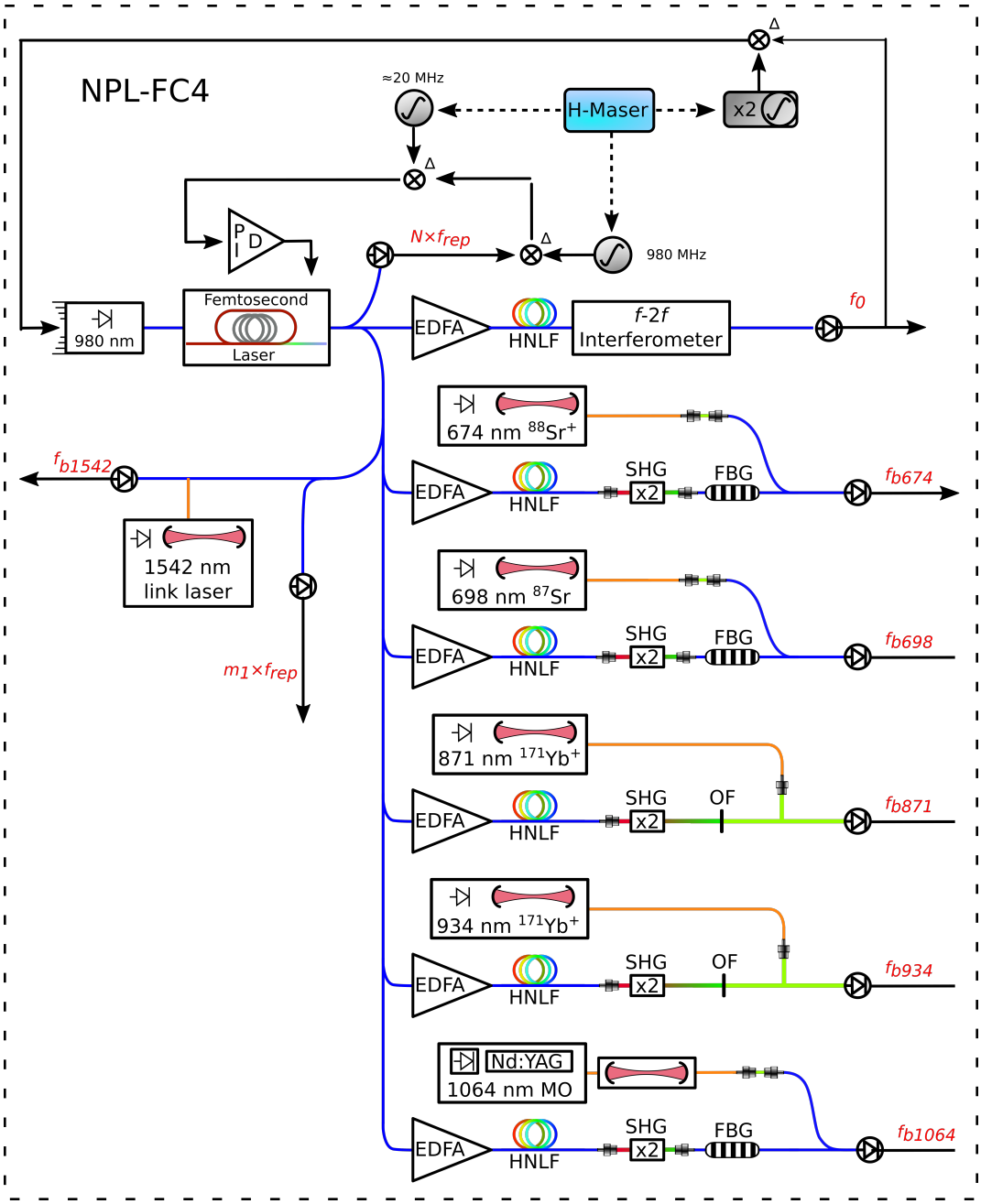

Fig. 5.1 Schematic of the comb used within the universal synthesizer. At the top is a simplified drawing of the locking of the f_{CEO} and f_{rep} frequencies to the H-maser. Note that the "branches" for the beatnote-generation at 1542 nm , 871 nm and 934 nm differ from the other three in that the 1542 nm has no EDFA and HNLF while the other two feature free-space beatnote detection. EDFA = Erbium doped fibre amplifier, HNLF = highly non-linear fibre, SHG = second harmonic generation, FBG = fibre Bragg grating, OF = optical filter, Orange (blue) lines mark fibres with (without) fibre noise compensation. Green = free-space paths.

to higher intensities suffering less loss, thus sparking pulsed operation. A simple Fourier-transform then leads to the well-known comb spectrum of equation 5.1.

The femtosecond laser output is centred around 1550 nm, spanning 80 nm Full-Width-Half-Maximum (FWHM). The comb light is split into 7 different branches, with the comb being directly heterodyned with the 1542 nm light of the laser used for the NPL-SYRTE fibre link in one arm and each of the other 6 branches featuring separate erbium-doped fibre amplifiers (EDFAs) and 4-wave mixing in highly non-linear fibres (HNLFs) to enable high SNRs in the beatnote detection. These 6 branches are all individually optimised by adjusting the amplifiers pump currents. This frequency comb features all polarisation-maintaining (PM) fibres. This leads to a more stable SNR in the beatnote-detection with external cw lasers as compared to just single mode fibres.

The 4-wave mixing process is similar to the Kerr-lens- or nonlinear polarisation-rotation-effect at the basis of the mode-locked laser, resulting from a third-order susceptibility. The HNLFs used in this work exploit self-phase modulation [235] or the soliton self frequency shift [236] to accomplish broadband cascaded 4-wave mixing. In the process two initial photons of different frequencies ν_1 and ν_2 are combined to form 2 new photons at frequencies $\nu_3 = 2\nu_1 - \nu_2$ and $\nu_4 = 2\nu_2 - \nu_1$. In the case of a frequency comb entering the HNLF thousands or even millions of waves mix to form an even broader comb. The mixing process can be adjusted by acting upon the fibre to favour a different main frequency in amplitude as opposed to the output of the mode-locked laser, enabling simultaneously a broadening and also a shift of the frequency comb emission [237].

Stabilisation of the carrier-envelope offset (CEO) frequency (and the repetition rate) is an important part of any frequency comb operation, since the spectra of free-running mode-locked lasers can drift several MHz in short timescales. The repetition-rate can easily be detected by direct observation of the comb-emission with a photo-diode, whereas the CEO frequency is a bit more demanding.

The top branch in figure 5.1 is the $f-2f$ interferometer, which is broadening the comb to span one octave and thereby enabling the detection of the CEO frequency f_0 with the built-in Menlo Systems $f-2f$ common-path interferometer scheme. This detection allows to stabilise the comb-spectrum (see e.g. [238–240]).

The second branch is optimised for the detection of the beatnote with the 1064 nm ultra-stable reference laser and the 3rd to 6th branch, utilising in addition to the

aforementioned EDFA and HNLF also frequency-doubling through a single-pass periodically-poled lithium-niobate (PPLN) crystal, enhance the signal for the respective optical atomic clock lasers at 934 nm, 871 nm, 698 nm and 674 nm, as shown in figure 5.1. Thanks to this multi-branch approach all beatnotes between the cw lasers and their nearest femtosecond comb teeth surpass 30 dB (in 100 kHz) easily, typically ranging from 35 dB to 40 dB, remaining stable for periods of several weeks.

All the wavelengths are sent to the NPL-FC4 reference comb by noise-compensated PM fibres. The femtosecond-laser cannot use the same path-noise cancellation technique as the cw light and is therefore not noise-cancelled along the whole way from the output of the femtosecond laser to the beat-detection PD. Along this path are EDFA, HNLF (except for 1542 nm), a free-space SHG stage (except for 1064 nm and 1542 nm) and additionally the pathways towards the beatnote detection, giving phase noise contributions to all branches .

To reduce their noise all EDFA, HNLF and SHG units are shielded inside metal boxes on the optical table of the comb and inside an acrylic enclosure protecting the whole setup from air currents. The universal-synthesizer branches dedicated to the optical atomic clock lasers are pairwise (934 nm and 871 nm , 698 nm and 674 nm) located in two separate metallic enclosures. The 1542 nm , 1064 nm , 698 nm and 674 nm beatnote detections use completely in-fibre beat-detection units providing ease-of-use, but with the disadvantage of about 2 m of uncompensated not common fibre in the paths of comb and cw light for each wavelength, whereas the 934 nm and 871 nm beatnote detection features full noise-compensation on all fibre-paths with only the cost of about 1 m uncompensated free-space path not common to comb- and cw-radiation, but shielded inside the acrylic enclosure.

The 1064 nm reference laser with the ultra-stable master oscillator cavity in place (see figure 5.4) is at the centre of this experiment with all other wavelengths (except for the femtosecond laser) stabilised to it.

Not a part of this work, but for completeness, it should be noticed that also the primary frequency (^{133}Cs) standard's microwave oscillator is linked to this laser by an optical-to-microwave spectral purity transfer.

5.2.2 Counting Of $f_{\mathbf{rep}}$, $f_{\mathbf{0}}$ And f_{beat}

With the frequency of one comb tooth displayed as in equation 5.1 we are left with three frequencies to detect for each beatnote between comb and cw laser to measure exact frequency ratios (or absolute frequencies, but that is not the scope of this work): The repetition rate f_{rep} , the carrier-envelope offset f_0 and the beatnote with the nearest comb tooth f_{beat}. In order for the removal of the femtosecond laser noise in the transfer oscillator scheme to function, it is important that these beatnotes are detected with high enough resolution, meaning that the counter noise must be well below the requirements for the targeted stability at all relevant timescales.

The repetition rate f_{rep} is first detected by sending a part of the femtosecond-laser output to a fast photo-diode (PD) measuring the 4th harmonic of f_{rep} around 1 GHz. This signal is then mixed down with H-maser referenced synthesizers (980 MHz and $\approx$ 20 MHz) to provide the error signal to the Menlo Systems electronics for the locking of the repetition rate.

The CEO frequency f_0 is detected in the $f-2f$ interferometer arm of the comb by recording the beatnote between several modes in the high frequency part of the octave-spanning broadened comb spectrum with the frequency doubled spectrum of the corresponding first sub-harmonics. Using eq. 5.1 it directly follows that the beatnote is equal to f_0 .

The beatnotes at 1542 nm , 1064 nm , 698 nm and 674 nm are detected by fully in-fibre beatnote detection units from Menlo Systems, whereas the 871 nm and 934 nm wavelengths feature free space optics and Thorlabs APD 430A avalanche PDs in order to reduce the effect of uncommon unstabilised fibre paths. The f_0 and the various f_{beat} from the cw lasers are used for the generation of the transfer beats (see section 5.2.5) and at the same time counted on C4, enabling software-based post-processing to determine all possible frequency-ratios.

5.2.3 Stabilisation Of $f_{\mathbf{rep}}$ And $f_{\mathbf{0}}$

Some published stability transfer schemes, such as [228], involve tight phase locking of one comb-mode (and hence all modes) to an ultra-stable reference oscillator to allow small-bandwidth beatnote detection with low-power signals resulting from a single-branch approach , cancelling residual noise as common-mode. In this

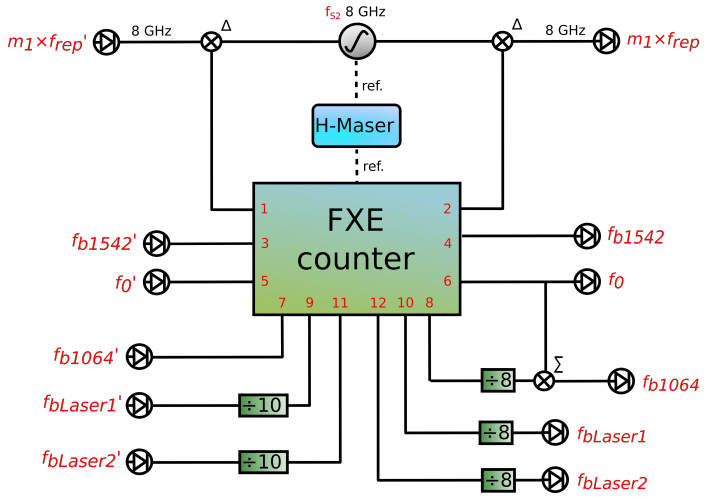

Fig. 5.2 Schematic of synchronous counting of all relevant beatnotes during one measurement by using only one counter (equivalent to using two synchronised counters)

work a multi-branch comb is used, giving the advantage of high SNRs by only loosely locking both, f_{rep} at 250 MHz and f_0 at 20 MHz, to the NPL maser HM3. The 4th harmonic of the repetition rate at around 1 GHz is taken and mixed down to about 20 MHz thus providing the error-signal for the phase-locked-loop (PLL) electronics of the Menlo comb system stabilising it to a (H-maser referenced) 20 MHz synthesizer. The maser-reference itself is a 10 MHz signal coming from the maser laboratory sent via RF cables (Andrew FSJ1-50A) and distributed by a low-noise 10 MHz amplifier. The repetition rate can be fine-tuned by changing the synthesizer frequency.

The error signal for the CEO-frequency locking is similarly generated by forming the difference between the detected f_0 and a H-maser referenced 20 MHz signal. The locking schemes are shown in figure 5.1. Locking of f_{rep} is achieved by acting upon a piezo actuator attached to one of the cavity mirrors and adjusting the cavity length. The stabilisation of f_0 on the other hand controls the pump laser power thereby changing the cavity dispersion.

5.2.4 Optical-To-Microwave Link

The transfer oscillator scheme as in [146, 148] combined with synchronous counting is used to eliminate the noise of the femtosecond lasers from all frequency ratio measurements, which generate the error signal for the universal synthesizer. The

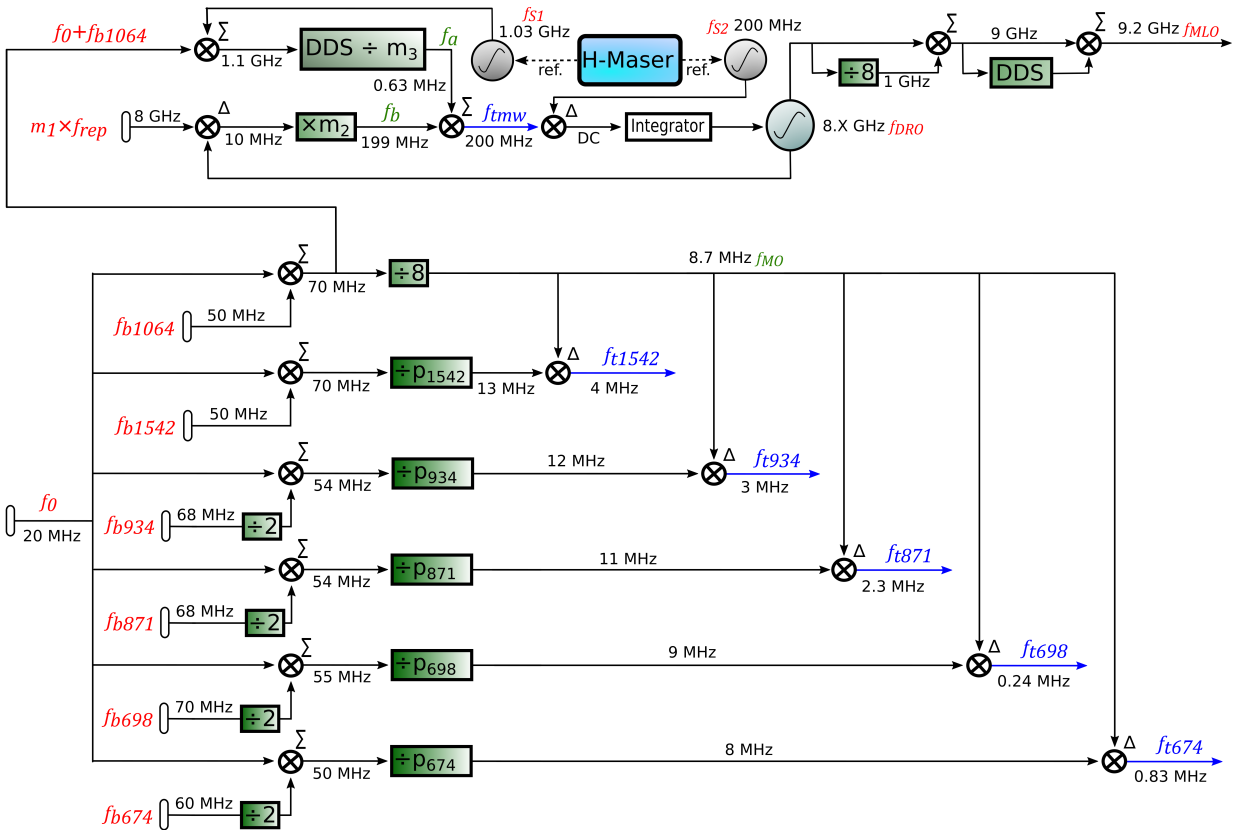

Fig. 5.3 Transfer beat generation scheme for optical-to-micrwave (top) and optical-to-optical (bottom) spectral purity transfer. The transfer uses a scheme similar to [146]. The microwave transfer beat is used to steer a dielectric resonator oscillator (DRO), whereas the slave-laser transfer beats provide an error signal to lock the optical lasers to the master oscillator.

transfer oscillator scheme works for both microwave-to-optical and optical-optical ratio measurements.

The optical-microwave link is not a part of this work, but for completeness is shortly described in the following:

The microwave-optical link is used to improve the Cs-fountain's microwave LO (local oscillator) by referencing it to the 1064 nm universal synthesizer laser. A sketch of the transfer-beat- and subsequent microwave-generation is given in figure 5.3.

At the start the mode number of the comb tooth, m, is separated into three factors m_i, with $i \in \{1,2,3\}$ and $m = m_1 m_2 m_3$. The notations used here are the same as in figure 5.3. Starting from the detection of f_{rep}, f_0 and f_{beat} of the 1064 nm master oscillator laser first the CEO-frequency-fluctuations-free signal f_0 + f_{b1064} is generated using a double-balanced mixer and then added to an H-maser referenced $f_{S1} = 1.03\,\text{GHz}$. The resulting 1.1 GHz signal is divided with a direct digital synthesizer by a factor (m_3) of around 1760 to less than 1 MHz:

$$f_a = \frac{1}{m_3}(f_0 + f_{b1064} + f_{S1}) \tag{5.2}$$

Meanwhile the 32nd (m_1) harmonic of the repetition rate f_{rep} (250 MHz) at 8 GHz is detected by sending a part of the laser output to a dedicated fast PD. This signal is subsequently mixed down to about 10 MHz with the 8 GHz f_{DRO} signal of the dielectric resonator oscillator (DRO), an adjustable microwave oscillator, and again multiplied by a factor (m_2) of 20.

$$f_b = m_2(m_1 f_{rep} - f_{DRO}) \tag{5.3}$$

In a separate channel the mixing with the DRO leads to a $\sim$2.8 MHz difference-signal that is counted on C4, serving as monitor signal for the repetition-rate.

Adding f_a and f_b one obtains the microwave transfer frequency:

$$f_{tmw} = m_2 m_1 f_{rep} + \frac{1}{m_3}(f_0 + f_{b1064}) + \frac{f_{S1}}{m_3} - m_2 f_{DRO} \tag{5.4}$$

But this again, from equation 5.1 and with f_{1064} the frequency of the master oscillator laser, is:

$$f_{tmw} = \frac{f_{1064}}{m_3} + \frac{f_{S1}}{m_3} - m_2 f_{DRO} \tag{5.5}$$

Looking at equation 5.5 the femtosecond laser noise does no longer appear in f_{tmw}. Since the DRO is supposed to steer the Cs-microwave generation the added maser signal f_{S1} in equation 5.2 does potentially degrade the signal stability, but its effect is reduced through the transfer beat by a factor of about $m_3/m_2 \approx 100$. With the Cs-fountain having Quantum Projection noise (QPN) limited stability of around $10^{-13}\ 1/\sqrt{\tau}$ this does not pose a serious issue.

But the question remains why the m_i are such "odd" values. In short this choice is not completely arbitrary, but governed by technical demands. The value m_1 is limited by the rise time of contemporary fast PDs (few hundred ps) and the choice of the DRO. The subsequent multiplication with m_2 is less of a concern, but led by the available low-noise electronics and narrow filtering. The m_3 value is then fixed by the previous choices.

Afterwards the problem arrives that with a convenient choice of $m_1 = 32$ and $m_2 = 20$ it follows that m_3 needs to be ≈ 1760. Dividing the incoming $f_0 + f_{beat} \approx 70\,\text{MHz}$ by this value would leave one with a very small RF frequency for f_a. But after the mixing to generate the transfer-beat f_{tmw} we have not only the sum of f_a and f_b, but also their difference which we then need to filter out. This filtering then also limits the bandwidth of our transfer-scheme (should be $\approx 1\,\text{MHz}$). Therefore in order to raise the frequency to a reasonable value the 1.03 GHz maser referenced signal is added before the input of the direct digital synthesizer (DDS).

In principle the optical-to-microwave link allows tracing of optical frequencies to the SI standard second, which might come in handy for future clock characterisations at NPL.

5.2.5 Optical Spectral Purity Transfer

The main purpose of the universal synthesizer is to transfer the superior spectral purity of the 1064 nm laser to a range of 4 different optical clock lasers and the NPL-SYRTE fibre-link laser. The transfer beat between the 1064 nm and any of the

other wavelengths can be considered as the beatnote between these lasers projected to the frequency of the 1064 nm laser, providing an easy to process error signal for the stability transfer.

The transfer-beat generation for all wavelengths (consider again 5.3) runs analogously, with the only exception being that the 1542 nm branch does not have a second harmonic generation (SHG) stage and therefore no divide-by-two unit in the signal path of the comb-cw-beatnote. The f_0 frequency is mixed with the beatnote of the 1064 nm laser and subsequently divided by 8 (for a more convenient scaling by the DDS of the other f_0 -free signals) , generating the f_0 -free f_{MO} frequency.

$$f_{MO} = \frac{1}{8}(f_{b1064} + f_0) = \frac{1}{8}(f_{1064} - m_{1064} \cdot f_{rep}) \tag{5.6}$$

,with m_{1064} the comb's mode-number of the universal synthesizer laser frequency f_{1064}.

Meanwhile the f_b of the other wavelengths is divided by two since their branches feature a SHG stage and therefore twice the carrier-envelope-offset appears in their f_b (exception: 1542 nm).

$$f_b = f_{laser} - (m_{laser} f_{rep} - 2f_0) \tag{5.7}$$

$$\frac{1}{2} f_b + f_0 = \frac{1}{2}(f_{laser} - m_{laser} f_{rep}) \tag{5.8}$$

This signal is then scaled by the mode numbers of 1064 nm and f_{laser} by a DDS an multiplied by a factor of 4 to correct for the signal divisions in the path. The difference of these frequencies and f_{MO} is then formed pairwise on individual mixers, giving the respective transfer beats:

$$f_t = f_{MO} - p_{laser}(\frac{1}{2}f_{beat} + f_0) \tag{5.9}$$

$$f_t = \frac{1}{8}(f_{1064} - \frac{m_{1064}}{m_{laser}}f_{laser}) \tag{5.10}$$

Again the contribution of the femtosecond laser is cancelled in the transfer beat, provided the f_0 and f_{beat} detection has sufficient bandwidth. The multiplication by the laser mode numbers is equivalent to forming a virtual beat between the two lasers with the same femtosecond comb mode number. The individual transfer beats are then sent to the optical clock / link -laser laboratories and there the lasers are feedback-stabilised on this signal.

The stability of laser 1 with respect to laser 2 is given by the ratio f_1/f_2 of their frequencies:

$$\frac{f_1}{f_2} = \frac{m_1}{m_2}\left(1 + \frac{8f_t}{f_2}\right) \tag{5.11}$$

5.2.6 Master Oscillator Cavity

The 1064 nm laser is locked to an ultra-stable cavity (see figure 5.4) by the well-known Pound-Drever-Hall (PDH) [119] method. The resonator consists out of a 28 cm square-shaped ULE spacer with silica mirrors and optically contacted ULE compensation rings. The dielectric coating is optimised for 1064 nm leading to a Finesse $F = 210000$. The cavity is suspended on four points inside a temperature-stabilised vacuum housing placed on an active-vibration-isolation platform.

The stability of the universal synthesizer laser locked to this cavity is about 5×10^{-16} at 1 s, determined by a three-cornered-hat measurement.

5.2.7 Feedback System

A quick calculation shows that already a fractional stability of the frequency f_2 (and therefore also of the repetition rate) of 10^{-12} is enough to supersede a stability of

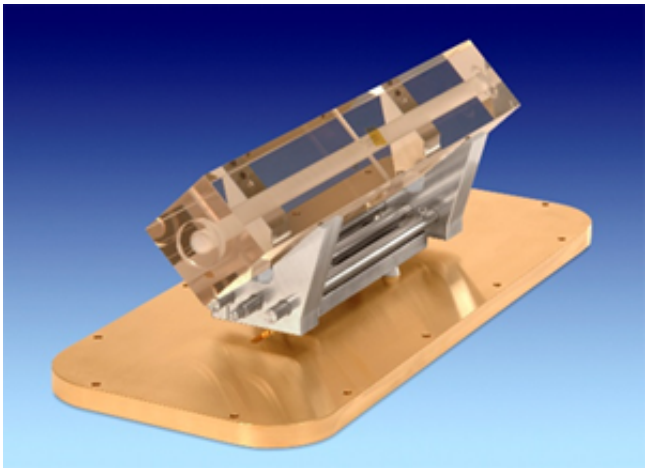

Fig. 5.4 The master oscillator reference cavity

10^{-19} in frequency-ratio measurements, since the second term in brackets in equation 5.11 is below 10^{-7} for our experiments.

All optical clock lasers have stabilisation systems of their own with inferior performance as compared to the 1064 nm cavity pre-stabilising the lasers to some parts in 10^{15} at 1 s, while also serving as back-up solutions in case of universal-synthesizer down-time. This given amount of pre-stabilisation is not necessary for the spectral purity transfer to work (the actual maximum bandwidth and thereby stability transfer limitation is given by the feedback-delay), but allows low-bandwidth feedback systems to be used.

The feedback error signals steering the clock / link- lasers are generated in their respective labs by mixing down to DC the individual transfer beats generated by the universal synthesizer with a H-maser referenced synthesizer frequency. Each signal is then fed to a PI(D) control of an AOM steering the laser's frequency, which has already been pre-stabilised by the respective stable cavity of the experiment. A sketch of the feedback system is given in figure 5.5.

5.2.8 Reference Comb NPL-FC3

The reference comb NPL-FC3 is an Er-doped fibre comb (as is the NPL-FC4) from Menlo Systems (FC-1500), with the difference that this comb features 3 separate branches as opposed to the full 7 branches of the universal synthesizer and it has been designed with a focus on transportability. Another important distinction is that

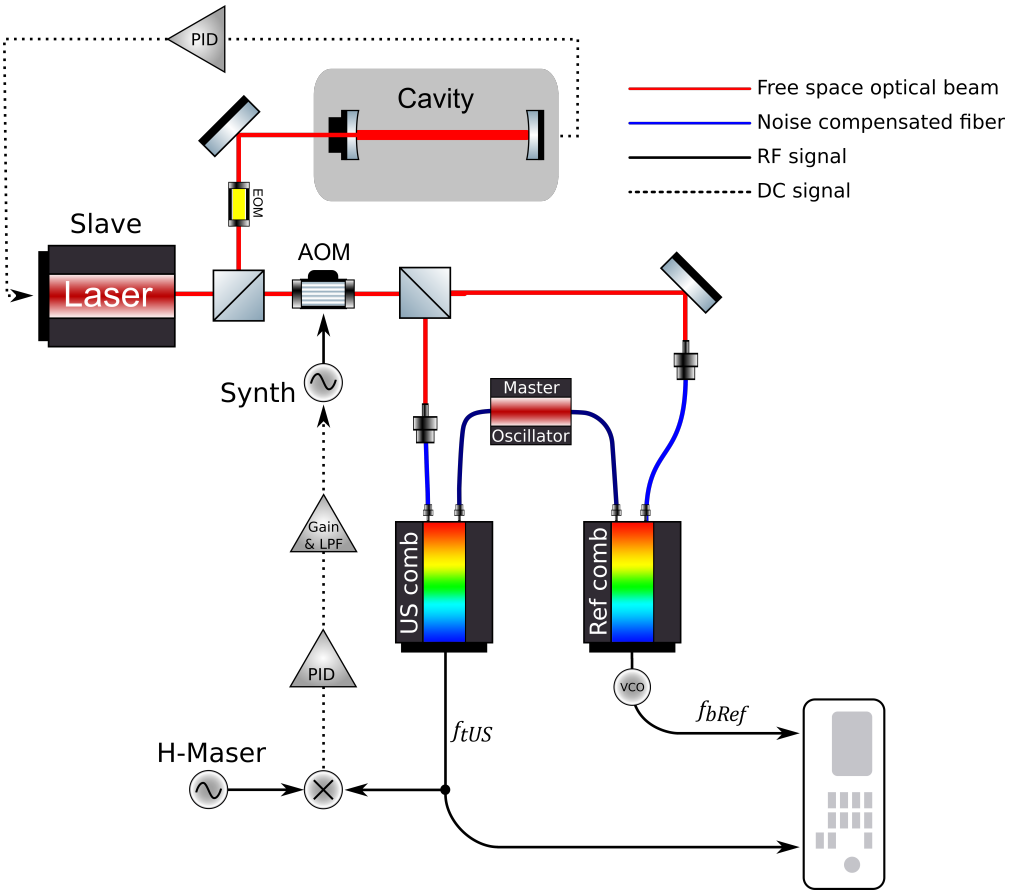

Fig. 5.5 The feedback system and the measurement scheme as in operation for the spectral purity transfer evaluation in this work. The slave laser is one of the atomic clock lasers (or the 1542 nm laser) and in a different laboratory than any of the two combs. The transfer beat f_t and the beatnote f_{bRef} are counted synchronously and the in-loop transfer, the comb agreement and the stability transfer performance calculated from these.

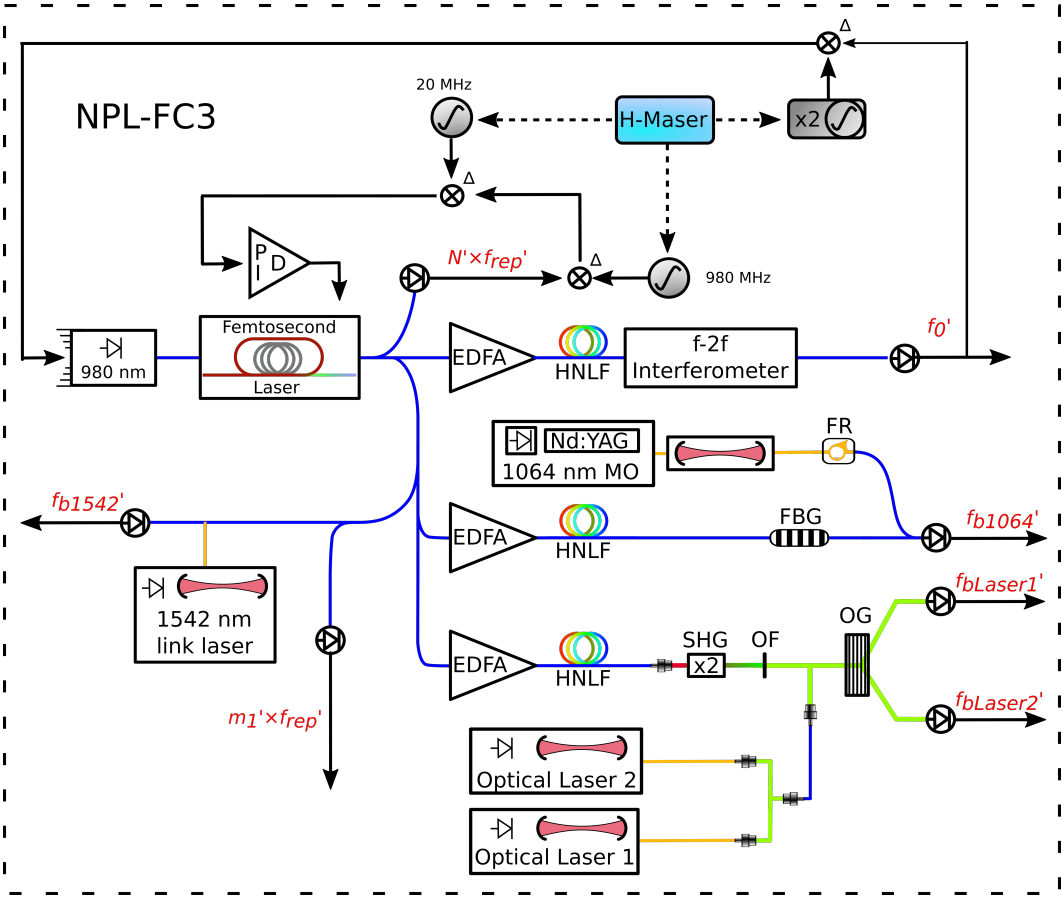

Fig. 5.6 Reference comb schematic. Note that the optical lasers are combined in the same optical fibre before sharing the same branch of the comb which, in combination with free-space beatnote detection, leads to rejection of the branch/pathlength noise as common-mode. FBG = fibre Bragg Grating, FR = Faraday-Rotator, OG= Optical Grating. Orange (blue) lines mark fibres with (without) fibre noise compensation. Green are free-space paths.

NPL-FC3 uses single mode fibres (SM), not PM as NPL-FC4. As a consequence the polarisation of the output spectrum is less stable, leading to a faster deterioration of beatnote-powers. Therefore during a measurement more care needs to be given to keeping the SNR of the comb and cw laser beatnote stable. The reference comb has already been described and evaluated in detail elsewhere, see [148], therefore the description here will centre on only the relevant attributes for our measurements.

The fundamental comb spectrum is centred around 1550 nm with 80 nm FWHM and a repetition rate of $f'_{rep} \simeq 100$ MHz and CEO frequency $f'_0 \simeq 20$ MHz. A sketch of the comb setup is given in figure 5.6. Similar to NPL-FC4 a small fraction of the femtosecond laser output is used to detect the 10th and 80th harmonic of the repetition rate, f'_{rep} , by fast PDs. Again the 1 GHz signal is processed in order to to lock the repetition rate to the H-maser and the other one for counting of f'_{rep} on the NPL-FC3 counter C3.

All three output branches of the laser feature their own EDFA and HNLF with the first branch broadening the comb output to span one octave, realising the Menlo Systems f-2f interferometer for detection of f'_0 . The second branch (from top) is dedicated for measurements in the near-infrared region (1 to 2 μm) and the third one, having in addition to the 2nd branch also a SHG element (PPLN crystal) inside, for detection of 500 to 1000 nm wavelengths. This means that all frequency ratios between the optical atomic clock lasers can be performed with the optical stage in a single-branch configuration where they are ultimately limited by the electronic noise floor at around $1.5 \times 10^{-17}\ \tau^{-1}$, assessed in a previous measurement campaign.

Frequency ratios to the 2 infrared wavelengths, especially any ratio measurement including the master oscillator laser itself is in addition affected by pathlength (comb-branch) noise (e.g. fibre noise inside EDFA and HNLF) and therefore most likely dominated by it. Locking of f'_{rep} and f'_0 is done analogously to NPL-FC4 by referencing the detected beatnotes to H-maser stabilised microwave signals (locking the 10th harmonic of f'_{rep} at 1 GHz and referencing f'_0 to about 20 MHz), exploiting the same 10 MHz H-maser signal as with the universal synthesizer.

For ratio or absolute frequency measurements f'_{rep} , f'_0 and f'_{beat} are recorded with the C3 K+K FXE counter referenced to the same H-maser as C4. Due to the single-branch setup the SNR of the optical beatnotes are smaller (here always given within a bandwidth of 100 kHz), around 30 dB, than in the case of NPL-FC4 (ca. 40 dB). In order to improve the reliability of the counting we use tracking oscillators

with high bandwidth (500 kHz) locking unto the beatnotes and subsequent division and counting of the tracking oscillators' outputs.

As in the case of the universal synthesizer noise introduced to any frequency ratio measurement by uncompensated pathlength fluctuations not common to the comb- and cw-laser-light poses a main performance limitation. The 1542 nm radiation is directly heterodyned with the output of the femtosecond laser, whereas the 1064 nm laser is routed through the infrared branch (see figure 5.6) and all the other wavelengths taking the route of the visible branch. The fibres inside the EDFA, HNLF and the free-space SHG stage are here common to all wavelengths of the optical atomic clocks, cancelling as common-mode, but so present a limitation for frequency ratios with the 1064 nm laser, since the fibres of the 2 branches are uncommon; the same is true for 1542 nm .

The pathways of the beatnote detection are again individually discerned in the following. The 1064 nm , 1542 nm , 934 nm , 934 nm , 698 nm and 674 nm lasers are sent to the reference comb via noise-cancelled fibre-links. The fibre noise cancellation for the in-fibre 1542 nm cw-light at NPL-FC3 is until the beat-detection unit, leaving only a few cm of uncompensated fibre inside the BDU not common to cw- and comb-light. The 1064 nm laser on the other hand exploits the back-reflection of the detection photodiode (again a fibre-based BDU), leaving only a few cm of uncommon comb-path.

All other optical wavelengths are sent to a fibre noise compensation stage situated outside the comb's enclosure and subsequently routed through a common fibre ($\approx$ 1 m) and another 1 m of free-space path inside an acrylic enclosure before being overlapped with the comb-light and detected on free-space PDs. Therefore in any frequency-ratio between the 934 nm , 934 nm , 698 nm and 674 nm lasers the path-noise (almost) completely cancels out, whereas for ratios with the 1064 nm or 1542 nm laser the aforementioned not-compensated path is added to the optical (and infrared) branch noise.

Much of the environmental noise is connected to Doppler noise and therefore scales with the frequency of the light. This can directly be seen from the formula of the linear or relativistic Doppler effect (equation 1.36). The noise is always the same in fractional units, regardless of the carrier frequency. Therefore it cancels out in the ratio between two frequencies, but not in their sum or difference. A small

residual optical path noise might origin from dispersion effects within the fibre (and to a much lesser degree in the free-space region).

In consequence frequency ratios between the optical atomic clock lasers are done in a single-branch configuration, whereas all other measurements are performed in a multi-branch way, meaning that only in the first case can one be sure that the NPL-FC3 comb is not limiting the evaluation of the spectral purity transfer in NPL-FC4.

5.2.9 Comb Synchronisation

The scope of this work is a stability transfer between optical wavelengths using the frequency comb as a transfer oscillator. The way to measure the accuracy of the comb is by looking for any offset between frequency ratios measured with the NPL-FC3 and NPL-FC4 comb. This difference between the two combs, described as "comb agreement" gives then the combined limit of frequency-ratio measurement stability and accuracy of the two combs.

The actual accuracy of the optical frequency ratios, hidden in the transfer-beat, is not central to achieving a good stability transfer, but nevertheless needs to be examined in order to give a complete characterization of the universal synthesizer and to avoid systematic errors going unnoticed.

In order to exclude from this measurement the optical clock lasers and to see only offsets that originate from the comb itself it is of vital importance to synchronise all measurements. This is ensured by synchronising the two counters in the two labs to the UTC (NPL). Alternatively it is possible to count all beatnotes, f_0 , f_{rep} , f_{beat} , f'_0 , f'_{rep} , and f'_{beat} on the same frequency counter C4 (the counter of the reference comb). The long signal route (ca. 50 m) from the universal synthesizer lab to C4 does not pose a limitation, since the counter gate time is around 1 s. No significant difference in the results between these two approaches was observed.

5.3 Spectral Purity Transfer

With the stability transfer at all wavelengths in place the performance of the universal synthesizer's spectral purity transfer can be evaluated. There are three relevant

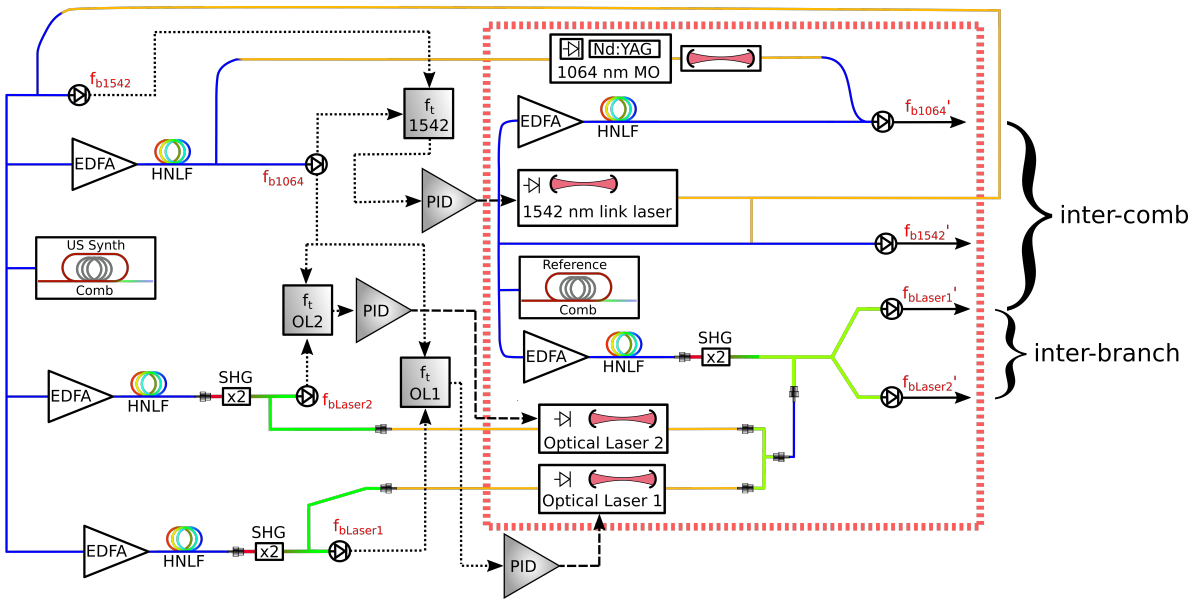

Fig. 5.7 Schematic of the comb branches (EDFA and HNLF) as well as optical/electronic paths introducing noise into the stability transfer evaluation. The red box signifies the reference comb, connections are: blue = uncompensated fibre, brown = compensated fibre, green = free-space

attributes to look at, which are a) electronic noise, b) systematic locking errors and c) the (optical pathlength and amplifier) noise introduced by the branch of the stabilised and the 1064 nm laser.

As a first estimate of the stability transfer a direct comparison between the 1064 nm and each slave laser as a virtual beat on the reference comb gives the inter-comb noise (meaning that the noise of both multi-branch combs, NPL-FC3 and NPL-FC4 is added). A scheme of the measurement setup is given in figure 5.7, showing how the noise of the reference-comb-branches and uncompensated fibre-paths is introduced into the spectral purity transfer evaluation.

For these measurements the reference comb detects a virtual beat between the 1064 nm laser and the slave lasers, revealing the phase-lock stability, which we take as the stability of the frequency ratios between the 1064 nm and the slave lasers. Since the reference comb and the universal synthesizer are in different laboratories with quite disparate temperature control systems, minimal correlated noise can be expected.

The next step then follows as an evaluation of the inter-branch noise of the universal synthesizer comb, which is the ultimate limitation to the spectral purity

transfer. This is done through a series of optical frequency ratio measurements of the stabilised slave lasers. The phase-difference is again measured on the reference comb, but with the branch-noise of NPL-FC3 common to both wavelengths (and thereby cancelled)

On the reference comb NPL-FC3 the 1542 nm and 1064 nm radiation is always available and its beatnote with the comb recorded, whereas for the clock lasers we can only evaluate two at the same time, since the EDFA and HNLF in their branch is shared between them, reducing the available light power. The stability of the transfer is the stability of the frequency ratio between 1064 nm and the wavelength under investigation. We choose to calculate the normal Allan deviation for all the measurements that follow, since it allows to compare the results directly to optical clock stabilities.

This assessment of the spectral purity transfer suffers from one slight complication: The reference comb has multi-branch noise introduced in every comparison of the 1064 nm laser to any of the other wavelengths, meaning that we are not able to separate this (potentially dominating) noise from the residual inter-branch noise introduced into the stability transfer by NPL-FC4 (the latter is likely the main limitation of the stability transfer).

But thankfully this problem does not exist for the inter-branch noise measurements. We take the atomic clock lasers and compare them pairwise (in a single-branch configuration) on the optical branch (see figure 5.7, inter-branch) of NPL-FC3. By measuring the frequency ratios between two optical slave lasers we can therefore determine the ultimate stability limit of the spectral purity transfer with the noise of the reference comb and its uncompensated fibre paths in common-mode and the reference comb's ratio stability limit being essentially electronic noise.

Confidence in the assumption of the absence of common noise introduced in both slave lasers is generated by a sequence of measurements, taking the frequency ratios of the lasers as an "unbroken chain" starting with the 674 nm to the 698 nm , the 698 nm to the 871 nm and finally the 871 nm to the 934 nm ratio. Since the laser feedback system for each laser is uniquely set up and the branches of NPL-FC4 for 674 nm and 698 nm in a common enclosure and for 871 nm and 934 nm in a second one, noise due to environmental changes should be detected.

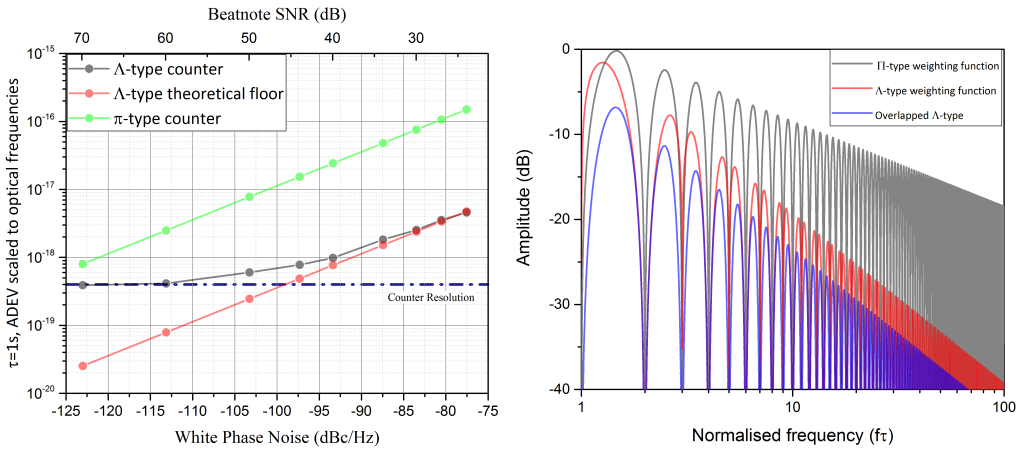

Fig. 5.8 Left: Comparison of the counted dummy-signal 1 s Allan-deviation (RF signal scaled to optical frequencies) in high-resolution counting mode (black) to theoretical low-bandwidth (100 Hz, Λ-mode) white phase noise counting (red) and Π-mode (bandwidth 100 kHz) counting of the same signals (green) Right: Sensitivity function of different counter operation modes

5.3.1 Electronic Noise Floor and Frequency Ratio Measurement

When evaluating the ratio-measurement limitations in section one would like to assume that the electronic noise of the beatnote measurement itself is not a limiting factor. Electronic noise appears as white phase noise in frequency measurements. A certain SNR therefore corresponds to one level of white phase noise. Consequently the higher the SNR the lower the phase-noise limit of the beatnote detection (counting) process.

In order to determine the white-phase noise contribution we compare the beatnotes of the individual cw lasers with the combs to calculated stabilities from the white phase noise levels of dummy signals. As a preparation step we first measure the stability limit of the counter C3 (C4 is an identical model) for different SNRs and compare it to the corresponding calculated white-phase noise limited stabilities. Results are given in figure 5.8.

The counting process for the dummy signals is dominated by white phase noise for short and medium integration times as can be seen by the $1/\tau$ behaviour of the Allan deviation and with the levels in agreement to the calculations.

With f_H the detection bandwidth, the white phase noise floor P_{noise} of a signal (with signal strength P_{signal}) is given by:

$$10log(P_{noise}) = 10log(P_{signal}) - 10log(SNR) - 10log(f_H) \tag{5.12}$$

And the stability in terms of the Allan-variance follows as:

$$\sigma^2(\tau) = P_{noise}\frac{3f_H}{4\pi^2\tau^2} \tag{5.13}$$

The observed SNRs of the beatnotes on the combs (27 dB to 40 dB in 100 kHz) correspond to white phase noise floors of $-81\,\frac{\mathrm{dBc}}{\mathrm{Hz}}$ and $-93\,\frac{\mathrm{dBc}}{\mathrm{Hz}}$ and measured electronic noise limited stabilities (bandwidth 100 Hz) are $4\times10^{-18}\tau^{-1}$ to $1\times10^{-18}\tau^{-1}$, well below the actual measured inter-branch and inter-comb stabilities (see section 5.3.3).

The stability assessed by the counter is showing a noise floor, caused by its resolution limit, of 4×10^{-19} and therefore deviates from the calculated white phase noise stabilities for SNRs of more than 35 dB.

The counter used here features a high-resolution counting mode in which multiple averages are arrayed to form a Λ-shaped weighting function (the bandwidth is 100 Hz, gate time 1 s). The differences between the Π- and Λ-weighting functions and their relation to the Allan variance are dealt with in detail in [241] and [223]. During one single gate time, τ, many such measurements are overlapped to again approximate the normal Allan-deviation as in Π-counting. This has the effect of suppressing noise at Fourier frequencies of harmonics of the reciprocal gate time while giving out the normal Allan variance just like a Π-counter (same τ^{-2} behaviour for white phase noise instead of τ^{-3} as in [241]).

5.3.2 Frequency Ratio Measurement Limit

In this part at first the frequency-ratios between the 1064 nm and the slave lasers on the universal synthesizer comb itself (figure 5.9) are examined. These values here, however, do not represent the actual stability transfer, since the stabilisation does not see the inter-branch noise added to the individual lasers before they interfere. Therefore they represent “in-loop” measurements.

The observed SNRs of the beatnotes on the universal synthesizer comb (typ. 30 to 35 dB for the slave lasers and 40 dB for the 1064 nm master oscillator) correspond to

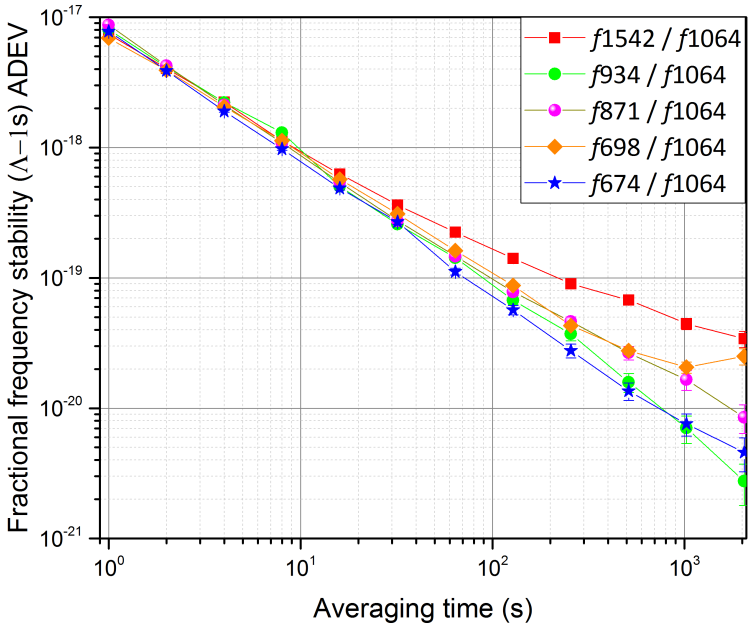

Fig. 5.9 Universal synthesizer in-loop residual instabilities. The slopes follow a $\frac{1}{\tau}$ behaviour, as expected for white phase noise.

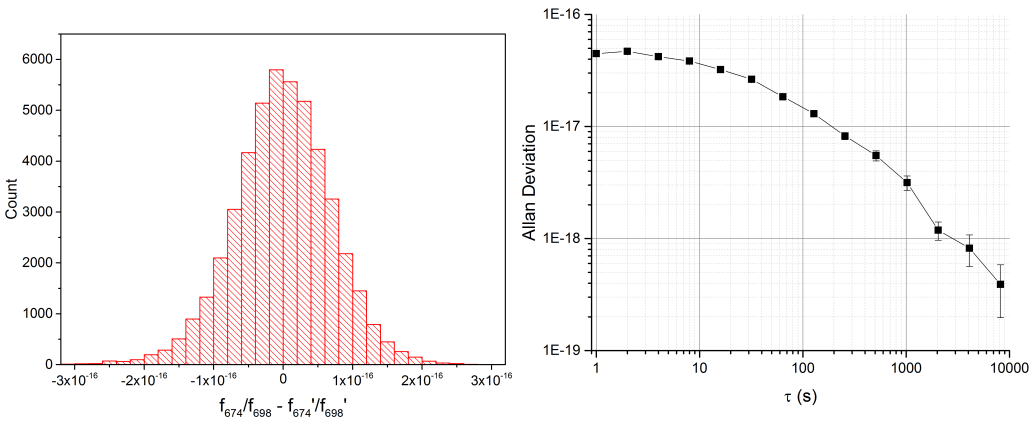

Fig. 5.10 Left: accuracy histogram and Right: stability of the same comb agreement measurement,the stability equals that of the 674/698 frequency ratio by NPL-FC3

white phase noise floors between $-83\,\mathrm{dBc/Hz}$ and $-93\,\mathrm{dBc/Hz}$ and corresponding electronic counter-stability limits from about $3\times10^{-18}\tau^{-1}$ to $1\times10^{-18}\tau^{-1}$ (see section 5.3.1). The residual instability of the virtual beatnote between a pair of locked lasers is around about $7\times10^{-18}\tau^{-1}$ (precise value depending on the SNRs). The exact values for each ratio-measurement are given in figure 5.9.

One can therefore see that the residual difference between the lasers on the universal synthesizer is only limited by the white phase noise of the beatnotes as the lasers are locked to the master oscillator and the femtosecond laser noise perfectly cancelled. A long term drift appears between the lasers starting at about 1000 s as a change of slope in the stability curves due to changes of SNR caused by unstable cw laser power (especially in the case of 698 nm), but also, albeit to a much smaller margin, by slight errors in the femtosecond laser cancellation caused by the finite DDS resolution (see also[148]).

In order to assess the accuracy of all ratio measurements, the same frequency ratio is measured pairwise between the various wavelengths on both combs simultaneously (using the same counter, C4, or synchronised counters, with 1 s gate time). The difference between the frequency ratios gives an ultimate accuracy limitation to any measurement with these two combs.

The calculated difference between the comb measurement of the ratios of the 698 nm and 674 nm lasers is shown in figure 5.10 as an example. The comb agreement accuracy for all measurements is given in table 5.1.

Table 5.1 The agreement between the two combs for all measured frequency ratios. The residual agreement uncertainty is only limited by statistics due to measurement time.

ratio	accuracy	ratio	accuracy
$\frac{f1542}{f1064}$	3.1×10^{-18}	$\frac{f934}{f871}$	5.7×10^{-19}
$\frac{f934}{f1064}$	9.7×10^{-19}	$\frac{f871}{f698}$	8.7×10^{-19}
$\frac{f871}{f1064}$	9.7×10^{-19}	$\frac{f698}{f674}$	3.9×10^{-19}
$\frac{f698}{f1064}$	1.1×10^{-18}	$\frac{f674}{f1064}$	3.8×10^{-18}

The observed SNRs of the beatnotes on the reference comb (27 dB to 35 dB) show white phase noise floors of $-81\,\frac{\mathrm{dBc}}{\mathrm{Hz}}$ and $-88\,\frac{\mathrm{dBc}}{\mathrm{Hz}}$, respectively, and corresponding stabilities are $4 \times 10^{-18}\tau^{-1}$ and $2 \times 10^{-18}\tau^{-1}$, well below the observed residual stability. This means the frequency ratios are not limited by electronic noise but rather from stability transfer errors resulting from inter-comb or inter-branch noise between the 1064 nm and the slave lasers, since the measured transfer-stabilities all lie above these values. The mismatch between SNR and phase-noise floor scaling is caused by the counter resolution.

5.3.3 Spectral Purity Transfer Evaluation

Figure 5.11 shows the inter-comb frequency instability between the 1064 nm master oscillator and the slave lasers as obtained by the reference comb. The stabilities of the spectral purity transfer achieved across all wavelengths used exceed the performance of the master oscillator cavity by factors of 5 to 10, showing that the comb poses no limitation to the stability transfer at present.

The stabilities achieved for the 871 nm and 934 nm radiation are approximately 5×10^{-17} for 1 s to 3 s, reaching 8×10^{-19} after about 2000 s. Possible limitations for the measured stability here are inter-branch noise between the 1064 nm and 871 nm and 934 nm branches on the two combs as well as uncompensated fibre noise. In both labs all wavelengths use phase-noise cancelled fibres for radiation dissemination until close before the beat-note detection apparatus (see figure 5.7), leaving about

2 meters of uncompensated fibre in each lab for each wavelength in addition to the fibre noise within the various comb-branches and the beat-detection units.

The electronic noise issue is addressed in section 5.3.1 and ,as demonstrated there, is irrelevant for the SNR levels of all beats (between 27 dB and 40 dB on either comb).

The 698 nm and 674 nm display a noise starting at 8×10^{-17} and 1×10^{-16} respectively. The higher values in comparison to the 871 nm and 934 nm are attributed to:

1. higher residual fibre noise along these cw laser paths in the laboratory of the reference comb, since the inter-branch measurements using these two wavelengths show better results (see 5.12), as far as the difference between 698 nm and 674 nm is concerned.

2. different scaling of the branch noise in the transfer-beat generation of the combs. In the transfer-beat (or software frequency-ratio calculation) the noise on the 1064 nm laser beatnote is scaled by a factor m_{slave}/m_{1064} to match the femtosecond-laser noise at the slave-laser's frequency. But the same happens to the branch-noise of the master oscillator, leading to an inflation of the inter-branch noise (including residual uncompensated fibre-noise, especially relevant on NPL-FC3). This multiplication factor is about 1.3 in regard to a 698 nm / 1064 nm ratio measurement versus a 871 nm / 1064 nm ratio measurement, agreeing with the short-term stability difference seen between those two frequency ratios.

The 1542 nm laser spectral purity transfer differs from the other slave lasers in so far that on the side of the universal synthesizer as well as the reference comb the output of the mode-locked laser is directly heterodyned with the 1542 nm radiation, avoiding any noise introduced by an EDFA or HNLF, but with the limitation of the 1064 nm branch noise still present. The residual stability limit of 1.5×10^{-16} at 1 s followed by a noise bump until about 10 s is most probably due to uncompensated fibre noise on the side of the 1542 nm laser laboratory at the time of these measurements.

As next step the inter branch noise is assessed by pairwise comparisons of slave lasers locked (virtual beatnotes, in software processing) to the master oscillator by the universal synthesizer comb. With regard to the inter-comb comparison the slave-slave laser stability evaluation here has the advantage of common-mode branch-

and fibre-noise on the side of the reference comb (single branch configuration). The stability transfer evaluated by these measurements therefore represents the actual inter-branch noise on NPL-FC4 and thereby also the stability transfer from the master oscillator more closely. The stabilities of these ratios are depicted in figure 5.12.

At 1 s the value is now in the $3-4\times10^{-17}$ range, reaching below 1×10^{-18} after about 500 s. For averaging times τ between 10 s and 300 s the noise behaviour resembles a $7\times10^{-17}\tau^{-1/2}$ slope. But at long timescales (beyond 500 s) the noise averages down faster than a $\tau-1/2$ slope, reaching 3.6×10^{-19} after 2000 s. This indicates excessive noise at short timescales.

With the branch and fibre noise at the side of the reference comb common to both slaves, the residual noise levels are traced to remaining uncompensated fibre noise and branch noise of the universal synthesizer. For these measurements the 871 nm and 934 nm beatnote detection- and branch-setups were still identical to the 698 nm and 674 nm ones.

The slave laser beatnote detection on the universal synthesizer described above is provided by commercial Menlo Systems beat-detection units featuring all-fibre paths to the photodiode. Despite of careful engineering these, just as the EDFA and HNLF, introduce fibre noise. In order to determine the origin of the remaining noise and to improve upon the spectral purity transfer, the 871 nm and 934 nm branches were both changed by eliminating the residual uncompensated fibre path and using free-space beatnote detection.

Thus not only is the fibre noise of the fibre beatnote detection systems avoided, but also became it possible to move the fibre noise compensation retro-reflector inside the comb's acrylic enclosure, leaving no more uncompensated fibres other than of the EDFAs and HNLFs in the path of the comb and cw laser light (see also figure 5.1). the exact laser paths are shown in figure 5.13. SNRs of 30 dB to 35 dB (bandwidth as usual 100 kHz) were achieved with the universal synthesizer in the free-space configuration. The fractional frequency stability transfer limit is now as low as 1.5×10^{-17} at 1 s. For timescales between 10 s and 500 s it follows a $3.5\times10^{-17}\tau^{-1/2}$ curve, averaging down steeper than $\tau^{-1/2}$ for $\tau\geq1000$ s and reaching 2.7 parts in 10^{19} after 2000 s. This is demonstrating significant improvement over the previous values.

This improvement is attributed to the reduced inter-branch noise, leaving no uncompensated fibre-paths and only short uncompensated uncommon free space

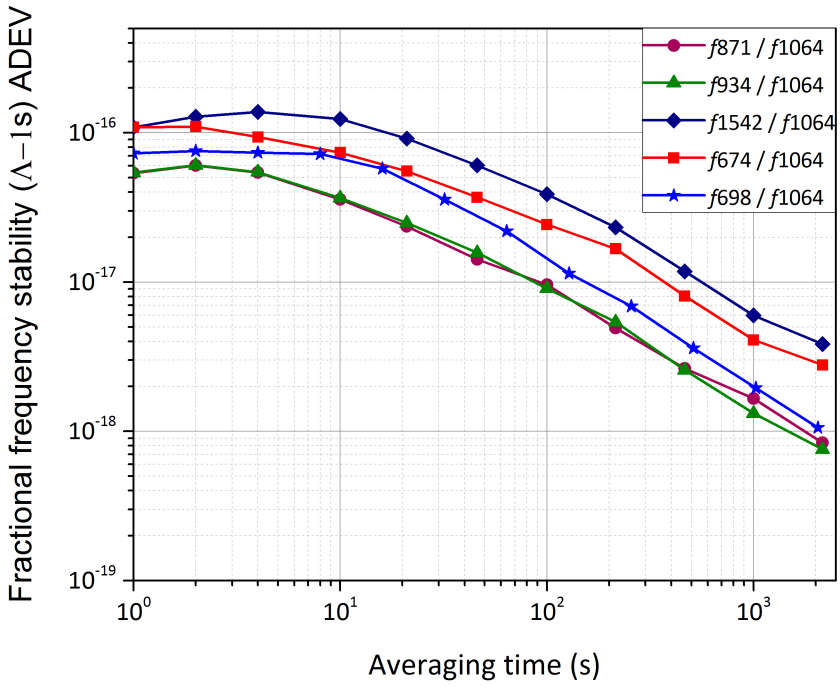

Fig. 5.11 The inter-comb stability transfer evaluation for all slave lasers. The differences in short-time (< 10 s) stabilities can be attributed to scaling effects (see text), whereas the long-term shape (> 10 s) appears to be governed by residual fibre noise.

pathlengths between the individual cw lasers and comb light. With the perspective of implementing free-space beatnote detection on all other branches (mixing each slave-laser with the 1064 nm branch) this represents the best estimate of the performance limitations to NPL's universal synthesizer system.

The residual noise level originating from uncompensated fibre paths and the fibre amplifier is uncommon between the slave lasers and the master oscillator. Therefore it is also uncorrelated. Consequently a scaling of the noise and stability with the slave-to-master laser frequency ratio can be expected (reversing the argumentation for Doppler noise in section 5.2.8). Taking the $f871/f934$ ratio as norm, the maximum factor appearing in the stability transfer would be the $f674/f1064$ one, giving an estimated relative stability scaling of 1.47.

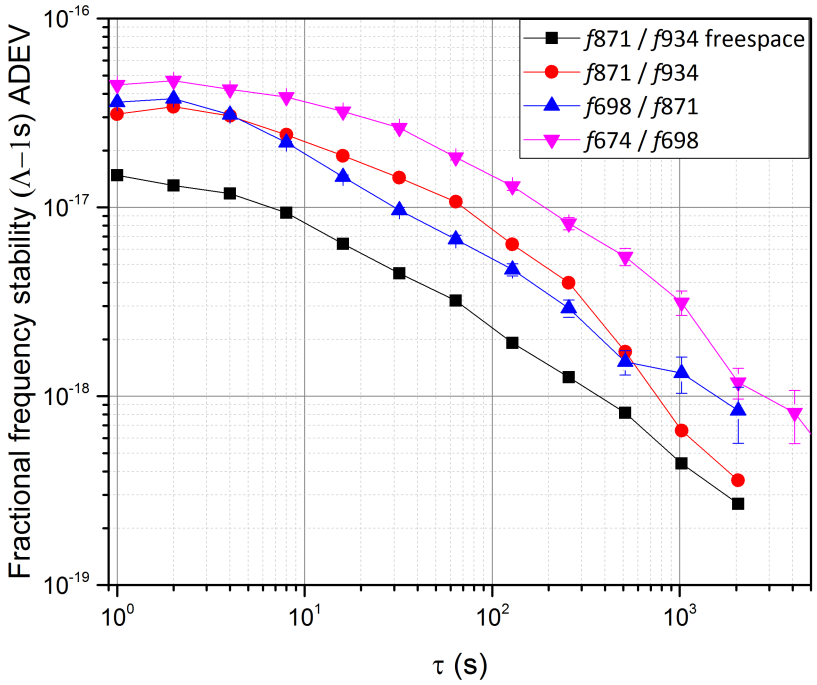

Fig. 5.12 The inter-branch noise measured by pairwise comparison of slave lasers, note the improvement in the stability by changing the beatnote detection from in-fibre to the free-space system.

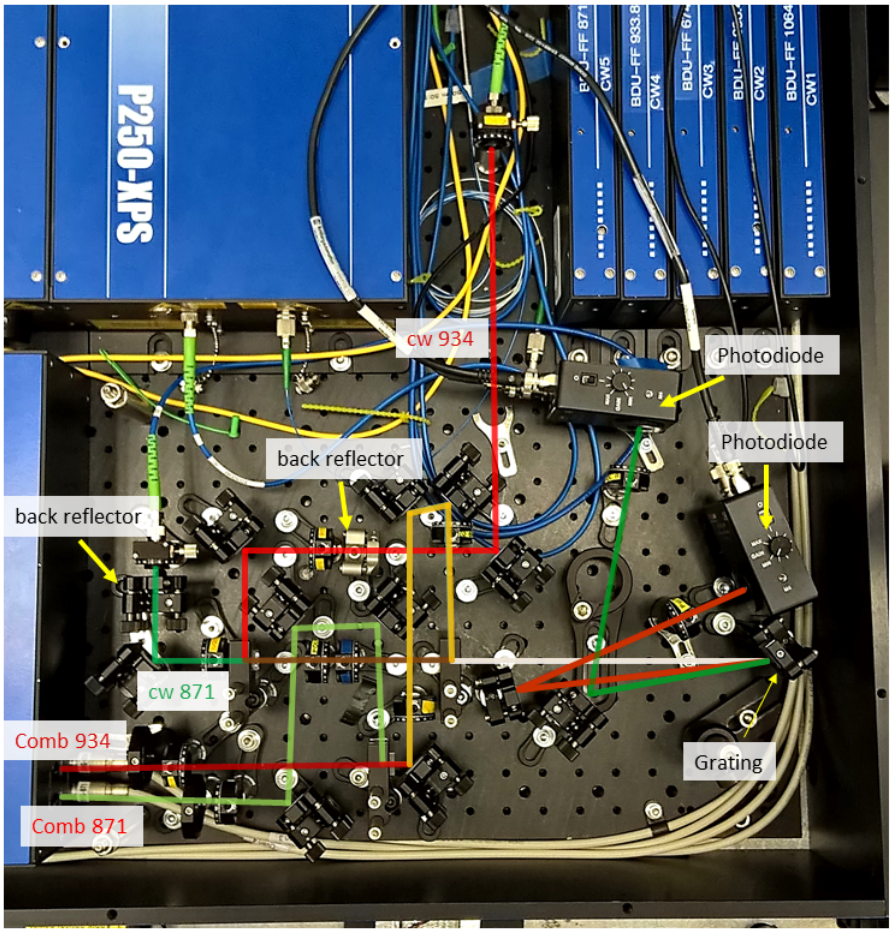

Fig. 5.13 The free space beatnote detection system. The laser paths are colourised. The overlapped cw lasers are depicted brown, the overlapped combs orange and all beams together white.

5.4 Discussion

One enormous obstacle to improving modern atomic clocks is the stability of the spectroscopy laser. The universal synthesizer concept could be a key part in overcoming this limitation. The key question therefore is whether the universal synthesizer can support a transfer of the spectral purity from the master oscillator to the slave lasers at a level excelling even the best current optical cavities. Optical cavities usually maintain their best stability (currently about 5×10^{-17}) only for timescales up to a few seconds. For longer timescales the stability is compromised by a linear drift. Therefore the stability transfer performance between 1 s and 100 s is of most interest here.

Figure 5.11 displays that all measurements show a pronounced instability bulge, typical of uncompensated fibre noise, reaching from a few seconds to about 10 s for the 698 nm/1064 nm and 100 s in case of the 1542 nm/1064 nm measurement. The long-term behaviour resembles a τ^{-1} slope for the 871 nm , 934 nm and 698 nm lasers and a slightly gentler slope for the other wavelengths. This resembles electronic noise, indicating that the limitation to these measurements is really given by the initial noise bulge. The short term stability of all inter-comb measurements is close to or below the best available optical oscillators. The presence of excess noise on the side of the reference comb compromising some of these measurements is upheld by the contrast of the inter-branch results.

Also the inter-branch noise evaluations, meaning optical slave lasers frequency-ratio-stabilities, feature a deterioration due to a cove in case of the 674 nm/698 nm and the 871 nm/934 nm measurements (with the later being the one with in-fibre beatnote detection), which is now really small in amplitude, but extended in time. In case of the 698 nm/871 nm ratio only a plateau from 1 s to 2 s can be seen, whereas the free-space 871 nm/934 nm ratio-measurement features a much less pronounced stability deterioration up to 4 s. The long-term slope is right between a $\tau^{-1/2}$ of white-frequency(e.g. optical pathlength noise) and τ^{-1} (e.g. electronic noise) type of behaviour. The inter-branch noise presented here exceeds by far even the best current stable laser systems based on ultra-stable cavities for all wavelengths under investigation and is also able to support optical frequency ratio measurements including state-of-the-art optical lattice clocks .

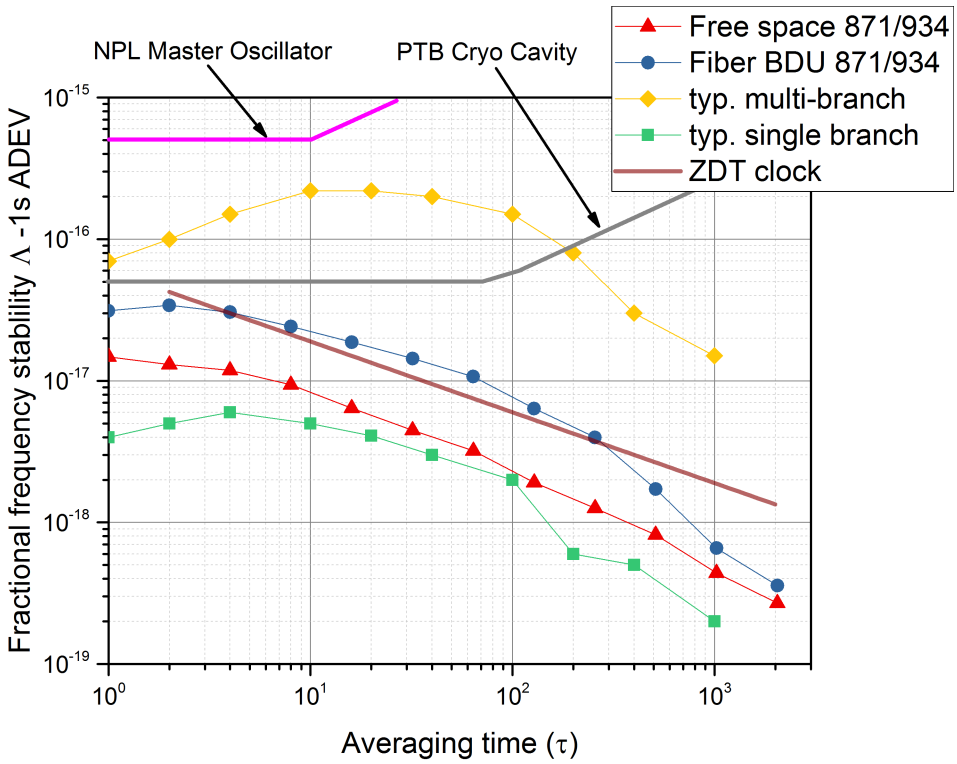

Fig. 5.14 Comparison to multi-branch (yellow diamonds) and single-branch (green cubes) results in [228]. The blue circles and red triangles are the stability evaluations of the inter-branch noise between the 871 nm and 934 nm branch with in-fibre and freespace beatnote detection, respectively. The stability of the current master oscillator cavity is shown (purple) and also the state-of-the-art performance of ultra-stable cavities [21] (black) and of an ensemble of optical lattice clocks [49] (brown) as future demands.

The residual noise can mostly be attributed to uncompensated fibre paths, as the improvement with the 871 nm/934 nm free-space beatnote detection shows, which also included the elimination of the remaining 1 m uncompensated fibre between the fibre noise cancellation back reflector and the frequency comb.

All DDS used for this setup support a 48-bit frequency tuning word, resulting in a systematic error at the 10^{-21} level [148], posing no limitation at the current level.

The comparison to previous published values on multi-branch [231, 227, 232] and single-branch [228] combs shows that a multi-branch universal synthesizer is able to achieve performances approaching a single-branch comb if care is taken to reduce uncompensated pathlength-noise.

5.4.1 Prospects

We have evaluated the spectral purity transfer of NPL's universal synthesizer comb from the ultra-stable master oscillator cavity to as many as five slave lasers. Our method of evaluation for frequency ratio measurements with a 2nd comb suffered from multi branch noise on the side of the reference comb introduced in the case of measurements involving the 1542 nm or 1064 nm lasers. Since the NPL-FC4 and NPL-FC3 combs are not identical in the way their branches are set up (most importantly the amount of residual out-of-loop fibre in the cw light path is generally not equal), the stability transfer assessments involving these wavelengths cannot be equally attributed to both combs and therefore overestimates the instability level.

This is not the case for the inter-branch noise evaluation conducted as a chain of measurements involving only the slave lasers. No noise correlation was found between the optical slave lasers situated in the same metallic enclosures (934 nm and 871 nm , 698 nm and 674 nm), affirming the assumption that the relative stability between those slave lasers is equal to their individual stability against the master oscillator.

A more complete picture and a further affirmation of the achievable stability transfer would be obtained by completing the chain with a measurement of the 934 nm/1064 nm inter-branch noise. This measurement would need to be conducted in a single-branch fashion on the infrared branch of the reference comb, demanding some changes to the current setup that uses in-fibre beatnote detection on this branch. The layout would need to be improved including a free-space detection scheme.

The reduced inter-branch noise for the 871 nm/934 nm-freespace measurement calls for a change of the other remaining beatnote detection units to free-space systems and including the elimination of the 1 m uncompensated fibre in the path of the cw light. Further improvements might include reducing the environmental noise on the comb-branches by improving acoustic/vibrational and thermal shielding or actively cancelling these perturbations.

Nevertheless in this work it has been demonstrated that a multi-branch comb in connection with the transfer-oscillator scheme is able to transfer the fractional stability of even the most advanced contemporary cavities to a wide range of slave lasers on multiple comb-branches simultaneously without deterioration of the spectral purity transfer.

References

[1] Ichiro Ushijima, Masao Takamoto, Manoj Das, Takuya Ohkubo, and Hidetoshi Katori. Cryogenic optical lattice clocks. *Nat Photon*, 9(3):185–189, March 2015.

[2] BIPM. *The International System of Units (SI)*. BIPM, 8th edition, 2006.

[3] Zeb W. Barber. *Ytterbium Optical Lattice Clock*. PhD thesis, University of Colorado, 2007.

[4] N. D. Lemke, A. D. Ludlow, Z. W. Barber, T. M. Fortier, S. A. Diddams, Y. Jiang, S. R. Jefferts, T. P. Heavner, T. E. Parker, and C. W. Oates. Spin-$1/2$ optical lattice clock. *Phys. Rev. Lett.*, 103(6):063001, Aug 2009.

[5] Masao Takamoto, Ichiro Ushijima, Manoj Das, Nils Nemitz, Takuya Ohkubo, Kazuhiro Yamanaka, Noriaki Ohmae, Tetsushi Takano, Tomoya Akatsuka, Atsushi Yamaguchi, and Hidetoshi Katori. Frequency ratios of sr, yb, and hg based optical lattice clocks and their applications. *Comptes Rendus Physique*, 16(5):489 – 498, 2015. The measurement of time / La mesure du temps.

[6] N. Hinkley, J. A. Sherman, N. B. Phillips, M. Schioppo, N. D. Lemke, K. Beloy, M. Pizzocaro, C. W. Oates, and A. D. Ludlow. An atomic clock with 10^{-18} instability. *Science*, 341(6151):1215–1218, 2013.

[7] F Bregolin, G Milani, M Pizzocaro, B Rauf, P Thoumany, F Levi, and D Calonico. Optical lattice clocks towards the redefinition of the second. *Journal of Physics: Conference Series*, 841(1):012015, 2017.

[8] K. Shibata, S. Kato, A. Yamaguchi, S. Uetake, and Y. Takahashi. A scalable quantum computer with ultranarrow optical transition of ultracold neutral atoms in an optical lattice. *Applied Physics B*, 97(4):753, 2009.

[9] Immanuel Bloch. Ultracold quantum gases in optical lattices. *Nat Phys*, 1(1):23–30, October 2005.

[10] Andrew J. Daley. Quantum computing and quantum simulation with group-ii atoms. *Quantum Information Processing*, 10(6):865, 2011.

[11] Hidetoshi Katori. Optical lattice clocks and quantum metrology. *Nat Photon*, 5(4):203–210, April 2011.

[12] Andrew D. Ludlow, Martin M. Boyd, Jun Ye, E. Peik, and P. O. Schmidt. Optical atomic clocks. *Rev. Mod. Phys.*, 87:637–701, Jun 2015.

[13] D.W. Allan. Statistics of atomic frequency standards. *Proc. IEEE*, 54(2):221–230, feb. 1966.

[14] W. M. Itano, J. C. Bergquist, J. J. Bollinger, J. M. Gilligan, D. J. Heinzen, F. L. Moore, M. G. Raizen, and D. J. Wineland. Quantum projection noise: Population fluctuations in two-level systems. *Phys. Rev. A*, 47:3554–3570, May 1993.

[15] G.J. Dick. Local oscillator induced instabilities in trapped ion frequency standards. Technical report, DTIC Document, 1987.

[16] G John Dick, John D Prestage, Charles A Greenhall, and Lute Maleki. Local oscillator induced degradation of medium-term stability in passive atomic frequency standards. Technical report, California Institute Of Technology Pasadena Jet Propulsion Lab, 1990.

[17] G. Santarelli, C. Audoin, A. Makdissi, P. Laurent, G.J. Dick, and A. Clairon. Frequency stability degradation of an oscillator slaved to a periodically interrogated atomic resonator. *IEEE Trans. Ultrason., Ferroelect., Freq. Cont.*, 45(4):887–894, july 1998.

[18] Andrew D. Ludlow. *The Strontium Optical Lattice Clock: Optical Spectroscopy with Sub-Hertz Accuracy*. PhD thesis, University of Colorado, 2008.

[19] Ali Al-Masoudi, Sören Dörscher, Sebastian Häfner, Uwe Sterr, and Christian Lisdat. Noise and instability of an optical lattice clock. *Phys. Rev. A*, 92:063814, Dec 2015.

[20] Sebastian Häfner, Stephan Falke, Christian Grebing, Stefan Vogt, Thomas Legero, Mikko Merimaa, Christian Lisdat, and Uwe Sterr. 8×10^{-17} fractional laser frequency instability with a long room-temperature cavity. *Opt. Lett.*, 40(9):2112–2115, May 2015.

[21] D. G. Matei, T. Legero, S. Häfner, C. Grebing, R. Weyrich, W. Zhang, L. Sonderhouse, J. M. Robinson, J. Ye, F. Riehle, and U. Sterr. 1.5 μm lasers with sub-10 mhz linewidth. *Phys. Rev. Lett.*, 118:263202, Jun 2017.

[22] G. D. Cole, W. Zhang, B. J. Bjork, D. Follman, P. Heu, C. Deutsch, L. Sonderhouse, C. Franz, A. Alexandrovski, O. H. Heckl, J. Ye, and M. Aspelmeyer. Low-loss crystalline coatings for the near- and mid-infrared. *Proc. SPIE*, 9822:98220Y–98220Y–7, 2016.

[23] Jérôme Lodewyck, Philip G. Westergaard, and Pierre Lemonde. Nondestructive measurement of the transition probability in a sr optical lattice clock. *Phys. Rev. A*, 79:061401, Jun 2009.

[24] Jérôme Lodewyck, Philip G Westergaard, Arnaud Lecallier, Luca Lorini, and Pierre Lemonde. Frequency stability of optical lattice clocks. *New Journal of Physics*, 12(6):065026, 2010.

[25] G Vallet, E Bookjans, U Eismann, S Bilicki, R Le Targat, and J Lodewyck. A noise-immune cavity-assisted non-destructive detection for an optical lattice clock in the quantum regime. *New Journal of Physics*, 19(8):083002, 2017.

[26] C. W. Chou, D. B. Hume, M. J. Thorpe, D. J. Wineland, and T. Rosenband. Quantum coherence between two atoms beyond $q = 10^{15}$. *Phys. Rev. Lett.*, 106:160801, Apr 2011.

[27] Masao Takamoto, Tetsushi Takano, and Hidetoshi Katori. Frequency comparison of optical lattice clocks beyond the dick limit. *Nat. Photon.*, 5(5):288–292, May 2011.

[28] Nils Nemitz, Takuya Ohkubo, Masao Takamoto, Ichiro Ushijima, Manoj Das, Noriaki Ohmae, and Hidetoshi Katori. Frequency ratio of yb and sr clocks with 5×10^{-17} uncertainty at 150 seconds averaging time. *Nat Photon*, advance online publication:–, February 2016.

[29] M. Schioppo, R. C. Brown, W. F. McGrew, N. Hinkley, R. J. Fasano, K. Beloy, T.H. Yoon, G. Milani, D. Nicolodi, J. A. Sherman, N. B. Phillips, C W Oates, and A. D. Ludlow. Ultrastable optical clock with two cold-atom ensembles. *Nat Photon*, 11(1):48–52, January 2017.

[30] N. Huntemann, C. Sanner, B. Lipphardt, Chr. Tamm, and E. Peik. Single-ion atomic clock with 3×10^{-18} systematic uncertainty. *Phys. Rev. Lett.*, 116:063001, Feb 2016.

[31] P. D. D. Schwindt, Y. Y. Jau, H. L. Partner, D. K. Serkland, A. Ison, A. McCants, E. Winrow, J. Prestage, J. Kellogg, N. Yu, C. D. Boschen, I. Kosvin, D. Mailloux, D. Scherer, C. Nelson, A. Hati, and D. A. Howe. Miniature trapped-ion frequency standard with $^{171}Yb^{+}$. In *2015 Joint Conference of the IEEE International Frequency Control Symposium the European Frequency and Time Forum*, pages 752–757, April 2015.

[32] Pierre Dubé, Alan A. Madej, Andrew Shiner, and Bin Jian. $^{88}Sr^{+}$ single-ion optical clock with a stability approaching the quantum projection noise limit. *Phys. Rev. A*, 92:042119, October 2015.

[33] A. Ashkin. Acceleration and trapping of particles by radiation pressure. *Phys. Rev. Lett.*, 24:156–159, Jan 1970.

[34] A. Ashkin. Trapping of atoms by resonance radiation pressure. *Phys. Rev. Lett.*, 40:729–732, Mar 1978.

[35] T.W. Hänsch and A.L. Schawlow. Cooling of gases by laser radiation. *Optics Communications*, 13(1):68 – 69, 1975.

[36] D. J. Wineland, R. E. Drullinger, and F. L. Walls. Radiation-pressure cooling of bound resonant absorbers. *Phys. Rev. Lett.*, 40:1639–1642, Jun 1978.

[37] Tetsuya Ido and Hidetoshi Katori. Recoil-free spectroscopy of neutral sr atoms in the lamb-dicke regime. *Phys. Rev. Lett.*, 91:053001, Jul 2003.

[38] Marco Pizzocaro, Pierre Thoumany, Benjamin Rauf, Filippo Bregolin, Gianmaria Milani, Cecilia Clivati, Giovanni A Costanzo, Filippo Levi, and Davide Calonico. Absolute frequency measurement of the $^1S_0 \rightarrow {}^3P_0$ transition of ^{171}Yb. *Metrologia*, 54(1):102, 2017.

[39] Masao Takamoto, Feng-Lei Hong, Ryoichi Higashi, and Hidetoshi Katori. An optical lattice clock. *Nature*, 435(7040):321–324, May 2005.

[40] H. Hachisu, K. Miyagishi, S. G. Porsev, A. Derevianko, V. D. Ovsiannikov, V. G. Pal'chikov, M. Takamoto, and H. Katori. Trapping of neutral mercury atoms and prospects for optical lattice clocks. *Phys. Rev. Lett.*, 100:053001, Feb 2008.

[41] L. Yi, S. Mejri, J. J. McFerran, Y. Le Coq, and S. Bize. Optical lattice trapping of ^{199}Hg and determination of the magic wavelength for the ultraviolet $^1S_0 \leftrightarrow {}^3P_0$ clock transition. *Phys. Rev. Lett.*, 106:073005, Feb 2011.

[42] Sergey G. Porsev, Andrei Derevianko, and E. N. Fortson. Possibility of an optical clock using the $6^1S_0 \rightarrow 6^3P_0$ transition in ^{171,173}Yb atoms held in an optical lattice. *Phys. Rev. A*, 69:021403, Feb 2004.

[43] Z. W. Barber, C. W. Hoyt, C. W. Oates, L. Hollberg, A. V. Taichenachev, and V. I. Yudin. Direct excitation of the forbidden clock transition in neutral ^{174}Yb atoms confined to an optical lattice. *Phys. Rev. Lett.*, 96(8):083002, Mar 2006.

[44] A. P. Kulosa, D. Fim, K. H. Zipfel, S. Rühmann, S. Sauer, N. Jha, K. Gibble, W. Ertmer, E. M. Rasel, M. S. Safronova, U. I. Safronova, and S. G. Porsev. Towards a mg lattice clock: Observation of the $^1S_0 - {}^3P_0$ transition and determination of the magic wavelength. *Phys. Rev. Lett.*, 115:240801, Dec 2015.

[45] Yushi Kaneda, J. M. Yarborough, Yevgeny Merzlyak, Atsushi Yamaguchi, Keitaro Hayashida, Noriaki Ohmae, and Hidetoshi Katori. Continuous-wave, single-frequency 229 nm laser source for laser cooling of cadmium atoms. *Opt. Lett.*, 41(4):705–708, Feb 2016.

[46] Carsten Degenhardt, Hardo Stoehr, Uwe Sterr, Fritz Riehle, and Christian Lisdat. Wavelength-dependent ac stark shift of the $^1S_0 - {}^3P_1$ transition at 657 nm in ca. *Phys. Rev. A*, 70:023414, Aug 2004.

[47] CIPM. *CIPM 2015 Recommendation 2 (CI-2015): updates to the list of standard frequencies*, 2015.

[48] T.L. Nicholson, S.L. Campbell, R.B. Hutson, G.E. Marti, B.J. Bloom, R.L. McNally, W. Zhang, M.D. Barrett, M.S. Safronova, G.F. Strouse, W.L. Tew, and J. Ye. Systematic evaluation of an atomic clock at 2×10^{-18} total uncertainty. *Nat Commun*, 6(6896):–, 2015.

[49] M. Schioppo, R. C. Brown, W. F. McGrew, N. Hinkley, R. J. Fasano, K. Beloy, T. H. Yoon, G. Milani, D. Nicolodi, J. A. Sherman, N. B. Phillips, C. W. Oates, and A. D. Ludlow. Ultra-stable optical clock with two cold-atom ensembles. *Nature Photonics*, (11):48–52, November 2016.

[50] B. J. Bloom, T. L. Nicholson, J. R. Williams, S. L. Campbell, M. Bishof, X. Zhang, W. Zhang, S. L. Bromley, and J. Ye. An optical lattice clock with accuracy and stability at the 10^{-18} level. *Nature*, 506(7486):71–75, February 2014.

[51] D. J. Wineland, J. J. Bollinger, W. M. Itano, F. L. Moore, and D. J. Heinzen. Spin squeezing and reduced quantum noise in spectroscopy. *Phys. Rev. A*, 46:R6797–R6800, Dec 1992.

[52] Ian D. Leroux, Monika H. Schleier-Smith, and Vladan Vuletić. Implementation of cavity squeezing of a collective atomic spin. *Phys. Rev. Lett.*, 104:073602, Feb 2010.

[53] Gilbert Grynberg Claude Cohen-Tannoudji, Jacques Dupont-Roc. *Atom-Photon Interactions: Basic Processes and Applications*. Wiley Science, 1998.

[54] JP Gordon and A Ashkin. Motion of atoms in a radiation trap. *Physical Review A*, 21(5):1606, 1980.

[55] John V. Prodan, William D. Phillips, and Harold Metcalf. Laser production of a very slow monoenergetic atomic beam. *Phys. Rev. Lett.*, 49:1149–1153, Oct 1982.

[56] Steven Chu, L. Hollberg, J. E. Bjorkholm, Alex Cable, and A. Ashkin. Three-dimensional viscous confinement and cooling of atoms by resonance radiation pressure. *Phys. Rev. Lett.*, 55:48–51, Jul 1985.

[57] Harold J. Metcalf and Peter van der Straten. *Laser cooling and trapping*. Springer, New York, 2002.

[58] William D. Phillips and Harold Metcalf. Laser deceleration of an atomic beam. *Phys. Rev. Lett.*, 48:596–599, Mar 1982.

[59] Claude Cohen-Tannoudji and David Guéry-Odelin. *Doppler Cooling*, chapter 12, pages 269–281. WORLD SCIENTIFIC, 2012.

[60] J Javanainen. Polarization gradient cooling in three dimensions: comparison of theory and experiment. *Journal of Physics B: Atomic, Molecular and Optical Physics*, 27(3):L41, 1994.

[61] G. Modugno, C. Benkő, P. Hannaford, G. Roati, and M. Inguscio. Sub-doppler laser cooling of fermionic ^{40}K atoms. *Phys. Rev. A*, 60:R3373–R3376, Nov 1999.

[62] J. Dalibard and C. Cohen-Tannoudji. Laser cooling below the doppler limit by polarization gradients: simple theoretical models. *J. Opt. Soc. Am. B*, 6(11):2023–2045, Nov 1989.

[63] N. Kostylev, E. Ivanov, M. E. Tobar, and J. J. McFerran. Sub-doppler cooling of ytterbium with the $^1S_0 \rightarrow {}^1P_1$ transition including 171yb ($i = 1/2$). *J. Opt. Soc. Am. B*, 31(7):1614–1620, Jul 2014.

[64] Wolfgang Ketterle and N.J. Van Druten. Evaporative cooling of trapped atoms. *Advances In Atomic, Molecular, and Optical Physics*, 37:181 – 236, 1996.

[65] Patrick Gill. Optical frequency standards. *Metrologia*, 42(3):S125, 2005.

[66] Rudolf Grimm, Matthias Weidemüller, and Yurii B. Ovchinnikov. Optical dipole traps for neutral atoms. volume 42 of *Advances In Atomic, Molecular, and Optical Physics*, pages 95 – 170. Academic Press, 2000.

[67] Steven Chu, J. E. Bjorkholm, A. Ashkin, and A. Cable. Experimental observation of optically trapped atoms. *Phys. Rev. Lett.*, 57:314–317, Jul 1986.

[68] C. Salomon, J. Dalibard, A. Aspect, H. Metcalf, and C. Cohen-Tannoudji. Channeling atoms in a laser standing wave. *Phys. Rev. Lett.*, 59:1659–1662, Oct 1987.

[69] N. D. Lemke, J. von Stecher, J. A. Sherman, A. M. Rey, C. W. Oates, and A. D. Ludlow. p-wave cold collisions in an optical lattice clock. *Phys. Rev. Lett.*, 107:103902, Aug 2011.

[70] S. Blatt, J. W. Thomsen, G. K. Campbell, A. D. Ludlow, M. D. Swallows, M. J. Martin, M. M. Boyd, and J. Ye. Rabi spectroscopy and excitation inhomogeneity in a one-dimensional optical lattice clock. *Phys. Rev. A*, 80:052703, Nov 2009.

[71] Andrei Derevianko and Hidetoshi Katori. Colloquium: Physics of optical lattice clocks. *Rev. Mod. Phys.*, 83:331–347, May 2011.

[72] Tomoya Akatsuka, Masao Takamoto, and Hidetoshi Katori. Three-dimensional optical lattice clock with bosonic ^{88}Sr atoms. *Phys. Rev. A*, 81:023402, Feb 2010.

[73] Matthew D. Swallows, Michael Bishof, Yige Lin, Sebastian Blatt, Michael J. Martin, Ana Maria Rey, and Jun Ye. Suppression of collisional shifts in a strongly interacting lattice clock. *Science*, 331(6020):1043–1046, 2011.

[74] R. H. Dicke. The effect of collisions upon the doppler width of spectral lines. *Phys. Rev.*, 89:472–473, Jan 1953.

[75] D. Leibfried, R. Blatt, C. Monroe, and D. Wineland. Quantum dynamics of single trapped ions. *Rev. Mod. Phys.*, 75:281–324, Mar 2003.

[76] V. D. Ovsiannikov, S. I. Marmo, V. G. Palchikov, and H. Katori. Higher-order effects on the precision of clocks of neutral atoms in optical lattices. *Phys. Rev. A*, 93:043420, Apr 2016.

[77] Fam Le Kien, Philipp Schneeweiss, and Arno Rauschenbeutel. Dynamical polarizability of atoms in arbitrary light fields: general theory and application to cesium. *The European Physical Journal D*, 67(5):92, May 2013.

[78] Z. W. Barber, J. E. Stalnaker, N. D. Lemke, N. Poli, C. W. Oates, T. M. Fortier, S. A. Diddams, L. Hollberg, C. W. Hoyt, A. V. Taichenachev, and V. I. Yudin. Optical lattice induced light shifts in an Yb atomic clock. *Phys. Rev. Lett.*, 100:103002, Mar 2008.

[79] Hidetoshi Katori, V. D. Ovsiannikov, S. I. Marmo, and V. G. Palchikov. Strategies for reducing the light shift in atomic clocks. *Phys. Rev. A*, 91:052503, May 2015.

[80] Pierre Lemonde and Peter Wolf. Optical lattice clock with atoms confined in a shallow trap. *Phys. Rev. A*, 72:033409, Sep 2005.

[81] C. Sias, H. Lignier, Y. P. Singh, A. Zenesini, D. Ciampini, O. Morsch, and E. Arimondo. Observation of photon-assisted tunneling in optical lattices. *Phys. Rev. Lett.*, 100:040404, Feb 2008.

[82] R. Le Targat, L. Lorini, Y. Le Coq, M. Zawada, J. Guéna, M. Abgrall, M. Gurov, P. Rosenbusch, D. G. Rovera, B. Nagòrny, R. Gartman, P. G. Westergaard, M. E. Tobar, M. Lours, G. Santarelli, A. Clairon, S. Bize, P. Laurent, P. Lemonde, and J. Lodewyck. Experimental realization of an optical second with strontium lattice clocks. *Nat Commun*, 4:–, July 2013.

[83] S. Friebel, C. D'Andrea, J. Walz, M. Weitz, and T. W. Hänsch. co_2-laser optical lattice with cold rubidium atoms. *Phys. Rev. A*, 57:R20–R23, Jan 1998.

[84] T. A. Savard, K. M. O'Hara, and J. E. Thomas. Laser-noise-induced heating in far-off resonance optical traps. *Phys. Rev. A*, 56:R1095–R1098, Aug 1997.

[85] R. Jáuregui, N. Poli, G. Roati, and G. Modugno. Anharmonic parametric excitation in optical lattices. *Phys. Rev. A*, 64:033403, Aug 2001.

[86] E.M. Lifshitz L.D. Landau. *Mechanics*. Pergamon, 1976.

[87] N. Poli, R. J. Brecha, G. Roati, and G. Modugno. Cooling atoms in an optical trap by selective parametric excitation. *Phys. Rev. A*, 65:021401, Jan 2002.

[88] A. D. Ludlow, T. Zelevinsky, G. K. Campbell, S. Blatt, M. M. Boyd, M. H. G. de Miranda, M. J. Martin, J. W. Thomsen, S. M. Foreman, Jun Ye, T. M. Fortier, J. E. Stalnaker, S. A. Diddams, Y. Le Coq, Z. W. Barber, N. Poli,

N. D. Lemke, K. M. Beck, and C. W. Oates. Sr lattice clock at 1×10^{-16} fractional uncertainty by remote optical evaluation with a Ca clock. *Science*, 319(5871):1805–1808, 2008.

[89] David Hayes, Paul S. Julienne, and Ivan H. Deutsch. Quantum logic via the exchange blockade in ultracold collisions. *Phys. Rev. Lett.*, 98:070501, Feb 2007.

[90] A. V. Gorshkov, A. M. Rey, A. J. Daley, M. M. Boyd, J. Ye, P. Zoller, and M. D. Lukin. Alkaline-earth-metal atoms as few-qubit quantum registers. *Phys. Rev. Lett.*, 102:110503, Mar 2009.

[91] A. V. Gorshkov, M. Hermele, V. Gurarie, C. Xu, P. S. Julienne, J. Ye, P. Zoller, E. Demler, M. D. Lukin, and A. M. Rey. Two-orbital su(n) magnetism with ultracold alkaline-earth atoms. *Nat Phys*, 6(4):289–295, April 2010.

[92] M A Cazalilla, A F Ho, and M Ueda. Ultracold gases of ytterbium: ferromagnetism and mott states in an su(6) fermi system. *New Journal of Physics*, 11(10):103033, 2009.

[93] Michael Foss-Feig, Michael Hermele, Victor Gurarie, and Ana Maria Rey. Heavy fermions in an optical lattice. *Phys. Rev. A*, 82:053624, Nov 2010.

[94] G. K. Campbell, M. M. Boyd, J. W. Thomsen, M. J. Martin, S. Blatt, M. D. Swallows, T. L. Nicholson, T. Fortier, C. W. Oates, S. A. Diddams, N. D. Lemke, P. Naidon, P. Julienne, Jun Ye, and A. D. Ludlow. Probing interactions between ultracold fermions. *Science*, 324(5925):360–363, 2009.

[95] A. D. Ludlow, N. D. Lemke, J. A. Sherman, C. W. Oates, G. Quéméner, J. von Stecher, and A. M. Rey. Cold-collision-shift cancellation and inelastic scattering in a yb optical lattice clock. *Phys. Rev. A*, 84:052724, Nov 2011.

[96] Sangkyung Lee, Chang Yong Park, Won-Kyu Lee, and Dai-Hyuk Yu. Cancellation of collisional frequency shifts in optical lattice clocks with rabi spectroscopy. *New Journal of Physics*, 18(3):033030, 2016.

[97] Kurt Gibble. Scattering of cold-atom coherences by hot atoms: Frequency shifts from background-gas collisions. *Phys. Rev. Lett.*, 110:180802, May 2013.

[98] Nobuyasu Shiga, Ying Li, Hiroyuki Ito, Shigeo Nagano, Tetsuya Ido, Katarzyna Bielska, Ryszard S. Trawiński, and Roman Ciuryło. Buffer-gas-induced collision shift for the ^{88}Sr $^1S_0 - ^3P_1$ clock transition. *Phys. Rev. A*, 80:030501, Sep 2009.

[99] J. A. Sherman, N. D. Lemke, N. Hinkley, M. Pizzocaro, R. W. Fox, A. D. Ludlow, and C. W. Oates. High-accuracy measurement of atomic polarizability in an optical lattice clock. *Phys. Rev. Lett.*, 108:153002, Apr 2012.

[100] K. Beloy, J. A. Sherman, N. D. Lemke, N. Hinkley, C. W. Oates, and A. D. Ludlow. Determination of the $5d6s\ ^3D_1$ state lifetime and blackbody-radiation clock shift in yb. *Phys. Rev. A*, 86:051404, Nov 2012.

[101] Sergey G. Porsev and Andrei Derevianko. Multipolar theory of blackbody radiation shift of atomic energy levels and its implications for optical lattice clocks. *Phys. Rev. A*, 74:020502, Aug 2006.

[102] Thomas Middelmann, Stephan Falke, Christian Lisdat, and Uwe Sterr. High accuracy correction of blackbody radiation shift in an optical lattice clock. *Phys. Rev. Lett.*, 109:263004, Dec 2012.

[103] K. Beloy, N. Hinkley, N. B. Phillips, J. A. Sherman, M. Schioppo, J. Lehman, A. Feldman, L. M. Hanssen, C. W. Oates, and A. D. Ludlow. Atomic clock with 1×10^{-18} room-temperature blackbody stark uncertainty. *Phys. Rev. Lett.*, 113:260801, Dec 2014.

[104] T. Middelmann, C. Lisdat, S. Falke, J.S.R.V. Winfred, F. Riehle, and U. Sterr. Tackling the blackbody shift in a strontium optical lattice clock. *IEEE Trans. Instrum. Meas.*, 60(7):2550–2557, july 2011.

[105] N. Poli, Z. W. Barber, N. D. Lemke, C. W. Oates, L. S. Ma, J. E. Stalnaker, T. M. Fortier, S. A. Diddams, L. Hollberg, J. C. Bergquist, A. Brusch, S. Jefferts, T. Heavner, and T. Parker. Frequency evaluation of the doubly forbidden $^1S_0 \rightarrow {}^1P_3$ transition in bosonic ^{174}Yb. *Phys. Rev. A*, 77(5):050501, May 2008.

[106] A. V. Taichenachev, V. I. Yudin, C. W. Oates, C. W. Hoyt, Z. W. Barber, and L. Hollberg. Magnetic field-induced spectroscopy of forbidden optical transitions with application to lattice-based optical atomic clocks. *Phys. Rev. Lett.*, 96:083001, Mar 2006.

[107] Yi Pang, Jeffrey J. Hamilton, and Jean-Paul Richard. Frequency noise induced by fiber perturbations in a fiber-linked stabilized laser. *Appl. Opt.*, 31(36):7532–7534, Dec 1992.

[108] Long-Sheng Ma, Peter Jungner, Jun Ye, and John L. Hall. Delivering the same optical frequency at two places: accurate cancellation of phase noise introduced by an optical fiber or other time-varying path. *Opt. Lett.*, 19(21):1777–1779, Nov 1994.

[109] C Lisdat, G Grosche, N Quintin, C Shi, SMF Raupach, C Grebing, D Nicolodi, F Stefani, A Al-Masoudi, S Dörscher, S Häfner, J-L Robyr, N Chiodo, S Bilicki, E Bookjans, A Koczwara, S Koke, A Kuhl, F Wiotte, F Meynadier, E Camisard, M Abgrall, M Lours, T Legero, H Schnatz, U Sterr, H Denker, C Chardonnet, Y Le Coq, G Santarelli, A Amy-Klein, R Le Targat, J Lodewyck, O Lopez, and P-E Pottie. A clock network for geodesy and fundamental science. *Nature Communications*, 7:12443–, July 2016.

[110] Tetsushi Takano, Masao Takamoto, Ichiro Ushijima, Noriaki Ohmae, Tomoya Akatsuka, Atsushi Yamaguchi, Yuki Kuroishi, Hiroshi Munekane, Basara Miyahara, and Hidetoshi Katori. Geopotential measurements with synchronously linked optical lattice clocks. *Nat Photon*, 10(10):662–666, October 2016.

[111] D. Calonico, E.K. Bertacco, C.E. Calosso, C. Clivati, G.A. Costanzo, M. Frittelli, A. Godone, A. Mura, N. Poli, D.V. Sutyrin, G. Tino, M.E. Zucco, and F. Levi. High-accuracy coherent optical frequency transfer over a doubled 642-km fiber link. *Applied Physics B*, 117(3):979–986, 2014.

[112] Arthur Matveev, Christian G. Parthey, Katharina Predehl, Janis Alnis, Axel Beyer, Ronald Holzwarth, Thomas Udem, Tobias Wilken, Nikolai Kolachevsky, Michel Abgrall, Daniele Rovera, Christophe Salomon, Philippe Laurent, Gesine Grosche, Osama Terra, Thomas Legero, Harald Schnatz, Stefan Weyers, Brett Altschul, and Theodor W. Hänsch. Precision measurement of the hydrogen $1s-2s$ frequency via a 920-km fiber link. *Phys. Rev. Lett.*, 110:230801, Jun 2013.

[113] Alfred Schild. Equivalence principle and red-shift measurements. *American Journal of Physics*, 28(9):778–780, 1960.

[114] C. W. Chou, D. B. Hume, T. Rosenband, and D. J. Wineland. Optical clocks and relativity. *Science*, 329(5999):1630–, September 2010.

[115] Jacopo Grotti, Silvio Koller, Stefan Vogt, Sebastian Häfner, Uwe Sterr, Christian Lisdat, Heiner Denker, Christian Voigt, Ludger Timmen, Antoine Rolland, Fred N. Baynes, Helen S. Margolis, Michel Zampaolo, Pierre Thoumany, Marco Pizzocaro, Benjamin Rauf, Filippo Bregolin, Anna Tampellini, Piero Barbieri, Massimo Zucco, Giovanni A. Costanzo, Cecilia Clivati, Filippo Levi, and Davide Calonico. Geodesy and metrology with a transportable optical clock. *Nature Physics*, pages –, 2018.

[116] B. Julsgaard, A. Walther, S. Kröll, and L. Rippe. Understanding laser stabilization using spectral hole burning. *Opt. Express*, 15(18):11444–11465, Sep 2007.

[117] Shon Cook, Till Rosenband, and David R. Leibrandt. Laser-frequency stabilization based on steady-state spectral-hole burning in $\mathrm{eu}^{3+}:\mathrm{y}_2\mathrm{sio}_5$. *Phys. Rev. Lett.*, 114:253902, Jun 2015.

[118] D. Hils and J. L. Hall. *Ultra-Stable Cavity-Stabilized Lasers with Subhertz Linewidth*, pages 162–173. Springer Berlin Heidelberg, Berlin, Heidelberg, 1989.

[119] Eric D. Black. An introduction to Pound-Drever-Hall laser frequency stabilization. *Amer. J. Phys.*, 69(1):79–87, 2001.

[120] Claus Lämmerzahl, Hansjörg Dittus, Achim Peters, and Stephan Schiller. Optis: a satellite-based test of special and general relativity. *Classical and Quantum Gravity*, 18(13):2499, 2001.

[121] Canuel, B., Amand, L., Bertoldi, A., Chaibi, W., Geiger, R., Gillot, J., Landragin, A., Merzougui, M., Riou, I., Schmid, S.P., and Bouyer, P. The matter-wave laser interferometer gravitation antenna (miga): New perspectives for fundamental physics and geosciences. *E3S Web of Conferences*, 4:01004, 2014.

[122] T. Kessler, C. Hagemann, C. Grebing, T. Legero, U. Sterr, F. Riehle, M. J. Martin, L. Chen, and J. Ye. A sub-40-mHz-linewidth laser based on a silicon single-crystal optical cavity. *Nat. Photon.*, 6(10):687–692, oct 2012.

[123] A. B. Matsko and V. S. Ilchenko. Optical resonators with whispering-gallery modes-part i: basics. *IEEE Journal of Selected Topics in Quantum Electronics*, 12(1):3–14, 2006.

[124] W. Liang, V. S. Ilchenko, A. A. Savchenkov, A. B. Matsko, D. Seidel, and L. Maleki. Whispering-gallery-mode-resonator-based ultranarrow linewidth external-cavity semiconductor laser. *Opt. Lett.*, 35(16):2822–2824, Aug 2010.

[125] H. Kogelnik and T. Li. Laser beams and resonators. *Appl. Opt.*, 5(10):1550–1567, 1966.

[126] Michael L. Gorodetsky. Thermal noises and noise compensation in high-reflection multilayer coating. *Physics Letters A*, 372(46):6813 – 6822, 2008.

[127] S. A. Webster, M. Oxborrow, S. Pugla, J. Millo, and P. Gill. Thermal-noise-limited optical cavity. *Phys. Rev. A*, 77:033847, Mar 2008.

[128] Yu. Levin. Internal thermal noise in the ligo test masses: A direct approach. *Phys. Rev. D*, 57:659–663, Jan 1998.

[129] Kenji Numata, Amy Kemery, and Jordan Camp. Thermal-noise limit in the frequency stabilization of lasers with rigid cavities. *Phys. Rev. Lett.*, 93(25):250602, Dec 2004.

[130] T. Kessler, T. Legero, and U. Sterr. Thermal noise in optical cavities revisited. *J. Opt. Soc. Amer. B*, 29:178, January 2012.

[131] Thomas Legero, Thomas Kessler, and Uwe Sterr. Tuning the thermal expansion properties of optical reference cavities with fused silica mirrors. *J. Opt. Soc. Amer. B*, 27(5):914–919, May 2010.

[132] C. T. Taylor, M. Notcutt, and D. G. Blair. Cryogenic, all-sapphire, fabry-perot optical frequency reference. *Rev. Sci. Inst.*, 66(2):955–960, feb 1995.

[133] Garrett D. Cole, Wei Zhang, Michael J. Martin, Jun Ye, and Markus Aspelmeyer. Tenfold reduction of brownian noise in high-reflectivity optical coatings. *Nat Photon*, 7(8):644–650, August 2013.

[134] J. Millo, D. V. Magalhães, C. Mandache, Y. Le Coq, E. M. L. English, P. G. Westergaard, J. Lodewyck, S. Bize, P. Lemonde, and G. Santarelli. Ultrastable lasers based on vibration insensitive cavities. *Phys. Rev. A*, 79:053829, May 2009.

[135] K. M. Evenson, J. S. Wells, F. R. Petersen, B. L. Danielson, G. W. Day, R. L. Barger, and J. L. Hall. Speed of light from direct frequency and wavelength measurements of the methane-stabilized laser. *Phys. Rev. Lett.*, 29:1346–1349, Nov 1972.

[136] A. Morinaga, F. Riehle, J. Ishikawa, and J. Helmcke. A ca optical frequency standard: Frequency stabilization by means of nonlinear ramsey resonances. *Applied Physics B*, 48(2):165–171, Feb 1989.

[137] A. N. Luiten, R. Kovachich, H. R. Telle, C. O. Weiss, and A. G. Mann. The uwa/ptb optical to microwave frequency chain. In *1998 Conference on Precision Electromagnetic Measurements Digest (Cat. No.98CH36254)*, pages 395–396, 1998.

[138] Marco Bellini and Theodor W. Hänsch. Phase-locked white-light continuum pulses: toward a universal optical frequency-comb synthesizer. *Opt. Lett.*, 25(14):1049–1051, Jul 2000.

[139] J.L. Hall. Optical frequency measurement: 40 years of technology revolutions. *Selected Topics in Quantum Electronics, IEEE Journal of*, 6(6):1136–1144, nov/dec 2000.

[140] John L. Hall. Nobel lecture: Defining and measuring optical frequencies. *Rev. Mod. Phys.*, 78:1279–1295, Nov 2006.

[141] Theodor W. Hänsch. Nobel lecture: Passion for precision. *Rev. Mod. Phys.*, 78:1297–1309, Nov 2006.

[142] Jorn Stenger and Harald R. Telle. Kerr-lens mode-locked lasers for optical frequency measurements. *Proc. SPIE*, 4269:72–76, 2001.

[143] Jens Rauschenberger, Tara M. Fortier, David J. Jones, Jun Ye, and Steven T. Cundiff. Control of the frequency comb from a mode-locked erbium-doped fiber laser. *Opt. Express*, 10(24):1404–1410, Dec 2002.

[144] David J. Jones, Scott A. Diddams, Matthew S. Taubman, Steven T. Cundiff, Long-Sheng Ma, and John L. Hall. Frequency comb generation using femtosecond pulses and cross-phase modulation in optical fiber at arbitrary center frequencies. *Opt. Lett.*, 25(5):308–310, Mar 2000.

[145] J. Reichert, R. Holzwarth, Th. Udem, and T.W. Hänsch. Measuring the frequency of light with mode-locked lasers. *Optics Communications*, 172(1):59 – 68, 1999.

[146] H.R. Telle, B. Lipphardt, and J. Stenger. Kerr-lens, mode-locked lasers as transfer oscillators for optical frequency measurements. *Applied Physics B*, 74(1):1–6, 2002.

[147] David J. Jones, Scott A. Diddams, Jinendra K. Ranka, Andrew Stentz, Robert S. Windeler, John L. Hall, and Steven T. Cundiff. Carrier-envelope phase control of femtosecond mode-locked lasers and direct optical frequency synthesis. *Science*, 288(5466):635–639, 2000.

[148] L A M Johnson, P Gill, and H S Margolis. Evaluating the performance of the npl femtosecond frequency combs: agreement at the 10^{-21} level. *Metrologia*, 52(1):62, 2015.

[149] Tao Hong, Claire Cramer, Eryn Cook, Warren Nagourney, and E. N. Fortson. Observation of the $^1S_0$ - $^3P_0$ transition in atomic ytterbium for optical clocks and qubit arrays. *Opt. Lett.*, 30(19):2644–2646, Oct 2005.

[150] S. Lukman Winoto, Marshall T. DePue, Nathan E. Bramall, and David S. Weiss. Laser cooling at high density in deep far-detuned optical lattices. *Phys. Rev. A*, 59:R19–R22, Jan 1999.

[151] Andrew J. Kerman, Vladan Vuletić, Cheng Chin, and Steven Chu. Beyond optical molasses: 3d raman sideband cooling of atomic cesium to high phase-space density. *Phys. Rev. Lett.*, 84:439–442, Jan 2000.

[152] S. G. Porsev, Yu. G. Rakhlina, and M. G. Kozlov. Electric-dipole amplitudes, lifetimes, and polarizabilities of the low-lying levels of atomic ytterbium. *Phys. Rev. A*, 60:2781–2785, Oct 1999.

[153] Chen Ning, Zhou Min, Chen Hai-Qin, Fang Su, Huang Liang-Yu, Zhang Xiao-Hang, Gao Qi, Jiang Yan-Yi, Bi Zhi-Yi, Ma Long-Sheng, and Xu Xin-Ye. Clock-transition spectrum of ^{171}yb atoms in a one-dimensional optical lattice. *Chinese Physics B*, 22(9):090601, 2013.

[154] Marco Pizzocaro, Davide Calonico, Pablo Cancio Pastor, Jacopo Catani, Giovanni A. Costanzo, Filippo Levi, and Luca Lorini. Efficient frequency doubling at 399 nm. *Appl. Opt.*, 53(16):3388–3392, Jun 2014.

[155] T.W. Hansch and B. Couillaud. Laser frequency stabilization by polarization spectroscopy of a reflecting reference cavity. *Optics Communications*, 35(3):441 – 444, 1980.

[156] M. Pizzocaro, G. A. Costanzo, A. Godone, F. Levi, A. Mura, M. Zoppi, and D. Calonico. Realization of an ultrastable 578-nm laser for an Yb lattice clock. *IEEE Trans. Ultrason., Ferroelect., Freq. Cont.*, 59(3):426–431, march 2012.

[157] Krzysztof Pawłowski and Kazimierz Rzążewski. Background atoms and decoherence in optical lattices. *Phys. Rev. A*, 81:013620, Jan 2010.

[158] M. Pizzocaro, D. Calonico, C. Calosso, C. Clivati, G. A. Costanzo, F. Levi, and A. Mura. Active disturbance rejection control of temperature for ultrastable optical cavities. *IEEE Trans. Ultrason., Ferroelect., Freq. Cont.*, 60(2):273–280, february 2013.

[159] J. Alnis, A. Matveev, N. Kolachevsky, Th. Udem, and T. W. Hänsch. Subhertz linewidth diode lasers by stabilization to vibrationally and thermally compensated ultralow-expansion glass Fabry-Pérot cavities. *Phys. Rev. A*, 77(5):053809, May 2008.

[160] J. Noda, K. Okamoto, and Y. Sasaki. Polarization-maintaining fibers and their applications. *Journal of Lightwave Technology*, 4(8):1071–1089, Aug 1986.

[161] Philip G. Westergaard. *Horloge à rèseau optique au Strontium: en quête de la performance ultime*. PhD thesis, Edite De Paris, 2010.

[162] Takuya Kohno, Masami Yasuda, Kazumoto Hosaka, Hajime Inaba, Yoshiaki Nakajima, and Feng-Lei Hong. One-dimensional optical lattice clock with a fermionic ^{171}yb isotope. *Applied Physics Express*, 2(7):072501, 2009.

[163] Chang Yong Park, Dai-Hyuk Yu, Won-Kyu Lee, Sang Eon Park, Eok Bong Kim, Sun Kyung Lee, Jun Woo Cho, Tai Hyun Yoon, Jongchul Mun, Sung Jong Park, Taeg Yong Kwon, and Sang-Bum Lee. Absolute frequency measurement of ^{1}S$_0$ ($f = 1/2$) - ^{3}P$_0$ ($f = 1/2$) transition of ^{171}Yb atoms in a one-dimensional optical lattice at KRISS. *Metrologia*, 50(2):119, 2013.

[164] Daisuke Akamatsu, Masami Yasuda, Hajime Inaba, Kazumoto Hosaka, Takehiko Tanabe, Atsushi Onae, and Feng-Lei Hong. Frequency ratio measurement of 171yb and 87sr optical lattice clocks. *Opt. Express*, 22(7):7898–7905, Apr 2014.

[165] R. C. Brown, N. B. Phillips, K. Beloy, W. F. McGrew, M. Schioppo, R. J. Fasano, G. Milani, X. Zhang, N. Hinkley, H. Leopardi, T. H. Yoon, D. Nicolodi, T. M. Fortier, and A. D. Ludlow. Hyperpolarizability and operational magic wavelength in an optical lattice clock. *Phys. Rev. Lett.*, 119:253001, Dec 2017.

[166] Huidong Kim, Myoung-Sun Heo, Won-Kyu Lee, Chang Yong Park, Hyun-Gue Hong, Sang-Wook Hwang, and Dai-Hyuk Yu. Improved absolute frequency measurement of the ^{171}yb optical lattice clock at kriss relative to the si second. *Japanese Journal of Applied Physics*, 56(5):050302, 2017.

[167] R. Le Targat, L. Lorini, M. Gurov, M. Zawada, R. Gartman, B. Nagórny, P. Lemonde, and J. Lodewyck. Comparison of two strontium optical lattice clocks in agreement at the 10^{-16} level. In *2012 European Frequency and Time Forum*, pages 19–22, April 2012.

[168] S. G. Porsev, M. S. Safronova, A. Derevianko, and Charles W. Clark. Long-range interaction coefficients for ytterbium dimers. *Phys. Rev. A*, 89:012711, Jan 2014.

[169] J. Lodewyck, M. Zawada, L. Lorini, M. Gurov, and P. Lemonde. Observation and cancellation of a perturbing dc stark shift in strontium optical lattice clocks. *IEEE Transactions on Ultrasonics, Ferroelectrics, and Frequency Control*, 59(3):411–415, 2012.

[170] S. Falke, M. Misera, U. Sterr, and C. Lisdat. Delivering pulsed and phase stable light to atoms of an optical clock. *Applied Physics B*, 107(2):301–311, May 2012.

[171] H.S. Margolis, R.M. Godun, P. Gill, L.A.M. Johnson, S.L. Shemar, P.B. Whibberley, D. Calonico, F. Levi, L. Lorini, M. Pizzocaro, P. Delva, S. Bize, J. Achkar, H. Denker, L. Timmen, C. Voigt, S. Falke, D. Piester, C. Lisdat, U. Sterr, S. Vogt, S. Weyers, J. Gersl, T. Lindvall, and M. Merimaa. International timescales with optical clocks (ITOC). In *European Frequency and Time Forum International Frequency Control Symposium (EFTF/IFC), 2013 Joint*, pages 908–911, July 2013.

[172] Timmen L. Denker H. and Voigt C. Gravity field modelling for optical clock comparisons. In *Earth and Environmental Sciences for Future Generations*, volume Abstract, pages G02p–431. XXVI General Assembly of the International Union of Geodesy and Geophysics (IUGG), 2015. Prague, Czech Republic, 22 June – 02 July 2015.

[173] D Calonico, A Cina, I H Bendea, F Levi, L Lorini, and A Godone. Gravitational redshift at inrim. *Metrologia*, 44(5):L44, 2007.

[174] Heiner Denker, Christian Voigt, and Ludger Timmen. Private communication. -, 2015.

[175] Heiner Denker. *Regional Gravity Field Modeling: Theory and Practical Results*, pages 185–291. Springer Berlin Heidelberg, Berlin, Heidelberg, 2013.

[176] Gérard Petit and Brian Luzum. Iers technical note no. 36. In *IERS Conventions*, Frankfurt am Main: Verl. es Bundesamtes für Kartographie und Geodäsie, 2010.

[177] Erwin Groten. Fundamental parameters and current (2004) best estimates of the parameters of common relevance to astronomy, geodesy, and geodynamics. *Journal of Geodesy*, 77(10):724–797, Apr 2004. IPGD, Darmstadt.

[178] Filippo Levi, Davide Calonico, Claudio E Calosso, Aldo Godone, Salvatore Micalizio, and Giovanni A Costanzo. Accuracy evaluation of itcsf2: a nitrogen cooled caesium fountain. *Metrologia*, 51(3):270, 2014.

[179] D.G. Luenberger. *Optimization by Vector Space Methods*. Wiley, New York, 1998.

[180] M G Cox, C Eiø¸, G Mana, and F Pennecchi. The generalized weighted mean of correlated quantities. *Metrologia*, 43(4):S268, 2006.

[181] H S Margolis and P Gill. Least-squares analysis of clock frequency comparison data to deduce optimized frequency and frequency ratio values. *Metrologia*, 52(5):628, 2015.

[182] Masami Yasuda, Hajime Inaba, Takuya Kohno, Takehiko Tanabe, Yoshiaki Nakajima, Kazumoto Hosaka, Daisuke Akamatsu, Atsushi Onae, Tomonari Suzuyama, Masaki Amemiya, and Feng-Lei Hong. Improved absolute frequency measurement of the ^{171}yb optical lattice clock towards a candidate for the redefinition of the second. *Applied Physics Express*, 5(10):102401, 2012.

[183] N. Huntemann, B. Lipphardt, Chr. Tamm, V. Gerginov, S. Weyers, and E. Peik. Improved limit on a temporal variation of m_p/m_e from comparisons of yb$^+$ and cs atomic clocks. *Phys. Rev. Lett.*, 113:210802, Nov 2014.

[184] R. M. Godun, P. B. R. Nisbet-Jones, J. M. Jones, S. A. King, L. A. M. Johnson, H. S. Margolis, K. Szymaniec, S. N. Lea, K. Bongs, and P. Gill. Frequency ratio of two optical clock transitions in ^{171}yb$^+$ and constraints on the time variation of fundamental constants. *Phys. Rev. Lett.*, 113:210801, Nov 2014.

[185] Fritz Riehle. Towards a redefinition of the second based on optical atomic clocks. *Comptes Rendus Physique*, 16(5):506–515, 2015.

[186] C. W. Chou, D. B. Hume, J. C. J. Koelemeij, D. J. Wineland, and T. Rosenband. Frequency comparison of two high-accuracy Al$^+$ optical clocks. *Phys. Rev. Lett.*, 104:070802, Feb 2010.

[187] Th. Udem, R. Holzwarth, and T. W. Hänsch. Optical frequency metrology. *Nature*, 416(6877):233–237, March 2002.

[188] Long-Sheng Ma, Zhiyi Bi, Albrecht Bartels, Lennart Robertsson, Massimo Zucco, Robert S. Windeler, Guido Wilpers, Chris Oates, Leo Hollberg, and Scott A. Diddams. Optical frequency synthesis and comparison with uncertainty at the 10^{-19} level. *Science*, 303(5665):1843–1845, 2004.

[189] T. Rosenband, D. B. Hume, P. O. Schmidt, C. W. Chou, A. Brusch, L. Lorini, W. H. Oskay, R. E. Drullinger, T. M. Fortier, J. E. Stalnaker, S. A. Diddams, W. C. Swann, N. R. Newbury, W. M. Itano, D. J. Wineland, and J. C. Bergquist. Frequency ratio of Al$^+$ and Hg$^+$ single-ion optical clocks; metrology at the 17th decimal place. *Science*, 319(5871):1808–1812, 2008.

[190] CCTF. Consultative committee for time and frequency. report of the 19th meeting (13–14 september 2012) to the international committee for weights and measures, 2012.

[191] Jean-Philippe Uzan. Varying constants, gravitation and cosmology. *Living Reviews in Relativity*, 14(1):2, Mar 2011.

[192] Martin Vermeer. *Chronometric levelling*. Geodeettinen Laitos, Geodetiska Institutet, 1983.

[193] K. Predehl, G. Grosche, S. M. F. Raupach, S. Droste, O. Terra, J. Alnis, Th. Legero, T. W. Hänsch, Th. Udem, R. Holzwarth, and H. Schnatz. A 920-kilometer optical fiber link for frequency metrology at the 19th decimal place. *Science*, 336(6080):441–444, 2012.

[194] S. B. Koller, J. Grotti, St. Vogt, A. Al-Masoudi, S. Dörscher, S. Häfner, U. Sterr, and Ch. Lisdat. Transportable optical lattice clock with 7×10^{-17} uncertainty. *Phys. Rev. Lett.*, 118:073601, Feb 2017.

[195] G. P. Barwood, G. Huang, H. A. Klein, L. A. M. Johnson, S. A. King, H. S. Margolis, K. Szymaniec, and P. Gill. Agreement between two $^{88}Sr^{+}$ optical clocks to 4 parts in 10^{17}. *Phys. Rev. A*, 89:050501, May 2014.

[196] L. Briatore and S. Leschiutta. Evidence for the earth gravitational shift by direct atomic-time-scale comparison. *Il Nuovo Cimento B (1971-1996)*, 37(2):219–231, Feb 1977.

[197] C. Cecilia, C. Davide, F. Matteo, M. Alberto, and L. Filippo. A fiber link for the remote comparison of optical clocks and geodesy experiments. In *2015 Joint Conference of the IEEE International Frequency Control Symposium the European Frequency and Time Forum*, pages 579–582, April 2015.

[198] Christian Grebing, Ali Al-Masoudi, Sören Dörscher, Sebastian Häfner, Vladislav Gerginov, Stefan Weyers, Burghard Lipphardt, Fritz Riehle, Uwe Sterr, and Christian Lisdat. Realization of a timescale with an accurate optical lattice clock. *Optica*, 3(6):563–569, Jun 2016.

[199] Martin M. Boyd, Andrew D. Ludlow, Sebastian Blatt, Seth M. Foreman, Tetsuya Ido, Tanya Zelevinsky, and Jun Ye. ^{87}sr lattice clock with inaccuracy below 10^{-15}. *Phys. Rev. Lett.*, 98:083002, February 2007.

[200] X. Baillard, M. Fouché, R. Le Targat, P. G. Westergaard, A. Lecallier, F. Chapelet, M. Abgrall, G. D. Rovera, P. Laurent, P. Rosenbusch, S. Bize, G. Santarelli, A. Clairon, P. Lemonde, G. Grosche, B. Lipphardt, and H. Schnatz. An optical lattice clock with spin-polarized ^{87}sr atoms. *The European Physical Journal D*, 48:11–17, 2008.

[201] Gretchen K Campbell, Andrew D Ludlow, Sebastian Blatt, Jan W Thomsen, Michael J Martin, Marcio H G de Miranda, Tanya Zelevinsky, Martin M Boyd, Jun Ye, Scott A Diddams, Thomas P Heavner, Thomas E Parker, and Steven R Jefferts. The absolute frequency of the ^{87}sr optical clock transition. *Metrologia*, 45(5):539, 2008.

[202] F.-L. Hong, M. Musha, M. Takamoto, H. Inaba, S. Yanagimachi, A. Takamizawa, K. Watabe, T. Ikegami, M. Imae, Y. Fujii, M. Amemiya, K. Nakagawa, K. Ueda, and H. Katori. Measuring the frequency of a sr optical lattice clock using a 120 km coherent optical transfer. *Opt. Lett.*, 34(5):692–694, Mar 2009.

[203] St Falke, H Schnatz, J S R Vellore Winfred, Th Middelmann, St Vogt, S Weyers, B Lipphardt, G Grosche, F Riehle, U Sterr, and Ch Lisdat. The ^{87}Sr optical frequency standard at ptb. *Metrologia*, 48(5):399, 2011.

[204] Atsushi Yamaguchi, Nobuyasu Shiga, Shigeo Nagano, Ying Li, Hiroshi Ishijima, Hidekazu Hachisu, Motohiro Kumagai, and Tetsuya Ido. Stability transfer between two clock lasers operating at different wavelengths for absolute frequency measurement of clock transition in ^{87}sr. *Applied Physics Express*, 5(2):022701, 2012.

[205] Kensuke Matsubara, Hidekazu Hachisu, Ying Li, Shigeo Nagano, Clayton Locke, Asahiko Nogami, Masatoshi Kajita, Kazuhiro Hayasaka, Tetsuya Ido, and Mizuhiko Hosokawa. Direct comparison of a ca$^+$ single-ion clock against a sr lattice clock to verify the absolute frequency measurement. *Opt. Express*, 20(20):22034–22041, Sep 2012.

[206] Stephan Falke, Nathan Lemke, Christian Grebing, Burghard Lipphardt, Stefan Weyers, Vladislav Gerginov, Nils Huntemann, Christian Hagemann, Ali Al-Masoudi, Sebastian Häfner, Stefan Vogt, Uwe Sterr, and Christian Lisdat. A strontium lattice clock with 3×10^{-17} inaccuracy and its frequency. *New Journal of Physics*, 16(7):073023, 2014.

[207] Daisuke Akamatsu, Hajime Inaba, Kazumoto Hosaka, Masami Yasuda, Atsushi Onae, Tomonari Suzuyama, Masaki Amemiya, and Feng-Lei Hong. Spectroscopy and frequency measurement of the ^{87}sr clock transition by laser linewidth transfer using an optical frequency comb. *Applied Physics Express*, 7(1):012401, 2014.

[208] H. Hachisu, M. Fujieda, S. Nagano, T. Gotoh, A. Nogami, T. Ido, St. Falke, N. Huntemann, C. Grebing, B. Lipphardt, Ch. Lisdat, and D. Piester. Direct comparison of optical lattice clocks with an intercontinental baseline of 9000 km. *Opt. Lett.*, 39(14):4072–4075, Jul 2014.

[209] Lin Yi-Ge, Wang Qiang, Li Ye, Meng Fei, Lin Bai-Ke, Zang Er-Jun, Sun Zhen, Fang Fang, Li Tian-Chu, and Fang Zhan-Jun. First evaluation and frequency measurement of the strontium optical lattice clock at nim. *Chinese Physics Letters*, 32(9):090601, 2015.

[210] Takehiko Tanabe, Daisuke Akamatsu, Takumi Kobayashi, Akifumi Takamizawa, Shinya Yanagimachi, Takeshi Ikegami, Tomonari Suzuyama, Hajime Inaba, Sho Okubo, Masami Yasuda, Feng-Lei Hong, Atsushi Onae, and Kazumoto Hosaka. Improved frequency measurement of the $^1\mathrm{S}_0 - ^3\mathrm{P}_0$ clock transition in ^{87}Sr using a cs fountain clock as a transfer oscillator. *Journal of the Physical Society of Japan*, 84(11):115002, 2015.

[211] Jerome Lodewyck, Slawomir Bilicki, Eva Bookjans, Jean-Luc Robyr, Chunyan Shi, Gregoire Vallet, Rodolphe Le Targat, Daniele Nicolodi, Yann Le Coq, Jocelyne Guena, Michel Abgrall, Peter Rosenbusch, and Sebastien Bize. Optical to microwave clock frequency ratios with a nearly continuous strontium optical lattice clock. *Metrologia*, 53(4):1123, 2016.

[212] Hidekazu Hachisu, Gérard Petit, and Tetsuya Ido. Absolute frequency measurement with uncertainty below 1×10^{-15} using international atomic time. *Applied Physics B*, 123(1):34, Dec 2016.

[213] Hidekazu Hachisu, Gérard Petit, Fumimaru Nakagawa, Yuko Hanado, and Tetsuya Ido. Si-traceable measurement of an optical frequency at the low 10^{-16} level without a local primary standard. *Opt. Express*, 25(8):8511–8523, Apr 2017.

[214] Gianmaria Milani, Benjamin Rauf, Piero Barbieri, Filippo Bregolin, Marco Pizzocaro, Pierre Thoumany, Filippo Levi, and Davide Calonico. Multiple wavelength stabilization on a single optical cavity using the offset sideband locking technique. *Opt. Lett.*, 42(10):1970–1973, May 2017.

[215] P D Gregory, P K Molony, M P Köppinger, A Kumar, Z Ji, B Lu, A L Marchant, and S L Cornish. A simple, versatile laser system for the creation of ultracold ground state molecules. *New Journal of Physics*, 17(5):055006, 2015.

[216] D. M. S. Johnson, J. M. Hogan, S. w. Chiow, and M. A. Kasevich. Broadband optical serrodyne frequency shifting. *Opt. Lett.*, 35(5):745–747, Mar 2010.

[217] J. I. Thorpe, K. Numata, and J. Livas. Laser frequency stabilization and control through offset sideband locking to optical cavities. *Opt. Express*, 16(20):15980–15990, Sep 2008.

[218] R. W. P. Drever, J. L. Hall, F. V. Kowalski, J. Hough, G. M. Ford, A. J. Munley, and H. Ward. Laser phase and frequency stabilization using an optical resonator. *Appl. Phys. B*, 31(2):97–105, June 1983.

[219] A. Nevsky, S. Alighanbari, Q.-F. Chen, I. Ernsting, S. Vasilyev, S. Schiller, G. Barwood, P. Gill, N. Poli, and G. M. Tino. Robust frequency stabilization of multiple spectroscopy lasers with large and tunable offset frequencies. *Opt. Lett.*, 38(22):4903–4906, Nov 2013.

[220] T Toyoda and M Yabe. The temperature dependence of the refractive indices of fused silica and crystal quartz. *Journal of Physics D: Applied Physics*, 16(5):L97, 1983.

[221] E. A. Donley, T. P. Heavner, F. Levi, M. O. Tataw, and S. R. Jefferts. Double-pass acousto-optic modulator system. *Rev. Sci. Inst.*, 76(6):063112, 2005.

[222] S.T. Dawkins, J.J. McFerran, and A.N. Luiten. Considerations on the measurement of the stability of oscillators with frequency counters. *IEEE Trans. Ultrason., Ferroelect., Freq. Cont.*, 54(5):918–925, 2007.

[223] C. E. Calosso, C. Clivati, and S. Micalizio. Avoiding aliasing in allan variance: An application to fiber link data analysis. *IEEE Transactions on Ultrasonics, Ferroelectrics, and Frequency Control*, 63(4):646–655, April 2016.

[224] Patrick Gill. Is the time right for a redefinition of the second by optical atomic clocks? *Journal of Physics: Conference Series*, 723(1):012053, 2016.

[225] H. S. Margolis. Optical frequency standards and clocks. *Contemporary Physics*, 51(1):37–58, 2010.

[226] D G Matei, T Legero, Ch Grebing, S Haefner, Ch Lisdat, R Weyrich, W Zhang, L Sonderhouse, J M Robinson, F Riehle, J Ye, and U Sterr. A second generation of low thermal noise cryogenic silicon resonators. *Journal of Physics: Conference Series*, 723(1):012031, 2016.

[227] C. Hagemann, C. Grebing, T. Kessler, S. Falke, N. Lemke, C. Lisdat, H. Schnatz, F. Riehle, and U. Sterr. Providing 10^{-16} short-term stability of a $1.5-\mu$m laser to optical clocks. *IEEE Transactions on Instrumentation and Measurement*, 62(6):1556–1562, June 2013.

[228] D. Nicolodi, B. Argence, W. Zhang, R. Le Targat, G. Santarelli, and Y. Le Coq. Spectral purity transfer between optical wavelengths at the 10^{-18} level. *Nature Photonics*, 8(-):219–223, January 2014.

[229] B. Lipphardt, G. Grosche, U. Sterr, C. Tamm, S. Weyers, and H. Schnatz. The stability of an optical clock laser transferred to the interrogation oscillator for a cs fountain. *IEEE Transactions on Instrumentation and Measurement*, 58(4):1258–1262, 2009.

[230] H. Leopardi, J. Davila-Rodriguez, F. Quinlan, S. Diddams, and T. Fortier. Er:fiber frequency comb for synthesis of optical frequencies at the 10^{-18} level. In *2016 IEEE Photonics Conference (IPC)*, pages 186–187, Oct 2016.

[231] Hajime Inaba, Kazumoto Hosaka, Masami Yasuda, Yoshiaki Nakajima, Kana Iwakuni, Daisuke Akamatsu, Sho Okubo, Takuya Kohno, Atsushi Onae, and Feng-Lei Hong. Spectroscopy of ^{171}yb in an optical lattice based on laser linewidth transfer using a narrow linewidth frequency comb. *Opt. Express*, 21(7):7891–7896, Apr 2013.

[232] Yoshiaki Nakajima, Hajime Inaba, Kazumoto Hosaka, Kaoru Minoshima, Atsushi Onae, Masami Yasuda, Takuya Kohno, Sakae Kawato, Takao Kobayashi, Toshio Katsuyama, and Feng-Lei Hong. A multi-branch, fiber-based frequency comb with millihertz-level relative linewidths using an intra-cavity electro-optic modulator. *Opt. Express*, 18(2):1667–1676, Jan 2010.

[233] V.J. Matsas, T.P. Newson, D.J. Richardson, and D.N. Payne. Self-starting, passively mode-locked fibre ring soliton laser exploiting non-linear polarisation rotation. *Electronics Letters*, 28(15):1391–1393, 1992.

[234] M. Nakazawa, E. Yoshida, T. Sugawa, and Y. Kimura. Continuum suppressed, uniformly repetitive 136 fs pulse generation from an erbium-doped fibre laser with nonlinear polarisation rotation. *Electronics Letters*, 29:1327–1329(2), July 1993.

[235] R. H. Stolen and Chinlon Lin. Self-phase-modulation in silica optical fibers. *Phys. Rev. A*, 17:1448–1453, Apr 1978.

[236] F. M. Mitschke and L. F. Mollenauer. Discovery of the soliton self-frequency shift. *Opt. Lett.*, 11(10):659–661, Oct 1986.

[237] Tonglei Cheng, Lei Zhang, Xiaojie Xue, Dinghuan Deng, Takenobu Suzuki, and Yasutake Ohishi. Broadband cascaded four-wave mixing and supercontinuum generation in a tellurite microstructured optical fiber pumped at 2 μm. *Opt. Express*, 23(4):4125–4134, Feb 2015.

[238] Takao Fuji, Alexander Apolonski, and Ferenc Krausz. Self-stabilization of carrier-envelope offset phase by use of difference-frequency generation. *Opt. Lett.*, 29(6):632–634, Mar 2004.

[239] F.W. Helbing, G. Steinmeyer, J. Stenger, H.R. Telle, and U. Keller. Carrier–envelope-offset dynamics and stabilization of femtosecond pulses. *Applied Physics B*, 74(1):s35–s42, 2002.

[240] J.-L. Peng, H. Ahn, R.-H. Shu, H.-C. Chui, and J.W. Nicholson. Highly stable, frequency-controlled mode-locked erbium fiber laser comb. *Applied Physics B*, 86(1):49–53, 2007.

[241] Erik Benkler, Christian Lisdat, and Uwe Sterr. On the relation between uncertainties of weighted frequency averages and the various types of allan deviations. *Metrologia*, 52(4):565, 2015.